Ionospheric Scintillation Sensitive GNSS Tracking Error Models and Mitigation Approaches

By

Kai Guo

MSc Eng

A THESIS
SUBMITTED TO THE UNIVERSITY OF NOTTINGHAM
FOR THE DEGREE OF DOCTOR OF PHILOSOPHY

NOTTINGHAM GEOSPATIAL INSTITUTE

NOTTINGHAM, UK
March 2021

Abstract

Ionospheric scintillation refers to the rapid and random fluctuations in intensity and phase of radio frequency signals when they propagate through plasma density irregularities in the ionosphere. It is more frequently observed in the auroral to polar regions and the equatorial to low latitude regions. When scintillation occurs on Global Navigation Satellite System (GNSS), the GNSS signal quality and receiver performance can be significantly degraded, thus increasing the errors in positioning and navigation. Under strong scintillation, the GNSS receiver can even lose the lock on the signals, posing serious threats to safety-critical GNSS applications and precise positioning.

For a better understanding of scintillation effects on GNSS signals and receivers, as well as to mitigate the scintillation effects on GNSS positioning, research is carried out in this thesis focusing on the following three aspects: (1) characterizing the GNSS signal intensity fadings under scintillation, (2) modelling scintillation effects on GNSS receiver tracking loops and (3) developing scintillation mitigation approaches to support high accuracy GNSS positioning under scintillation.

Signal intensity fadings is one of the reasons that degrade the GNSS receiver tracking performance. By exploiting three months of raw scintillation data recorded by an ionospheric scintillation monitoring receiver (ISMR) deployed at low latitudes, signal intensity fadings due to scintillation are detected and characterized. Their effects on receiver tracking performance are analysed, which contributes to better understanding the low latitude scintillation effects on GNSS receivers. In order to quantitatively model the scintillation effects on GNSS receiver Phase Locked Loops (PLLs) and Delayed Locked Loop (DLLs), the phase and code jitter are estimated, respectively, at the output of PLL and DLL, taking scintillation effects into consideration. The existing models to estimate the phase and code jitters are studied. To address the concerns of the existing models, an alternative approach is developed to estimate the phase and code jitter under scintillation using the output of tracking loop discriminators, which better reflects the actual PLL and DLL tracking performance under scintillation. Additionally, the distribution of the tracking errors are analysed in the presence of scintillation. A customer-defined probability density function is proposed for the first time, which successfully describes the distribution of the PLL tracking errors under different levels of scintillation.

The approach to mitigate scintillation effects on GNSS positioning is studied. This thesis employs a phase and code jitter weighting approach to reduce the positioning errors caused by scintillation. In this approach, the positioning stochastic models are improved using the estimated phase and code jitter values considering scintillation effects. In order to improve the performance of this approach, 1-second scintillation indices are proposed in this thesis, which shows more effectiveness in describing the signal fluctuations under scintillation compared with the widely used 1-minute scintillation indices. Additionally, the 1-second scintillation indices outperform the 1-minute ones when used in mitigating positioning errors under scintillation. To implement the scintillation mitigation approach on generic receivers, which are not able to estimate the scintillation indices and consequently the phase and code jitter, the concept of phase and code jitter maps is exploited in this thesis. In this way, generic receivers can extract and calculate the jitter values directly from these maps for each measurement. Regional phase and code jitter maps are constructed in northern Canada using the scintillation data recorded during the geomagnetic storm in September 2017. Results show that with the help of the jitter maps constructed in this thesis, the positioning accuracy at both the ISMR and generic receiver stations can be greatly improved under scintillation.

List of publications

The list includes the published and submitted peer reviewed publications presentations evolved from the research in this thesis.

Guo K, Vadakke Veettil S, Weaver B, Aquino M (2021) Mitigating high latitude ionospheric scintillation effects on GNSS Precise Point Positioning exploiting 1-second scintillation indices. Journal of Geodesy 95(3):1-15. https://doi.org/10.1007/s00190-021-01475-y

Guo K, Aquino M, Vadakke Veettil S (2020) Effects of GNSS receiver tuning on the PLL tracking jitter estimation in the presence of ionospheric scintillation. Space Weather 18:e2019SW002362. https://doi.org/10.1029/2019SW002362

Guo K, Aquino M, Vadakke Veettil S (2019) Ionospheric scintillation intensity fading characteristics and GPS receiver tracking performance at low latitudes. GPS Solutions 23(2):43. https://doi.org/10.1007/s10291-019-0835-1

Guo K, Aquino M, Vadakke Veettil S, Liu Z, Chen W, Antonio MH (2019) Analysis of ionospheric scintillation and its impact on PPP at low latitudes. In: Proceedings of the ION 2019 Pacific PNT Meeting, Honolulu, Hawaii, April 2019, pp.835-845. https://doi.org/10.33012/2019.16842

Acknowledgements

I would like to sincerely thank my supervisor Dr. Marcio Aquino for his professional suggestions, strong support and continued encouragement on my research. He was kind and friendly, and positively impacted me on my study and daily life. He has been continuing following my thesis writing up and helping to review my thesis since he retired in August 2020. It was my great honour to work with him in my Ph.D. journey.

I wish to thank my co-supervisor Dr. Sreeja Vadakke Veettil, who was always ready to help and responded my questions promptly. Her suggestions were influential in shaping my experiment methods. I want to thank my co-supervisor Dr. Paul Blunt, who helped to review my thesis and contributed many valuable suggestions. I also thank my co-supervisor Dr. Chris Hill who advised me in the first year of my Ph.D. and helped me with the data collection experiment personally.

I would like to thank my colleagues and friends in Nottingham Geospatial Institute. Thanks to Dr. Lei Yang for the helpful discussions throughout my whole Ph.D. period. Thanks to Brian Weaver who provides the support for the PPP software used in this thesis. Thanks to Prof. Xiaolin Meng, Yijian Cui, Dr. Muhammad Ammar, Dr. Francesco Basile, Lei Zhao from NGI, Dr. Xiangdong An and Dr. Fei Yang from Wuhan University, Dr. Wang Gao and Rui Shang from Southeast University, Dr. Giz Gulnerman from Istanbul Technical University, to be good friends and for the good memories together. They made my study and life in UK more wonderful.

I thank all the TREASURE family. Thanks to Dr. Wenjian Qin and Dr. Caner Savas from Politecnico di Torino, Dr. Hongyang Ma from Delft University of Technology, Juliana Garrido

Damaceno from Istituto Nazionale di Geofisica e Vulcanologia (INGV) in Italy, for doing the collaborations in the TREASURE project. It was my pleasure to work with you.

I would like to thank Prof. João Francisco Galera Monico at Sao Paulo State University (UNESP) in Brazil, Prof. Wu Chen and Prof. Zhizhao Liu at The Hong Kong Polytechnic University (PolyU) in Hong Kong, China, Prof. Fabio Dovis at Politecnico di Torino in Italy, for providing the professional training during the secondments. Thanks to Dr. Bruno Vani and Italo Tsuchiya from UNESP, Dr. Junhua Ye, Dr. Jing Qiao and Dr. Wenfeng Nie from PolyU for the great help during my visiting in their group. Thanks to Dr. Jean-Marie Sleewaegen from Septentrio Satellite Navigation for the technique support for the research in this thesis. Thanks to Dr. Yang Liu from Beihang University and Prof. Weidong Yang from Hebei University of Technique for the support and guidance during my study in UK.

Finally, I would like to thank my family and friends in China for their constant support. Thanks to my girlfriend Yueyue Qiu for supporting and accompanying me to finish this thesis.

Dedicated to those people who sacrificed themselves in the combat of COVID-19.

Table of contents

List of tables

List of figures

List of acronyms

ADC	A/D convert
AGC	Automatic Gain Control
BDS	BeiDou Navigation Satellite System
BOC	Binary Offset Carrier
BPSK	Binary Phase Shift Keying
CALIBRA	Countering GNSS high Accuracy applications Limitations due to Ionospheric disturbances in Brazil
CHAIN	Canadian High Arctic Ionospheric Network
CIGALA	Concept for Ionospheric Scintillation Mitigation for Professional GNSS in Latin America
CODE	Centre for Orbit Determination in Europe
$C/N0$	Carrier to Noise Density Ratio
DCB	Differential Code Bias
DIA	Detection Identification Adaptation
DLL	Delayed Locked Loop
DOY	Day of Year
EIA	Equatorial Ionization Anomaly
ESR	Early Stage Researcher
FLL	Frequency Locked Loop
GISTM	GPS Ionospheric Scintillation and TEC Monitor

GNSS	Global Navigation Satellite System
GPS	Global Positioning System
GUI	Graphical User Interface
HDOP	Horizontal Dilution of Precision
IF	Intermediate Frequency
ISMR	Ionospheric Scintillation Monitoring Receiver
IPP	Ionosphere Pierce Points
KF	Kalman Filter
MWWL	Melbourne-Wübbena Wide-Lane
NCO	Numerical Control Oscillators
OTL	Ocean Tide Loading
PCV	Phase Centre Variation
PDF	Probability Density Function
PLL	Phase Locked Loop
PPP	Precise Point Positioning
PRN	Pseudorandom Noise
PSD	Power Spectral Density
RAIM	Receiver Autonomous Integrity Monitoring
RF	Radio Frequency
RFCS	Radio Frequency Constellation Simulator
RFE	Radio Front-End
RMS	Root Mean Square
RTK	Real-Time Kinematic
SAMA	South Atlantic Magnetic Anomaly
SBAS	Satellite-Based Augmentation System

SDR	Software defined radio
TECR	Total Electron Contents Rate
TREASURE	Training REsearch and Applications Network to Support the Ultimate Real-Time High Accuracy EGNSS Solution
WAAS	Wide Area Augmentation System
WP	Work Package

1 Introduction

The ionosphere is an ionized region in the earth's upper atmosphere from about 50 to 1000 km above the earth surface containing a large number of ions and electrons caused by solar radiation effects. The ionosphere has adverse effects on communication and navigation systems, such as Global Navigation Satellite System (GNSS), including Global Positioning System (GPS), GLONASS, Galileo and BeiDou Navigation Satellite System (BDS), which rely on the Radio Frequency (RF) signals broadcasted from the satellites in space to provide position, velocity, and time (PVT). On one hand, the transmission direction and speed of RF signals may change due to the variation in the refractive index of the ionosphere. As a result, a delay or advance in the signal transmission may occur, which can induce large errors in GNSS measurements, and accordingly decrease positioning accuracy. On the other hand, due to ionospheric plasma density irregularities, the amplitude and phase of RF signals may suffer random and rapid fluctuations, a phenomenon known as ionospheric scintillation. When scintillation occurs, GNSS measurements become nosier or even unavailable, thus degrading positioning accuracy. With the implementation of dual-frequency GNSS receivers, measurement errors caused by ionospheric delay can be estimated and mostly corrected. However, scintillation remains a major challenge to GNSS performance.

The occurrence of scintillation is associated with the solar and geomagnetic activities (Aarons et al. 1980). During the peaks of the solar cycle, the ionospheric turbulent plasma becomes more active, thus the propagation of GNSS signals is more affected. Similarly, the occurrence of geomagnetic storms encourages the formation and movement of ionospheric irregularities, which correspondingly increases the probability of scintillation occurrence. Scintillation occurrence has strong spatial dependencies. It is more frequent in the auroral and polar regions as well as in the equatorial and low latitude regions (Aarons 1982; Basu et al. 1988). However, the mechanism that govern the generation of scintillation in these regions are different. In the auroral to polar regions, scintillation is associated with the fast movement of large-scale ionospheric plasma structures along geomagnetic field lines (Basu et al. 2002; Forte and Radicella 2002) and is usually dominated by phase fluctuations (Jiao and Morton 2015). It can be significantly active during geomagnetic storms and can occur at any time of the day. On the other hand, equatorial and low latitude scintillation is associated with the post-sunset small-scale F-region irregularities and can be severe in both signal intensity and phase (Basu et al. 2002; Hysell and Kudeki 2004; Jiao and Morton 2015). Thus, scintillation at equatorial and low latitudes mostly occurs between post-sunset to midnight period. Additionally, scintillation occurrence presents large day-to-day variabilities. During vernal and autumnal equinoxes, there is a higher probability of scintillation occurrence at equatorial and low latitudes.

Scintillation is usually distinguished as amplitude and phase scintillation, respectively referring to the fluctuations in signal amplitudes and phases, and characterized by $S4$ and $Phi60$ indices (Briggs and Parkin 1963; Yeh and Liu 1982). Scintillation indices are used to measure the scintillation levels observed RF signals crossing the ionospheric irregularities. Meanwhile, these indices also provides a way to study the ionospheric climatology.

Scintillation adversely affects the GNSS signal quality, availability and receiver performance. In a strong scintillation scenario, receivers can even lose lock on the GNSS signals due to the deep intensity fading and/or the fast phase dynamics, posing serious threats to safety critical GNSS applications and precise positioning. The aims of this thesis are (1) characterization of GNSS signal intensity fadings under scintillation, (2) modelling of scintillation effects on receivers and (3) development of scintillation mitigation approaches, aiming to realize high accuracy GNSS positioning. In this chapter, a literature review on scintillation effects on receivers and scintillation mitigation approaches is given. The limitations of the previous studies are provided. The objectives of this thesis and the main achievements are summarised next, followed by a description of the thesis outline.

1.1 Literature review and limitations of previous work

GNSS receivers are used to track signals transmitted by GNSS satellites and to extract measurements that can be used for positioning. Thus, the availability and quality of GNSS signals strongly impact the performance of receivers and the accuracy of positioning. Extensive research effort has been placed to analyse and model the scintillation effects on receivers and positioning performance. Various approaches have been developed in the last decade aiming to improve the positioning accuracy under scintillation.

1.1.1 Scintillation effects on GNSS receivers

The effects of scintillation on GNSS receivers occur notably at receiver tracking stages. Under scintillation, the intensity of the signal arriving at the receivers could suffer abrupt deep fadings. When the intensity is lower than the signal carrier to noise density ratio ($C/N0$) threshold in the receiver Delayed Locked Loop (DLL), a loss of lock or cycle slip event is declared, leading to the unavailability of GNSS measurements. In carrier tracking loops, phase fluctuations caused by scintillation increase the noise levels of the carrier phase measurements. Frequent cycle slips may occur under severe phase dynamics. The analysis of scintillation impacts on receiver tracking loops has drawn extensive attention over the years. Skone et al. (2001) investigated the scintillation effects on different GPS receivers deployed at both equatorial and high latitudes. It was pointed out that the tracking performance of receivers above 62° geographic latitudes and close to the anomaly peak are more susceptible to scintillation. The difference in receiver tracking loop configurations and tracking loop models could result in large differences in tracking performance even under comparable levels of scintillation. Hegarty et al. (2001) investigated the GPS-Wide Area Augmentation System

(WAAS) receiver performance with a proposed scintillation simulation model. Results showed that the non-coherent DLLs are more robust to scintillation, while carrier tracking loops are more affected. Based on the scintillation data recorded in the European Arctic region during the November 2004 storms, Meggs et al. (2008) concluded that the losses of lock events in GPS receivers are more closely related to the rapid phase fluctuations caused by scintillation. Humphreys et al. (2010) used a scintillation testbed to study the carrier phase tracking error variance and the performance of the Phase Locked Loop (PLL) under scintillation. A cycle slip prediction model was developed as a function of scintillation index, signal decorrelation time and $C/N0$. By analysing the scintillation data collected at Presidente Prudente in Brazil, Sreeja et al. (2012) studied the correlation between scintillation levels and GPS and GLONASS signal tracking performance. It was shown that scintillation has more significant effects on signals with lower transmitting frequency. The relationship between scintillation levels and the PLL tracking errors can also be represented by a quadratic function. Breitsch et al. (2020) investigated the dependence of the cycle slip rate on scintillation, intensity fading and $C/N0$, using simulated strong equatorial scintillation data. It was pointed out that phase transition is the dominant reason for cycle slips in the presence of scintillation.

Signal intensity fading is one of the main challenges that affect the signal tracking in receivers under scintillation. Based on one month's scintillation data collected at low latitudes, Moraes et al. (2012) investigated the characteristics of intensity fading and its effects on GPS receiver tracking loops. They concluded that a GPS receiver with the $C/N0$ threshold around or higher than 30 dB-Hz could be severely influenced by deep fading caused by scintillation. Furthermore, 45 minutes of 50 Hz scintillation data were analysed by Seo et al. (2016) to characterize the signal fading behaviour. A fading duration model was built which is important for designing an aviation receiver with short reacquisition time to counter the adverse scintillation effects. To investigate the signal intensity fading characteristics on GPS L1, L2 C and L5 signals in the equatorial region, Jiao et al. (2016) analysed the scintillation data collected on Ascension Island in 2013. Results showed that the fading rarely occurs on all GPS bands simultaneously. These analyses on signal intensity fading were mostly based on scintillation data collected within a short period of time and lacking severe scintillation events. In addition, the relationship between intensity fading and tracking loop performance was not fully investigated.

To quantify the effects of scintillation on GNSS receivers, jitter estimation models were developed in Knight and Finn (1998) and Conker et al. (2003), which are capable of evaluating the PLL phase jitter and the DLL code jitter for GPS L1 C/A and L2 P signals using the measured scintillation indices. In these models, the probability density function (PDF) of signal intensity under scintillation is assumed to follow the Nakagami-m fading channel. Following the approach in Conker et al. (2003), Moraes et al. (2014) further improved these models by applying a different fading channel model in characterizing the signal intensity distribution under scintillation. Vadakke Veettil et al. (2018) built statistical models to estimate the standard deviation of the receiver PLL tracking errors as a function of scintillation levels exploiting the models in Conker et al. (2003) and Moraes et al. (2014), using the scintillation data recorded over 4 years at low and high latitudes. These jitter estimation models have been used by many researchers to describe the scintillation effects on receiver tracking loops (Strangeways et al. 2011; Sreeja et al. 2012; Aquino and Sreeja 2013). However, there are still concerns regarding these models. For example, these models assume that the phase or code errors are in the linearity region of PLL and DLL discriminators, while this assumption may not always be true in practice, particularly under severe scintillation conditions. Additionally, the jitter estimated using these models depends on the configurations of the receiver tracking loops. Receivers with different tracking loops might produce a different phase and code jitter even under comparable scintillation levels. Thus, it is necessary to investigate how the tracking loop tuning could influence the jitter estimation using these models. A detailed description of the limitations inherent to these models is given in Chapter 4.

1.1.2 Mitigating scintillation effects on GNSS positioning

Effects of scintillation on GNSS positioning have been extensively studied. Datta-Barua et al. (2003) investigated the scintillation effects on single and dual frequency GPS based positioning using two weeks of scintillation data recorded in February 2002 in Brazil. They pointed out that the single frequency positioning can experience frequent changes in the position estimation due to the loss of L1 data, while for dual frequency positioning, the fact that the L2 signal is more susceptible to loss of lock and cycle slips induces positioning errors or even failure of position estimation during scintillation. By analysing the scintillation data collected in Northern Europe during the solar maximum from 2001 to 2003, Aquino et al. (2005) presented the potential implications of scintillation for GNSS users. It was shown that the loss of satellite locks is correlated with the occurrence of scintillation. The accuracy of the static carrier phase positioning is degraded under phase scintillation. Based on 7 years of GPS scintillation data collected at eight low latitude scintillation monitoring stations, Steenburgh et al. (2008) investigated the variation of the Horizontal Dilution of Precision (HDOP) under scintillation. The results showed that if GPS signals suffering from moderate scintillation are removed, the position cannot be estimated at times and the remaining HDOP values could reach more than 10. Xu et al. (2012) analysed the impacts of low latitude scintillation on Precise Point Positioning (PPP) by processing the GPS scintillation data collected in July and August 2012 in Hong Kong. It was found that the positioning errors can reach more than 34 cm in the vertical and more than 20 cm in the horizontal directions in the presence of severe scintillation. Jacobsen and Andalsvik (2016) analysed the impact of ionospheric disturbances on the network real-time kinematic (NRTK) positioning and PPP techniques by processing the data collected in the Norway region during the 2015 St. Patrick’s day storm. Increased positioning errors calculated by RTK and PPP were observed under ionospheric disturbances, while PPP can achieve a higher accuracy compared with the NRTK positioning. Pi et al. (2017) calculated the kinematic PPP using the data recorded by an ionospheric scintillation monitoring receiver (ISMR) deployed in Alaska in 2013. It was suggested that the dual-frequency PPP errors could be one to two orders of magnitude worse under scintillation. Both cycle slips and/or losses of carrier phase lock induced by scintillation can increase the positioning errors. Juan et al. (2018) investigated the scintillation effects on GNSS positioning by processing data collected from 35 receivers at low and high latitudes. Results show that due to the fact that the generation of scintillation at low and high latitudes have different mechanisms, its impacts on GNSS positioning also differ. At high latitudes, cycle slips caused by scintillation are less frequent, thus it is possible to achieve precise positioning even during strong scintillation. By contrast, scintillation at low latitudes is more severe and produces more cycle slips, thus achieving precise positioning is more challenging. The effects of low-latitude scintillation on BDS were investigated by Luo et al. (2018). It was found that the code and phase residuals of static PPP processing could reach up to 7.096 and -0.469 m, respectively.

Various approaches have been studied to mitigate scintillation effects on GNSS positioning. The modern GNSS signals and multi-GNSS positioning techniques provide an opportunity to increase the available satellite observations for users under scintillation. Marques et al. (2016) investigated the performance of using GPS L2 C measurements in kinematic PPP calculation instead of using L2 P under equatorial scintillation. Results showed that using L2 C against L2 P can improve the positioning accuracy by up to 59% under weak scintillation, while no improvement is observed under strong scintillation conditions. Furthermore, Marques et al. (2018) analysed the integrated GPS and GLONASS kinematic PPP technique under different scintillation levels in the equatorial region. It was suggested that compared with GPS-only PPP, a multi-GNSS solution could improve the positioning accuracy by up to 60% under strong scintillation. Similar experiments were conducted in Dabove et al. (2019), which investigated the benefits of multi-GNSS positioning under high latitude ionospheric activity. Results showed that adding GLONASS and Galileo satellites in positioning could both improve the positioning accuracy and reduce the convergence time in PPP calculation. However, the effectiveness of these approaches largely depends on the severity of scintillation conditions. During the solar maximum, a large percent of all the visible satellites may suffer from scintillation at a same epoch at low latitudes (Guo et al. 2019b), thus the positioning accuracy may still be significantly degraded even with multi-GNSS positioning.

In order to better detect cycle slips under scintillation, an improved cycle slip detection approach was proposed in Zhang et al. (2014), which helped to avoid unnecessary reinitialization of phase ambiguity and to achieve a positioning accuracy of 0.2 to 0.3 m in the vertical direction under equatorial scintillation. A similar approach was proposed in Luo et al. (2019), where an improved cycle slip threshold model was developed to decrease the frequent false alarm of cycle slip under scintillation. With the improved model, the accuracy improved by up to 47.9 % in the up direction of BDS PPP. A new scintillation index was proposed in Juan et al. (2017) using the ionospheric-free combination of the phase measurements. The proposed index can help to isolate the measurements suffering cycle slips, thus the positioning errors under ionospheric disturbances are only due to the increased phase measurement noise. Furthermore, to detect and remove the measurements affected by scintillation, Bougard et al. (2013) applied the receiver autonomous integrity monitoring (RAIM) method in the PPP calculation under scintillation observed in Brazil. Although results showed that the method can help to mitigate the scintillation effects on positioning by different extents, the performance of this approach is affected by the amount and locations of the excluded satellites in relation to the overall satellite geometry (Vadakke Veettil et al. 2020), as the positioning accuracy depends on the resulting satellite geometry. Instead of removing the measurements affected by scintillation, an approach to modify the least square stochastic models in positioning was introduced in Aquino et al. (2009). In this approach, the stochastic models are modified using the receiver PLL phase jitter and DLL code jitter, estimated by the models developed in Conker et al. (2003). In the improved stochastic models, the carrier phase and pseudorange measurement noise levels are represented, respectively, by the phase and code jitter, thus measurements more affected by scintillation will have higher jitter levels and lower weights in the stochastic model, which results in a decreased contribution of the measurements affected by scintillation to the position estimation.

This mitigation approach has been applied successful in many studies (da Silva et al. 2010; Strangeways et al. 2011; Park et al. 2017; Vani et al. 2019; Luo et al. 2020; Vadakke Veettil et al. 2020). However, its inherent limitations still remain. On one hand, the 1-minute phase and code jitter, estimated based on the 1-minute scintillation indices, are used to represent the noise levels of GNSS instantaneous measurements in this approach. Based on the analysis in this thesis, it is found that the 1-minute phase and code jitter may not provide the best representation of the measurement noise. It is necessary to calculate the phase and code jitter at a higher rate, which depends on a higher rate of scintillation indices. On the other hand, as scintillation indices are required in the estimation of the phase and code jitter, this mitigation approach has so far been used only in connection with ISMRs. For generic receivers, which are not capable of estimating scintillation indices and consequently the phase and code jitter, this mitigation approach cannot be implemented directly. Consequently, a new scintillation mitigation approach or tool is required to provide the phase and code jitter values to generic receivers. For example, a generic receiver can obtain the jitter values from a nearby ISMR, as these two receivers would experience similar scintillation levels if they are close enough. Or the generic receiver can estimate the phase and code jitter values through alternative approaches which do not involve scintillation index calculation, e.g., the mathematical phase jitter estimation models developed in Vadakke Veettil et al. (2018). Another possible solution is to exploit the concept of phase and code jitter maps (Sreeja et al. 2011), which contain the phase and code jitter values verticalized to the ionospheric layer. In this way, a generic receiver can retrieve the jitter values for each measurement directly from these maps, and thus implement them in the aforementioned mitigation approach. A detailed description of using the phase and code jitter maps for scintillation mitigation can be found in Chapter 6.

1.2 Thesis objectives and main achievements

The major objectives of this thesis are summarised as follows:

1) **Characterize GNSS signal intensity fading under scintillation and investigate its effects on receiver tracking loops**

   Signal intensity fading is one of the main factors leading to the degradation of the GNSS receiver tracking performance. For a better understanding of the intensity fading characteristics under scintillation, the fading depth, duration and speed, which is defined as the ratio between fading depth to duration, are analysed. The relationship between the widely used scintillation indices and the intensity fading characteristics is studied. In order to analyse how the signal intensity fading degrades the receiver tracking performance, the variation of tracking errors in relation to fading depth, duration and speed is analysed.

2) **Develop alternative approaches to measure the scintillation effects on receiver PLL and DLL tracking loops**

   Although the effects of scintillation on receiver tracking loops can be evaluated by using the jitter estimation models developed in Conker et al. (2003), there are still some limitations and concerns, as mentioned previously. To address the concern, alternative approaches to estimate the phase and code jitter under scintillation are developed, which can be used to verify the accuracy of the jitter estimation models described in Conker et al. (2003). Additionally, the distribution of the tracking errors under scintillation is investigated and modelled, thus providing a method to quantify the effects of scintillation on receiver tracking loops.

3) **Investigate the receiver tuning effects on the receiver tracking performance under scintillation**

   As previously discussed, the tracking performance of receivers may vary even under similar levels of scintillation, due to the differences in their tracking loop configurations. Thus, the scintillation induced phase and code tracking errors calculated for receivers with various tracking loop configurations are analysed, aiming to investigate and better understand the receiver tracking loop tuning effects on the tracking performance in the presence of scintillation.

4) **Develop an approach to calculate 1-second scintillation indices based on the raw scintillation data recorded by ISMRs**

   To more accurately describe the signal fluctuation levels under scintillation, as well as to calculate the phase and code jitter at a higher rate, e.g., 1 second, an approach to calculate 1-second scintillation indices is proposed in this study. The 1-second scintillation indices are shown to better describe the signal distortions under scintillation. Additionally, the 1-second phase and code jitter, calculated using the 1-second scintillation indices, can better represent the measurement noise.

5) **Generate the phase and code jitter maps and investigate their potential to assist GNSS users in scintillation mitigation**

   Due to the fact that the phase and code jitter maps can be exploited by generic receivers in the mitigation of scintillation effects on GNSS positioning, the concept of jitter maps is studied and regional jitter maps are generated. The capability of the jitter maps in identifying potential tracking issues for GNSS users is investigated.

6) **Mitigate GNSS positioning errors under scintillation for generic receivers by exploiting the jitter maps**

   With the help of the phase and code jitter maps generated in this study, the scintillation induced positioning errors calculated for generic receivers are mitigated by exploiting the jitter values retrieved from the jitter maps. The improvements in the positioning accuracy are presented.

The main achievements in the frame of this thesis are summarised as follows:

(1) A better understanding of the signal intensity fading characteristics under scintillation is obtained. Mathematical models describing the relationship between intensity fading characteristics and scintillation indices are built for the first time in this study. Additionally, the rationale of how the intensity fading affects the receiver tracking performance is presented, which is of great importance for receiver manufacturers to design robust GNSS receivers that can account for scintillation effects. Results and conclusions of this analysis have been published in the peer reviewed journal "GPS Solutions" (Guo et al. 2019a).

(2) An alternative approach to estimate the PLL phase jitter and DLL code jitter using the discriminator output is proposed in this study. The proposed approach achieves a good match with the jitter estimation models described in Conker et al. (2003), thus verifying the accuracy of these models. Due to the fact that the proposed approach can be used without involving the calculation of scintillation indices, it is applicable to a wide range of generic receivers that are not able to estimate scintillation indices. Moreover, a custom-defined PDF is proposed for the first time in this study which successfully describes the distribution of the tracking errors under different levels of scintillation. The results are summarised in a manuscript which is ready to submit to peer reviewed journals at the time of writing.

(3) A comprehensive analysis of the PLL bandwidth and integration time tuning effects on the phase jitter calculation under scintillation is presented. It is found that there is a trade-off when selecting the PLL bandwidth. An optimal value of the bandwidth can be defined aiming to maximize the receiver tracking performance under scintillation. Results obtained in this analysis have been published in the peer reviewed journal "Space Weather" (Guo et al. 2020a).

(4) An approach to estimate the 1-second scintillation indices is proposed for the first time in this study. The newly proposed indices show more effectiveness in describing the signal fluctuations under scintillation compared with the widely used 1-minute scintillation indices. More importantly, improvement in the positioning accuracy is achieved when they are exploited in the scintillation mitigation compared with using the 1-minute indices. The proposed approach and the achievements in the positioning error mitigation are published in the peer reviewed journal "Journal of Geodesy" (Guo et al. 2021).

(5) The phase and code jitter maps are produced in this study by exploiting the dense network of ISMRs deployed in the northern Canada. The use of these maps to identify the potential occurrence of cycle slips is presented. With the help of these maps, the positioning errors caused by scintillation are successfully mitigated for generic receivers. An improvement of up to 50% is achieved in the positioning accuracy. A manuscript related to this analysis is currently in preparation and will be submitted to one of the top-rated peer reviewed journals.

This study is undertaken in the framework of the Training REsearch and Applications Network to Support the Ultimate Real-Time High Accuracy EGNSS Solution (TREASURE) project (http://www.treasure-gnss.eu/), which focused on modelling GNSS errors, like ionospheric and tropospheric errors, and developing advanced positioning algorithms to support real-time high accuracy GNSS positioning techniques. The research in this project was carried out by 13 individual Early Stage Researchers (ESRs) in different work packages (WPs). Research in this thesis was carried out in the scope of WP3 and in synergy with the research in WP1, as shown in Figure 1.1, so that outcomes from the latter can be suitably incorporated. This study also entailed close collaboration with ESR5 and ESR6 in WP3, who focuses on developing advanced software receivers and interference purifying techniques, respectively. The scintillation mitigation approach and interference purifying models, along with the ionospheric and tropospheric models developed in WP1,can be integrated and exploited by ESRs in WP4 to enhance GNSS positioning accuracy.

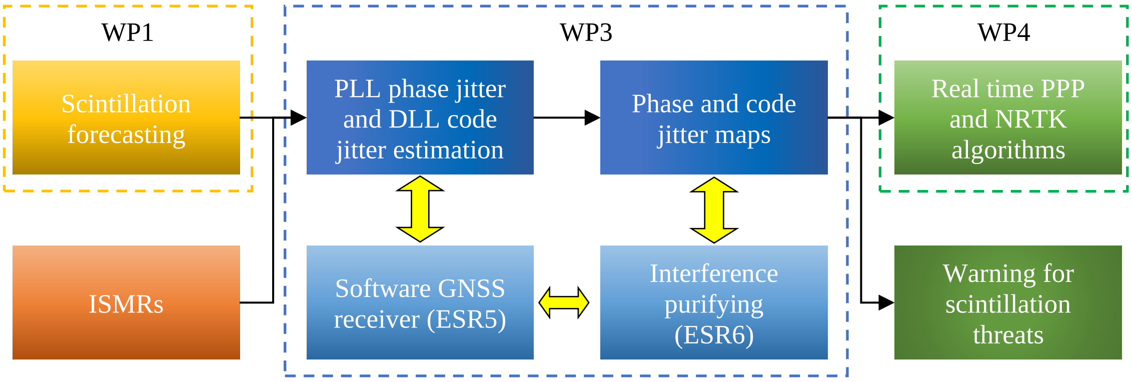

Figure 1.1 Studies in this thesis in connection with other research in the scope of the TREASURE project

1.3 Thesis outline

The structure of this thesis is given as follows:

Chapter 2 provides a focused overview of GNSS and scintillation monitoring using GNSS receivers. A brief description of GNSS signals, receivers and GNSS positioning algorithms is provided. Receiver carrier phase and code tracking loops and tracking errors are described, followed by the introduction to advanced PPP algorithms. The widely used specialised GNSS receivers, namely ISMRs, for scintillation data collection are described, followed by the introduction to the GNSS signal simulator used for generating simulated scintillation data processed in this study.

Chapter 3 reviews the essential GNSS scintillation data processing techniques. The detrending of high frequency scintillation data is introduced first, followed by the description of scintillation indices and spectral parameters which are used to characterize the scintillation levels. The difference of two types of widely used ISMRs in scintillation monitoring and the effects of receiver PLL tuning on scintillation index estimation are then presented. Subsequently, the signal intensity fading characteristics and their relationship with scintillation levels are investigated. Finally, the effects of scintillation induced intensity fading on GNSS receiver tracking loops are analysed.

Chapter 4 discusses the modelling of scintillation effects on GNSS receiver tracking loops. The phase and code jitter estimation models described in Conker et al. (2003) are described and studied. Following the derivation in Conker et al. (2003), the jitter estimation models for Galileo E1 and E5a signals are described. A case study to investigate the PLL tuning effects on the phase jitter estimation under scintillation is then carried out. Alternative approaches to estimate the phase and code jitter are then proposed. Finally, the scintillation effects on the distribution of the PLL phase tracking errors are studied.

Chapter 5 focuses on the mitigation of scintillation effects on GNSS positioning. The mitigation approach used in this study as well as its limitations are described. To address the limitations, the proposed approach to estimate the 1-second scintillation indices is described, followed by the comparison of the newly proposed 1-second scintillation indices and the 1-minute indices calculated at low and high latitudes. The positioning errors caused by scintillation effects at the low and high latitude stations are shown thereafter. Finally, the mitigation of the positioning errors by exploiting the newly proposed 1-second scintillation indices is presented.

Chapter 6 discusses the mitigation of scintillation effects on positioning errors using the phase and code jitter maps. The procedure for the generation of the jitter maps and their potential uses are first provided, followed by the jitter maps generated by exploiting the dense ISMR network deployed in northern Canada during a geomagnetic storm. The cycle slips experienced by the ISMRs and their relationship with the phase jitter extracted from the jitter maps are addressed subsequently. The positioning errors calculated under scintillation during the geomagnetic storm at the selected stations are shown thereafter, followed by the mitigation of the positioning errors by exploiting the phase and code jitter maps. Finally, a preliminary analysis of the jitter errors induced by the mapping function in the generation of the jitter maps is given.

Chapter 7 summarises the conclusions drawn from the research objective of this thesis and the recommendations for future work.

The logic interconnections among the chapters and the main topic studied in each chapter are shown in Figure 1.2.

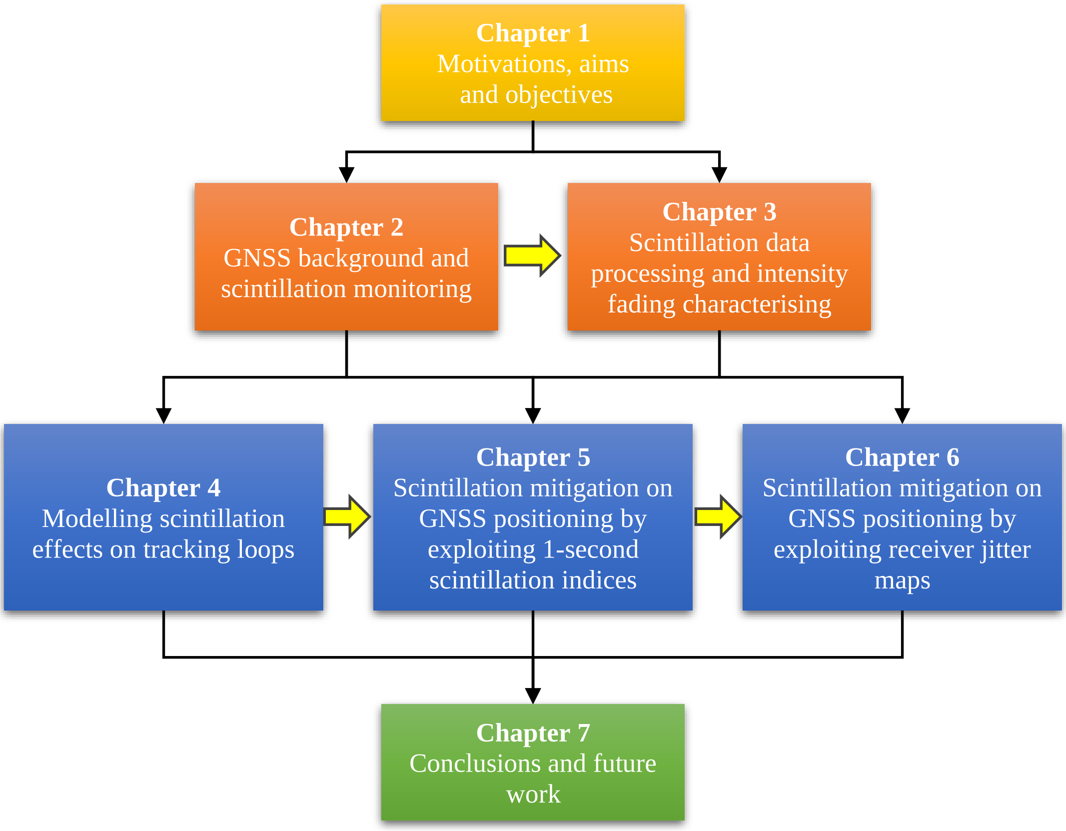

Figure 1.2 Thesis structure and the logic interconnections among each chapter

2 GNSS and scintillation monitoring in the context of this thesis

This chapter provides a focused overview of GNSS and scintillation monitoring using GNSS receivers in what relates to the main aims of this thesis. In this context, the fundamentals of GNSS, including signal structure, signal tracking, receivers and position determination, are given. Receiver carrier phase and code tracking loops and tracking errors are described, followed by the introduction to advanced PPP techniques. Finally, the specialised GNSS receivers used for scintillation data measuring and logging, as well as GNSS hardware simulators used for scintillation simulation are introduced.

2.1 GNSS overview

GNSS has been playing an important role in human life, such as in surveying, civil aviation, financial sector, construction etc. The principle of GNSS positioning can be briefly summarised as following:

(1) Satellites transmit signals to the Earth

(2) Ground control stations calculate the satellite orbits using the data from the received signals. The orbit information is then transferred back to satellites and modulated on the signals

(3) Receivers track and process the signals broadcasted by the satellites to generate range measurements between the receiver and satellites and the orbit information of satellites, which are further used to determine the receiver location

An overview of GNSS signals, receivers and the basic positioning determination techniques are introduced next.

2.1.1 GNSS signals

The structure of the GNSS signal can be generally described in three layers, i.e., RF carrier, pseudorandom noise (PRN) codes and navigation data (Kaplan et al. 2017), as shown in Figure 2.1. Every GNSS satellite has a unique PRN code which has excellent autocorrelation performance. GNSS uses PRN codes to distinguish different satellites. Additionally, the PRN code can also be used to define the signal propagation time, which in turn allows to estimate the range between satellites and receivers. The navigation data provides the digital information related to the satellite orbits, clock errors, satellite health status, etc. In the generation of GNSS signals, the PRN codes and navigation data are modulated on the RF carrier, which is in the bottom layer. Most GNSS signals use one or more RF carriers in the L-band covering the range from 1 to 2 GHz (Borre et al. 2007; Kaplan et al 2017).

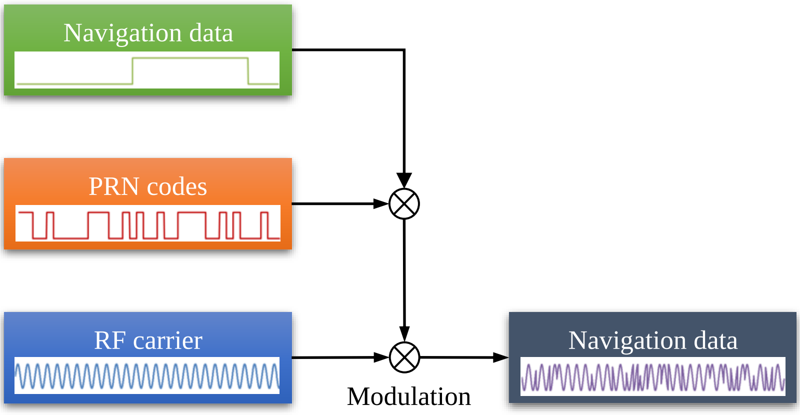

Figure 2.1 Three-layer structure of GNSS signals

GNSS signals can be generated by exploiting different modulation schemes, which are distinguished by their respective chip pulse shapes resulting in different autocorrelation function curves. The shapes of these curves are directly related to the signal tracking performance of the receiver, which is introduced in the next section. The commonly used modulation schemes include Binary Phase Shift Keying (BPSK) and Binary Offset Carrier (BOC). The BPSK is widely used in the GNSS legacy signals, for example, GPS L1 C/A and L2 P, while the implementation of BOC modulation contributes to the improved performance of modernized signals, like Galileo E1, GPS L1 C and L2 M signals (Borre et al. 2007). In the generation of BOC(m, n) signals, an extra square wave subcarrier is modulated in the structure shown in Figure 2.1. The m and n parameters indicate the ratios of the subcarrier frequency and code rate over the reference frequency f_0, respectively (Borre et al. 2007). For modernized signals, the total power is split into two components, i.e., the data component modulating the navigation data, and the dataless pilot component (Kaplan et al. 2017). Table 2.1 summarises the carrier bands and modulation schemes of some of the GPS and Galileo signals analysed in this thesis (Meurer and Antreich 2017; Grewal et al. 2020).

Table 2.1 Summary of GPS and Galileo signal characteristics

Signal	Frequency (MHz)	Component	Modulation type	Data/Pilot
GPS L1 C/A	1575.42	--	BPSK(1)	Data
GPS L2 P	1227.6	--	BPSK(10)	Data
Galileo E1	1575.42			
		E1-B	CBOC(6,1,1/11)	Data
		E1-C	CBOC(6,1,1/11)	Pilot
Galileo E5a	1176.45		AltBOC(15, 10)	
		E5a-I	BPSK(10)	Data
		E5a-Q	BPSK(10)	Pilot
Galileo E5b	1207.14		AltBOC(15, 10)	
		E5b-I	BPSK(10)	Data
		E5b-Q	BPSK(10)	Pilot

2.1.2 GNSS receivers

GNSS receivers are designed to extract navigation data and generate pseudorange and phase measurements from the incoming signals. As shown in Figure 2.2, a typical GNSS receiver usually contains an RF front-end, as well as baseband digital signal processing and navigation modules. In the RF front end, the analog signal received by the antenna is first amplified and filtered by a preamplifier to minimize the out-of-band interference. Then, through a down-converter, the signal is down-converted to IF signals in the baseband, which is further fed to an A/D convert (ADC) to achieve the digitalized IF signal. An automatic gain control (AGC) is usually implemented to adjust the amplitude of the IF signal input to ADC, aiming to maintain the output signal power at a relatively stable level.

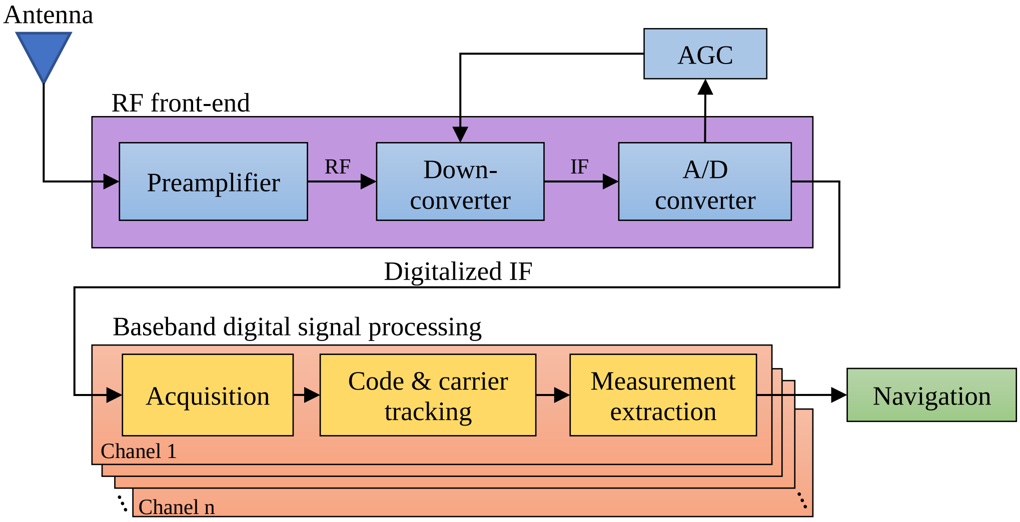

Figure 2.2 Structure of typical GNSS receivers

The digitalized IF signal is then parsed by the baseband signal processing module, which usually contains parallel channels that enable to process signals from different visible satellites simultaneously. An acquisition process is first implemented in each channel to acquire the satellite signals and provide rough estimates of carrier frequency and code, which are further exploited to initialise the carrier and code tracking process. The aims of the code and carrier tracking are to wipe off the signal carrier and code data and obtain the pseudorange and carrier phase measurements and related navigation message. The receiver carrier and code tracking loops and tracking errors are described in detail in Section 2.3.

2.1.3 Positioning estimation

GNSS user position is estimated using the navigation data and the GNSS observations, including pseudorange and carrier phase measurements, all provided by the receivers. The navigation data contains the parameters related to the satellite location, while the observations are the range measurements and its changing rate between the receiver and the satellites. Taking the pseudorange measurements as an example, the observation equation can be written as (Kaplan et al. 2017)

$$P_u^n = \rho_u^n + ct_u \tag{2.1}$$

where P_u^n denotes the pseudorange measured by receiver u. ρ_u^n is the geometric distance between receiver u and satellite n. c is the speed of light in vacuum. t_u is the receiver clock offset with respect to system time. By representing the distance ρ_u^n using the receiver and satellite coordinates, Eq. (2.1) can be rewritten as

$$P_u^n = \sqrt{(x_n - x_u)^2 + (y_n - y_u) + (z_n - z_u)} + ct_u \tag{2.2}$$

where (x_n, y_n, z_n) and (x_u, y_u, z_u) are the satellite and receiver positions in three dimensions, respectively. As there are four unknown variables in Eq. (2.2), i.e., x_u, y_u, z_u and t_u, the receiver position can only be solved when there are at least four pseudorange measurements from at least four satellites.

The carrier phase measurement can be used to solve the receiver position following a similar procedure, however, it is generally more precise compared with the pseudorange measurement (Hauschild 2017a). Different positioning algorithms, like Single Point Positioning, PPP, differential positioning, RTK, have been developed exploiting the different GNSS observables (such as the code and phase observables) to achieve varying accuracy levels, from several meters to centimetres. The positioning accuracy significantly depends on the precision of the pseudorange and carrier phase measurements and the number and spatial distribution of usable satellites. The main error sources affecting the range measurements include satellite and receiver clock errors, satellite orbits errors, atmospheric delays, scintillation, multipath, jamming and spoofing, etc (Groves 2013). In practice, an accuracy of centimetres can be realized by applying error modelling and advanced positioning techniques, such as PPP, which is introduced in detail in Section 2.3. On the other hand, with the development of new GNSS satellites, different systems can be combined in position estimation, exploiting what is known as multi-GNSS techniques, which can help to improve the positioning accuracy (Hauschild 2017b). The main focus of this thesis is on the positioning errors caused by the ionospheric scintillation effects. Potential tools to mitigate these errors and their impact on PPP techniques are studied.

2.2 Carrier and code tracking loops

The signal tracking in GNSS receivers is accomplished by carrier tracking loops and code tracking loops. For both loops, the main aim is to adjust the local duplicated signal to match the incoming signals (Won and Pany 2017). The commonly used carrier tracking loops include PLLs, Costas PLLs and frequency locked loops (FLLs), determined by the type of discriminator implemented in the loops (Ward 2017), while the code tracking loops usually adopt DLLs to track the code data. In the framework of this thesis, the analysis of scintillation effects on receiver tracking loops is carried out based on PLLs and DLLs. The mechanism of phase and code tracking in PLLs and DLLs and the tracking errors are introduced in this section.

2.2.1 Signal tracking engine

A general GNSS signal tracking engine, including the PLL and the DLL branches, is shown in Figure 2.3 (Ward 2017; Won and Pany 2017). As it can be seen from the figure, the phase of the incoming digital IF is stripped by the duplicated carrier phase signals generated by the carrier Numerical Control Oscillators (NCO) in the PLL shown in the bottom branch, to produce the In-phase (I) and Quadra-phase (Q) signals. Then the I and Q signals are correlated with the early (E), prompt (P) and late (L) replica codes generated by the code NCO and generator at the DLL branch in the top. After the carrier and code correlation process, the digital IF is converted to the baseband. An integrate and dump accumulator is then used to filter and resample the baseband signal (Ward 2017). The outputs are fed into the DLL and PLL discriminators, respectively, which measure the code and phase error between the incoming and the replica signals. The output error is filtered by the loop filters which produce an adjustment to alter the local replica code and carrier phase in the NCOs. The updated code and carrier phase enter the loops and are again compared with the incoming signal.

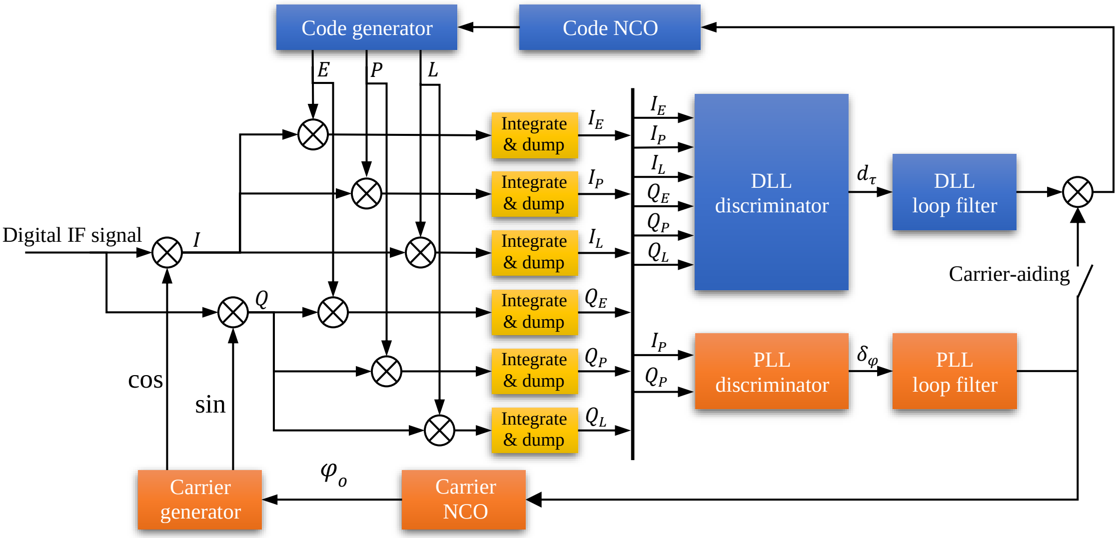

Figure 2.3 Receiver tracking loops in generic GNSS receivers

The receiver tracking performance is jointly determined by the integration time in the correlators, the type of discriminators and the loop filters (Won and Pany 2017). The commonly used discriminators in PLLs include arctangent and Costas decision directed, while in DLLs, early minus late and dot-product discriminators are widely implemented (Ward 2017; Van Dierendonck 1992). A signal is considered to be tracking correctly when the phase error and code error between the incoming and replica signals are near zero. However, under challenging situations, like scintillation, the quality of the incoming signal may decrease significantly, such as due to a decreased signal intensity and/or high phase dynamics, which could potentially cause cycle slips and/or losses of satellite lock (Groves 2013; Humphreys et al. 2010; Meggs et al. 2008; Skone et al. 2001). The receiver tracking performance is widely analysed in terms of rates of loss of signal lock, cycle slips and tracking errors, which directly affects the precision of GNSS observations and the positioning accuracy.

2.2.2 PLL tracking performance

A simplified PLL linear model is introduced to show the PLL phase error and tracking error, as shown in Figure 2.4 (Gardner 2005; Curran 2015). The phase error $\Delta\varphi$ is defined as the difference between the incoming phase φ_i and its replica phase φ_o. Its standard deviation $\sigma_{\Delta\varphi}$, which is also called phase jitter, is commonly used to indicate the phase noise level at the output of the PLL. On the other hand, the phase error is measured by the loop discriminator. The output of the discriminator δ_φ is defined as the PLL tracking error. Both the phase and the tracking errors can be used to represent the tracking performance of the PLL, the phase error being more sensitive to the phase dynamics in the incoming signals. Carrier tracking loops perform normally when the phase error over the update interval is within the linear region of the discriminator (Curran 2015). If the phase error overtakes the linear region, the assumption of linear carrier tracking loop will fail.

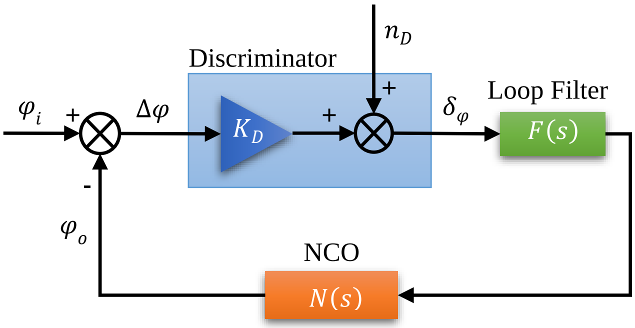

Figure 2.4 A simplified linear model of GPS carrier tracking loops

According to Ward (2017), the phase jitter is given by

$$\sigma_{\Delta\varphi} = \sqrt{\sigma_t^2 + \sigma_v^2 + \theta_A^2} + \frac{\theta_e}{3} \tag{2.3}$$

where σ_t is the thermal noise induced phase jitter, given by (Van Dierendonck 1996; Groves 2013; Ward 2017)

$$\sigma_t = \sqrt{\int_0^\infty |H(f)|^2 S_n(f) \mathrm{d}f} \approx \sqrt{\frac{B_n}{c/n_0}\left(1 + \frac{1}{2\eta c/n_0}\right)} \tag{2.4}$$

where $H(f)$ is the frequency response of the transfer function for the linear PLL model shown in Figure 2.4. $S_n(f)$ is the single side power spectral density (PSD) of the thermal noise input to the PLL. B_n is the noise bandwidth and η is the coherent integration time. c/n_0 is linear form of $C/N0$, given by $c/n_0 = 10^{0.1*(C/N0)}$. The noise bandwidth and coherent integration time are essential parameters that determine the loop tracking performance. The noise bandwidth B_n controls the amount of noise allowed in the loop filter, which is defined as (Razavi et al. 2008)

$$B_n = \int_0^\infty \frac{|H(f)|^2}{|H(0)|^2} \mathrm{d}f \tag{2.5}$$

A larger bandwidth is beneficial for the robustness of tracking loops to dynamics, while a narrow bandwidth contributes to a more accurate tracking (Won and Pany 2017). On the other hand, the integration time is related to the tracking loop sensitivity and stability. It should be longer for the high sensitivity in weak or interfered signal tracking and shorter for the robustness to high signal dynamics (Gardner 2005; Won and Pany 2017).

The oscillator induced phase jitter σ_v and θ_A in Eq. (2.3) are due to external vibrations and Allan-variance, respectively. θ_e is the dynamic stress error. Considering a stationary receiver, which is usually the case in this thesis, σ_v and θ_e are negligible. The Allan-variance induced oscillator jitter θ_A results from the instability of the oscillators in both receiver and satellite clocks. As GNSS satellites use a stable atomic clock, the satellite oscillator noise is ignorable. Thus, according to Irsigler and Eissfeller (2002), the Allan-variance induced oscillator noise for a third order PLL is calculated by

$$\theta_A^2 = 2\pi^2 f_L^2 \left[\frac{\pi^2 h_{-2}}{3\omega_n^3} + \frac{\pi h_{-1}}{3\sqrt{3}\omega_n^2} + \frac{h_0}{6\omega_n}\right] \text{ (rad}^2\text{)} \tag{2.6}$$

where f_L is the signal carrier frequency. h_{-2}, h_{-1} and h_0 are clock parameters determined by the type of oscillator. ω_n is the radian frequency, related to the loop bandwidth by $\omega_n = 1.2B_n$ for a third order PLL. A high-quality oven-controlled crystal oscillator (OCXO) is widely used in ISMRs to accurately measure the phase dynamics under scintillation. According to the clock parameters given by Irsigler and Eissfeller (2002), θ_A is calculated as a function of PLL bandwidth on GPS L1 band, and shown in Figure 2.5. It is seen that θ_A decreases gradually with the increase in B_n. It is much larger when B_n=5 Hz compared with 10 and 15 Hz.

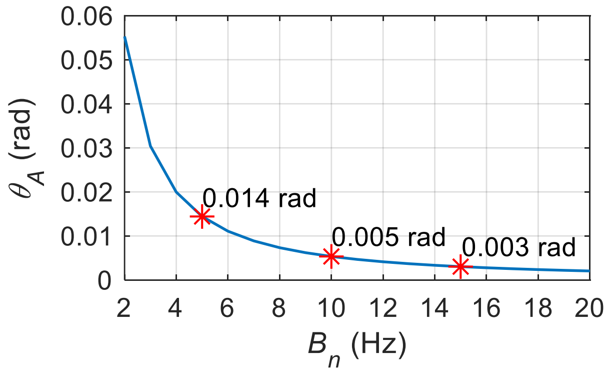

Figure 2.5 Allan variance induced oscillator phase jitter θ_A in relation to bandwidth B_n for a third order PLL

On the other hand, the standard deviation of the phase tracking errors, i.e., phase tracking jitter, is defined as (Razavi et al. 2008)

$$\sigma_{\delta_\varphi} = \sqrt{\sigma_w^2 + \sigma_{\varphi_c}^2} \tag{2.7}$$

where σ_w is the white noise at the discriminator output. According to Van Dierendonck (1996) and Groves (2013), σ_w is given as

$$\sigma_w = \sqrt{\frac{1}{2\eta c/n_0}\left(1 + \frac{1}{2\eta c/n_0}\right)} \tag{2.8}$$

The coloured (or correlated) noise σ_{φ_c} is due to the satellite and receiver oscillator instability, ionospheric effects and dynamic stress effects (Razavi et al. 2008). It can be seen from Eq. (2.8) that σ_w is independent of loop bandwidth, which is different from the thermal noise in phase jitter calculated by Eq. (2.4). Additionally, it is worth mentioning that in PLLs, the white noise in Eq. (2.8) is propagated through the closed-loop noise time-update function to the thermal noise in the phase jitter, given by (Van Dierendonck et al. 1992; Groves 2013)

$$\sigma_t \approx \sqrt{2B_n\eta}\sigma_w \tag{2.9}$$

The tracking error δ_φ and tracking jitter σ_{δ_φ} can be estimated if the post-correlation In-phase I_P and Quadra-phase Q_P measurements at the signal tracking stage are provided. For a PLL with an arctangent discriminator, the tracking error and tracking jitter are respectively given by (Ward 2017)

$$\delta_\varphi = \mathrm{atan}\left(\frac{Q_P}{I_P}\right)\ (\mathrm{rad}) \tag{2.10}$$

$$\sigma_{\delta_\varphi} = \mathrm{std}\left(\delta_\varphi\right)\ (\mathrm{rad}) \tag{2.11}$$

When there is only white noise in the discriminator output, the tracking jitter can be approximated by $\sigma_{\delta_\varphi} \approx \sigma_w$. In order to verify the relationship between the phase jitter and the phase tracking jitter given by Eq. (2.9), 10 second raw IF GPS L1 C/A data with $C/N0 = 45$ dB-Hz containing only Gaussian noise is generated using a MATLAB GNSS signal simulation tool. A SDR receiver, described in Section 2.4.2, with the PLL configured to different bandwidths B_n and integration times η is applied to process the simulated data. The phase jitter is then calculated, respectively, by Eq. (2.4) with the measured $C/N0$, denoted as $\sigma_{\Delta\varphi}$, and Eq. (2.9) and (2.11) with the PLL discriminator output (considering the case when there is only white noise), denoted as $\sigma_{\Delta\varphi\_discri}$. As Figure 2.6 shows, $\sigma_{\Delta\varphi\_discri}$ aligns closely with the lines of $\sigma_{\Delta\varphi}$, except when $B_n = 15$ Hz and $\eta = 20$ ms, where a clear bias of around 0.003 rad is observed. The reason for this bias is not due to the Gaussian noise and is explained in Razavi et al. (2008) and Stevanovic and Pervan (2018). Nevertheless, the bias is quite small and produces little effect on this study. In this thesis, Eq. (2.9) is used to develop alternative approaches to estimate the phase jitter in the presence of scintillation by exploiting the SDR receiver, which is introduced in detail in Chapter 4.

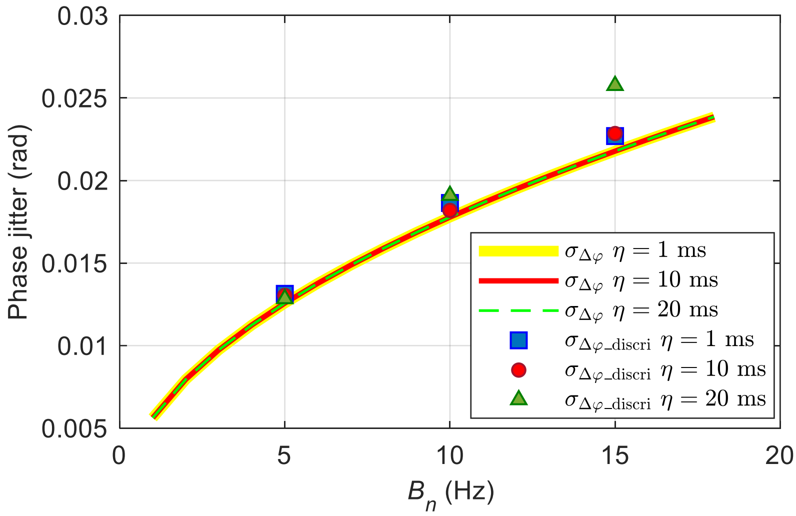

Figure 2.6 Variations of the phase jitter calculated, respectively, using Eq. (2.4) with the measured $C/N0$, denoted as $\sigma_{\Delta\varphi}$, and Eq. (2.9) and (2.11) using the PLL discriminator output, denoted as $\sigma_{\Delta\varphi\_discri}$, based on the simulated GPS L1 C/A data

2.2.3 DLL tracking performance

The code noise errors at the output of DLL are mainly due to the thermal noise. A general expression of the code noise for a dot-product discriminator is given by (Sleewaegen et al. 2004; Tawk et al. 2012)

$$\sigma_\tau = \sqrt{\frac{B_L(1-R(d))}{2\alpha^2 c/n_0}\left(1+\frac{1}{\eta c/n_0}\right)} \text{ (chip)} \tag{2.12}$$

and for an early minus late (E-L) discriminator is given by (Tawk et al. 2012)

$$\sigma_\tau = \sqrt{\frac{B_L(1-R(d))}{2\alpha^2 c/n_0}\left(1+\frac{2}{(2-\alpha d)\eta c/n_0}\right)} \text{ (chip)} \tag{2.13}$$

where B_L is the DLL bandwidth in Hz. d is the early-to-late correlator spacing in chips. $R(d)$ is the correlation peak evaluated at a delay of d. η is the DLL integration time. $\alpha = \frac{\mathrm{d}R(-\frac{d}{2})}{\mathrm{d}(-\frac{d}{2})}$ is the slope of the correlation evaluated at $-\frac{d}{2}$. It should be noted that the calculation of α is simplified as the dependence of the slope on the front-end bandwidth is not considered. For BPSK modulation signals, for example GPS L1 and Galileo E5a pilot signals, $R(d) = 1 - d$ and $\alpha = 1$, while for BOC(1, 1) signals, $R(d) = 1 - 3d$ and $\alpha = 3$. Figure 2.7 shows the DLL code jitter in relation to $C/N0$ and correlator spacing d for GPS L1 C/A signal. As it can be seen, the code jitter decreases gradually when $C/N0$ increases from 25 to 50 dB-Hz. The curve with the largest correlator spacing, i.e., $d = 1$ chip, has the largest code noise. Additionally, it is seen that the dot-product and E-L discriminator presents less difference in the code jitter. In this case, the loop bandwidth B_L is set to 0.25 Hz and the integration time is set to 20 ms.

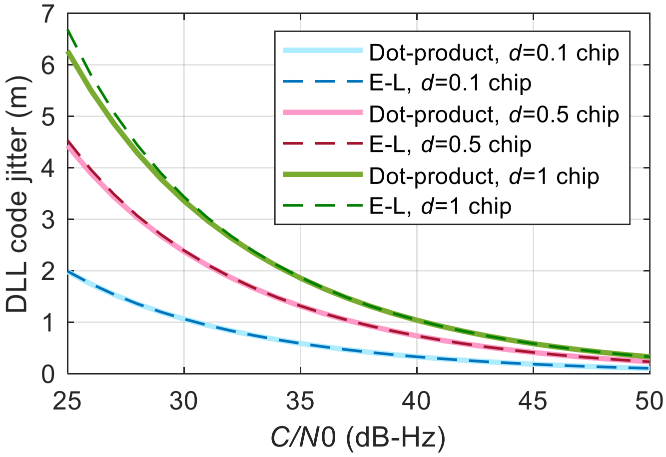

Figure 2.7 Variation of code jitter in the output of the DLL in relation to $C/N0$ and correlator spacing d

Similar to Eq. (2.9), the code jitter at the DLL output is related to the discriminator noise by (Groves 2013)

$$\sigma_\tau \approx \sqrt{2B_L\eta}\sigma_{ND} \tag{2.14}$$

where σ_{ND} is the standard deviation of the discriminator output in DLL. Using the SDR receiver introduced in Section 2.4.2, the simulated GPS L1 C/A IF data containing only the white noise with $C/N0$ varying from 35 to 55 dB-Hz is processed. The code jitter is then estimated using Eq. (2.14), denoted as σ_{τ_discri}, and compared with that calculated by Eq. (2.12) with $R(d) = 1 - d$ and $\alpha = 1$, as shown in Figure 2.8. It can be seen that σ_{τ_discri} falls on the lines for different DLL bandwidth B_L and correlator spacing d. Eq. (2.14) is further used to estimate the code jitter caused by scintillation and is described in Chapter 4.

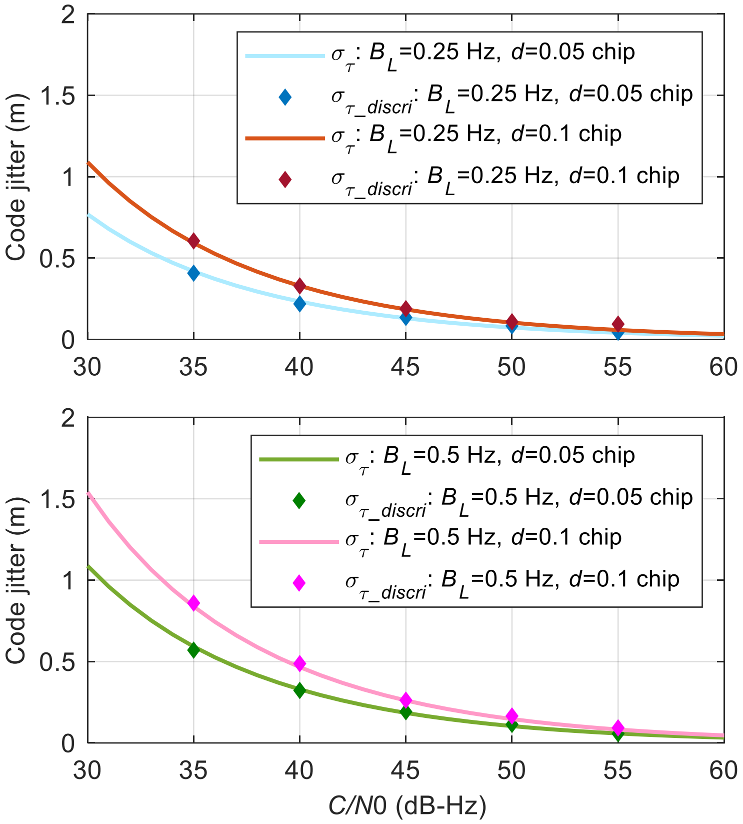

Figure 2.8 Variations of the code jitter calculated, respectively, by Eq. (2.12) and Eq. (2.14) based on processing the simulated GPS L1 C/A data using the SDR receiver

2.3 Precise Point Positioning - PPP

In this thesis, PPP is used to estimate receiver positions. PPP is an advanced technique which can deliver an accuracy of centimetres in real time. By implementing advanced error models in position estimation, the non-scintillation effects on GNSS positioning can be minimized to enable the analysis of scintillation effects on GNSS positioning, as well as to test the performance of scintillation mitigation approaches. The introduction of the PPP algorithm and the PPP software used in this thesis are given in this section.

2.3.1 PPP estimation

PPP is a global positioning technique which usually uses pseudorange and carrier phase measurements on dual- or multi-frequency signals. For a dual-frequency GNSS receiver tracking signals at frequencies f_1 and f_2, the observation equations for pseudorange and carrier phase measurements can be written as (Hauschild 2017a)

$$P_1^n = \rho^n + c(\mathrm{d}t - \mathrm{d}T^n) + c(d_1 - d_1^n) + I + T \tag{2.15}$$

$$P_2^n = \rho^n + c(\mathrm{d}t - \mathrm{d}T^n) + c(d_2 - d_2^n) + \gamma I + T \tag{2.16}$$

$$\lambda_1\varphi_1^n = \rho^n + c(\mathrm{d}t - \mathrm{d}T^n) + c(\delta_1 - \delta_1^n) - I + T + \lambda_1 N_1^n \tag{2.17}$$

$$\lambda_2\varphi_2^n = \rho^n + c(\mathrm{d}t - \mathrm{d}T^n) + c(\delta_2 - \delta_2^n) - \gamma I + T + \lambda_2 N_2^n \tag{2.18}$$

where:

P_1^n and P_2^n are the pseudorange measurements,

ρ^n is the geometrical distance between the satellite n and the receiver,

c is the speed of light in vacuum,

$\mathrm{d}t$ and $\mathrm{d}T^n$ are the receiver and satellite clock errors, respectively,

d_1, d_2, δ_1 and δ_2 are the signal biases induced during the reception of the signals by receivers,

d_1^n, d_2^n, δ_1^n, and δ_2^n are the signal biases that occur when the signals are generated from satellites,

I is the ionospheric delay, which accounts for the first-order effects of ionosphere,

T is the tropospheric delay,

γ equals $\frac{f_1^2}{f_2^2}$ which relates the ionospheric delay on different frequencies,

λ_1 and λ_2 are the wavelengths corresponding to signals at frequencies of f_1 and f_2,

φ_1^n and φ_2^n are carrier phase measurements,N_1 and N_2 are the integer number of cycles on φ_1^n and φ_2^n measurements, respectively, which are usually called ambiguities.

In PPP calculation, the errors included in Eq. (2.15) to (2.18) are mostly modelled or removed. Satellite and receiver clock errors and satellite orbits errors are corrected by exploiting the precise clock and orbits correction products broadcasted by a network of GNSS reference stations, like the International GNSS Service (IGS). The first order ionospheric delay I is determined by the frequency of the signal and the number of free electrons along its path (Hauschild 2017a). It can be removed by the ionospheric-free combination, which is given by (Hauschild 2017a)

$$P_3^n = \frac{1}{f_1^2 - f_2^2}\left(f_1^2 P_1^n + f_2^2 P_2^n\right) \tag{2.19}$$

for the pseudorange measurements and

$$\varphi_3^n = \frac{1}{f_1^2 - f_2^2}\left(f_1^2 \varphi_1^n + f_2^2 \varphi_2^n\right) \tag{2.20}$$

for the carrier phase measurements. P_3^n and φ_3^n are, respectively, the ionosphere-free pseudorange and carrier phase combination. It is worth mentioning that although by forming the ionosphere-free combination the ionospheric-delay effect is mostly removed, this approach does not mitigate the effect of the scintillation, which remains as a challenge in GNSS positioning.

The tropospheric delay T is due to the dry gas, water vapour and moist gases that are concentrated in the troposphere (Groves 2013; Hauschild 2017a). The corresponding effects are related to the temperature, the relative humidity and the pressure along the signal path (Hauschild 2017a). Signals from satellites with a low elevation tend to experience more tropospheric delay as they pass through relatively longer paths in the troposphere (Groves 2013). The tropospheric delay is usually divided into two components, namely the hydrostatic delay, which contributes to around 90% of the total bias, and the wet delay, which contributes to the remaining 10%. The hydrostatic delay is modelled by mathematical models, such as the Saastamoinen model (Saastamoinen 1972), or the EGNOS tropospheric model (RTCA 1996), while the wet delay can be corrected by adjusting to a standard tropospheric activity and estimated at a regular fixed interval (Pace et al. 2010).

The signal biases are due to the GNSS instrument delays, which results in the imperfect synchronization of the different signals (Hauschild 2017a). In the PPP calculation, these biases can be mitigated by processing double differences of observations using a reference station, or with corrections estimated from a reference station network (Hauschild 2017a).

A Kalman Filter (KF) is widely implemented in PPP estimation. In this case, the receiver coordinates, receiver clock errors, tropospheric delay and phase ambiguities are estimated KF states, which are improved with successive GNSS measurements. The KF states can converge to stable and accurate values after a convergence period, which is usually 20 to 40 minutes and significantly depends on the number of visible satellites and their geometry, ionospheric conditions and receiver environment (Verhagen and Teunissen 2017). In PPP processing, the receiver coordinates can be estimated based on all observations accumulated over a period of time, referred to as a static solution/processing, or based on an epoch per epoch adjustment, referred to as a kinematic solution/processing. The static PPP solution can achieve a better positioning accuracy, while the kinematic approach is more sensitive to the transient noise in GNSS measurements, e.g., scintillation effects. In the framework of this thesis, static PPP is performed to obtain the precise coordinates of receiver, which are then set as reference coordinates. The positioning errors obtained using kinematic PPP are estimated against the reference coordinates, aiming to show the change in PPP accuracy under scintillation effects.

2.3.2 Stochastic models

The least square stochastic model in PPP estimation usually assigns weights to GNSS measurements according to a prior knowledge of the noise level for each individual observable. Ignoring the correlation between GNSS measurements, the standard stochastic model used in PPP is in the form of

$$W = \begin{bmatrix} \frac{1}{(\sigma^i)^2} & 0 & \cdots & 0 \\ 0 & \frac{1}{(\sigma^j)^2} & \cdots & 0 \\ \vdots & \vdots & \ddots & \vdots \\ 0 & 0 & \cdots & \frac{1}{(\sigma^n)^2} \end{bmatrix} \qquad (2.21)$$

where σ^i, σ^j, … σ^n are the precisions of measurements $i, j, \ldots n$, which can be pseudorange or carrier phase measurements or their combinations, e.g., the ionosphere-free combinations given by Eq. (2.19) and (2.20). An easy method to define the stochastic model is to assign a constant precision to all the pseudorange measurements and a constant precision to all the carrier phase measurement, which is also referred to as “constant weighting”. The precision value allocated to the carrier phase measurements is usually smaller than that allocated to the pseudorange measurements, as the former is usually more precise.

The constant weighting strategy is in most cases not realistic, as measurements obtained from different satellites may be affected by different effects (for instance related to different scintillation levels), thus their precisions may vary significantly. Therefore, it would be much more reasonable to define the measurement precisions in Eq. (2.21) as a function of the satellite elevation, an approach known as “elevation weighting”, which is based on the fact that signals from satellites at a lower elevation are more susceptible to multipath and atmospheric diffraction effects. An example of the function used in defining elevation weighting is given by (Teunissen and Montenbruck 2017)

$$\sigma^n = \sigma_{default} * \frac{1}{\sin(E)} \qquad (2.22)$$

where E is the satellite elevation. $\sigma_{default}$ is the default measurement noise. The commonly used values of $\sigma_{default}$ for GPS L1 C/A and L2 P pseudorange and carrier phase measurements are 0.3 m and 0.01 cycles, respectively.

The elevation weighting strategy has been used in PPP studies and applications, and generally achieves an excellent positioning accuracy. In order to account for the adverse effects of scintillation, an improved weighting scheme was proposed in Aquino et al (2009). In this approach, the precision of the measurements is represented respectively by the phase and code error variances at the PLL and DLL outputs estimated by the models described in Conker et al. (2003). Therefore, measurements more affected by scintillation will have a higher phase or code error variance and a lower precision and weight in the stochastic model, which leads to a decreased contribution to the positioning estimation. The details of estimating scintillation induced phase and code errors in receiver tracking loops are introduced in Chapter 4.

2.3.3 PPP software

In this thesis, the PPP calculations are performed using the University of Nottingham in-house POINT software (Mohammed 2017), which is capable of performing single- and multi-GNSS PPP. In additional to the commonly used constant and elevation weighting strategies which have been included in POINT, it also provides the interaction for users to manually define the stochastic models.

In order to isolate the measurements affected by cycle slips in the coordinate estimation, the Melbourne-Wübbena Wide-Lane (MWWL) combination, involving code and carrier phase measurements on dual-frequency signals, and ionospheric total electron content rates (TECRs), involving the geometry-free combination of carrier phase measurements, are both calculated to jointly detect the cycle slips (Liu 2011) in the PPP estimation. When a cycle slip is detected, the biased carrier phase ambiguity is reset. Moreover, a detection identification adaptation (DIA) algorithm using KF post-fit measurement residuals normalized by the variance-covariance matrix elements is also implemented to detect model errors (Teunissen 1998). If the DIA algorithm identifies a carrier phase measurement as an outlier, then the corresponding ambiguity is reinitialized. The implementation of DIA algorithm aims to isolate the carrier phase measurement outliers to the utmost, which helps to highlight the performance of scintillation mitigation approaches on reducing GNSS positioning errors under scintillation.

Using the POINT software, PPP based on GPS L1 C/A and L2 P measurements is estimated to analyse the scintillation effects on GNSS positioning. The performance of scintillation mitigation approaches is analysed in Chapters 5 and 6.

2.4 Scintillation monitoring using GNSS

Ionospheric scintillation can seriously disturb GNSS signals. However, the affected signals conversely provide an opportunity to characterise scintillation and study the ionospheric morphology. In order to monitor ionospheric scintillation, specialised GNSS receivers that measure scintillation indices as well as record raw signal intensity and phase measurements are employed. This type of GNSS receiver is commonly referred to as an ISMR. In this section, the typical ISMRs used for scintillation data collection are introduced. Regional networks of ISMRs deployed for scintillation study at both high and low latitudes are also presented.

2.4.1 Ionospheric scintillation monitoring receiver - ISMR

ISMRs are specialized GNSS receivers dedicated for ionospheric monitoring and space weather research. Two types of commercial ISMRs are used in this thesis for scintillation data collection, namely the PolaRxS Pro, developed by Septentrio Satellite Navigation, and the GSV4004B, developed by Novatel and AJ Systems. The PolaRxS Pro receiver is a multi-frequency multi-constellation receiver that can simultaneously track the GPS, GLONASS, Galileo, BDS and SBAS signals, covering multi-frequency L1/L2/L5/E5 AltBOC signals (www.septentrio.com/en/support/polarx/polarxs). It is able to log and output 50 to 100 Hz post-correlation I_P and Q_P measurements in the prompt branches and carrier phase φ_o samples in the PLL output, as shown in Figure 2.3. Scintillation indices, including $S4$, $Phi60$, p and T, on different signals are estimated and output along with other parameters such as satellite elevation and azimuth, $C/N0$, signal lock time, TEC etc. An ultra-low noise OCXO is implemented to ensure a low background noise in carrier phase which is suitable for scintillation monitoring.

Details of scintillation index estimation using the high frequency amplitude and phase measurements are introduced in Section 3.1.

The PolaRxS Pro receiver enables users to configure the PLL and DLL tracking loop parameters through a user-friendly graphical user interface (GUI), which provides the opportunity to analyse the effects of receiver tracking loop tuning on scintillation index estimation and receiver tracking performance under scintillation. It is worth mentioning that due to the fact that the receiver AGC could be activated to automatically adjust the gain of signal intensity, which indeed affects the calculation of scintillation index, the AGC was disabled during the scintillation data collection (Van Dierendonck et al. 1993). In addition, the $C/N0$ mask under which the receiver would declare a loss of lock is configured to 15 dB-Hz, in order to maintain the receiver locked to the satellite as much as possible even under strong scintillation conditions.

The GSV4004B is a GPS ionospheric scintillation and TEC monitor (GISTM), which tracks GPS L1 and L2 signals. The receiver can output 50 Hz amplitude and phase measurements for visible satellites tracked on L1 signals. Scintillation indices, including $S4$ and $Phi60$, as well as TEC, estimated using both L1 and L2 measurements are measured and output. An OCXO is also implemented in the receiver to provide clock reference.

PolaRxS Pro and GSV4004B receivers are widely deployed over the world to monitor the ionosphere and study scintillation. An interesting question is raised whether these two types of ISMRs perform comparably in monitoring scintillation, as the estimation of scintillation indices may be related to the receiver tracking loop models and configurations (Rougerie et al. 2016). If the scintillation indices measured by both types of ISMRs are comparable, they can be combined in scintillation studies. In order to verify the performance of these two types of ISMRs, GNSS signals with scintillation effects superimposed on them are simulated using a signal simulator and processed by both the receivers. The scintillation indices are then calculated and compared, as described in Section 3.2. The simulation of GNSS scintillation data is accomplished by a hardware simulator, which is described in Section 2.5.

2.4.2 Scintillation monitoring using an SDR receiver

SDR based GNSS receivers with the tracking loops and associated internal measurements accessible to users have been widely applied to monitor and analyse scintillation (Fortes et al. 2015; Ganguly et al. 2004; Xu and Morton 2017; Cristodaro et al. 2018; Linty et al. 2018). While both ISMRs and SDR receivers can be exploited for scintillation analysis, the software approach provides flexibility and full data access to the receiver chain, allowing a deeper analysis of the scintillation impact on the receiver internal parameters (Linty et al. 2018). Leveraging on the advantages of SDR receivers, the raw IF scintillation data on GPS L1 C/A signals collected at equatorial and Antarctic regions are analysed in this thesis to evaluate the scintillation effects on tracking loops.

The scintillation data collection setup using an SDR receiver, shown in Figure 2.9, is a custom-design solution based on a multi-frequency radio front-end (RFE). Through the processes in the RFE, the captured RF GPS L1 C/A signal is down-converted to the IF signal, sampled at 5 MHz and digitized to complex eight-bit data (Curran et al. 2014) and stored. The digital IF data are then post-processed in the MATLAB based SDR receiver (Savas et al. 2019), developed by ESR5 in Politecnico di Torino under the framework of the TREASURE project. The accuracy of GNSS phase measurements significantly depends on the characteristics of the RF chain from the GNSS antenna to the RFE (Demyanov et al. 2019) and the clock used to provide time reference. In the RFE shown in Figure 2.9, an OCXO is implemented. Additionally, as the SDR receiver is not operating in real time, the scintillation indices output by the ISMR in the data collection are used to first detect the occurrence of scintillation. Once scintillation is detected, the IF data in the corresponding period is stored for further analysis by the SDR receiver.

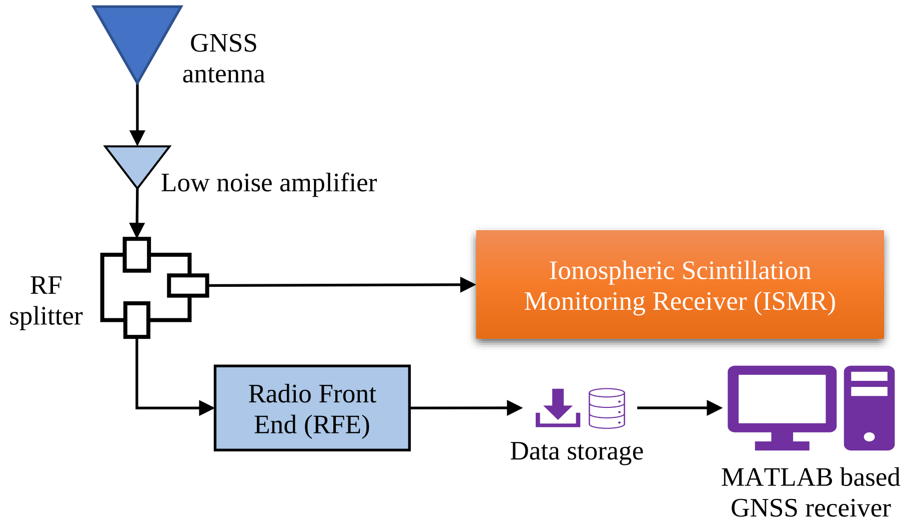

Figure 2.9 GNSS scintillation data collection setup using the SDR defined receiver

Compared with the typical ISMRs, like PolaRxS Pro and GSV4004B, which can log up to 100 Hz amplitude and phase measurements, the SDR receiver is able to output 1000 Hz measurements when the loop integration time is set to 1 ms, which provides sufficient samples for scintillation analysis. Additionally, according to McCaffrey and Jayachandran (2017), the deviation frequency, which distinguishes scintillation effects and white noise in scintillation spectra, is much less than 1000 Hz. Thus, in this thesis, the 1000 Hz intensity and carrier phase measurements are down sampled to 50 Hz in the scintillation indices estimation, while in the tracking loop phase error and tracking error analysis, the raw intensity and phase measurements without down-sampling are used.

2.4.3 Regional ionospheric monitoring networks

The GNSS scintillation data sets analysed in this thesis are collected from ISMR stations built in different networks at both high and low latitudes. These ISMR networks include:

(1) The CIGALA (Concept for Ionospheric Scintillation Mitigation for Professional GNSS in Latin America) and CALIBRA (Countering GNSS high Accuracy applications

Limitations due to Ionospheric disturbances in Brazil), networks in Brazil (https://is-cigala-calibra.fct.unesp.br/is/), funded by the EC 7th Framework Program. Scintillation over the Brazilian territory is particularly active as it is close to both the Equatorial Ionization Anomaly (EIA) and the South Atlantic Magnetic Anomaly (SAMA) (Spogli et al. 2013). In the CIGALA/CALIBRA network, 18 PolaRxS Pro receivers are currently operational to record scintillation indices and raw amplitude and phase measurements, as shown in Figure 2.10. A web-based software named ISMR Query Tool was established to allow the visualisation and analysis of scintillation events and to enable registered users to download scintillation data (Vani et al. 2017).

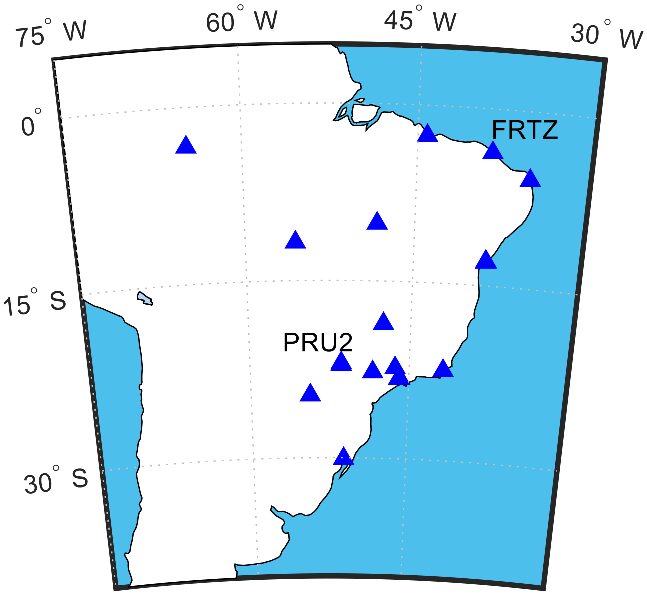

Figure 2.10 Distribution of the operational PolaRxS Pro receivers in CIGALA/CALIBRA

(2) The Canadian High Arctic Ionospheric Network (CHAIN) (Jayachandran et al. 2009), equipped with 6 Canadian Advanced Digital Ionosondes and 24 ISMRs, including 15 PolaRxS Pro and 9 GSV4004B active receivers (http://chain.physics.unb.ca/chain/), as listed in Table 2.2.

Table 2.2 Locations of the ISMR stations in CHAIN network

Station Abbreviation	Lat. (°N)	Long. (°E)	Receiver	Station Abbreviation	Lat. (°N)	Long. (°E)	Receiver
EURC	79.99	274.10	GSV4004B	KUGC	67.82	244.87	PolaRxS Pro
RESC	74.75	265.00	GSV4004B	REPC	66.52	273.77	PolaRxS Pro
PONC	72.69	282.04	GSV4004B	CORC	64.19	276.65	PolaRxS Pro
TALC	69.54	266.44	GSV4004B	RANC	62.82	267.89	PolaRxS Pro
CBBC	69.10	254.88	GSV4004B	FSIC	61.76	238.77	PolaRxS Pro
HALC	68.77	278.74	GSV4004B	ARVC	61.10	265.93	PolaRxS Pro
QIKC	67.56	295.97	GSV4004B	FSMC	60.03	248.07	PolaRxS Pro
IQAC	63.74	291.46	GSV4004B	CHUC	58.76	265.91	PolaRxS Pro
SANC	56.54	280.77	GSV4004B	RABC	58.23	256.32	PolaRxS Pro
ARCC	73.00	274.97	PolaRxS Pro	MCMC	56.65	248.78	PolaRxS Pro
SACC	71.99	234.74	PolaRxS Pro	GILC	56.38	265.36	PolaRxS Pro
GJOC	68.63	264.15	PolaRxS Pro	EDMC	53.35	247.03	PolaRxS Pro

The CHAIIN network aims to allow understanding the polar cap ionosphere under solar and interplanetary magnetic field conditions. Scintillation indices, TEC measurements and 50 Hz amplitude and phase measurements are logged by the ISMRs and are available through FTP services. The distribution of ISMRs in CHAIN is presented in Figure 2.11.

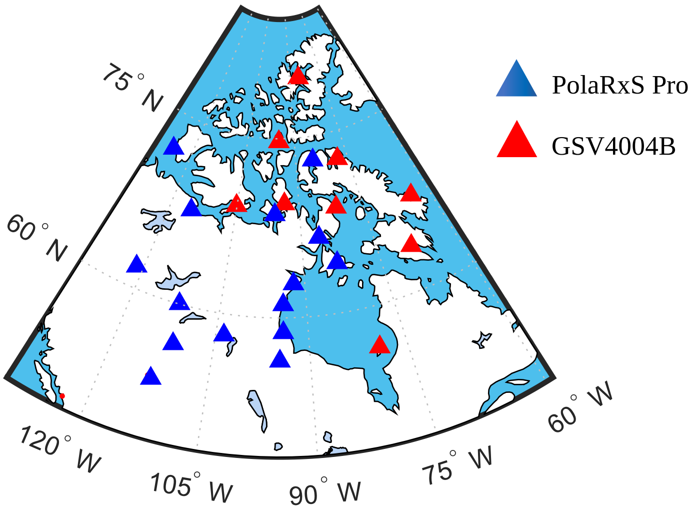

Figure 2.11 Distribution of the PolaRxS Pro and GSV4004B ISMRs in CHAIN

(3) INGV ionospheric monitoring network deployed under the framework of the DemoGRAPE project (Alfonsi et al. 2016; Linty et al. 2018) and eSWua project (http://www.eswua.ingv.it/index.php), with stations operational in Arctic, Africa, Mediterranean, South America and Antarctic.

The analysis of scintillation data collected from both low and high latitude stations benefits a full understanding of scintillation as well as its effects on GNSS.

2.5 Scintillation simulation using hardware simulator

A GNSS hardware signal simulator is used to generate scintillation affected signal data comparable to real open-sky data collected by ISMRs. It can re-generate the signals with the same scenarios, thus allowing for testing the performance of different GNSS devices. Additionally, the simulator can select and configure the noise contaminating the GNSS signals. This is different from the real GNSS data which may be contaminated by several unknown effects. In this thesis, a Spirent GNSS signal simulator, GSS8000-series Radio Frequency Constellation Simulator (RFCS) (Spirent Communication plc 2016), available at the University of Nottingham is used to generate GNSS signals. The Spirent SimGEN ® software is used to set up a simulation scenario. A user command file (.ucd file) is activated in the simulation to superimpose scintillation effects on the signals. The .ucd file was generated based on real scintillation data set. It contains the profile of the signal intensity and phase fluctuations under scintillation. The simulated GNSS scintillation data are recorded by the two types of ISMRs introduced in Section 2.4.1 in order to investigate their performance in scintillation monitoring. The results are shown and discussed in Section 3.2.2.

2.6 Summary

This chapter provided a focused review of GNSS, targeting the topics of interest to this thesis, including signals, receivers and positioning determination algorithms. In particular, receiver code and phase tracking loops and tracking errors are introduced, which benefits a better understanding of the modelling of scintillation effects on tracking loops given in Chapter 4. Among all the GNSS positioning techniques, PPP algorithms are described in detail, which is applied hereafter to investigate the scintillation effects on GNSS positioning and to test the performance of scintillation mitigation approaches. Additionally, two types of ISMRs that are widely used for scintillation data collection and the ISMR networks deployed at low and high latitudes are described. The SDR receiver used in this thesis is also introduced. Scintillation simulation using the GNSS hardware signal simulator is described finally. In the next Chapter, the scintillation indices estimation based on the high frequency data logged by ISMRs is described. The signal intensity fading under scintillation and its effects on receiver tracking loops are analysed.

3 Scintillation data processing and intensity fading characterisation

This chapter covers the scintillation data detrending and scintillation indices estimation techniques used in this thesis, which involve processing high frequency signal amplitude and phase measurements logged by the ISMRs. Based on the simulated GNSS scintillation data, the difference of two types of ISMRs in scintillation monitoring and the effects of receiver PLL bandwidth and integration time tuning on the scintillation indices estimation are fully analysed. Additionally, the signal intensity fadings due to scintillation is characterized using three months of real scintillation data collected during solar maximum at low latitudes, where scintillation is more severe and frequently observed. The relationship between fadings and scintillation levels is modelled and the effects of intensity fadings on PLL tracking loop performance are investigated. Based on the analysis, it is found that it is necessary to estimate the scintillation indices at a higher sampling rate.

3.1 Scintillation indices estimation

Ionospheric scintillation is normally distinguished as amplitude and phase scintillation, referring to the rapid and random fluctuations in signal intensity and phase, respectively. Using the high frequency amplitude and phase measurements logged by the ISMRs introduced in Section 2.4, amplitude and phase scintillation indices are estimated to indicate the respective scintillation levels. A data detrending process is implemented in order to minimize the non-scintillation related effects before the scintillation index estimation. Figure 3.1 shows the data flow to calculate scintillation indices using the 50 Hz amplitude and phase measurements logged by PolaRxS Pro receiver. Details of the data processing in the figure are introduced hereafter.

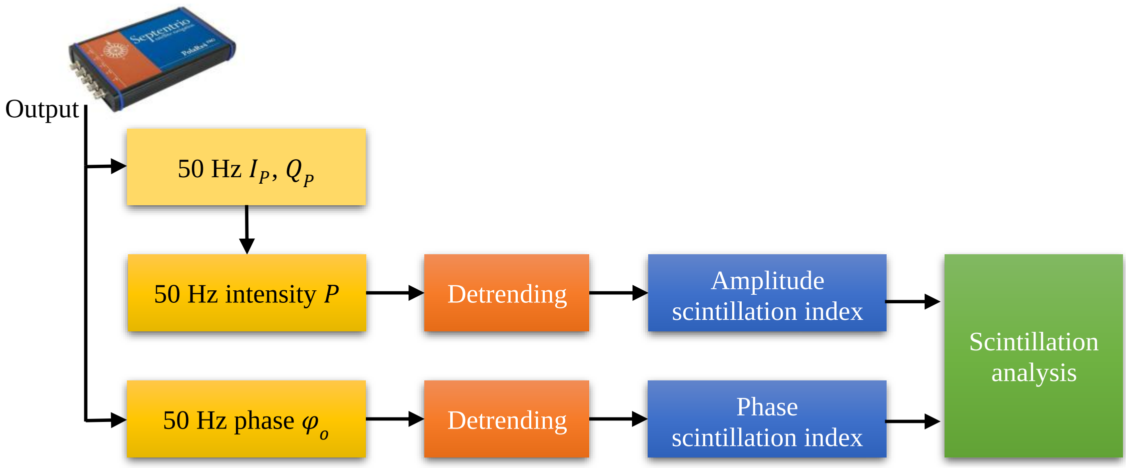

Figure 3.1 Amplitude and phase scintillation index estimation process using 50 Hz amplitude and phase measurements logged by PolaRxS Pro receiver

3.1.1 Amplitude scintillation index

Before the amplitude scintillation index estimation, raw signal intensity measurements need to be detrended in order to remove the low-frequency variation in signal intensity caused by non-scintillation effects, e.g., satellite motion, antenna pattern and multipath. Using the high frequency post-correlation In-phase I_P and Quadra-phase Q_P measurements in the prompt branches, as shown in Figure 2.3, the signal intensity P is calculated by

$$P = I_P^2 + Q_P^2 \tag{3.1}$$

In data detrending, the intensity measurements are first passed through a sixth-order Butterworth low-pass filter with a cut-off frequency of 0.1 Hz to obtain the intensity trend, denoted as P_{trend}. Then the raw intensity P is normalized by its 60-second averaged trend to obtain the detrended signal intensity P_{det}, as shown in the following equation (Van Dierendonck et al. 1993; Van Dierendonck and Arbesser-Rastburg 2004)

$$P_{det} = \frac{P}{\langle P_{trend} \rangle_{60\,s}} \tag{3.2}$$

where P_{det} is the detrended signal intensity. $\langle \cdot \rangle$ denotes arithmetic mean. After detrending, the low-frequency variations in P_{det} can be significantly removed, and the value of P_{det} will fluctuate around 1 (0 dB). It is interesting to note that the cut-off frequency can influence the fluctuation of the detrended intensity, thus affecting the calculation of the scintillation index (Forte and Radicella 2002; Mushini et al. 2012).

With the detrended signal intensity measurements, the amplitude scintillation index $S4$, defined as the standard deviation of the detrended signal intensity normalized by its mean over 60 second, is calculated as (Van Dierendonck et al. 1993; Van Dierendonck, 1999)

$$S4_{total} = \sqrt{\frac{\langle P_{det}^2 \rangle_{60\mathrm{s}} - \langle P_{det} \rangle_{60\mathrm{s}}^2}{\langle P_{det} \rangle_{60\mathrm{s}}^2}} \tag{3.3}$$

As there is still ambient noise included in P_{det}, the $S4_{total}$ calculated by Eq. (3.3) needs to be corrected to remove the ambient noise contribution, which is estimated as (Van Dierendonck et al. 1993)

$$S4_{noise} = \sqrt{\frac{100}{c/n_0}\left[1 + \frac{500}{19 * c/n_0}\right]} \tag{3.4}$$

Thus, the corrected $S4$ is calculated as (Van Dierendonck et al. 1993)

$$S4 = \begin{cases} \sqrt{S4_{total}^2 - S4_{noise}^2} & if\ S4_{total} > S4_{noise} \\ 0 & if\ S4_{total} \leq S4_{noise} \end{cases} \tag{3.5}$$

The corrected $S4$ is employed to carry out the analysis throughout this thesis.

Figure 3.2 shows an example of the intensity measurement detrending process on GPS L1 C/A signal for PRN 18 observed between UTC 00:00 and 02:20 on 11 December 2014 at Presidente Prudente (Lat. 22.12°S, Long. 51.41°W, Magnetic Lat. 12.74°S), denoted PRU2, a low latitude scintillation monitoring station near the geomagnetic equator in the CIGALA/CALIBRA network in Brazil, as shown in Figure 2.10. During this period, significant and rapid fluctuations in the signal intensity can be observed in the top panel. Apart from these rapid fluctuations, the intensity also varies slowly with time as denoted by the red line. This slow trend is mainly caused by the range change due to the satellite motion. In intensity detrending, this trend is removed and the detrended intensity fluctuates around 0 dB, as shown in the middle panel. Based on the detrended intensity, the amplitude scintillation index $S4$ is estimated, as shown in the bottom panel. It can be seen that the level of $S4$ is substantially modulated by the extent of signal intensity fluctuations.

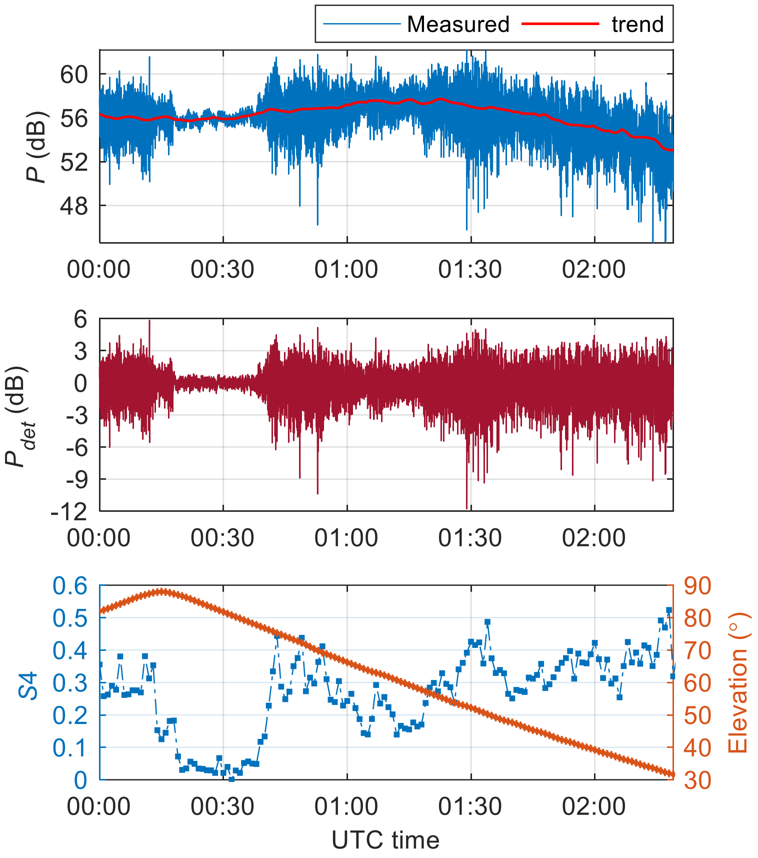

Figure 3.2 Intensity measurement detrending and scintillation index estimation on GPS L1 C/A signal for PRN18 observed between UTC 00:00 and 02:20 on 11 December 2014 at PRU2 station. Panels respectively show the measured signal intensity and trend (top), the

detrended signal intensity (middle) and the variation of $S4$ and satellite elevation (bottom) as a function of time

It is worth mentioning that even after the data detrending process, there still might be non-scintillation effects present in the detrended signal intensity, e.g., multipath, which may contaminate the estimation of scintillation index, as well as affect the scintillation study. To minimize the effects of multipath on scintillation analysis, a common approach is to remove the scintillation data captured on satellites with elevations lower than 30°. Readers interested in the study of distinguishing scintillation and multipath may refer to McCaffrey et al. (2017).

3.1.2 Phase scintillation index

The detrending of the carrier phase can be realized by passing the high frequency phase measurements φ_o through a sixth-order high pass Butterworth filter with a cut-off frequency of 0.1 Hz (Van Dierendonck et al. 1993), which is a value widely used in scintillation studies as well as in the ISMRs. The phase scintillation index $Phi60$, is defined as the standard deviation of the detrended carrier phase measurements in 60 seconds, given by (Van Dierendonck 1999)

$$Phi60 = \sqrt{\langle \varphi_{det}^2 \rangle_{60\mathrm{s}} - \langle \varphi_{det} \rangle_{60s}^2}\ \text{(rad)} \tag{3.6}$$

where φ_{det} is the detrended carrier phase. PSD of the detrended carrier phase measurements is also calculated to characterize phase scintillation in the frequency domain. According to Rino (1979), the PSD of phase scintillation can be represented by a wave diffraction phase screen model, defined as

$$S_\varphi(f) = \frac{T}{[f^2 + f_0^2]^{p/2}} \tag{3.7}$$

where f_0 is the frequency corresponding to the outer scale size of irregularities. f is the frequency component of the detrended phase measurements. p is the spectral index corresponding to the opposite of the PSD slope in log-log axis. T is the spectral strength, which is the value of the PSD at 1 Hz. When $f \gg f_0$, which is usually the practical case, $S_\varphi(f) \approx Tf^{-p}$.

Figure 3.3 gives an example of the phase PSD curves in two different minutes calculated based on the carrier phase recorded by a PolaRxS Pro receiver. The linear fitting functions of the PSD curves over 0.1 to 25 Hz in log-log axes are also included in the figure. As it can be observed, when there is no scintillation with $Phi60 = 0.02\,\text{rad}$, the phase PSD curve, in pink, is relatively flat between 0.1 to around 5 Hz. By contrast, under phase scintillation with $Phi60 = 0.48\,\text{rad}$, the PSD curve in blue obviously shifts upward resulting in an increased spectral energy, leading to a steeper slope and a larger p value. It should be noted that for both curves, the energy of the phase spectrum is at a low level when the frequency is lower than 0.1 Hz. This is due to the phase measurement detrending process where a high pass filter with a cut-off frequency of 0.1 Hz is used.

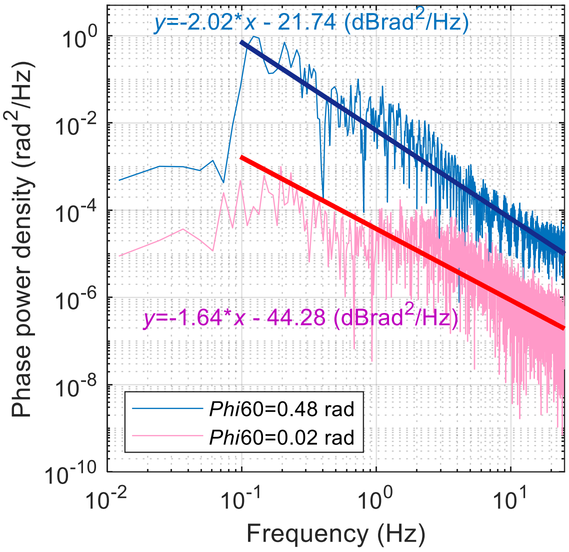

Figure 3.3 PSD curves of the detrended phase measurements with and without scintillation calculated based on phase measurements recorded by a PolaRxS Pro receiver

On the other hand, the phase variance is related to p and T by (Rino 1979; Conker et al. 2003; Aquino et al. 2007)

$$\sigma_{\varphi}^{2} = 2\int_{f_{lower}}^{f_{upper}} T f^{-p} \mathrm{d}f \tag{3.8}$$

In Eq. (3.8), f_{upper} is defined by half of the sampling frequency, while f_{lower} is given by the inverse of the time interval for the estimation, or by the cut-off frequency used for the phase measurement detrending, whichever is higher (Aquino et al. 2007). When using 50 Hz data to estimate the scintillation index at a rate of 1 minute, f_{upper} and f_{lower} are set as 25 and 0.1 Hz, respectively. Performing the integration of Eq. (3.8), the following equation is obtained (Aquino et al. 2007)

$$\sigma_{\varphi}^{2} = 2T\left[\frac{25^{r} - 0.1^{r}}{r}\right] \tag{3.9}$$

where $r = 1 - p$. If the integration is performed based on 60 seconds data, σ_{φ} is equivalent to $Phi60$. Figure 3.4 presents the relationship between σ_{φ}, p and T according to Eq. (3.9). As the figure shows, when the value of p is fixed, T increases dramatically with the increase in σ_{φ}, while the increase in p will not cause significant increase in T when σ_{φ} is unchanged, indicating that T is less sensitive to the variation of p.

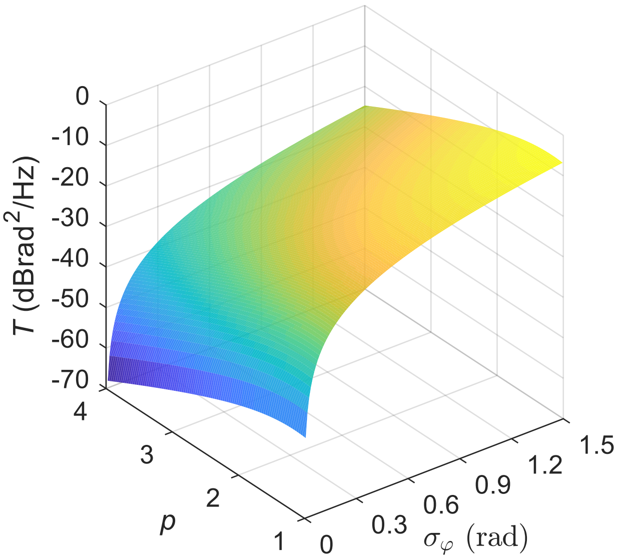

Figure 3.4 Relationship among phase scintillation indices σ_φ, p and T

3.1.3 Scintillation index across carrier frequency bands

The scintillation intensity is related to the RF signal carrier frequency. A signal with a lower frequency is more vulnerable to scintillation. For two RF signals with the carrier frequencies of f_1 and f_2, the scintillation indices on different signals satisfy the following relationships (Rino 1979; Hegarty et al. 2001; Conker et al. 2003)

$$S4(f_2) = \left(\frac{f_1}{f_2}\right)^{1.5} S4(f_1) \tag{3.10}$$

$$Phi60(f_2) = \left(\frac{f_1}{f_2}\right) Phi60(f_1) \tag{3.11}$$

$$p(f_2) = p(f_1) \tag{3.12}$$

Figure 3.5 shows an example of the relationship between $Phi60$ measured respectively on Galileo E1 and E5a signals. The scintillation data was collected by a PolaRxS Pro ISMR deployed at Longyearbyen ($78.169°N$, $15.992°E$) in the Arctic during a geomagnetic storm in September 2019. As it can be seen, the ratio of the measured $Phi60$ index on E5a to that on E1 is 1.35, which is approximately the ratio between f_{E1} and f_{E5a}.

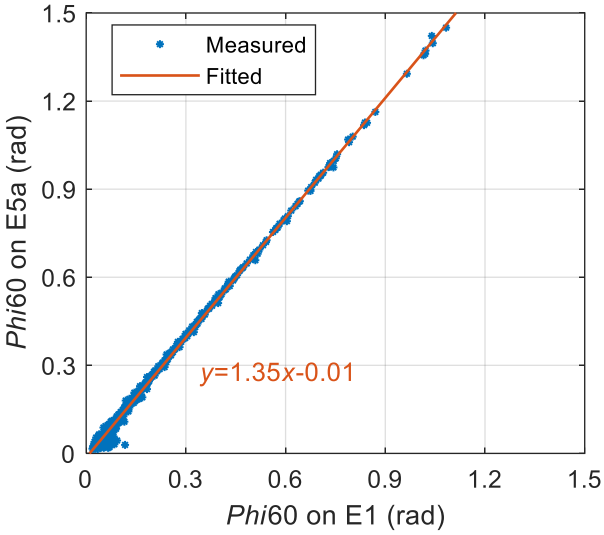

Figure 3.5 Relationship between $Phi60$ measured respectively on Galileo E1 and E5a signals. The data were collected by a PolaRxS Pro receiver deployed at Longyearbyen in the Arctic during a geomagnetic storm which took place from 29 August to 3 September 2019

Since the high frequency amplitude and carrier phase measurements for GPS L2 P signals are not logged by the ISMRs, the scintillation indices for L2 P signals are approximated using Eq. (3.10) to (3.12) in this thesis. With the estimated scintillation indices, the phase and code error variances in the receiver PLL and DLL are calculated. This is described in Chapter 4.

3.2 Tracking loop tuning effects on scintillation monitoring

As described in Section 2.4, different types of ISMRs are employed to monitor scintillation. However, the estimation of scintillation indices may be related to the receiver tracking loop models and configurations. By processing simulated scintillation data, this section investigates the effects of PLL bandwidth and integration time tuning on scintillation index estimation. The different characteristics of ISMRs in scintillation estimation are also analysed.

3.2.1 Scintillation data simulation

Using the GNSS hardware simulator introduced in Section 2.5, scintillation data on GPS L1 C/A signal were simulated. In the simulation, the scintillation profile file, i.e., the .ucd file, was generated from a 2-hour real scintillation data set collected at PRU2 station. In this analysis, the PolaRxS Pro and GSV4004B receivers with the default settings are first connected to the simulator output to record the simulated scintillation data. Scintillation indices calculated using the recorded data are then compared between receivers.

In addition, the simulation and data collection were replayed by changing the PLL bandwidth B_n and coherent integration time η in PolaRxS Pro receiver through the GUI. A total of five simulations were carried out. The configurations of B_n and η in the PLL for each simulation are summarized in Table 3.1. Based on the 50 Hz amplitude and phase measurements logged by the receiver, the amplitude and phase scintillation indices in each case are calculated and compared. It is worth mentioning that Case 3 has the same parameters as the default receiver configuration. Clean data is also generated in Case 5 for comparison. It is worth mentioning that the same scintillation scenario is applied to all the visible satellites in the simulation. Therefore, only one satellite is selected for the analysis hereafter.

Table 3.1 PLL configurations for each case in the analysis

	B_n (Hz)	η (ms)	Scintillation effects
Case 1	5	10	Enabled
Case 2	10	10	Enabled
Case 3	15	10	Enabled
Case 4	15	20	Enabled
Case 5	15	10	Disabled

3.2.2 Comparison of different types of ISMRs in scintillation monitoring

This section presents the performance of different types of ISMRs in scintillation monitoring. As mentioned in Section 3.2.1, the simulated data was recorded by PolaRxS Pro and

GSV4004B ISMRs with the default configurations, respectively. Using the 50 Hz amplitude and phase data, the scintillation indices, $S4$, $Phi60$, p and T, are calculated following the procedure introduced in Section 3.1. Figure 3.6 shows the variations of the $S4$ and $Phi60$ indices calculated using the data logged by the two ISMRs. As it can be seen, the scintillation indices obtained by both ISMRs generally match well, while slight biases are seen in $Phi60$ shown in the bottom panel.

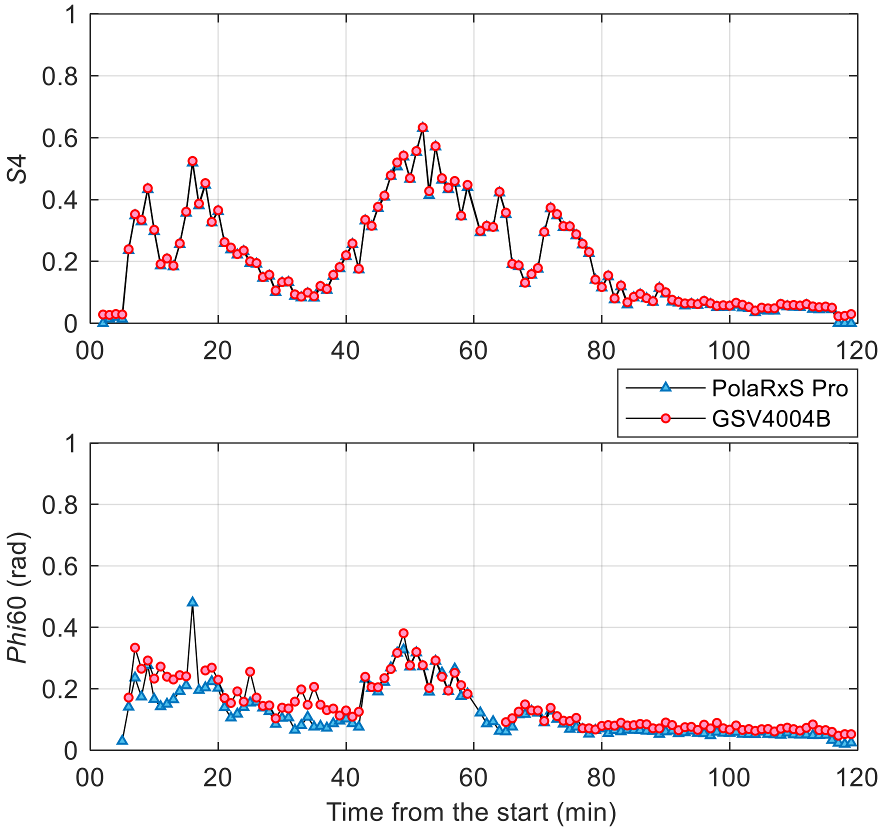

Figure 3.6 Comparison of scintillation indices $S4$ (top) and $Phi60$ (bottom) calculated using 50 Hz amplitude and phase measurements respectively logged by PolaRxS Pro and GSV4004B receivers

To compare the phase scintillation spectrum, the PSDs of the phase scintillation in the 48th minute are calculated using the phase measurements, as shown in Figure 3.7. In this minute, the $Phi60$ calculated using the PolaRxS Pro logged data is 0.33 rad, while it reaches 0.38 rad for GSV4004B receiver. It can be seen that the PSD curves in both panels are quite similar from 0.1 to around 2 Hz. The slope of the PSD in the left panel keeps decreasing with the increase in frequency, while in the right panel, the PSD starts to deviate from the slope, which indicates that the high frequency noise component is stronger in the phase measurements recorded by GSV4004B receiver. This high frequency component is mainly the white noise that contaminates the incoming signal and the receiver thermal noise (McCaffrey and Jayachandran 2017). Due to this high frequency noise component, using a range of 0.1 to 25 Hz would result in an underestimation of the spectral index p, as the green line in the right panel shows. To address this issue, an alternative range of 0.1 to 5 Hz is applied to calculate the p and T values for GSV4004B receiver (Strangeways et al. 2011).

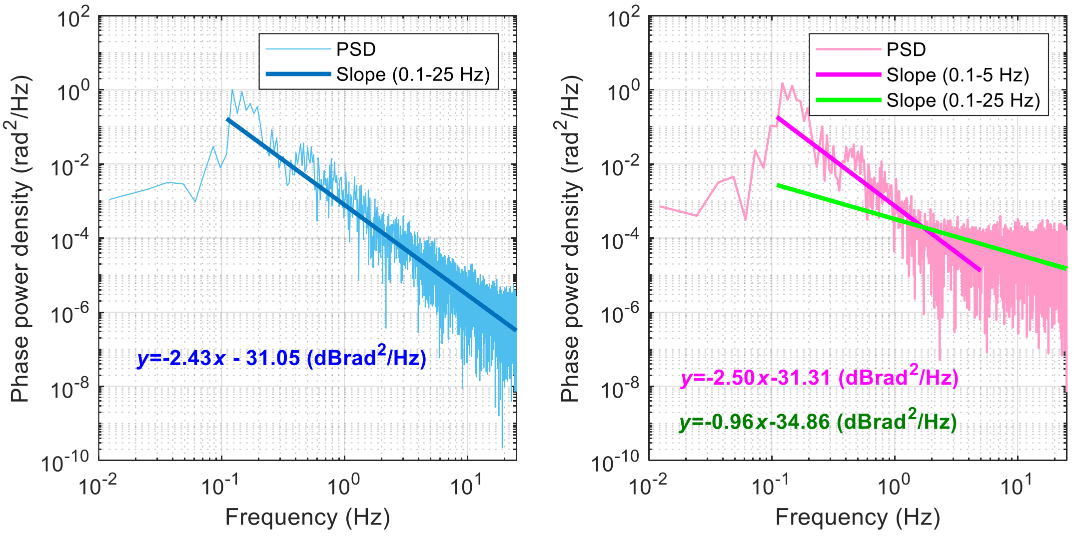

Figure 3.7 Comparison of phase scintillation PSDs in the 48th minute calculated using the 50 Hz phase measurements logged by PolaRxS Pro (left) and GSV4004B (right) ISMRs

Figure 3.8 shows the spectral index p and spectral strength T calculated using the 50 Hz phase measurements logged by the PolaRxS Pro and GSV4004B receivers. For the latter, the indices are calculated based on a linear fitting of 0.1 to 25 Hz and 0.1 to 5 Hz, respectively. As the top panel shows, the p index estimated using the data logged by the PolaRxS Pro ISMR is relatively larger. It increases slightly during the scintillation occurrence. Large differences are seen between the p values estimated for these two ISMRs, especially from the 60th to 120th minute. The smallest values occur when fitting the slope of the PSD over a range of 0.1 to 25 Hz. On the other hand, although there are still obvious differences in the estimated T index as the bottom panel shows, they are generally small. Compared with fitting the slope of PSD over a range of 0.1 to 25 Hz, the T values estimated based on a fitting range of 0.1 to 5 Hz achieve more comparable values to those estimated for the PolaRxS Pro receiver. This is reasonable as the high frequency fluctuations caused by scintillation are buried in the carrier phase background noise which is at a relatively higher levels at high frequency, as the right panel in Figure 3.7 shows.

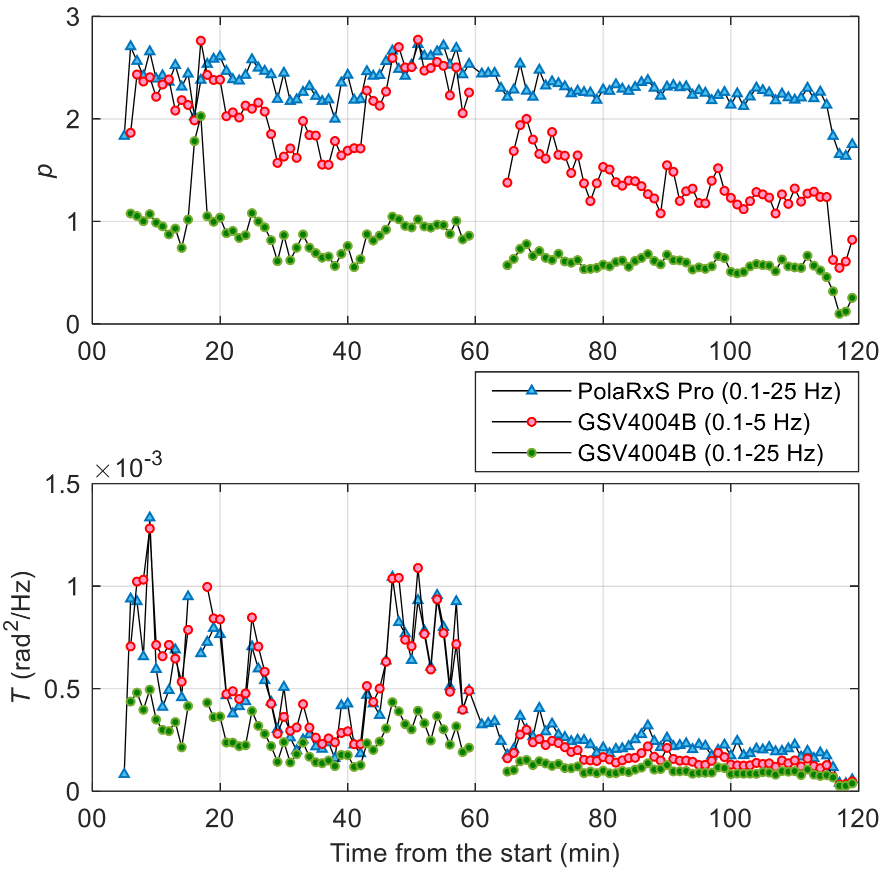

Figure 3.8 Comparison of phase scintillation spectral indices p (top) and T (bottom) calculated using 50 Hz phase measurements logged by PolaRxS Pro and GSV4004B ISMRs

Based on the analysis in this section, it can be seen that the difference in the scintillation indices $S4$ and $Phi60$ measured by PolaRxS Pro and GSV4004B ISMRs is smaller, suggesting they can be combined in scintillation studies. However, for the phase scintillation spectral indices p and T, relatively larger differences are observed between these two types of ISMRs. Thus, it should be specially considered when combining the spectral indices p and T in scintillation studies. This conclusion is meaningful for the generation of receiver code and phase jitter maps introduced in Chapter 6.

3.2.3 Scintillation index comparison with respect to PLL tuning

To analyse the PLL bandwidth and integration time tuning effects on scintillation index estimation, the amplitude and phase scintillation indices are calculated and compared for each case listed in Table 3.1 in this section. Figure 3.9 shows the variation of $S4$ and $Phi60$ in relation to time in Cases 1 to 5. It can be seen from the figure that both $S4$ and $Phi60$ increase from the 5th to 20th minute and the 40th to 60th minute. The $S4$ indices calculated with different PLL bandwidth B_n and integration time η have small differences, which indicates that both loop bandwidth and integration time have almost no effect on $S4$ calculation. This agrees with the conclusions in Rougerie et al. (2016). On the other hand, there are slight differences in $Phi60$ when B_n and η are different, as shown in the bottom panel. In Case 5 when scintillation effects are not added in the signal simulation, both $S4$ and $Phi60$ show extremely low levels.

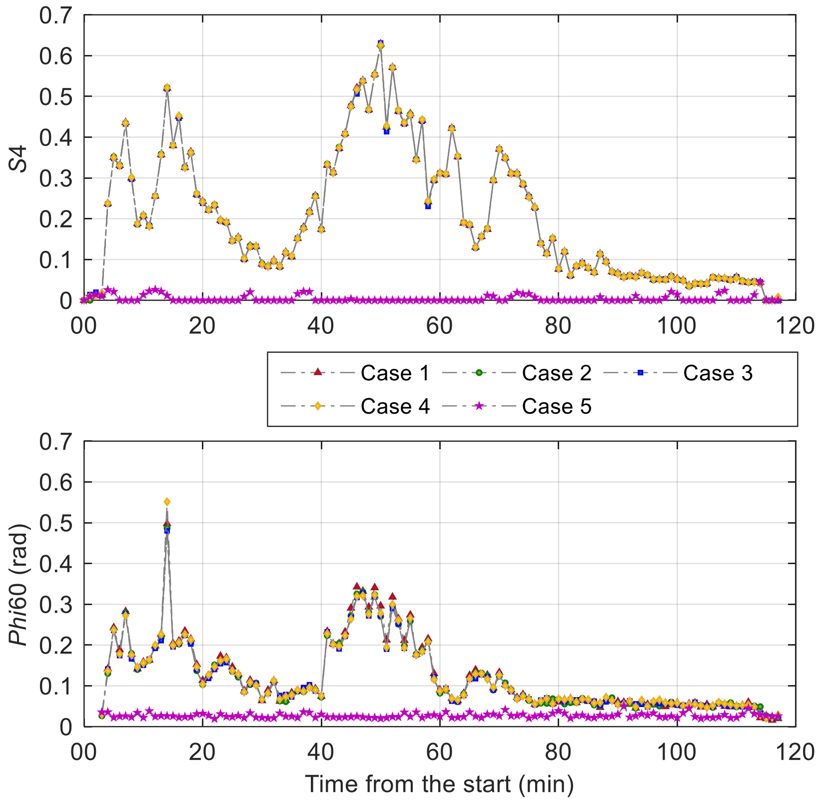

Figure 3.9 Variations of $S4$ (top) and $Phi60$ (bottom) in relation to time calculated with receiver PLL bandwidth and integration time tuning in each case summarised in Table 3.1

The phase scintillation spectral slope p and spectral strength T are then calculated, as shown in Figure 3.10. As it can be seen from the top panel, increases in p values can be observed with the increase in scintillation levels between the 40th and 60th minute. When the PLL integration time η is configured to 10 ms, the p values of tracking loop with B_n of 5 Hz, 10 Hz and 15 Hz are comparable, which means that the PLL bandwidth has low impacts on the estimation of p values. By contrast, when integration time is increased from 10 ms in Case 3 to 20 ms in Case 4, obvious higher values are seen, especially when scintillation levels are not strong between the 70th and 115th minute. The mean of the p values in each case is summarised in Table 3.2.

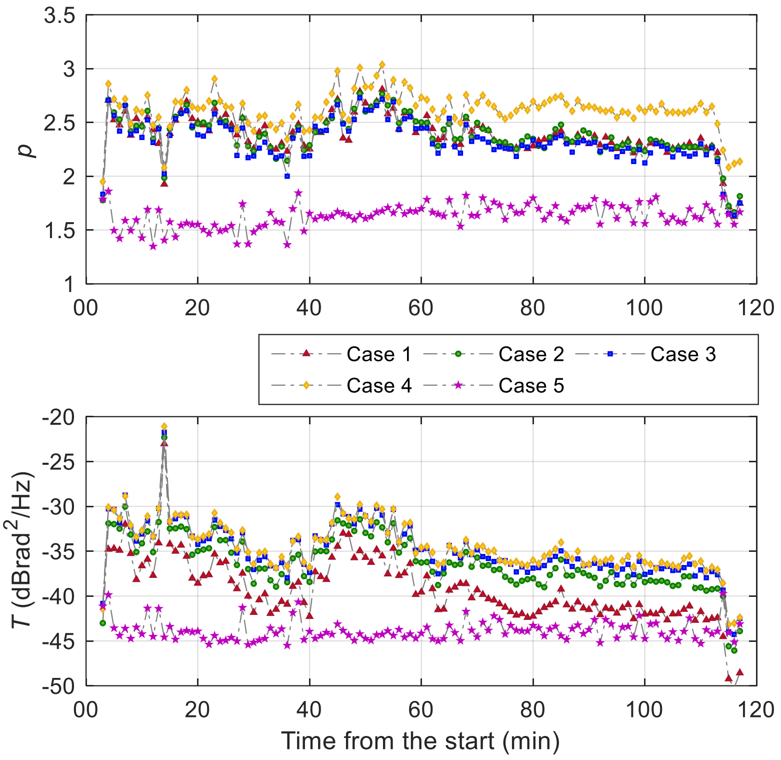

Figure 3.10 Variation of the spectral slop p and spectral strength T in relation to time calculated with receiver PLL bandwidth and integration time tuning in each case summarised in Table 3.1

On the other hand, similar variations are seen in the phase scintillation spectral strength T values as a function of time, as shown in the bottom panel of Figure 3.10. However, increasing the PLL bandwidth can correspondingly increase the level of T values, which is different from its effect on the estimation of p values shown in the top panel. Furthermore, the increase of PLL integration time from 10 ms in Case 3 to 20 ms in Case 4 also results in very little effects on the estimation of T values. The averaged T values in each case are calculated and listed in Table 3.2.

Table 3.2 Averaged phase scintillation spectral slop p and strength T values for Cases 1 to 5

	Case 1	Case 2	Case 3	Case 4	Case 5
Averaged p	2.38	2.38	2.33	2.61	1.63
Averaged T ($\mathrm{dBrad^2Hz}$)	-37.18	-34.75	-33.56	-33.14	-43.74

Based on the analysis in this section, it is seen that the PLL bandwidth and integration time tuning have almost no effect on the estimation of $S4$ and $Phi60$. However, slight effects are observed in the estimation of phase scintillation spectral slop p and spectral strength T. By exploiting the estimated scintillation indices in each case, the receiver PLL phase jitter in each case is also estimated, aiming to analyse the PLL tuning effects on phase jitter estimation under scintillation. Results and discussion are given in Chapter 4.

3.3 Signal intensity fading under scintillation

In the presence of scintillation, the signal intensity fadings can significantly degrade the receiver performance by inducing frequent losses of signal lock and cycle slips, as well as increasing tracking errors. This section characterises the signal intensity fadings by processing the scintillation data collected at PRU2 station. The data recorded on the GPS L1 C/A signal from 1 October to 31 December 2014 was selected to carry out the study. It was chosen according to the solar activity, which peaked in 2014, and data availability. As the low latitude scintillation mainly occurs in the period from post-sunset to midnight, the data collected during daytime was not analysed. Thus, a total of 1068 hours of scintillation data was processed. In the rest of this section, an overview of scintillation occurrence is given and the signal intensity fadings are defined. Fadings with different depths and durations are counted. The relationship between fading depth and duration and $S4$ is then investigated.

3.3.1 Overall scintillation occurrence and fading characterization

Figure 3.11 presents the daily occurrence of various levels of amplitude scintillation observed at PRU2 station over the 3 months. The scintillation index $S4$ was computed using the detrended signal intensity measurements. It can be seen that strong scintillation with $S4 > 0.7$ occurs almost every day. However, large day-to-day variabilities are observed. Due to the unavailability of scintillation data on 25, 26 October and 1, 2, 5 November, the scintillation occurrences for these days are not shown. Additionally, it should be noted that only scintillation observed on satellites with elevation higher than 30° are considered in this analysis, in order to remove as much as possible multipath effects.

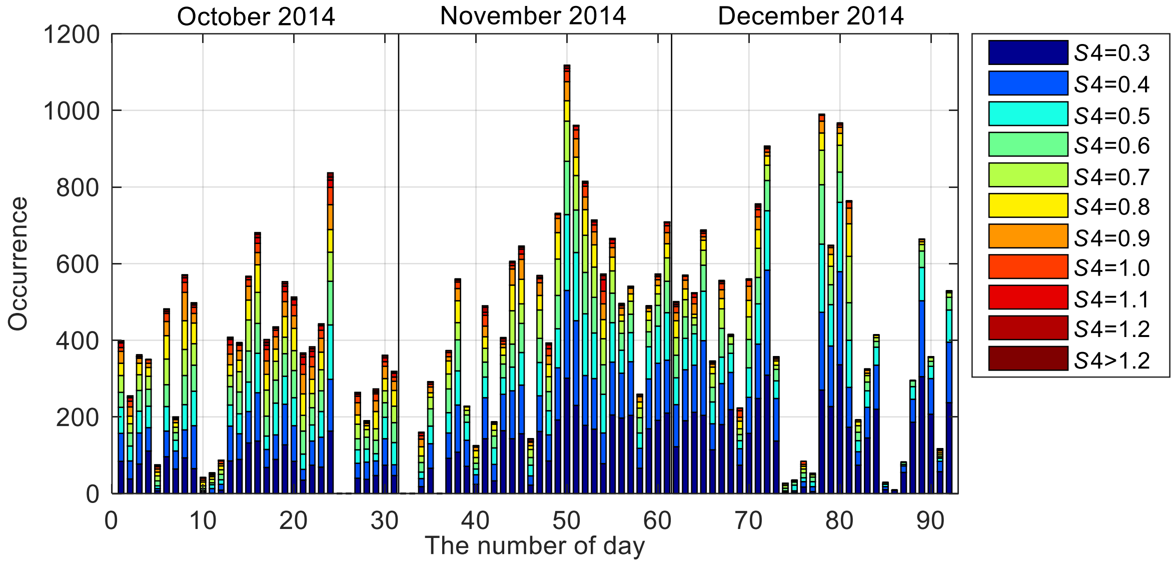

Figure 3.11 Daily occurrence of various levels of amplitude scintillation observed at PRU2 station from 1 October to 31 December 2014

Figure 3.12 illustrates the occurrence of scintillation in relation to $S4$. It is obvious that the occurrence of scintillation decreases with the increase in $S4$. Although scintillation with $S4 > 1.0$ has a relatively lower occurrence, these scintillation events may severely degrade the receiver tracking performance.

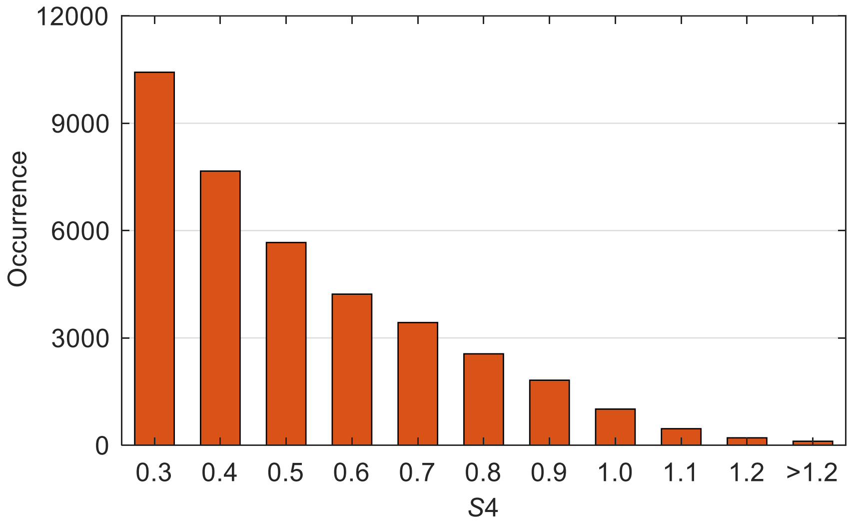

Figure 3.12 Occurrence of scintillation in relation to $S4$ captured at PRU2 station from 1 October to 31 December 2014

The signal intensity fadings due to scintillation are detected based on the detrended intensity measurements introduced in Section 3.1.1. The fading duration, t_f, defined as the time difference between the beginning and end of the fading, and the fading depth, d_f, defined as the minimum intensity within the fading (Akala et al. 2012; Jiao et al. 2016; Moraes et al. 2012), are shown in Figure 3.13. As it shows, the depth of the first fading is around -40 dB and the duration is around 1.2 second. Different thresholds are used to detect intensity fadings in the literature. A threshold of -5 dB is applied in this study, as it can clearly distinguish between the fadings caused by scintillation and ambient noise, which is explained hereafter. It is worth mentioning that even after the detrending process introduced in Section 3.1.1, high frequency noise still remains in the detrended intensity. Therefore, a threshold of 0.1 second was also applied to detect intensity fadings. In other words, only intensity fadings lasting longer than 0.1 second were considered.

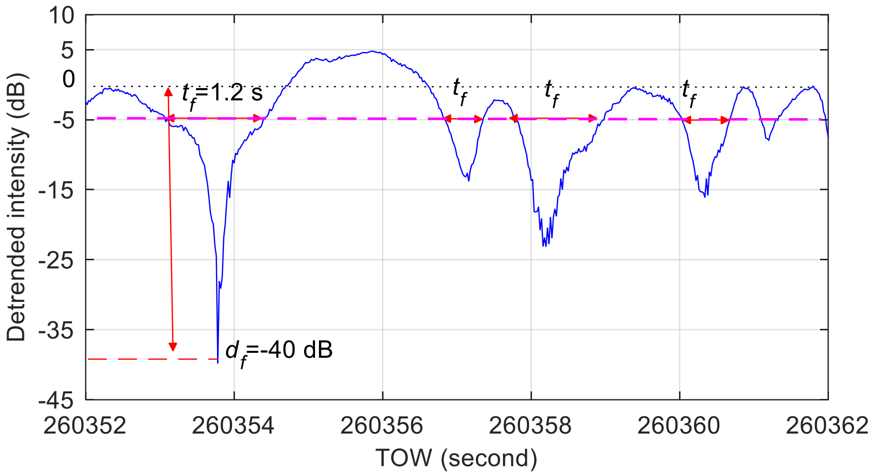

Figure 3.13 A demonstration of fading depth and duration on detrended signal intensity with a threshold of -5 dB. The detrended intensity was obtained based on the real scintillation data collected at PRU2 station

3.3.2 Overview of fading depth and duration

Using -5 dB as the threshold, a total number of 144891 fadings were detected based on the three months of scintillation data. The occurrence of fadings in relation to $S4$ is shown in the top panel of Figure 3.14. It can be seen that most fadings occurs when $S4 = 0.8$, although the scintillation occurrence at this level is not very high, as shown in Figure 3.12. Meanwhile, the number of fadings increases significantly from 26 for $S4 = 0.2$ to 1067 for $S4 = 0.3$ when scintillation is considered to occur. Thus, it can be concluded that the threshold of -5 dB can be effectively used to distinguish between intensity fadings caused by scintillation and signal fluctuations caused by ambient noise. The number of detected fadings using -10 dB as the threshold is also shown in the bottom panel. It can be seen that even when $S4 = 0.4$, the number of detected fadings is only 144. This may be due to the fact that the threshold of -10 dB dismisses plenty of intensity fadings caused by weak scintillation. Consequently, a threshold of -5dB is applied in this study to give a general understanding of the intensity fadings under low latitude scintillation.

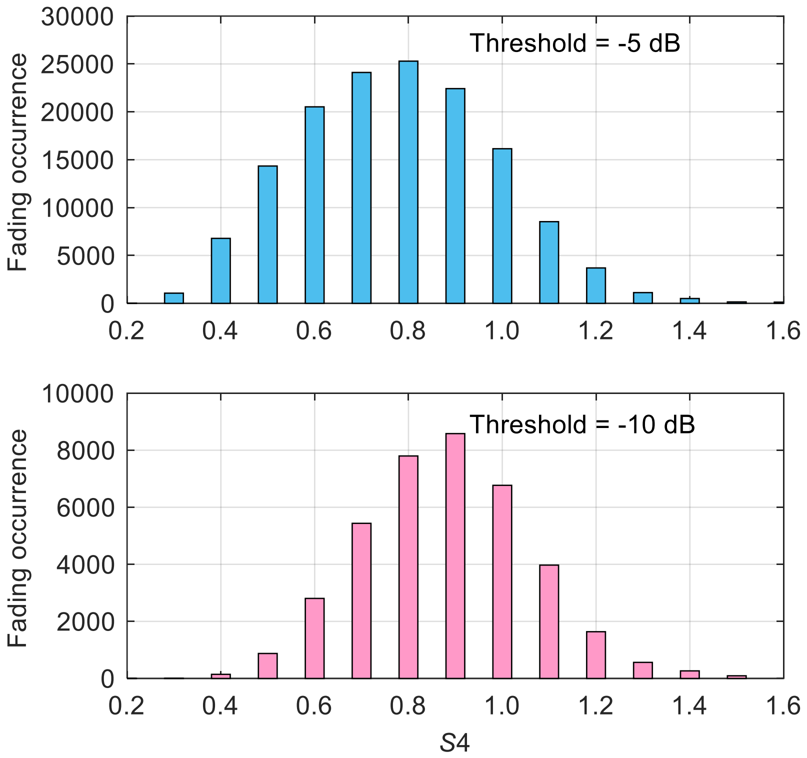

Figure 3.14 Fading occurrences in relation to *S*4 detected using thresholds of -5 dB (top) and -10 dB (bottom). The fadings were detected based on the scintillation data collected at PRU2 station from 1 October to 31 December 2014

The distribution of the detected fadings in relation to fading depth is demonstrated in the top panel of Figure 3.15. It can be seen that as the fading becomes deeper, the fading occurrence decreases rapidly. Most of the fading depths are between -5 dB to -15 dB. Similarly, the bottom panel presents the distribution of fadings as a function of fading duration. It can be seen that most of the fadings are within 1 second. The occurrence decreases dramatically with the increase in fading duration.

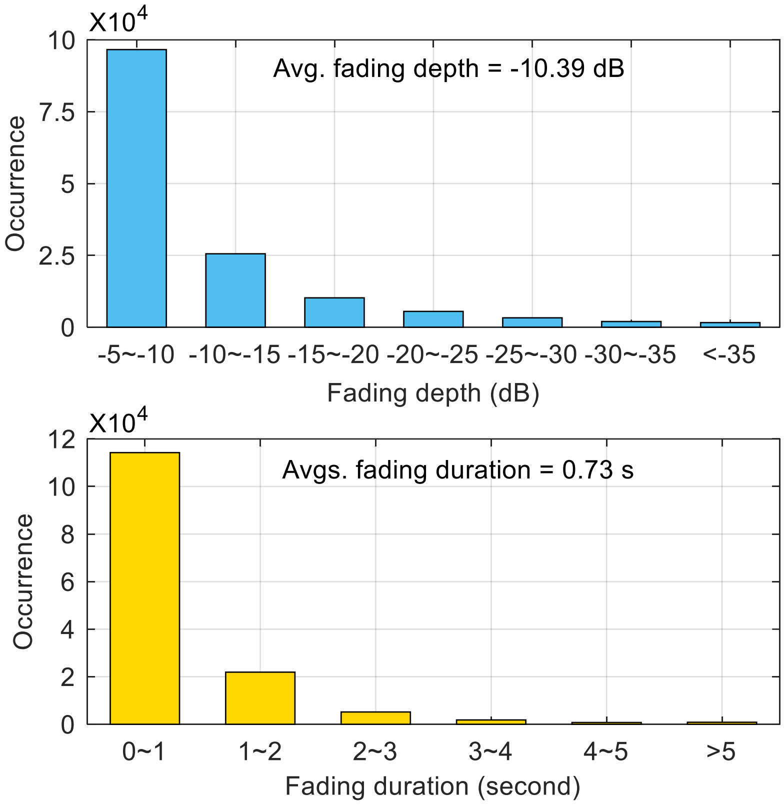

Figure 3.15 Distribution of fadings in relation to fading depth (top) and duration (bottom). The fadings were detected based on the scintillation data collected at PRU2 station from 1 October to 31 December 2014

The relationship between fading depth and duration is illustrated in Figure 3.16. It is seen that although the average fading depth and duration are -10.39 dB and 0.73 second, respectively, the fading can be as deep as -58 dB and as long as 31 second. Additionally, an inverse relationship is observed between the fading depth and duration. In other words, for fadings with depth lower than -40 dB, the duration is usually less than around 3 second, while for longer fadings, it tends to be not too deep.

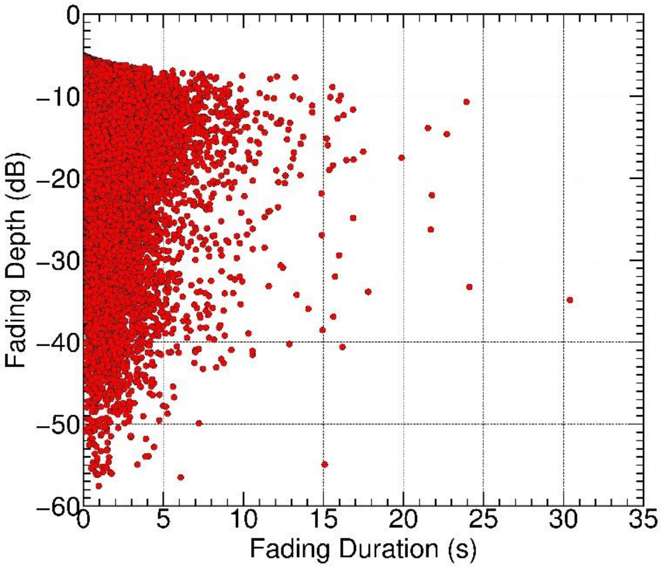

Figure 3.16 Relationship between fading depth and duration for all the fadings detected based on the scintillation data collected at PRU2 station from 1 October to 31 December 2014

3.3.3 Relationship between intensity fading and $S4$

This section investigates the relationship between the amplitude scintillation $S4$ and the signal intensity fading depths and durations. The analysis is carried out from two perspectives, i.e. (i) analysing the overall distribution of fading depth and duration in relation to $S4$; (ii) analysing the average fading depth, duration and occurrence based on every single scintillation event. Figure 3.17 demonstrates the percentage of fadings under various levels of fading depths and durations in relation to $S4$. It is seen from the top panel that the fadings with depth from -5 dB to -10 dB account for a large part of the total. The percentage of these fadings decreases gradually with the increase in $S4$. Conversely, the percentages of deeper fadings increase when $S4$ increases. From the bottom panel, fadings with duration shorter than 1 second account for a large part across all the scintillation levels, whereas fadings with duration longer than 3 second occur only when $S4 \geq 0.5$.

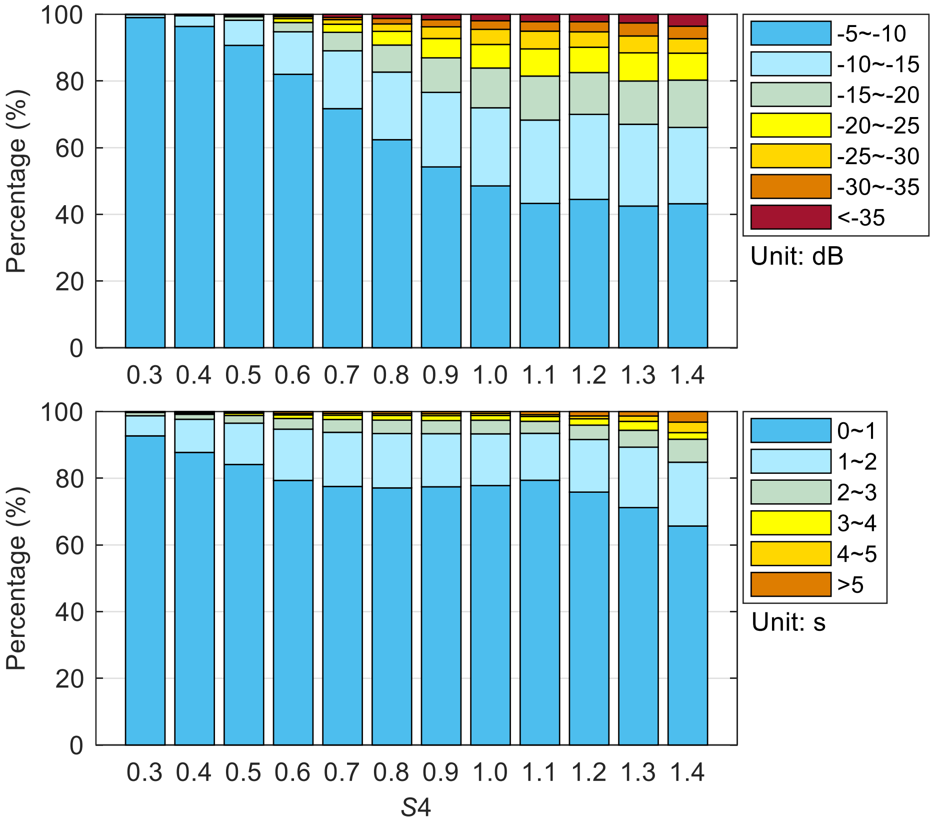

Figure 3.17 Percentages of fadings for various fading depths (top) and durations (bottom) with respect to $S4$. The fadings were detected based on the scintillation data collected at PRU2 station from 1 October to 31 December 2014

Figure 3.17 emphasizes the distribution of fading depth and duration for all the detected fadings with respect to scintillation levels. However, the intensity fadings do not occur for all scintillation events. The ratio of the fading occurrence over scintillation occurrence as a function of $S4$ is shown in Figure 3.18. It can be seen that the ratio increases from around 8% when $S4 = 0.3$ to nearly 80% when $S4 = 0.5$, following which it mostly remains over 80% when $S4$ keeps increasing, indicating a higher probability of the signal intensity fadings when $S4$ is over 0.5. However, it can be seen that even when $S4 > 1.2$, not all the scintillation events contain fadings with depth lower than -5 dB.

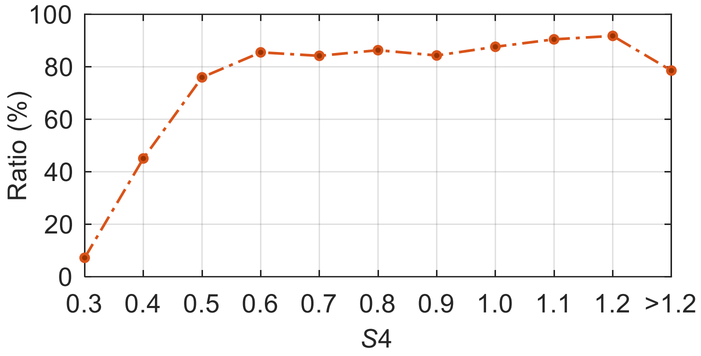

Figure 3.18 Ratio of the fading occurrence over scintillation events in relation to $S4$. The fadings were detected based on the scintillation data collected at PRU2 station from 1 October to 31 December 2014

The average fading depth, duration and occurrence for every single scintillation event, i.e., within 60 second, are calculated for all scintillation levels. Only scintillation events with $0.3 \leq S4 \leq 1.4$ are considered due to the lack of samples when $S4$ is over 1.4. The variation of the average fading depth in relation to $S4$ is presented in the top panel of Figure 3.19. A gradual decrease is observed with the increase in $S4$ from 0.3 to around 1.2. Then it remains at roughly the same level, indicating that strong scintillation is likely to correlate with deeper fadings generally, but the fading depth does not always decrease. Conversely, the average fading duration in the middle panel increases as the scintillation becomes more intense. Thus, the fading tends to last longer for strong scintillation on average, while for the variation of the average fading number in the bottom panel, a slight decrease is observed following the gradual increase. Therefore, it can be concluded that when $S4$ is over 1.2, the fading occurrence and depth tend to change slightly but the duration probably lasts longer.

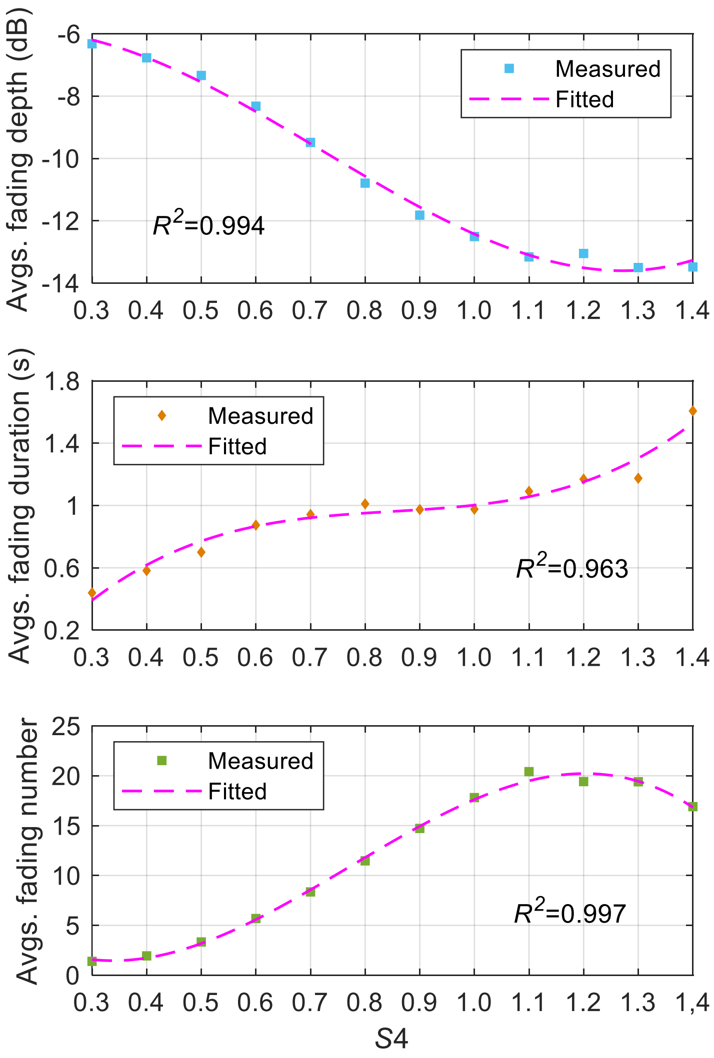

Figure 3.19 Variation of average fading depth (top), duration (middle) and fading occurrence (bottom) in relation to various $S4$ levels

The trends shown by the magenta lines in Figure 3.19 are then fitted using a third-order polynomial function, defined as

$$y = a * (S4)^3 + b * (S4)^2 + c * S4 + d \tag{3.13}$$

where y can be replaced by fading depth d_f, fading duration t_f and N_f, which is the fading occurrence over the scintillation index estimation interval, i.e., 60 second. Table 3.3 lists the coefficients of the functions in fitting the trends in Figure 3.19. In this way, the relationship between the general intensity fading depth, duration, occurrence and $S4$ is mathematically modelled. This contributes to a better understanding of the relationship between intensity fadings and $S4$. It is worth mentioning that although cycle slips are related to both signal intensity fading depths, durations and scintillation indices, it is not clear how their occurrences are correlated with these coefficients listed in Table 3.3. This can be further investigated in future studies.

Table 3.3 Coefficients of the functions for the fitted curves

	a	b	c	d
d_f	11.57	-25.05	7.582	-6.528
t_f	2.731	-6.969	6.137	-0.8966
N_f	-58.15	134.4	-70.98	12.34

3.4 Scintillation fading effects on PLL tracking performance

This section investigates the effect of intensity fadings on the PLL tracking loop performance based on the high frequency amplitude measurements logged by the PolaRxS Pro ISMR deployed at PRU2 station. The PLL tracking error and tracking jitter are calculated using Eq. (2.10) and (2.11) to indicate the tracking loop performance. Figure 3.20 illustrates an example of the PLL tracking error with and without intensity fadings caused by scintillation. In the left two panels when there is no scintillation, the detrended signal intensity P_{det} is relatively smooth and stable. The corresponding tracking errors in the bottom left panel are small and only include the ambient noise effects. On the other hand, in the right panels when strong scintillation occurs with $S4 = 0.95$, the intensity fluctuates significantly and very deep fadings are frequently observed, which results in the sharper fluctuations in the tracking errors shown in the bottom right panel. In this case, the tracking jitter increases to 0.56 rad. Consequently, it can be seen that the intensity fadings caused by amplitude scintillation can severely affect the tracking performance.

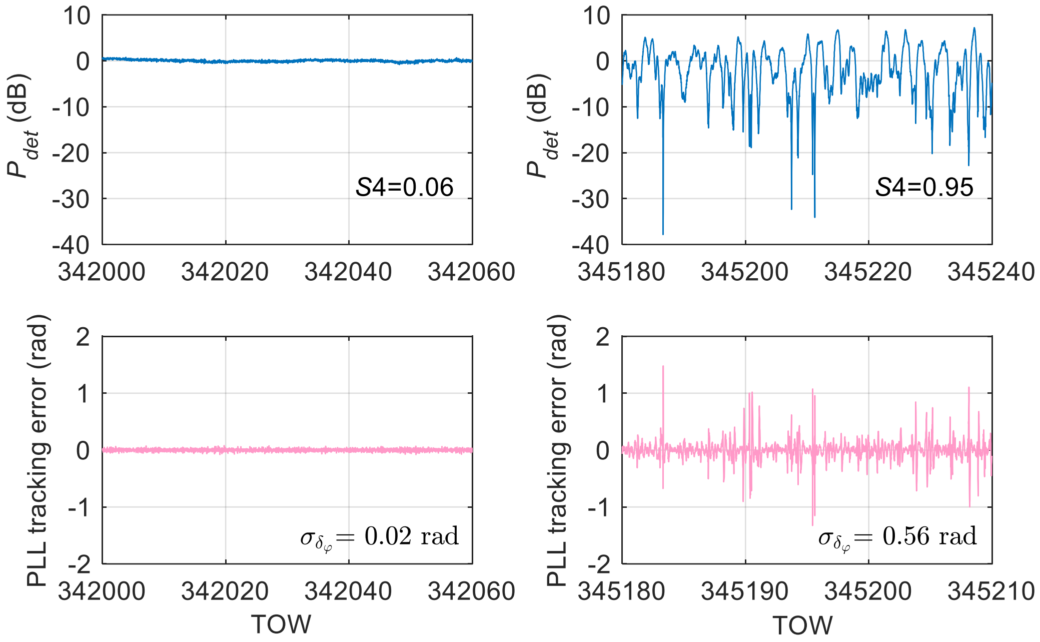

Figure 3.20 Variations of the detrended signal intensity and corresponding PLL tracking errors without (left panels) and with (right panels) the effects of scintillation. The signal intensity and tracking errors are calculated based on the real scintillation data collected at PRU2 station

Scatter plots of the post correlation In-phase I_P and Quadra-phase Q_P measurements corresponding to the two cases in Figure 3.20 are shown in Figure 3.21. When there is no scintillation as shown in the left panel, the I_P and Q_P measurements tend to concentrate on two clusters, indicating that the carrier phase is well tracked in the PLL, as almost all the signal intensity is maximum at I_P measurements (Ward 2017). Concurrently, the noise level, which is indicated by the spread of the clusters, is relatively low. By contrast, the I_P measurement in the right panel presents obvious fluctuations. The noise due to scintillation is evident by the large spread of the points within the two clusters (Ward 2017; Parkinson et al 1996). This further shows the adverse effects of fadings on the PLL tracking performance.

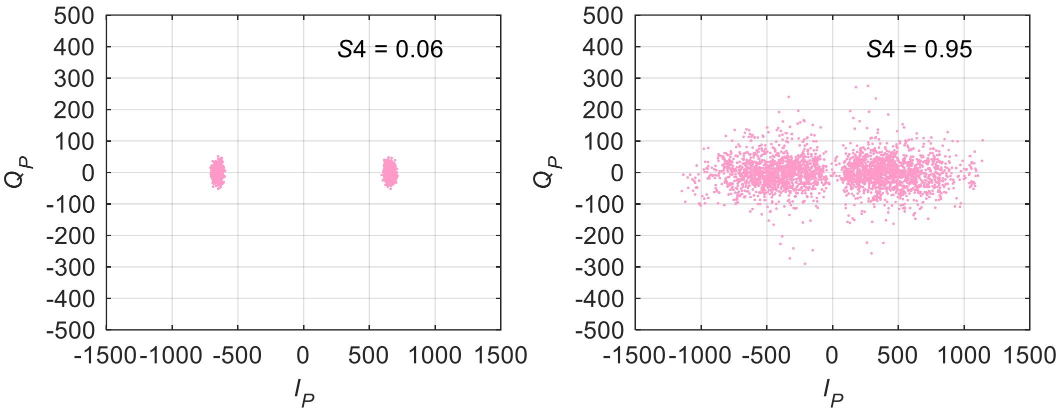

Figure 3.21 Distribution of I_P and Q_P measurements without (left) and with (right) the effects of scintillation corresponding to the two cases shown in Figure 3.20

The tracking error variance for every detected fading is calculated using the 50 Hz I_P and Q_P measurements. As these measurements are raw measurements including the ambient noise, only fadings detected on the satellite-to-receiver links over a satellite elevation of 45° are considered, aiming to minimize the influence of the ambient noise. Figure 3.22 presents the variation of the tracking error variance as a function of fading depth and duration. In the top panel, it is seen that the tracking error variance varies significantly for a fixed fading depth, while for the average tracking error variance shown as the red diamonds, it increases gradually and peaks at around -25 dB, followed by a slight fluctuation around 0.17 rad^2. Additionally, most of the PLL tracking error variances are lower than 0.4 rad^2 even when the fadings are deeper than -45 dB. Regarding the maximum tracking error variance shown in the larger blue dots, it increases gradually with the deeper fadings and peaks when the depth is around -20 dB. Then the maximum tracking error variance tends to decrease. This indicates that the fadings with depth around -20 dB to -25 dB may be more damaging and more likely to degrade the PLL tracking performance. On the other hand, the PLL tracking error variance tends to be larger when the duration is shorter than 3 second shown in the bottom panel. The maximum tracking error variance decreases gradually as the fading duration increases, indicating that shorter fadings tend to significantly increase the PLL tracking errors. It is worth mentioning that only fadings with duration shorter than 10 seconds are shown in the bottom panel due to the lack of samples when it is longer than 10 seconds.

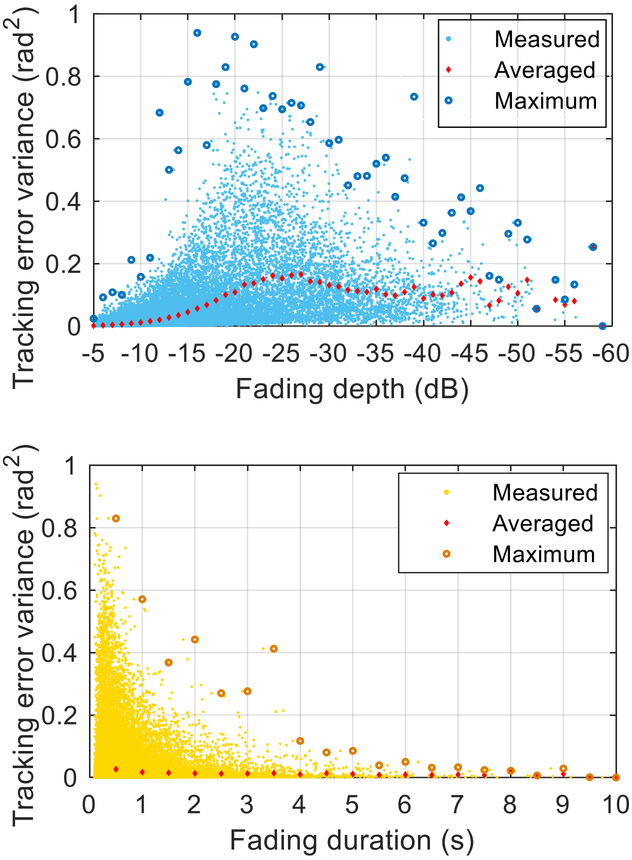

Figure 3.22 PLL tracking error variance in relation to fading depth (top) and fading duration (bottom). The fadings were detected based on the scintillation data collected at PRU2 station from 1 October to 31 December 2014

To further investigate how intensity fadings affects the PLL tracking performance, the fading speed is introduced in this study, which is defined as $v_{fading} = \frac{|d_f|}{t_f/2}\,(\mathrm{dB}/s)$. The PLL tracking error variance is then plotted as a function of v_{fading}, as shown in Figure 3.23. It can be clearly seen that the overall tracking error variance increases gradually when the fading speed increases. This tendency is reasonable as it is the sharp fadings with large fading speeds that actually degrade the PLL tracking performance under scintillation.

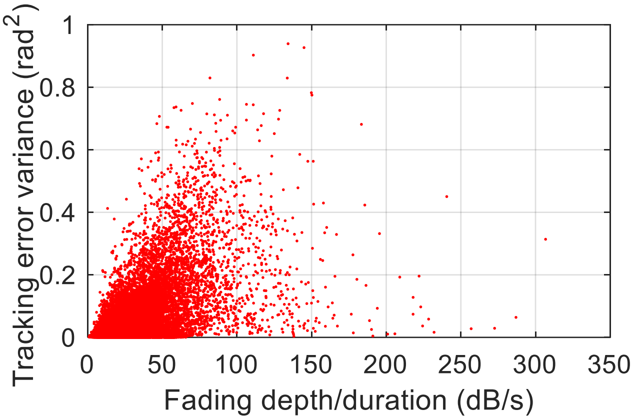

Figure 3.23 PLL tracking error variance in relation to fading speed

This section presented the effect of scintillation, mainly amplitude scintillation on PLL tracking performance by characterizing the relationship between the signal intensity fadings and the tracking error variances. The quantitative modelling of scintillation effects on receiver tracking loops will be given in detail in Chapter 4.

3.5 Towards a high-rate scintillation index

Based on the analyses in Sections 3.3 and 3.4, it is seen that scintillation can obviously increase the PLL tracking errors. However, most of the signal fadings last less than 2 seconds even under strong scintillation. Thus, it might not be accurate enough to characterise the scintillation levels using 1-minute indices, like $S4$, $Phi60$.

To further investigate the signal fluctuation under scintillation, the variation of $C/N0$ within 60 seconds, i.e. the interval for scintillation index calculation, is analysed using the simulated scintillation data in each case in Table 3.1, presented in Section 3.2.1. $C/N0$ is a crucial indicator of the signal strength and quality. According to Eq. (2.4), (2.12) and (2.13), the decrease in $C/N0$ can correspondingly increase the thermal noise in both the PLL and DLL. In the presence of scintillation, particularly amplitude scintillation, $C/N0$ can be attenuated to different extents due to the signal intensity fadings (Seo et al. 2009), thus affecting the tracking loop performance.

By exploiting the 1-second $C/N0$ values logged by the PolaRxS Pro ISMR, Figure 3.24 presents an example of the $C/N0$ variation in the 51st minute of the simulated data, when strong scintillation occurs with $S4$ = 0.63. As the figure shows, the $C/N0$ values for the PLL in each case are quite similar, indicating that the PLL bandwidth and integration time tuning produces little effects on the $C/N0$ calculation under the scintillation level observed in this minute. Additionally, the $C/N0$ values fluctuate dramatically. The highest $C/N0$ is more than 50 dB-Hz, which is much higher than the average value around 46 dB-Hz. Meanwhile, the $C/N0$ can be as low as almost 35 dB-Hz, which is far lower than the average value and may cause serious receiver tracking problems.

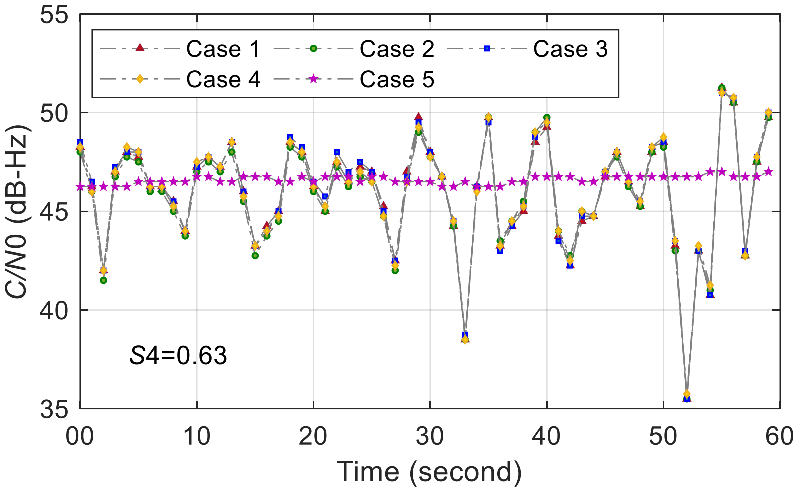

Figure 3.24 Variations of 1-second $C/N0$ values in the 51st minute in each case of Table 3.1 when amplitude scintillation occurs with $S4$ = 0.63

Thus, it can be seen that the signal intensity may change significantly within 1 minute under scintillation, indicating that using a 1-minute scintillation index to represent the signal strength and quality under scintillation is not accurate enough. To address this limitation, an approach to estimate 1-second scintillation index is proposed which uses the 50 Hz amplitude and phase measurements recorded by ISMRs. The reasons of selecting 1 second as the period for the proposed scintillation indices are: (1) Based on the analysis in this study, most of the signal intensity fadings only last less than 2 seconds; (2) Nowadays most of GNSS receivers can log pseudorange, carrier phase measurements and signal intensity measurements, such as $C/N0$, at a rate of 1 second. By matching the sampling rate of scintillation indices with those measurements, it benefits the implementation of those indices to the scintillation mitigation approaches on reducing positioning errors, which are introduced in Chapters 5 and 6. The proposed 1-second index is proved to better describe the signal distortion under scintillation and successfully applied in the scintillation mitigation. The details of the 1-second scintillation index estimation are given in Chapter 5.

3.6 Summary

This chapter introduced the scintillation data detrending and scintillation index estimation using the high frequency amplitude and phase measurements logged by the ISMRs. The effects of PLL bandwidth and integration time tuning on the scintillation index calculation are investigated. It is found that changing the PLL bandwidth or the integration time has less effects on the calculation of $S4$ and $Phi60$, while it can affect the estimation of spectral indices p and T to different extents. The signal intensity fadings due to scintillation and its relationship with the scintillation index $S4$ are characterized. The effect of intensity fadings on the PLL tracking errors is studied. The results showed that the tracking errors clearly increase with the increase in the fading speed, which is introduced in this study and defined as the ratio between fading depth and duration. Based on the analysis in this chapter, it was pointed out that the 1-minute scintillation indices are not accurate enough to describe the signal variation under scintillation, as most of the intensity fadings only last lest than 2 seconds. Thus, it is necessary to develop scintillation indices calculated at a higher rate, which is described in detail in Chapter 5. In the next chapter, the scintillation effects on receiver PLL and DLL tracking loops are modelled and evaluated by exploiting the calculated scintillation indices and scintillation sensitive receiver tracking error models. The distribution of the tracking errors in the PLL and the DLL under scintillation is also modelled by using a custom-defined PDF proposed in this study.

4 Modelling scintillation effects on receiver tracking loops

GNSS receiver tracking loop performance can be significantly decreased in the presence of signal intensity fading and phase dynamics caused by scintillation. This chapter evaluates the adverse effects of scintillation on receiver tracking loops by estimating the phase jitter in the PLL output and the code jitter in the DLL output. The models developed in Conker et al. (2003) for phase and code jitter estimation, which focused on GPS L1 C/A and L2 P signals under scintillation, are introduced first. Following a similar process, the models for modern Galileo E1 and E5a signals are developed in this study. By processing simulated GPS scintillation data logged by an ISMR with differently configured PLL bandwidths and coherent integration times, the PLL tuning effects on the estimation of total phase jitter are then fully studied, which contributes to better understanding the scintillation effects on the PLL. To address the limitations of the models described in Conker et al. (2003), alternative approaches are proposed in this study which successfully estimate the phase and code jitter by exploiting the PLL and DLL discriminator outputs, respectively. Finally, the scintillation effects on the distribution of the PLL phase tracking error are studied. A custom-defined PDF is proposed in this work aiming to model the tracking error distribution in the presence of scintillation.

4.1 Scintillation sensitive jitter estimation models

To evaluate the scintillation effects on the receiver tracking loops, different models were developed in Knight and Finn (1998) and Conker et al. (2003) to estimate the phase and code jitter in the output of the PLL and DLL, respectively. These models were developed for GPS

L1 C/A and L2 P signals and use the scintillation indices as input. Following the derivation process in Conker et al. (2003), similar models are proposed in this section which are applicable to Galileo E1 and E5a signals. The PLL phase jitter is then calculated based on real Galileo scintillation data recorded at low latitudes. It should be noted that in Conker et al. (2003), the "PLL tracking error" and "DLL tracking error" are used to, respectively, represent the errors at the output of the PLL and DLL. In this thesis, the phase and code errors are distinguished from the phase and code tracking errors, as discussed in Section 2.2. The terminology of "phase jitter" and "code jitter" is used respectively to indicate the noise levels at the PLL and DLL outputs in this chapter as well as throughout this thesis.

4.1.1 Phase and code jitter estimation for GPS signals

According to Knight and Finn (1998) and Conker et al. (2003), the total PLL phase jitter for the GPS L1 C/A signal under scintillation is given by

$$\sigma_{\Delta\varphi} = \sqrt{\sigma_T^2 + \sigma_{pha}^2 + \theta_A^2} \qquad (4.1)$$

where σ_T is the thermal noise induced phase jitter taking the amplitude scintillation into consideration. σ_{pha} is the phase scintillation induced phase jitter. θ_A is the Allan-variation induced phase jitter which is estimated by Eq. (2.6). It should be noted that the phase errors due to dynamics are excluded in Eq. (4.1). Under amplitude scintillation, due to the decrease in $C/N0$ caused by intensity fading, the thermal noise σ_T is enhanced, as given by (Conker et al. 2003)

$$\sigma_T = \sqrt{\int_0^\infty \sigma_t^2(A)p(A)\mathrm{d}A} \approx \sqrt{\frac{B_n\left[1+\frac{1}{2\eta c/n_0\left(1-2(S4)^2\right)}\right]}{c/n_0\left(1-(S4)^2\right)}}, S4 < \frac{\sqrt{2}}{2} \qquad (4.2)$$

where A denotes the signal amplitude, which is assumed to follow a Nakagami-m distribution $p(A)$ under scintillation (Fremouw et al. 1978; Fremouw et al. 1980). σ_t is the thermal noise phase jitter in the absence of scintillation, given by Eq. (2.4). When $S4$ equals to 0, the right side of Eq. (4.2) becomes Eq. (2.4). B_n and η are the PLL bandwidth and coherent integration time, respectively. Figure 4.1 shows the variation of the thermal noise phase jitter σ_T as a function of $C/N0$ under different levels of amplitude scintillation. As it can be seen, σ_T decreases gradually with the increase in $C/N0$ for all scintillation levels. The σ_T estimated when $S4$ is 0.3 and 0.5 is slightly higher than when there is no scintillation, i.e., $S4$ = 0, while the curve with $S4 = 0.7$ presents relatively larger values, especially when $C/N0$ is lower than 40 dB-Hz. It should be noted that Eq. (4.2) is only valid when $S4$ is lower than $\frac{\sqrt{2}}{2}$. In the results shown in Figure 4.1, a PLL with the bandwidth B_n set to 15 Hz and the integration time η set to 10 ms is used for the calculation.

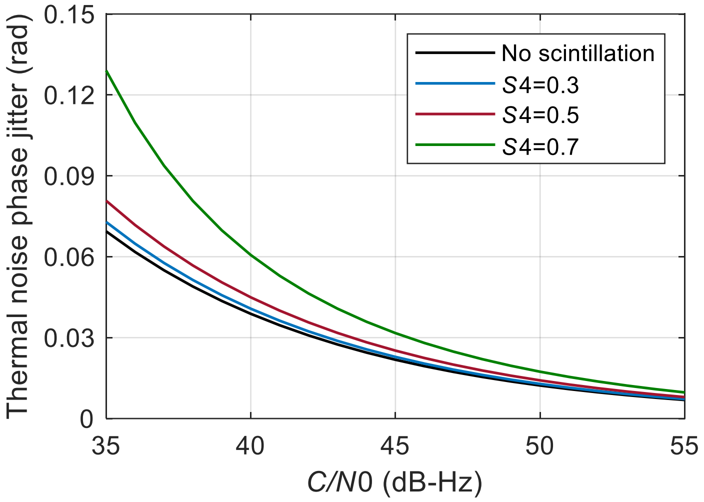

Figure 4.1 Variation of thermal noise phase jitter σ_T in relation to $C/N0$ under different levels of amplitude scintillation

The phase scintillation induced phase jitter σ_{pha} is calculated through (Knight & Finn 1998; Conker et al. 2003)

$$\sigma_{pha} = \sqrt{\int_{-\infty}^{\infty} |1 - H(f)|^2 S_{\varphi}(f) \mathrm{d}f} \approx \sqrt{\frac{\pi T}{k f_n^{p-1} \sin\left(\frac{[2k+1-p]\pi}{2k}\right)}}, 1 < p < 2k \quad (4.3)$$

where $S_\varphi(f)$ is the PSD of the detrended phase measurement under phase scintillation, given by Eq. (3.7). k is the loop order. f_n is the loop natural frequency, given by $f_n = \frac{1.2}{2\pi} B_n$. T and p are phase scintillation indices which are introduced in Section 3.1.2.

By exploiting the relationship between $Phi60$, T and p described in Eq. (3.9), i.e., $\sigma_\varphi^2 = 2T\left[\frac{25^r - 0.1^r}{r}\right]$, T index in Eq. (4.3) is substituted by $Phi60$ and p. The variation of phase scintillation induced phase jitter σ_{pha} in relation to p and $Phi60$ is then calculated and presented in Figure 4.2. It can be seen that under different levels of phase scintillation, σ_{pha} clearly decreases with an increase of p from 1 to around 2.5. When p keeps increasing, σ_{pha} is seen to vary slightly, indicating that the phase scintillation induced phase jitter σ_{pha} is not sensitive to the variation of p when the latter is higher than 2.5. Additionally, an increase in $Phi60$ can affect the σ_{pha} to different extents. For larger p values, e.g., $p > 2.5$, increasing $Phi60$ only has minor effects on σ_{pha}.

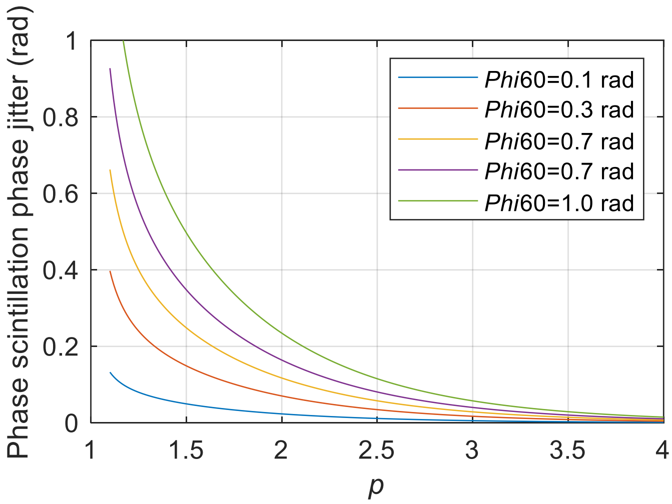

Figure 4.2 Variation of phase scintillation induced phase jitter σ_{pha} in relation to phase scintillation indices p and $Phi60$

On the other hand, the code jitter for the GPS L1 C/A signal in the output of DLL is calculated as (Conker et al. 2003)

$$\sigma_\tau = \sqrt{\frac{B_L d\left[1+\frac{1}{\eta_{DLL} c/n_0 (1-2*S4^2)}\right]}{2c/n_0(1-S4^2)}} \text{(chip)}, S4 < \frac{\sqrt{2}}{2} \tag{4.4}$$

where B_L is the DLL one-side bandwidth. d is the correlator spacing in C/A chips. η_{DLL} is the DLL integration time. Figure 4.3 shows the variation of DLL code jitter σ_τ as a function of $C/N0$ and $S4$. As it can be seen, σ_τ decreases gradually with the increase in $C/N0$. Under weak scintillation with $S4 = 0.3$ and moderate scintillation with $S4 = 0.5$, the estimated code jitter is very close to that when there is no scintillation denoted by the black curve, while under stronger scintillation with $S4 = 0.7$, the code jitter is obviously larger especially under low $C/N0$ values. In the code jitter estimation shown in Figure 4.3, a DLL bandwidth of 0.25 Hz and correlator spacing of 0.05 chip is used.

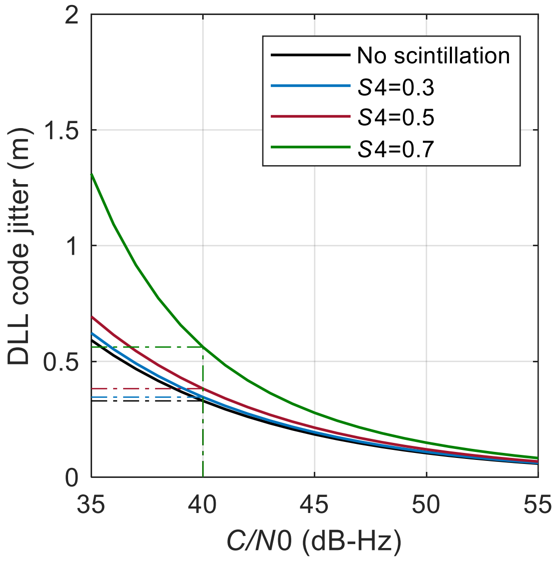

Figure 4.3 Variation of DLL code jitter σ_τ in relation to $C/N0$ and amplitude scintillation index $S4$

Considering the case that the phase measurements on GPS L1 C/A and L2 P signals are uncorrelated, the PLL phase jitter and DLL code jitter for the L2 P signal are respectively given by (Conker et al. 2003)

$$\sigma_{\Delta\varphi} = \sqrt{\frac{B_n\left[1+\frac{1}{2\eta_Y (c/n_0)_{L1P}(1-S4(L1)^2)}\right]}{(c/n_0)_{L2P}(1-S4(L2)^2)} + \frac{\pi T}{k f_n^{p-1}\sin\left(\frac{[2k+1-p]\pi}{2k}\right)}\left(\alpha^2 + {}^{1}/_{\alpha^2}\right) + \theta_A^2}, S4(L1) < 0.687 \tag{4.5}$$

$$\sigma_{\tau} = \sqrt{\frac{B_L\left[1+\frac{1}{2\eta_Y (c/n_0)_{L1P}(1-S4(L1)^2)}\right]}{2(c/n_0)_{L2P}(1-S4(L2)^2)}}\ \text{(chip)} \tag{4.6}$$

where the parameters B_n, k, f_n, B_L are the same as in Eq. (4.2), (4.3) and (4.4) but for the GPS L2 P signal tracking loops. η_Y is the integration time for GPS Y code. $(c/n_0)_{L1P}$ and $(c/n_0)_{L2P}$ are the fractional forms of $C/N0$ values on L1 P and L2 P signals, respectively. α is the ratio of the carrier frequencies of L2 and L1. The $C/N0$ on L2 P used in this analysis is obtained from the ISMR output files, while for L1 P signal, it is approximately calculated by $(C/N0)_{L1P} \cong (C/N0)_{L1C/A} - 3$dB (Conker et al. 2003).

Except for the $S4(L1)$ which is measured on L1 C/A signal, the $S4(L2)$, p and T in Eq. (4.5) and (4.6) are all for L2 P signal and estimated through Eq. (3.10), (3.11) and (3.12). It is worth mentioning that the values of all the PLL and DLL parameters required for the jitter estimation in this work are known from the ISMR set up during the data collection. For the PolaRxS Pro receiver, the default values of the related parameters are listed in Table 4.1.

Table 4.1 Default configurations of the PLL and DLL for GPS L1 C/A and L2 P signal tracking in the PolaRxS Pro receiver

	PLL	DLL
GPS L1 C/A	B_n = 15 Hz	B_L = 0.25 Hz
	η = 10 ms	η = 100 ms
	k = 3	d = 0.04 chips
GPS L2 P	B_n = 0.25 Hz	B_L =0.3 Hz
	η_Y = 1.96e μs	η_Y = 1.96 μs
	k = 2	

4.1.2 Phase and code jitter estimation for Galileo signals

Following the approach in Conker et al. (2003), the scintillation sensitive phase and code jitter estimation models for modern Galileo signals are provided for the first time in this study. According to Sleewaegen et al. (2004), for Galileo E1 and E5a signals, the PLL phase jitter is not changed with respect to the GPS L1 C/A signal, thus it can be estimated using the same models expressed in Eq. (4.1) to (4.3). By contrast, as a BOC(1, 1) modulation is used in the generation of Galileo E1 signal, the DLL code jitter estimation is different. Based on Eq. (2.12) and following the derivation in Conker at al. (2003), the DLL code jitter for Galileo E1 signal is given by

$$\sigma_\tau = \sqrt{\frac{B_L d * {}^1\!/_3}{2c/n_0(1-(S4)^2)}\left[1+\frac{1}{\eta c/n_0(1-2(S4)^2)}\right]}\ \text{(chip)}, S4 < \frac{\sqrt{2}}{2} \qquad (4.7)$$

where the B_L and η are the parameters of the DLL tracking loops for the E1 signal. In terms of the E5a signal, which uses a BPSK modulation, the code jitter can be estimated using the same equation as for the GPS L1 C/A signal, namely Eq. (4.4).

Figure 4.4 presents an example of the estimated phase jitter for Galileo E1 and E5a signal based on the scintillation data recorded at PRU2 station in 2019. As the middle panel shows, amplitude and phase scintillation is observed on both signals from around UTC 00:15 to 00:31

and from 00:35 to 00:40. The scintillation index on the E5a signal is generally larger than that on the E1 signal, which agrees with the relationship expressed in Eq. (3.10) and (3.11). It can be seen in the bottom panel that when there is no scintillation or only weak scintillation, from around UTC 00:01 to 00:15, the phase jitter on the E5a signal is smaller than that on the E1 signal, which agrees with the conclusion that the E5a signal provides better accuracy compared with the E1 signal. However, during the scintillation occurrence, the phase jitter on both signals increases, while on the E5a signal it overtakes that on the E1 signal, indicating that E5a signal is more susceptible to scintillation due to the lower frequency band, as mentioned in Section 3.1.3.

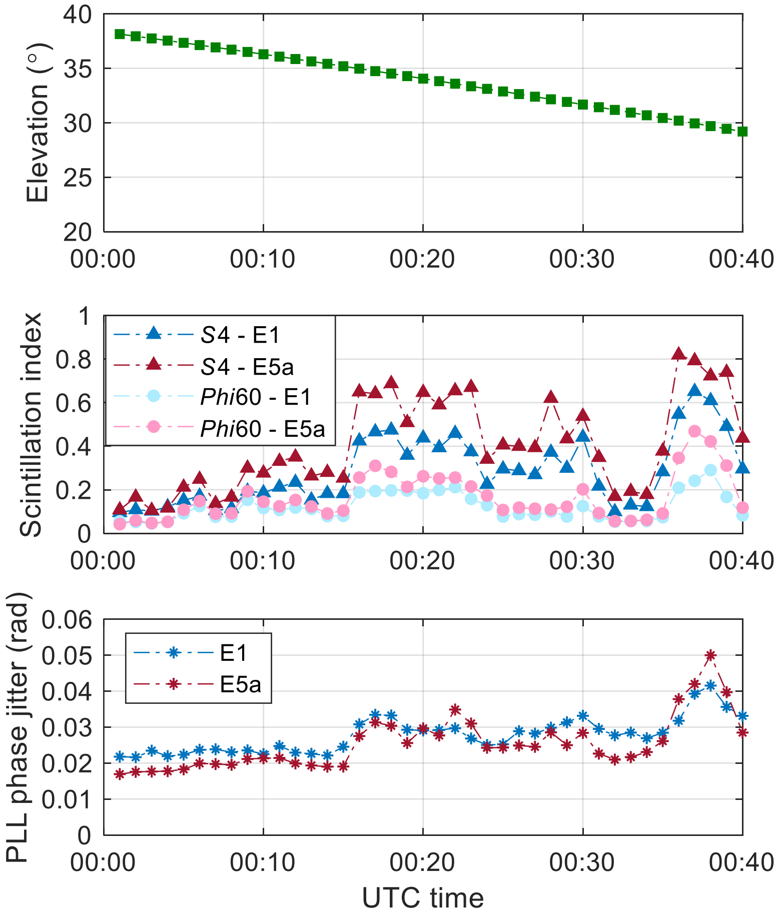

Figure 4.4 PLL phase jitter estimated on Galileo E1 and E5a signals for PRN25 based on scintillation data logged by PolaRxS Pro receiver

from UTC 00:00 to 00:40 on 8 October 2019 at PRU2 station. Panels respectively show the satellite elevation (top), amplitude and phase scintillation index measured on E1 and E5a signals (middle) and the corresponding PLL phase jitter (bottom)

4.1.3 Limitations of phase and code jitter estimation models

The scintillation sensitive phase and code jitter estimation models expressed by Eq. (4.1) to (4.6) have been used by researchers to describe the scintillation effects on receiver tracking loops (Strangeways et al. 2011; Sreeja et al. 2012; Aquino and Sreeja 2013) and to mitigate scintillation effects on GNSS positioning (Aquino et al. 2009; da Silva et al. 2010; Vani et al. 2019; Vadakke Veettil et al. 2020). However, the performance and accuracy of these models are questioned. The main limitations for these models include:

(1) The phase and code jitter estimation models given by Eq. (4.1) to (4.6) have a strong dependence on the PLL and DLL configurations. Receivers with different tracking loop bandwidth and integration time may lead to different estimation of the phase and code jitter under similar scintillation conditions.

(2) The phase and code jitter estimated by these models is based on the assumption that the phase or code errors are in the linearity region of PLL and DLL discriminators, while this assumption may not be always true in practice. For example, under severe scintillation conditions, the phase error may overtake the linear range of the PLL discriminator input-output curve (Humphreys et al. 2010). Thus, the phase error in the non-linear regimes should be considered in the phase jitter estimation (Forte 2012).

(3) Eq. (4.1) to (4.6) require scintillation indices as input which are normally only available from ISMRs. For general navigation receivers, external scintillation information is required in order to estimate the jitter using these models. Additionally, the thermal

noise estimation using Eq. (4.2) and (4.5) is only valid when $S4 < \frac{\sqrt{2}}{2}$. If $S4$ overtakes this threshold, which actually happens frequently under low latitude scintillation, Eq. (4.2) and (4.5) are not applicable even if the tracking loops are still locked to the signals. Although an improved model was proposed in Moraes et al. (2014), which can be applied without any limitation on the $S4$ values, it requires the estimation of extra parameters related to the signal amplitude fading channels which involves a complex curve-fitting process, when renders it impractical.

To address the concerns mentioned above, the receiver tuning effects on the estimation of PLL phase jitter are fully studied in the next section, aiming to investigate the difference in the phase jitter calculated on PLLs with various settings under the same scintillation conditions. In addition, leveraging on the flexibility of the SDR receivers, alternative approaches to estimate the phase and code jitter under scintillation are proposed in this study. By comparing the phase and code jitter calculated, respectively, using the proposed approach and the jitter estimation models of Eq. (4.1) to (4.6), the accuracy of these estimation models is studied. The details of the approach and the comparison are given in Section 4.3.

4.2 PLL configuration tuning effects on phase jitter estimation

This section investigates the receiver tuning effects on the jitter estimation based on the models introduced in Section 4.1. According to Eq. (4.4), (4.6) and (4.7), the DLL code jitter mainly contains the thermal noise component, which is a function of $S4$, loop bandwidth and correlator spacing. It is clear from these equations that decreasing either the bandwidth or correlator spacing can help to reduce the code jitter under scintillation. However, in terms of the PLL phase jitter, it is not clear from Eq. (4.1) to (4.3) how the PLL bandwidth and integration time tuning may affect the jitter estimation. For example, according to Eq. (4.2), increasing the PLL bandwidth will increase the thermal noise phase jitter, while also decreasing the phase scintillation induced phase jitter based on Eq. (4.3). Thus, it is more difficult to determine how the total phase jitter will change with the increase of the bandwidth. In order to investigate the PLL tuning effects on the phase jitter estimation, Eq. (4.1) to (4.3) are used and results are compared among the cases listed in Table 3.1.

4.2.1 Thermal noise and phase scintillation induced phase jitter

The thermal noise induced phase jitter σ_T is estimated using Eq. (4.2) for each case listed in Table 3.1, as shown in Figure 4.5. It can be seen that σ_T in Cases 1 to 3 is generally at different levels, but following a very similar pattern. Obvious increases in σ_T are observed during the occurrence of scintillation as shown in Figure 3.9. When the PLL bandwidth B_n is set to 5 Hz in Case 1, σ_T presents the smallest value all the time. By contrast, the largest values of σ_T are seen when $B_n = 15$ Hz in Cases 3 and 4. This is due to the fact that the thermal noise component is proportional to loop bandwidth, as expressed in Eq. (4.2). Furthermore, it is seen that the estimated σ_T in Cases 3 and 4 are very close, indicating that increasing the integration time has a minor effect on the thermal noise estimation under scintillation.

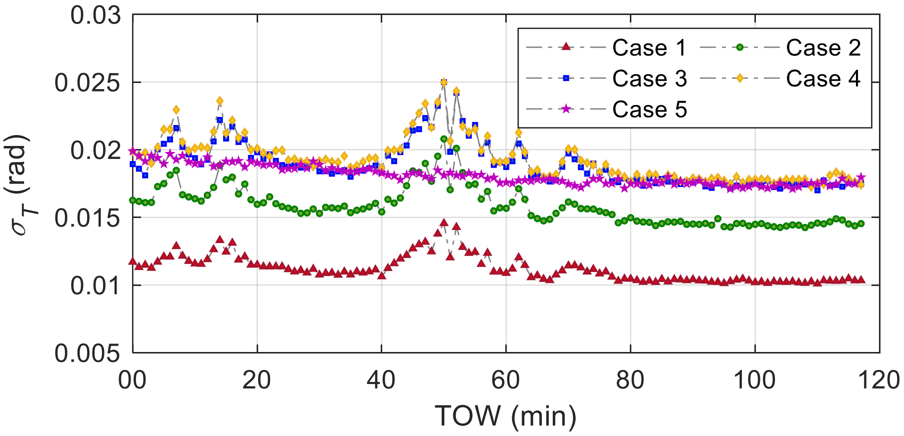

Figure 4.5 Variation of thermal noise induced phase jitter σ_T in relation to time estimated based on the simulated scintillation data processed by the PLL configurated with different bandwidths and integration times as listed in Cases 1 to 5 in Table 3.1

The phase scintillation induced phase jitter σ_{pha} calculated using Eq. (4.3) is shown in Figure 4.6. It is seen that in all Cases that σ_{pha} generally is at low levels with values less than 0.03 rad, except for the 14th minute when σ_{pha} suddenly jumps over 0.06 rad in Cases 1 to 4. In this minute, the measured phase scintillation indices $Phi60$ and T reach the largest value simultaneously, as shown in Figure 3.9 and Figure 3.10. Additionally, when increasing the PLL bandwidth from 5 Hz in Case 1 to 10 Hz in Case 2 and 15 Hz in Case 3, the value of σ_{pha} decreases gradually, indicating that the PLL with narrower bandwidth is more susceptible to phase scintillation, which is in agreement with the conclusion by Knight and Finn (1998). Moreover, when the loop integration time is increased from 10 ms in Case 3 to 20 ms in Case 4, only a slight decrease in σ_{pha} is seen.

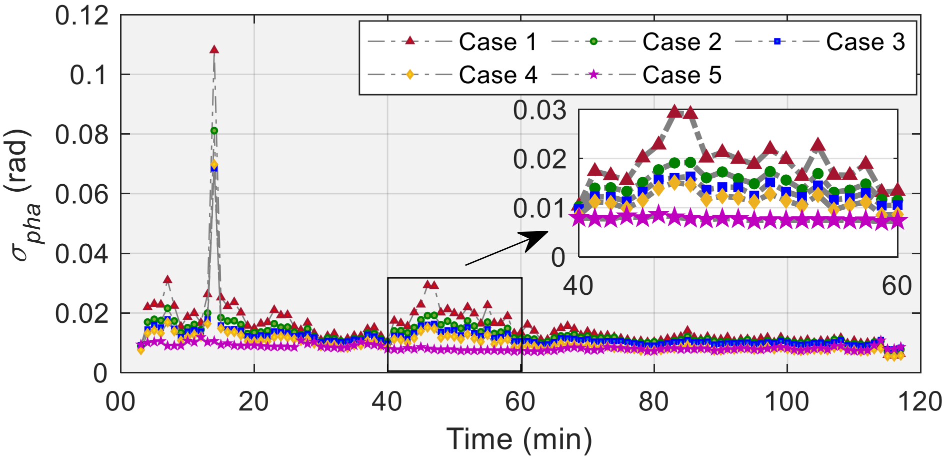

Figure 4.6 Variation of phase scintillation induced phase jitter σ_{pha} in relation to time estimated based on the simulated scintillation data processed by the PLL configurated using different bandwidths and integration times as listed in Cases 1 to 5 in Table 3.1

Consequently, a PLL with a narrow bandwidth could be less affected by thermal noise under scintillation. But it has an opposite effect on the phase scintillation induced phase jitter and oscillator noise, as both will increase with the decrease in the loop bandwidth. Therefore, there is a trade-off when selecting the PLL bandwidth in order to maximize the tracking performance under scintillation. Due to the time limitation in this thesis, the strategy to select the optimal PLL bandwidths under scintillation is not studied and is suggested as future work in Section 7.2.

4.2.2 Total phase jitter estimation

The total PLL phase jitter, including the thermal noise σ_T, the phase scintillation induced phase jitter σ_{pha} and the Allan-Deviation induced oscillator jitter θ_A, are calculated for each case in Table 3.1, as Figure 4.7 shows. During the scintillation occurrence, the total phase jitter estimation for Case 1 with a PLL bandwidth of 5 Hz has relatively larger values, even if it has the smallest thermal noise as shown in Figure 4.5. This again indicates that a suitable bandwidth in the PLL should be selected, aiming to decrease the phase jitter and improve the tracking performance under scintillation. On the other hand, it is seen that although the phase jitter estimation models given by Eq. (4.1) to (4.3) have a dependence on the loop bandwidth and integration time, the total phase jitter estimated in the PLL with different configurations in Cases 1 to 4 are generally quite close.

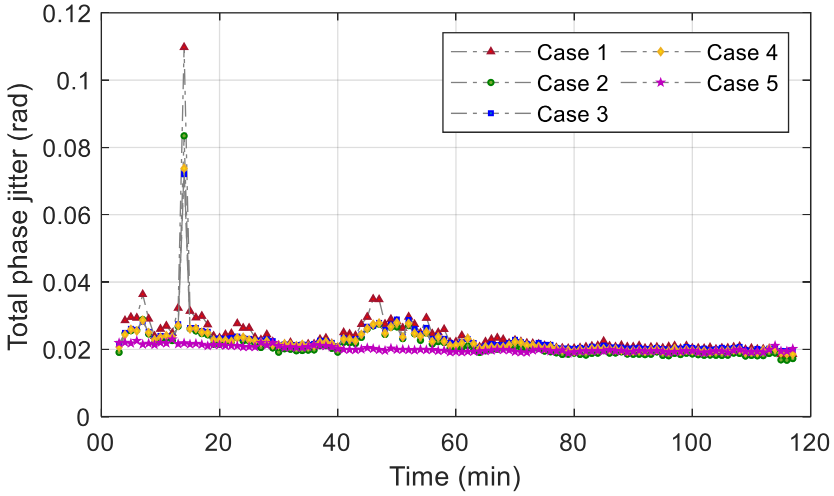

Figure 4.7 Variation of total phase jitter in relation to time estimated based on the simulated scintillation data processed by the PLL configured with different bandwidths and integration times as listed in Cases 1 to 5 in Table 3.1

4.3 Measuring phase and code jitter using an SDR GNSS receiver

As mentioned in Section 4.1.3, the performance and accuracy of the scintillation sensitive phase and code jitter estimation models given by Eq. (4.1) to (4.6) have been questioned. To address this concern, this section proposes approaches which measure the phase and code jitter by exploiting the PLL and DLL discriminator outputs, i.e., the tracking errors. An SDR GNSS receiver is used to process the IF scintillation data collected at both low and high latitudes. The newly proposed approaches are introduced first, followed by the description of the scintillation data sets used for the analysis. Based on the newly proposed approach, the PLL phase jitter and DLL code jitter are then calculated and compared with the estimates obtained by using Eq. (4.1) to (4.6).

4.3.1 Measuring phase and code jitter by exploiting tracking errors

Alternative approaches are developed in this section to calculate the phase and code jitter in the output of the PLL and the DLL. According to Razavi et al. (2008), the PLL phase jitter cannot be measured directly in practice, while the tracking error is measurable in a wide range of GNSS receivers. Thus, the purpose of this analysis is to develop an approach to estimate the phase jitter by exploiting the discriminator output. For a static receiver and considering only the scintillation and oscillator instability induced phase jitter, the total phase jitter in Eq. (4.1) can be redefined as

$$\sigma_{\Delta\varphi} = \sqrt{\sigma_t^2 + \sigma_{\varphi_c}^2} \tag{4.8}$$

where σ_t is the thermal noise component given by Eq. (2.4). σ_{φ_c} is the coloured noise component in phase jitter, which includes amplitude and phase scintillation induced phase jitter and the Allan-Variance induced phase jitter, i.e.,

$$\sigma_{\varphi_c} = \sqrt{\sigma_{amp}^2 + \sigma_{pha}^2 + \theta_A^2} \tag{4.9}$$

where σ_{amp} is the amplitude scintillation induced phase jitter. If the σ_{φ_c} is known, the total phase jitter can be calculated with Eq. (4.8) and (2.4).

According to Eq. (2.7) and (2.8), the coloured noise component in the phase jitter can be also estimated as

$$\sigma_{\varphi_c} = \sqrt{\sigma_{\delta_\varphi}^2 - \sigma_w^2} \tag{4.10}$$

where σ_{δ_φ} and σ_w is the total noise and white noise component in the PLL discriminator output, estimated by Eq. (2.11) and (2.8), respectively. Therefore, with Eq. (2.4), (4.8) and (4.10), the total phase jitter is estimated as

$$\sigma_{\Delta\varphi} = \sqrt{\sigma_{\delta_\varphi}^2 + \frac{1}{c/n_0}\left(B_n - \frac{1}{2\eta}\right)\left(1 + \frac{1}{2\eta c/n_0}\right)} \tag{4.11}$$

Compared with the phase jitter estimation models in Eq. (4.1) to (4.3), no scintillation index is involved in the proposed approach expressed by Eq. (4.11). Additionally, as the tracking error δ_φ is widely measured in GNSS receivers and at a much higher frequency, Eq. (4.11) can be adopted to a wide range of GNSS receivers to estimate the phase jitter in shorter intervals, like 1, 10, or 15 second.

On the other hand, according to the DLL code jitter estimation models in Conker et al. (2003), given by Eq. (4.4) and (4.6), the thermal noise component dominates the code jitter, which is enhanced due to the signal intensity fading caused by amplitude scintillation. Assuming that in the presence of scintillation the code jitter and the code discriminator noise still satisfy the relationship expressed by Eq. (2.14), the code jitter is then alternatively calculated by using the DLL discriminator noise, namely,

$$\sigma_\tau = \sqrt{2B_L\eta}\sigma_{ND\_scint} \tag{4.12}$$

where σ_{ND_scint} is the standard deviation of the code discriminator noise under scintillation, given by

$$\sigma_{ND\_scint} = \mathrm{std}(d_\tau) \tag{4.13}$$

where d_τ is the DLL discriminator output, calculated based on the discriminator type and the early, prompt and late in-phase and quadra-phase measurements, as shown in Figure 2.3.

In this analysis, raw IF scintillation data collected at low and high latitudes are processed by the SDR receiver described in Section 2.4.2, which logged the raw PLL and DLL discriminator outputs. The total phase jitter and code jitter are then estimated respectively using the equations developed in this section. The results and discussions are given in Sections 4.3.3 and 4.3.4.

4.3.2 Raw IF scintillation data sets

The IF scintillation data on GPS L1 C/A signal analysed in this study were collected at Brazilian Centre for Radio Astronomy and Astrophysics at Mackenzie, denoted as CRAAM, and the South African Antarctic research base, denoted as SANAE IV, following the data collection setup shown in Figure 2.9. These stations were built under the framework of the DemoGRAPE project (Alfonsi et al. 2016; Linty et al. 2018). Table 4.2 lists the locations and data collection dates for both stations. The satellite at each station was selected according to the measured scintillation occurrence, which is considered as representative of scintillation events in the equatorial region and in the auroral to polar region, respectively. These scintillation data were then processed by the SDR receiver introduced in Section 2.4.2 as a case study for testing the proposed phase and code jitter estimation approaches in Section 4.3.1 and analysing the tracking error distributions which is given in Section 4.4.

Table 4.2 Stations and dates for the scintillation data collection

Station	Location	Latitude, longitude	Date and time (UTC)	PRN
CRAAM	São Paulo, Brazil	23.55°S, 46.63°W	02:06-02:35 13 September 2017	10
SANAE IV	Vesleskarvet, Queen Maud Land	71.67°S, 2.84°W	19:46-20:07 8 May 2016	31

The scintillation indices measured for PRN10 at CRAAM station are shown in Figure 4.8. Due to the convergence period at the beginning of the phase measurement detrending process, the $Phi60$ index in the first 3 minutes is not shown. As it can be seen amplitude and phase scintillation events are frequently observed between the 5th to 10th minute and the 24th to 29th minute from the start of the data collection. The largest $S4$ is recorded in the 28th minute, reaching a value of 0.81, indicating a strong amplitude scintillation event.

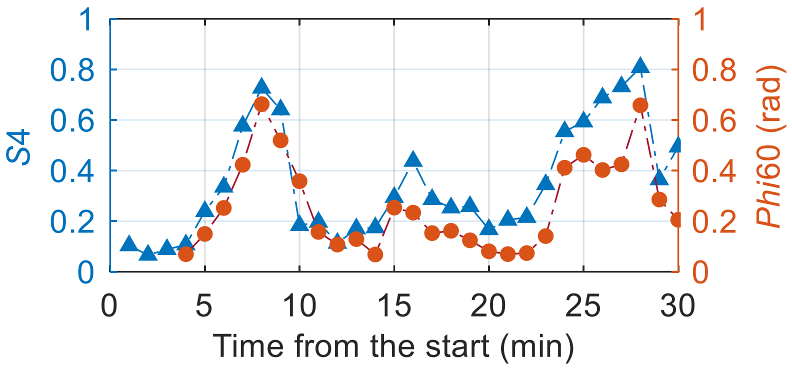

Figure 4.8 Amplitude and phase scintillation indices measured on the GPS L1 C/A signal for PRN10 at CRAAM station from UTC 02:06 to 02:35 on 13 September 2017

The scintillation indices measured for PRN31 at SANAE IV station are shown in Figure 4.9. Compared with amplitude scintillation, which stays at a lower level with $S4$ less than 0.1 throughout the period, phase scintillation is generally stronger and more frequently observed. The strongest phase scintillation is captured in the 10th minute from the start of data collection, with $Phi60$ reaching 2.35 rad.

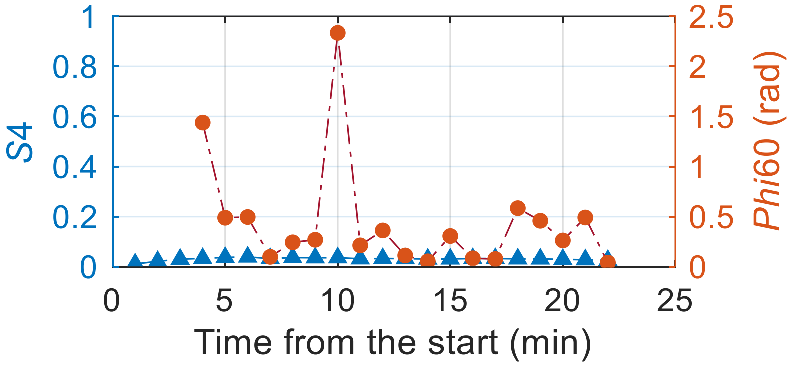

Figure 4.9 Amplitude and phase scintillation indices measured on the GPS L1 C/A signal for PRN31 at SANAE IV station from UTC 19:46 to 20:07 on 8 May 2016

It is worth mentioning that strong amplitude and phase scintillation are both frequently observed and present a higher correlation at CRAAM station, while the phase scintillation is dominated at SANAE IV station. This is due to the different mechanisms that govern the generation of scintillation at low and high latitudes, as described in Chapter 1.

4.3.3 Measuring phase jitter using the PLL discriminator output

Based on the scintillation data observed at CRAAM and SANAE IV stations, the total PLL phase jitter is estimated using Eq. (4.1) to (4.3), denoted as $\sigma_{\Delta\varphi\_Conker}$, and the newly proposed approach expressed by Eq. (4.11), denoted as $\sigma_{\Delta\varphi\_Measured}$, respectively. Figure 4.10 shows the estimated PLL phase jitter under the scintillation observed at CRAAM station. It can be seen that when scintillation occurs from the 5th to 10th and 25th to 29th minute, both $\sigma_{\Delta\varphi\_Measured}$ and $\sigma_{\Delta\varphi\_Conker}$ clearly increase in all the panels. Generally, a better match is observed between $\sigma_{\Delta\varphi\_Measured}$ and $\sigma_{\Delta\varphi\_Conker}$ in the bottom panels, where the PLL bandwidth B_n is set to 15 Hz, while in the top panels where $B_n = 5$ Hz, the $\sigma_{\Delta\varphi\_Measured}$ are obviously larger than $\sigma_{\Delta\varphi\_Conker}$ during the scintillation occurrence, indicating that the phase jitter is underestimated by using Eq. (4.1) to (4.3) in this case. It should be noted that in the 8th, 27th and 28th minute, as the measured $S4$ values are larger than $\frac{\sqrt{2}}{2}$ (≈ 0.71), Eq. (4.2) is not valid to estimate the thermal noise in the phase jitter and may contribute to the gaps in $\sigma_{\Delta\varphi\_Conker}$. To address this issue, the $S4$ is manually set as 0.70 in these minutes, thus removing the gaps.

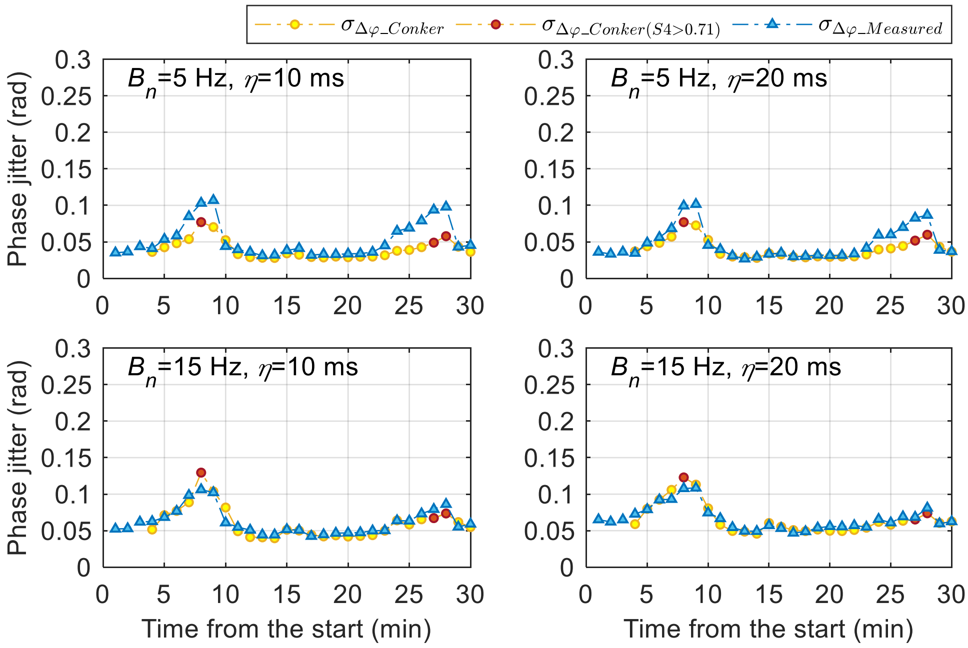

Figure 4.10 PLL phase jitter for PRN10 at CRAAM station estimated using Eq. (4.1) to (4.3) and the proposed approach expressed by Eq. (4.11), respectively. The PLL of different bandwidth B_n and integration time η is used to process the data in each panel

Figure 4.11 presents the PLL phase jitter estimated based on the scintillation captured at SANAE IV station. It is seen that $\sigma_{\Delta\varphi\_Measured}$ and $\sigma_{\Delta\varphi\_Conker}$ share a very similar trend in all the panels. However, $\sigma_{\Delta\varphi\_Conker}$ is obviously smaller than $\sigma_{\Delta\varphi\_Measured}$ in the 10th minute in the top panels. This may be due to the fact that when $B_n = 5$ Hz, phase fluctuations caused by refractive and diffractive effects would both contribute to phase jitter (Demyanov et al. 2019b), while $\sigma_{\Delta\varphi\_Conker}$ only considers the diffractive effects, thus it is less than $\sigma_{\Delta\varphi\_Measured}$ which is estimated based on the raw discriminator output and considers both effects. However, when B_n is increased to 15 Hz in the bottom panels, the phase fluctuations caused by refractive effects can be mostly reduced. Thus, a better match between $\sigma_{\Delta\varphi\_Measured}$ and $\sigma_{\Delta\varphi\_Conker}$ is achieved.

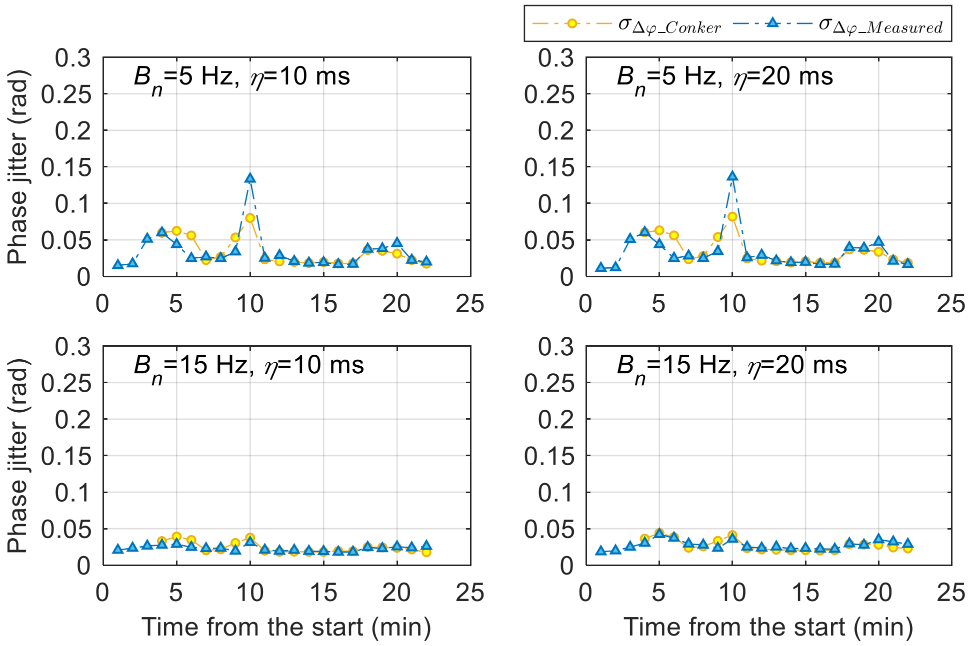

Figure 4.11 PLL phase jitter for PRN31 at SANAE IV station estimated using Eq. (4.1) to (4.3) and the proposed approach expressed by Eq. (4.11). The PLL of different bandwidths B_n and integration times η is used to process the data in each panel

Additionally, as it can be seen in the top panels of Figure 4.11, where the PLL bandwidth B_n is 5 Hz, both $\sigma_{\Delta\varphi\_Measured}$ and $\sigma_{\Delta\varphi\_Conker}$ increase significantly with the increase in $Phi60$ shown in Figure 4.9. Concurrently, only slight increases are observed in the bottom panels where $B_n = 15$ Hz. Even under extremely strong phase scintillation in the 10th minute, the estimated phase jitter remains lower than 0.05 rad. Therefore, increasing the bandwidth can greatly help to reduce the total PLL phase jitter under phase scintillation in this analysis. This is different from the results shown in Figure 4.10 where a wider bandwidth produces minor effects in the total phase jitter. It is worth mentioning that according to Eq. (4.2), a wider bandwidth also increases the thermal noise in the total phase jitter. Thus, an optimal or variable bandwidth can be defined to balance the thermal noise and scintillation induced phase jitter in the PLL design.

4.3.4 Measuring code jitter using the DLL discriminator output

The DLL code jitter for the scintillation data recorded at CRAAM and SANAE IV stations described in Section 4.3.2 is estimated using Eq. (4.4), denoted as σ_{τ_Conker}, and Eq. (4.12), denoted as $\sigma_{\tau\_Measured}$, respectively. Figure 4.12 shows the calculated code jitter for PRN10 at CRAAM station. It can be seen that during the scintillation occurrence period, from the 5th to 10th minute, the code jitter visibly increases, while only very slight increases are observed from the 24th to 29th minute, although there is still scintillation. On the other hand, the code jitter σ_{τ_Conker} and $\sigma_{\tau\_Measured}$ estimated by different approaches are generally highly correlated. However, obvious biases are observed in the bottom panels when the DLL bandwidth B_L is set to 0.5 Hz. Note that in the 8th, 27th and 28th minute when the $S4$ values are over $\frac{\sqrt{2}}{2}$, the $S4$ is manually set to 0.68 in σ_{τ_Conker} estimation using Eq. (4.4).

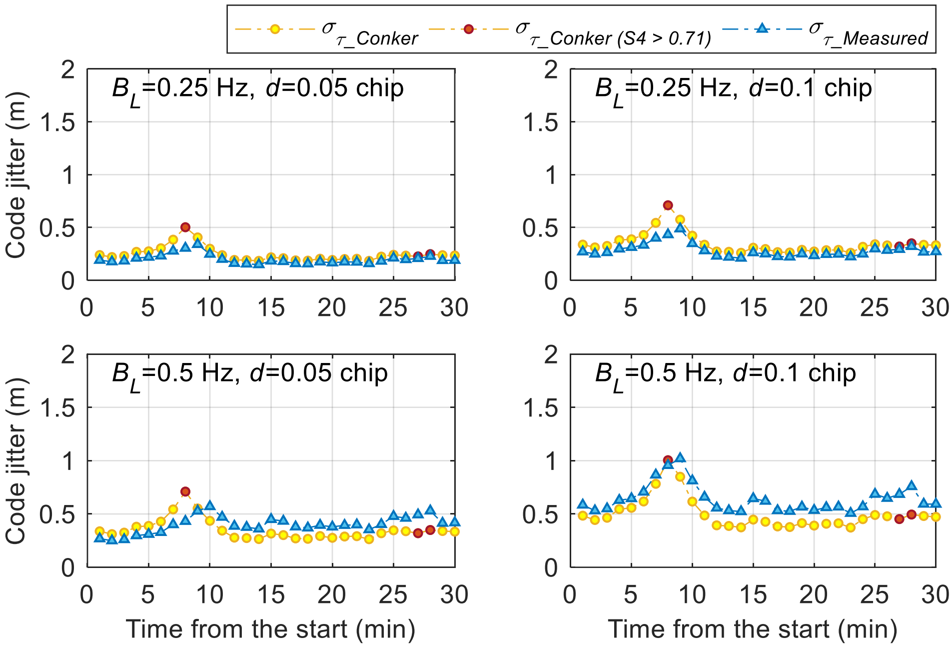

Figure 4.12 DLL code jitter for PRN10 at CRAAM station estimated using Eq. (4.4) and the proposed approach expressed by Eq. (4.12). The DLL of different bandwidth B_L and correlator spacing d is used in each panel

Figure 4.13 shows the code jitter estimated for PRN31 at SANAE IV station. As the figure shows, the values of both σ_{τ_Conker} and $\sigma_{\tau\_Measured}$ are at low levels and match very well in all panels with different DLL configurations. It is worth mentioning that compared with the code jitter estimated at CRAAM station shown in Figure 4.12, it is much smaller at SANAE IV station shown in Figure 4.13. This is due to the different $C/N0$ levels measured on the different signals at these two stations. At CRAAM station, the $C/N0$ for PRN10 is in the range of 36.78 to 43.31 dB-Hz, while it is from 49.48 to 51.54 dB-Hz for PRN31 at SANAE IV station.

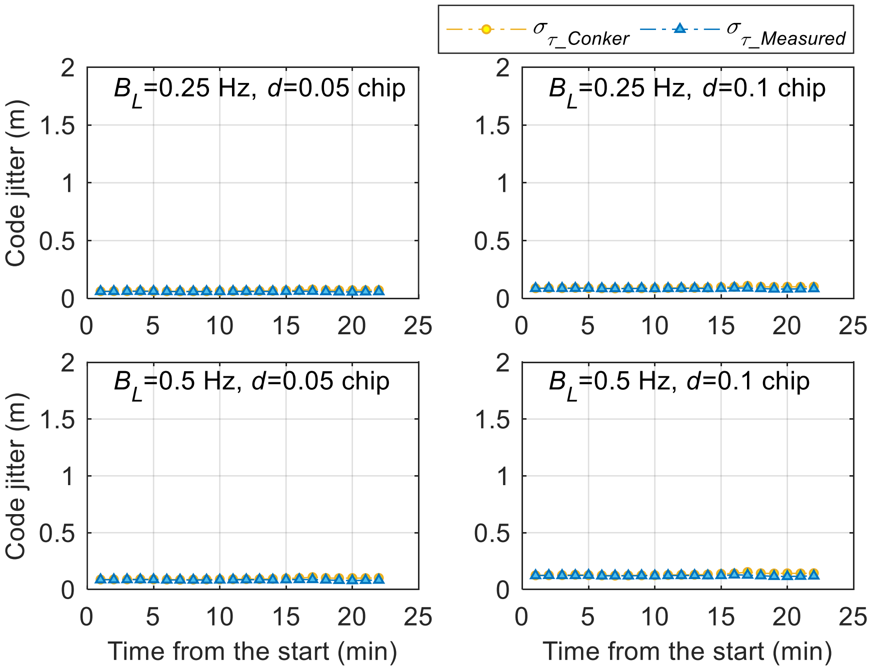

Figure 4.13 DLL code jitter for PRN31 at SANAE IV station estimated using Eq. (4.4) and the proposed approach expressed by Eq. (4.12). A DLL of different bandwidth B_L and correlator spacing d is used in each panel

Based on the analyses in this and the previous sections, it is seen that phase and code jitter estimated by Eq. (4.1) to (4.6) described in Conker et al. (2003) generally achieves a good match with those estimated using the newly proposed approach given by Eq. (4.11) and (4.12), respectively. Although the thermal noise phase jitter estimation by Eq. (4.2) and the code jitter estimation by Eq. (4.4) are only valid when $S4$ is lower than $\frac{\sqrt{2}}{2}$, which results in gaps in the estimation results, by manually assigning a fix value of 0.70 to $S4$ the gaps can be removed and their replacements agree with the estimation by the newly proposed approach. On the other hand, the proposed approaches have their own specific advantages. The estimation is based on the raw output of the tracking loop discriminators, thus it best reflects the practical tracking performance under scintillation. Additionally, as the proposed approaches can be used without involving the calculation of scintillation indices, they are applicable to a wide range of generic navigation receivers.

In the frame of this thesis, the estimation models given by Eq. (4.1) to (4.6) are used to estimate the PLL phase jitter and DLL code jitter, which are further used to modify the stochastic models in PPP following the scintillation mitigation approach described in Aquino et al. (2009). The mitigation approach and results are described in detail in Chapters 5 and 6.

4.4 Modelling scintillation effects on PLL tracking errors

This section focuses on the modelling of scintillation effects on the receiver tracking errors in the loop discriminator output. Due to the fact that the DLL tracking errors are dominated by the thermal noise, this section only analyses the PLL tracking error, which is more complicated and includes more error sources under scintillation. Based on the scintillation data described in Section 4.3.2, the PLL tracking errors are calculated and the scintillation effects are first demonstrated. The distributions of the tracking errors under different levels of scintillation are then modelled using a custom-defined PDF proposed in this study.

4.4.1 PLL tracking errors at CRAAM station

Based on the high frequency I_P and Q_P measurements output by the PLL in the SDR receiver, the tracking error and its standard deviation, i.e., tracking jitter, at the discriminator output are estimated using Eq. (2.10) and (2.11). To demonstrate the scintillation effects on the tracking errors, Figure 4.14 first presents an example of the detrended signal intensity P_{det} and the detrended phase φ_{det} in the 27th minute of the scintillation data collected for PRN10 at CRAAM station. In this minute, $S4 = 0.73$ and $Phi60 = 0.66$ rad. As the figure shows, rapid fluctuations frequently appear in both the intensity and phase measurements. A deep intensity fading occurs in the 31st second, reaching around -24 dB.

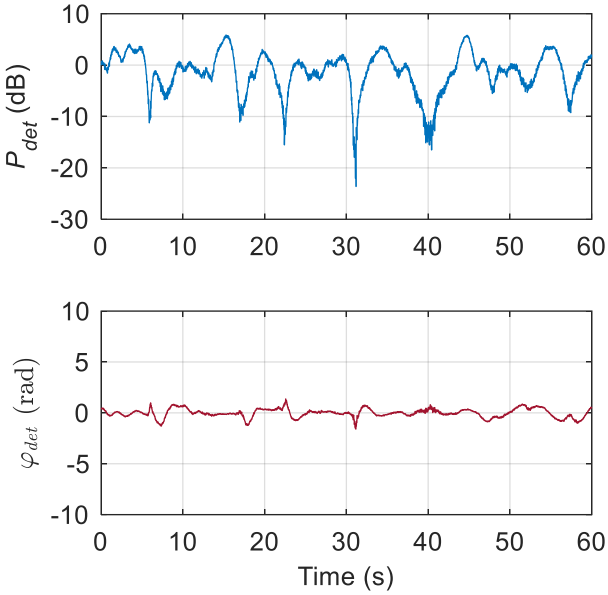

Figure 4.14 Variations of the detrended signal intensity P_{det} (top) and carrier phase φ_{det} (bottom) measurements in the 27th minute of the scintillation data collected for PRN10 at CRAAM station

The tracking error δ_{φ} along with the 1-second tracking jitter $\sigma_{\delta_{\varphi}}$ in the same period of Figure 4.14 are presented in Figure 4.15. As it can be seen that δ_{φ} and $\sigma_{\delta_{\varphi}}$ increases correspondingly following the rapid and strong fluctuations in the detrended intensity and phase shown in Figure 4.14. When the PLL integration time η is increased from 1 ms in the left two panels to 10 ms in the right panels, δ_φ generally decreases and mostly falls into the range of -0.5 to 0.5 rad. Additionally, comparing the top and bottom panels with different PLL bandwidth B_n, both δ_φ and σ_{δ_φ} present very comparable values, indicating that increasing the PLL bandwidth has a lesser impact on the tracking error. On the other hand, large second-to-second variabilities are observed in the calculated 1-second σ_{δ_φ} in all the panels. The largest σ_{δ_φ} in each panel can be around 5 to 6 times that when there is no strong intensity fading.

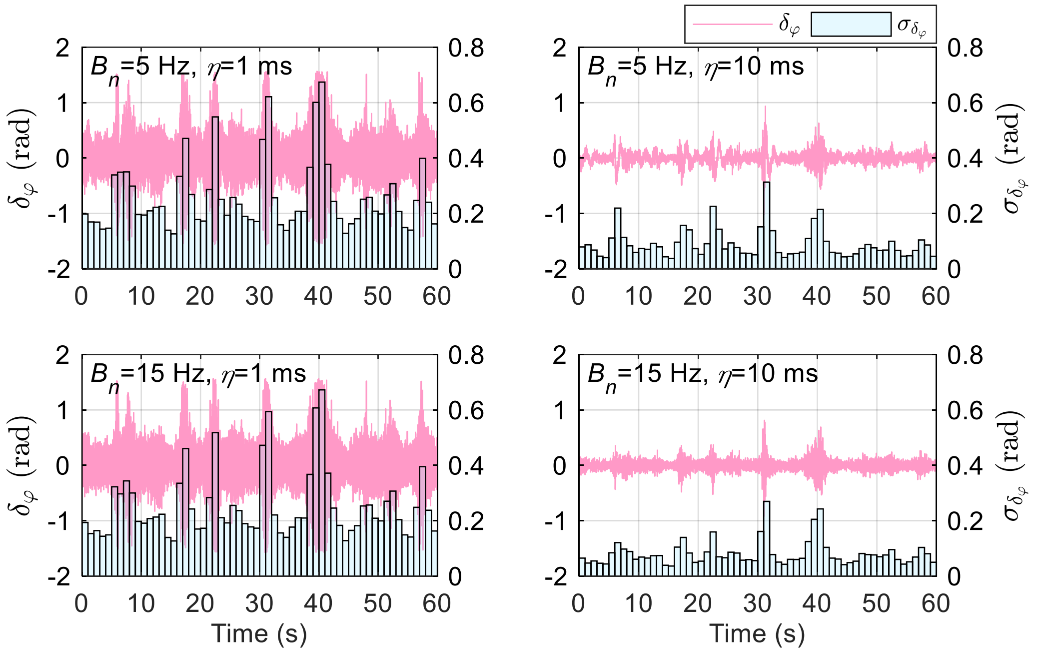

Figure 4.15 Variations of the tracking error δ_φ and tracking jitter σ_{δ_φ} calculated in the 27th minute of the scintillation data recorded for PRN10 at CRAAM station. The data was processed using different PLL configurations with respect to bandwidth B_n and integration time η

Figure 4.16 further shows the 1-minute tracking jitter calculated for PRN10 at CRAAM station. It can be seen that for the PLL with all configurations, apparent increases in σ_{δ_φ} are observed during the scintillation period. When η is increased from 1 ms to 10 and 20 ms, σ_{δ_φ} is significantly reduced. By contrast, it is quite close for configurations where the PLL has the same value of η but different B_n, indicating that increasing the bandwidth makes little difference on the tracking jitter under low latitude scintillation. This is in good agreement with the results shown in Figure 4.15 and the conclusion in Forte (2012).

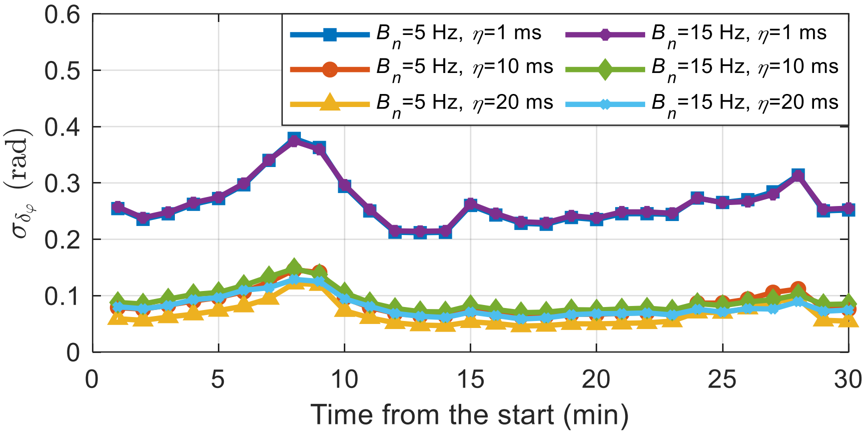

Figure 4.16 Variations of the tracking jitter σ_{δ_φ} estimated in each minute for PRN10 at CRAAM station. The data was processed by the PLL with the bandwidth B_n configured to 5 and 15 Hz and the integration time η configured to 1, 10 and 20 ms, respectively

4.4.2 PLL tracking errors at SANAE IV station

The tracking error and tracking jitter estimated based on the scintillation data collected for PRN31 at SANAE IV station is presented in this section. First, Figure 4.17 shows an example of the detrended signal intensity and phase in the 10th minute of the scintillation data. As the top panel shows, P_{det} remains stable and no fading is present in the whole period, while strong fluctuations are seen in φ_{det} in the bottom panel. This is reasonable as the phase dynamics is the dominant effect and more severe under the high latitude scintillation.

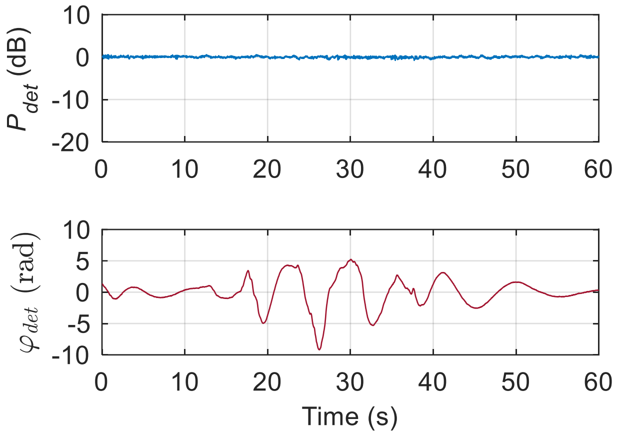

Figure 4.17 Variations of the detrended signal intensity P_{det} (top) and carrier phase φ_{det} (bottom) measurements in the 10th minute of the scintillation data collected for PRN31 at SANAE IV station

Figure 4.18 shows the tracking error δ_φ along with the 1-second tracking jitter σ_{δ_φ} related to the scintillation shown in Figure 4.17. It can be seen that although the detrended phase φ_{det} in Figure 4.17 fluctuates over the whole minute, δ_φ only increases from around the 35th to 38th second, except in the bottom panels, where the phase scintillation induced tracking error is reduced by a higher PLL bandwidth and probably buried in the background thermal noise. Additionally, when the integration time η is increased from 1 ms in the top left panel to 10 ms in the top right panel, σ_{δ_φ} remains almost unchanged from the 35th to 38th second, while in general it is significantly reduced during the rest of the time in this minute, when the tracking error is dominated by the white noise. This indicates that increasing the PLL integration time can greatly reduce the thermal noise in the PLL tracking error, which agrees with the results shown in Figure 4.15, however, it has little effects on the phase scintillation induced tracking errors.

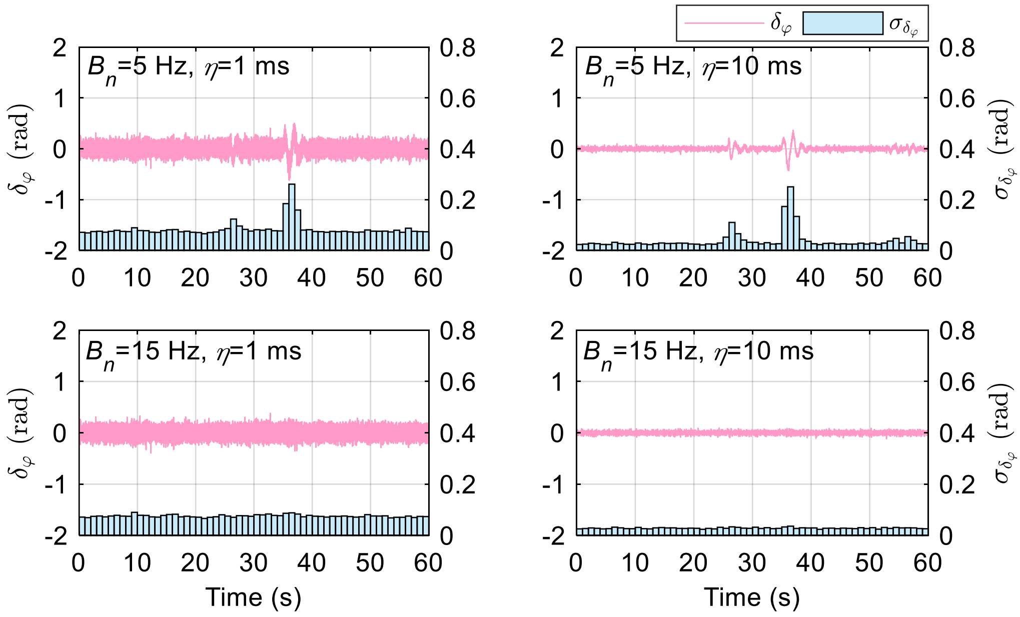

Figure 4.18 Variation of the tracking error δ_φ and tracking jitter σ_{δ_φ} calculated in the 10th minute of the scintillation data recorded for PRN31 at SANAE IV station. The data was processed using different PLL configurations with respect to bandwidth B_n and integration time η

The variation of the 1-minute tracking jitter calculated for PRN31 at SANAE IV station is presented in Figure 4.19. It is seen that for the PLL configuration with a bandwidth of 5 Hz, σ_{δ_φ} increases visibly during scintillation and reaches the peak in the 10th minute when the strongest phase scintillation occurs. When the integration time η is increased to 10 and 20 ms, a smaller value of σ_{δ_φ} is generally achieved, but not in the 10th minute when the tracking jitter only slightly changes. By contrast, when selecting the same integration time, the increase in bandwidth can significantly mitigate the phase scintillation induced tracking jitter, as shown from the 3rd to 5th minute, the 10th minute and the 17th to 21st minute in the figure. This is different from the results shown in Figure 4.16. A possible explanation is that compared with the low latitude scintillation, where both the amplitude and phase scintillation are severe, phase scintillation is the dominant effect at high latitudes. Signals with only phase dynamics can be well-tracked by a PLL with a wider bandwidth.

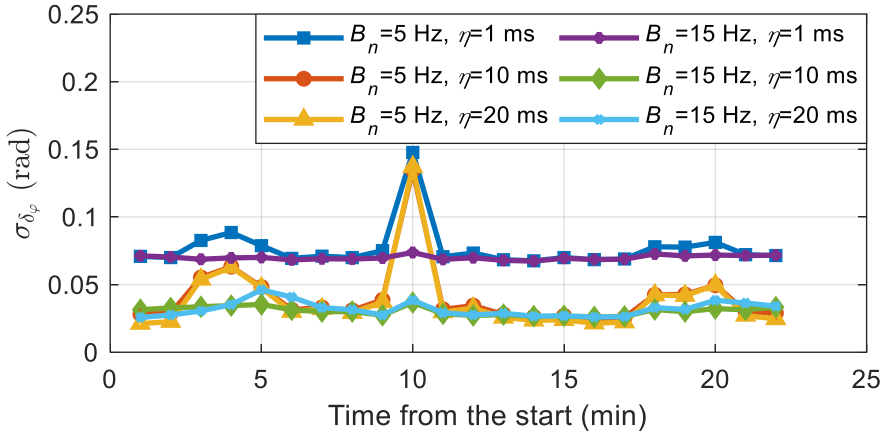

Figure 4.19 Variation of the tracking jitter σ_{δ_φ} estimated in each minute for PRN31 at SANAE IV station. The data was processed by the PLL with the bandwidth configured to 5 and 15 Hz and the integration time configured to 1, 10 and 20 ms, respectively

Based on the analysis in this and the previous sections, the effects of PLL bandwidth and integration time changes on the tracking jitter under low and high latitude scintillation are summarised in Table 4.3. It is worth mentioning that compared with Figure 4.16, the tracking jitter shown in Figure 4.19 is generally lower. This is due to the differences in the $C/N0$ levels observed at CRAAM and SANAE IV stations mentioned in Section 4.3.4.

Table 4.3 Effects of PLL bandwidth B_n and integration time η tuning on the phase tracking jitter under the low latitude scintillation observed at CRAAM station and the high latitude scintillation observed at SANAE IV station

	CRAAM station (Low latitude)	SANAE IV station (High latitude)
Increasing B_n	Total phase tracking jitter is slightly affected	Only reduces the phase scintillation induced noise component
Increasing η	Total phase tracking jitter reduces significantly	Only reduces the white noise component

4.4.3 Discriminator output noise distribution under scintillation

The distribution of the PLL tracking error δ_φ under low and high latitude scintillation is analysed and modelled in this section. When there is only white noise in the tracking jitter, i.e., $\sigma_{\delta_\varphi} \approx \sigma_w$, the PDF of δ_φ is represented by a zero-mean standard Gaussian distribution, given by

$$f(\delta_\varphi) = \frac{1}{\sqrt{2\pi}\sigma_w} e^{-\frac{1}{2}\left(\frac{\delta_\varphi}{\sigma_w}\right)^2} \tag{4.14}$$

where σ_w can be estimated by Eq. (2.8). In the presence of scintillation, σ_{δ_φ} increases due to the intensity fading and phase dynamics, as shown in Figure 4.16 and Figure 4.19. Under strong amplitude scintillation, the signal can suffer from intensity fading of 20 dB or even deeper, which drastically increases the tracking errors and degrades the tracking performance. Figure 4.20 shows the probability density distribution curves of δ_φ obtained by processing the MATLAB simulated raw IF data for GPS L1 C/A signals containing only white noise generated at $C/N0$ values varying from 35 to 55 dB-Hz. The standard Gaussian distribution curves calculated by Eq. (4.14) are also shown. It is seen that the measured curves follow closely the standard Gaussian distribution curves at each $C/N0$ level. When it is decreased from 55 to 35 dB-Hz, the distribution curve becomes shorter and flatter. This indicates that the PLL discriminator would output much larger tracking errors due to the decreased signal intensity.

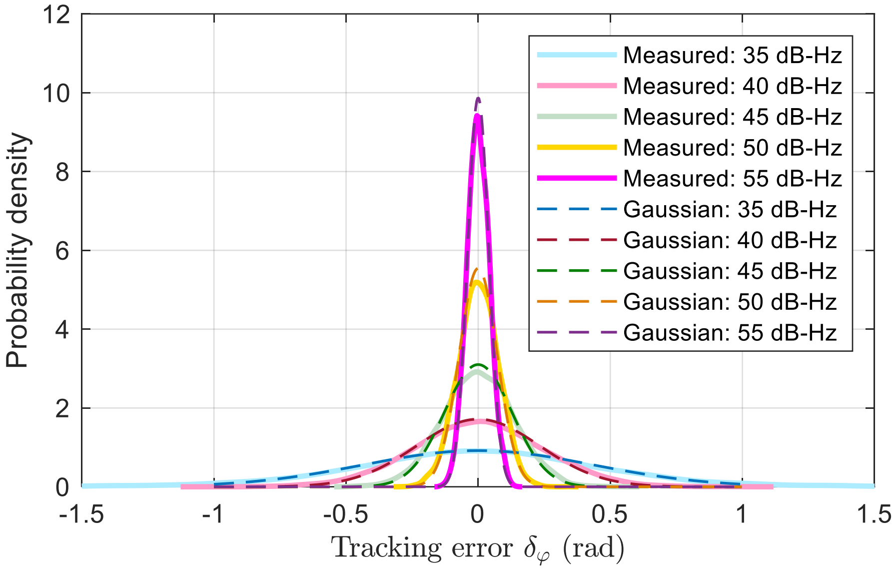

Figure 4.20 Measured and standard Gaussian probability density distribution curves of the tracking error δ_φ obtained by processing the simulated IF data for GPS L1 C/A signals containing only white noise with $C/N0$ varying from 35 to 55 dB-Hz

In order to model the scintillation effects on the PLL tracking error δ_φ, its probability density distribution is fitted by a custom-defined PDF proposed in this analysis, which is defined as

$$f(\delta_\varphi) = \frac{1}{\sqrt{2\pi}k_1\sigma_w} e^{-\frac{1}{2}\left(\frac{\delta_\varphi - k_3}{k_2\sigma_w}\right)^2} \tag{4.15}$$

where k_1, k_2 and k_3 are the parameters related to the height, 1-σ width and the symmetry axis of the curve, respectively. Particularly, when $k_1 = k_2$ and $k_3 = 0$, Eq. (4.15) becomes the zero-mean standard Gaussian distribution, however, with the 1-σ width of $k_1\sigma_w$ (or $k_2\sigma_w$). To fit the measured curves using the PDF defined by Eq. (4.15) and to estimate the k_1, k_2 and k_3 parameters, a nonlinear least square model, which minimizes the summed square of residuals, as well as an iterative approach, are implemented through a MATLAB curve-fitting tool (Mathwoks 2021). Figure 4.21 shows an example of the fitted probability density distribution curve of the tracking errors in the 24th minute of the scintillation data for PRN10 at CRAAM station. It is seen that compared with the standard Gaussian distribution, the fitted curve better represents the measured distribution curve. It should be noted that the IF data in this case was processed using a PLL with $B_n = 15$ Hz and $\eta = 1$ ms.

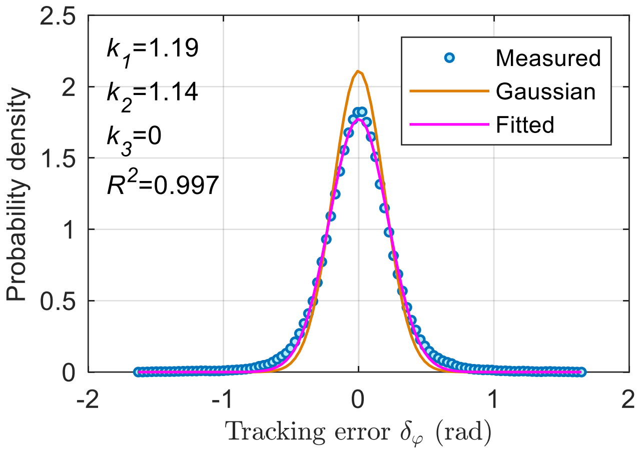

Figure 4.21 An example of the probability density distribution curve of the tracking error δ_φ in the 24th minute of the scintillation data collected for PRN10 at CRAAM station. The curve was fitted using the custom-defined PDF defined by Eq. (4.15)

Figure 4.22 presents the k_1 and k_2 parameters obtained when fitting the distribution of tracking errors in each minute using Eq. (4.15) at CRAAM station. The scintillation data are processed by PLL configurations with $B_n = 5$, 15 Hz and $\eta = 1$ and 10 ms, respectively. In all fittings, the values of R^2 are over 0.99, indicating excellent goodness of fit. It can be seen from the figure that obvious biases between k_1 and k_2 parameters are observed from the 7th to 9th and the 24th to 29th minute when scintillation occurs, which indicates that the scintillation captured at this station causes the distribution of tracking errors to deviate from the standard Gaussian distribution. It is worth mentioning that the fitted $k3$ in all fittings are near 0 over all the period. The average and standard deviation of its value for all the panels are less than 0.001 rad, which means that on average the tracking error is approximately 0 and the symmetry axis of the distribution curve stays at the origin even under strong scintillation at low latitudes.

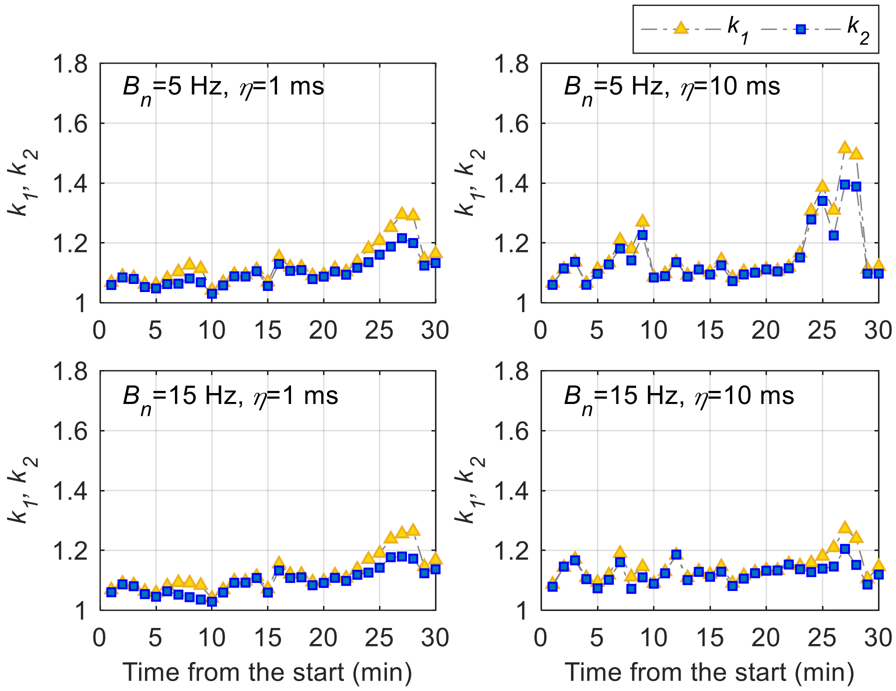

Figure 4.22 Variations of the obtained k_1 and k_2 parameters when fitting the tracking errors in each minute using the custom-defined PDF defined by Eq. (4.15). The tracking errors are obtained by processing the scintillation data collected on PRN10 at CRAAM station using different PLL configurations with respect to bandwidth B_n and integration time η

The fitted k_1 and k_2 parameters for the measured distribution curves of the tracking errors at SANAE IV station are shown in Figure 4.23. In all fittings, the R^2 values, again, are over 0.99 and the average and standard deviation of $k3$ values are less than 0.001 rad. In the top two panels where the PLL bandwidth B_n is 5 Hz, obvious biases between the k_1 and k_2 parameters are observed from the 3rd to 5th minute and in the 10th minute, indicating the distortion of the tracking error distribution due to moderate and strong phase scintillation at high latitudes. By contrast, no obvious bias is seen between the k_1 and k_2 values in the bottom panels, especially in the bottom left panel when $B_n = 15$ Hz and $\eta = 1$ ms. Thus, when the PLL bandwidth is set to 15 Hz, the tracking error still closely follows a standard Gaussian distribution even under the strong phase scintillation captured at this station. This is different from the low latitude scintillation effects shown in Figure 4.22.

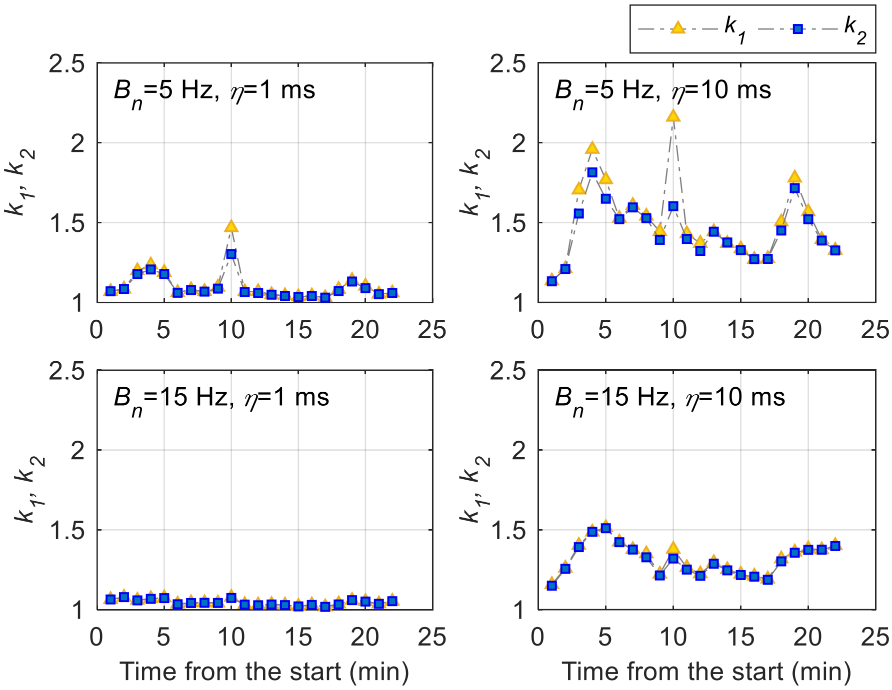

Figure 4.23 Variations of the k_1 and k_2 parameters obtained when fitting the tracking errors in each minute using the custom-defined PDF defined by Eq. (4.15). The tracking errors are obtained by processing the scintillation data collected on PRN31 at SANAE IV station using different PLL configurations with respect to bandwidth B_n and integration time η

It is worth mentioning that although the k_1, k_2 and k_3 parameters in Eq. (4.15) are only estimated using a curve-fitting method in this study, future work can be conducted to model the relationships between the scintillation indices, like $S4$ and $Phi60$, and the k_1, k_2 parameters. In this way, it will be possible to directly determine the PDF of the tracking error through Eq. (4.15) and the scintillation index. Furthermore, the biases between k_1 and k_2 parameters in Eq. (4.15) mainly indicate the distortion of the tracking error with respect to the standard Gaussian distribution. If $k_1 = k_2 \approx 1$ and $k_3 = 0$, Eq. (4.15) becomes Eq. (4.14), indicating that there is only white noise in the PLL tracking errors. Therefore, when the values of k_1 and k_2 are higher than 1, it also indicates that there is more than white noise in the tracking errors.

4.5 Summary

This chapter introduced the approaches to model the adverse effects of scintillation on GNSS receiver tracking loops. The phase and code jitter for GPS L1 C/A signal estimated using the models developed in Conker et al. (2003) are introduced first. Similar models for the modern Galileo E1 and E5a signals are developed in this work. To address the concerns inherent to these models, the PLL bandwidth and integration time tuning effects on the phase jitter estimation are studied based on the simulated scintillation data processed using different PLL configurations. Alternative approaches are proposed which estimate the phase and code jitter by exploiting the raw PLL and DLL discriminator output. By processing the real scintillation data collected at low and high latitude stations using an SDR receiver, the phase and code jitter are estimated respectively using the jitter estimation models described in Conker et al. (2003) and the approaches proposed in this work. The results showed that both approaches achieve a good match in the phase and code jitter estimation. Furthermore, the probability density distribution of phase tracking errors in the PLL discriminator output is analysed. It is found that moderate and strong scintillation can cause the distribution of tracking error to deviate from the standard Gaussian distribution. A custom-defined PDF is then proposed to fit the measured tracking error distribution curves. The results show that the proposed PDF can achieve an excellent fit to the distribution of tracking errors under scintillation. As further work to this thesis, a follow-on study could be conducted to model the relationships between the scintillation indices and the proposed PDF parameters, which would provide the possibility to directly determine the PDF of the PLL tracking error under scintillation.

In the next chapter, scintillation mitigation on GNSS positioning by exploiting the estimated phase and code jitter is presented. In order to improve the performance of the mitigation method, an approach to calculate the 1-second scintillation indices is proposed. The effectiveness of the proposed 1-second scintillation index with respect to the 1-minute index is shown. The scintillation mitigation on GNSS positioning by exploiting the 1-second index at low and high latitudes is provided.

5 Scintillation mitigation on positioning by exploiting 1-second scintillation indices

In Chapters 3 and 4, the adverse effects of scintillation on GNSS receiver tracking loops are analysed and modelled. These effects pose a serious threat to GNSS positioning by significantly degrading the positioning accuracy. In this chapter, the approach used for mitigating scintillation effects on GNSS positioning is studied. First the scintillation mitigation approach, mainly focusing on what is proposed in Aquino et al. (2009), is described in detail. The limitations of this approach and the potential solutions to overcome them are discussed next. To address these limitations, a new approach to estimate the 1-second scintillation indices is proposed in this study, which is proved to better describe the signal distortion under scintillation. Based on the scintillation data collected at low and high latitude stations, scintillation effects on GNSS positioning are presented thereafter. The mitigation of the scintillation effects on positioning by exploiting the proposed 1-second scintillation indices is presented finally.

5.1 Scintillation mitigation approach for GNSS positioning

The mitigation of scintillation effects on GNSS positioning has been studied by many researchers. Various scintillation mitigation tools and approaches have been developed (Aquino et al. 2009; Bougard et al. 2011; Zhang et al. 2014; Juan et al. 2017; Marques et al. 2018; Dabove et al. 2019; Luo et al. 2019), which are described in Section 1.1.2. In the framework of this thesis, the scintillation mitigation approach developed in Aquino et al. (2009) is exploited, i.e., to modify the least square stochastic models in the position estimation by using the receiver PLL phase jitter and DLL code jitter. In this approach, satellites affected by scintillation are not excluded, thus ensuring the satellite geometry to provide the best positioning solution. Additionally, it can be applied with less depends on the scintillation conditions. Even when most of the visible satellites are affected by scintillation, it can still be implemented. Details of this approach is described in this section. The limitations and potential solutions to improve the performance of this mitigation approach are provided.

5.1.1 Improving the stochastic model in GNSS positioning

As described in Section 2.3.2, the stochastic models in PPP calculation can be defined according to different strategies to allocate weights to GNSS code and carrier phase measurements. In order to mitigate the scintillation effects on the positioning estimation, an approach to improve the stochastic models was developed in Aquino et al. (2009). In this approach, the code and carrier phase measurement noise levels are respectively represented by the DLL code jitter and PLL phase jitter, which are estimated using the scintillation sensitive jitter estimation models described in Section 4.1.1. The inverses of the estimated jitter variance values are then applied to modify the stochastic models in the positioning determination. Thus, GNSS measurements more affected by scintillation will have a higher phase and code jitter and therefore a lower weight in the stochastic model, which leads to a decreased contribution to the positioning estimation. Compared with the commonly used elevation weighting defined by Eq. (2.22), the phase and code jitter weighting considers the scintillation effects on the GNSS measurements, which is more realistic in the scintillation environment.

Figure 5.1 shows an example of the measurement noise in the stochastic models for the ionosphere-free combinations of GPS L1 C/A and L2 P measurements when using elevation and jitter weighting strategies in position calculation. The scintillation data was collected on PRN21 at PRU2 station in November 2014. It can be seen from the top panel that the amplitude and phase scintillation indices measured on GPS L1 C/A signal increase significantly from around UTC 00:10 to 01:50 and 02:40 to 03:30. When an elevation weighting strategy is used, the noise levels in the middle and bottom panels vary slowly as a function of the satellite elevation angle. Larger values are observed when the satellite elevation is low, considering that the measurement is more contaminated by the atmospheric diffraction and multipath effects. By contrast, when using a phase jitter or code jitter weighting strategy, the measurement noise in the middle and bottom panels is sensitive not only to satellite elevation but also to the scintillation levels. During scintillation occurrence, it increases to higher levels following the variation of the scintillation intensities, even when the satellite has a higher elevation. This clearly demonstrates the advantages of using the jitter weighing strategy in position estimation.

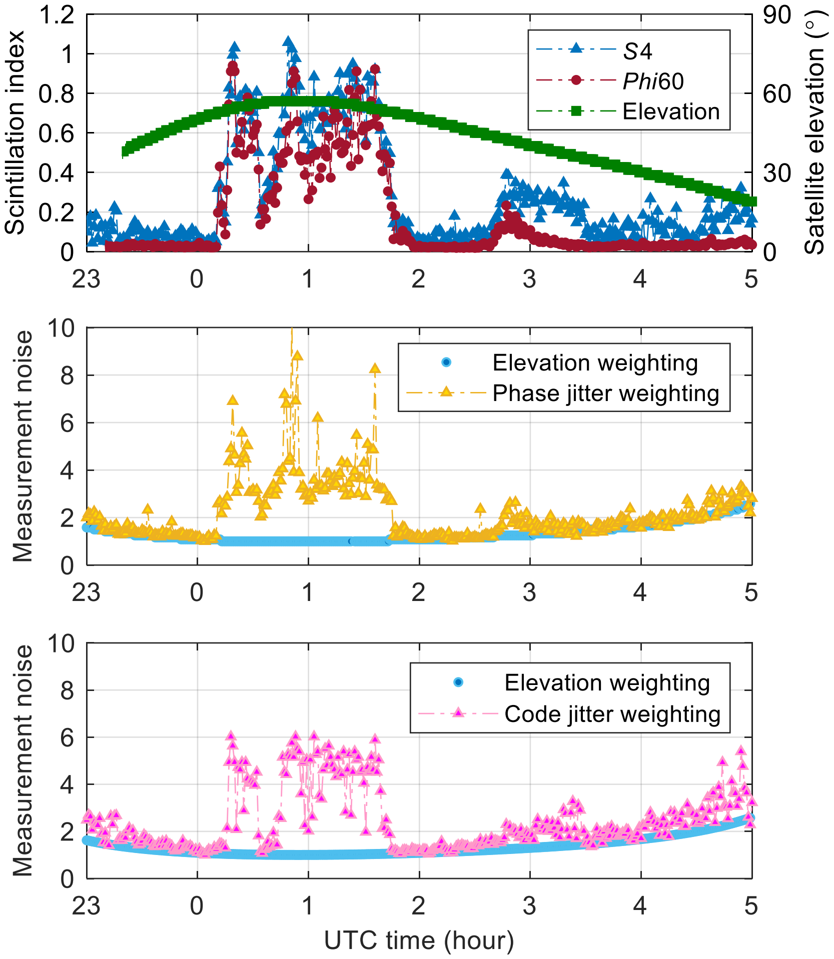

Figure 5.1 Example of the measurement noise in the stochastic models for the ionosphere-free combinations of GPS L1 C/A and L2 P measurements on PRN21 observed at PRU2 station from UTC 23:00 12 November to 05:00 13 November 2014. The panels are: the amplitude and phase scintillation indices measured on L1 C/A signals and the satellite elevation (top); the measurement noise values for the ionosphere-free combinations of the carrier phase (middle) and the code (bottom) measurements for the elevation and jitter weighting strategies

5.1.2 Limitations and solutions

The scintillation mitigation approach given in Section 5.1.1 has been found successful in many studies (da Silva et al. 2010; Strangeways et al. 2011; Park et al. 2017; Vani et al. 2019; Luo et al. 2020; Vadakke Veettil et al. 2020). However, there are still limitations in applications which need to be addressed, such as:

(1) The 1-minute phase and code jitter calculated based on the 1-minute scintillation indices are used to represent the noise levels of GNSS instantaneous measurements in this approach. However, it is shown in this thesis that the signal fluctuations caused by scintillation vary significantly within 1 minute and present large second-to-second variabilities. For example, according to the analysis in Section 3.3.3, the signal intensity fading with its duration shorter than 1 second accounts for the majority of events across all the scintillation levels. Additionally, by analysing the variation of the 1-second $C/N0$ values within 1 minute under strong scintillation shown in Figure 3.24, it was observed that the signal intensity changes significantly among individual 1-second epochs. Moreover, based on the analysis in Sections 4.4.1 and 4.4.2, the PLL tracking errors present large differences within 1 minute. As a result, a 1-minute scintillation index probably does not perfectly describe the signal distortion under scintillation, thus, a 1-minute based phase and code jitter may not provide the best representation of the instantaneous GNSS measurement noise. Calculating the phase and code jitter at a higher rate, which depends on a higher rate of scintillation indices, is necessary. A 1-second amplitude scintillation index was proposed in Park et al. (2017) to describe the signal intensity fluctuations under low latitude scintillation. However, the estimation of the proposed 1-second index still requires 1-minute raw scintillation data. More importantly, the 1-second indices describing the phase fluctuations caused by scintillation are not developed, which is particularly essential for precise positioning techniques which rely heavily on phase measurements.

(2) Due to the fact that scintillation indices are required prior to estimating the PLL phase jitter and DLL code jitter and thereafter modifying the stochastic models in positioning,

this mitigation approach has so far been only used in connection with ISMRs. For generic navigation receivers which are not capable of estimating the scintillation indices and consequently the phase and code jitters, the mitigation approach cannot be implemented directly. Although an alternative approach is proposed in Section 4.3.1, to estimate the phase and code jitter without involving the scintillation index calculation, it still requires the high frequency raw discriminator output in receiver tracking loops, which is usually not available for generic GNSS users.

To address the first limitation, a new approach is proposed in this study which enables to calculate the 1-second amplitude and phase scintillation indices using the 50 Hz amplitude and phase measurements logged by ISMRs. With the newly estimated 1-second scintillation indices, the 1-second phase and code jitter can be correspondingly estimated and further used in the scintillation mitigation strategy. In the next section, details of the approach for the 1-second index estimation are introduced. The mitigation of scintillation effects on GNSS positioning by exploiting the newly proposed index is given thereafter.

To address the second limitation, a possible solution is to provide the phase and code jitter values to the generic navigation receivers through external scintillation information or tools. For example, a generic receiver can obtain the scintillation indices for each measurement from a nearby ISMR, as these two receivers may probably experience very similar ionospheric environment if the distance between them is close enough. Another possible solution is to exploit the concept of phase and code jitter maps, which provides phase and code jitter values for different signals verticalized to the ionospheric layer. In this way, the generic receivers can extract and calculate the jitter values directly from these maps for each measurement. In this thesis, the scintillation mitigation strategy by exploiting the phase and code jitter maps is described in detail in Chapter 6. However, due to the limitation of this study, the scintillation mitigation for a generic receiver with the help of a nearby ISMR has not been addressed and is suggested for future study.

5.2 Towards 1-second scintillation index

This section introduces the newly proposed approach for the estimation of the 1-second scintillation index. The scintillation data used in this analysis were collected by ISMRs deployed in the Brazilian region and in the Auroral to Arctic region, which are selected to represent the scintillation at low and high latitudes, respectively. Based on the raw scintillation data logged by the ISMRs, the 1-second scintillation index is then calculated, following the proposed approach, which is described hereafter.

5.2.1 Scintillation data sets

The locations of the ISMR stations used for the scintillation data collection in this analysis are listed in Table 5.1. The low latitude stations, PRU2 and FRTZ, are part of the Brazilian CIGALA/CALIBRA network as described in Section 2.4.3. The data analysed at these two stations were logged from the post-sunset to the early morning hours on each day between 10 November, Day of year (DOY) 314, to 16 November, DOY 320, in 2014, which is in the maximum of the solar activity. At PRU2 station, the analysed data covered from UTC 21:00 to 05:00 on the following day (Local time 18:00 to 02:00), while at FRTZ station, it covered from UTC 20:00 to 04:00 (Local time 17:00 to 01:00).

Table 5.1 Stations and dates for the scintillation data collection

Station abbreviation	Location	Latitude and longitude	Date and time (UTC)	DOY
PRU2	Presidente Prudente, Brazil	22.12°S, 51.41°W	10 to 16 November 2014	314 to 320
FRTZ	Fortaleza, Brazil	3.72°S, 38.58°W	10 to 16 November 2014	314 to 320
LYB0	Longyearbyen, Svalbard, Norway	78.35°N, 15.63°E	29 August to 3 September 2019	241 to 246
SACC	Sachs Harbour, Canada	71.99°N, 125.26°W	29 August to 3 September 2019	241 to 246

The LYB0 station is located in the Arctic region and operational as part of the INGV ionospheric monitoring network as mentioned in Section 2.4.3, while the SACC station is part of the CHAIN network in northern Canada. At these two stations, scintillation data was analysed during the geomagnetic storm that took place from 29 August, DOY 241, to 3 September, DOY 246, in 2019. Figure 5.2 presents the variation of the geomagnetic activity index Kp on these days. It can be seen that the Kp index increases from around 1 on DOY 241 to a maximum of 6- on DOY 243, followed by a gradual decrease to less than 2 on DOY 246, indicating that the geomagnetic activity on DOY 243 and 244 was more severe.

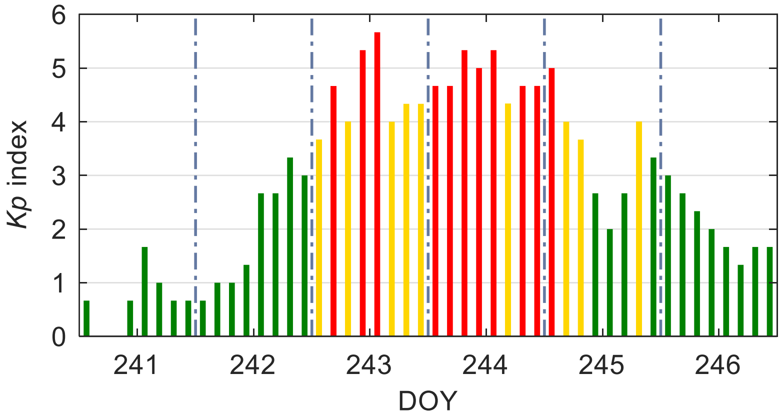

Figure 5.2 Variation of Kp index from DOY 241 to 246 in 2019

Each station listed in Table 5.1 is equipped with a PolaRxS Pro ISMR, which can measure scintillation indices and log 50 Hz raw signal amplitude and carrier phase measurements, as described in Section 2.4.1. Figure 5.3 shows the occurrence of the amplitude and phase scintillation of different levels captured on GPS L1 C/A signal at PRU2 and FRTZ stations from DOY 314 to 320 in 2014. As it can be seen, the occurrence of scintillation at PRU2 station in the left panels presents large day-to-day variabilities. Almost no amplitude or phase scintillation is observed on DOY 314, while on DOY 316 and 317, extremely strong scintillation with $S4 > 1.2$ or $Phi60 > 1.2$ rad is frequently observed. By contrast, the scintillation observed at FRTZ station in the right panels is generally much less significant. Although strong amplitude and phase scintillation is also observed, it only accounts for a small part of the total scintillation occurrence. It should be noted that the satellites with an elevation lower than 30° are not considered in this analysis in order to minimize the contamination by non-scintillation related effects, like multipath.

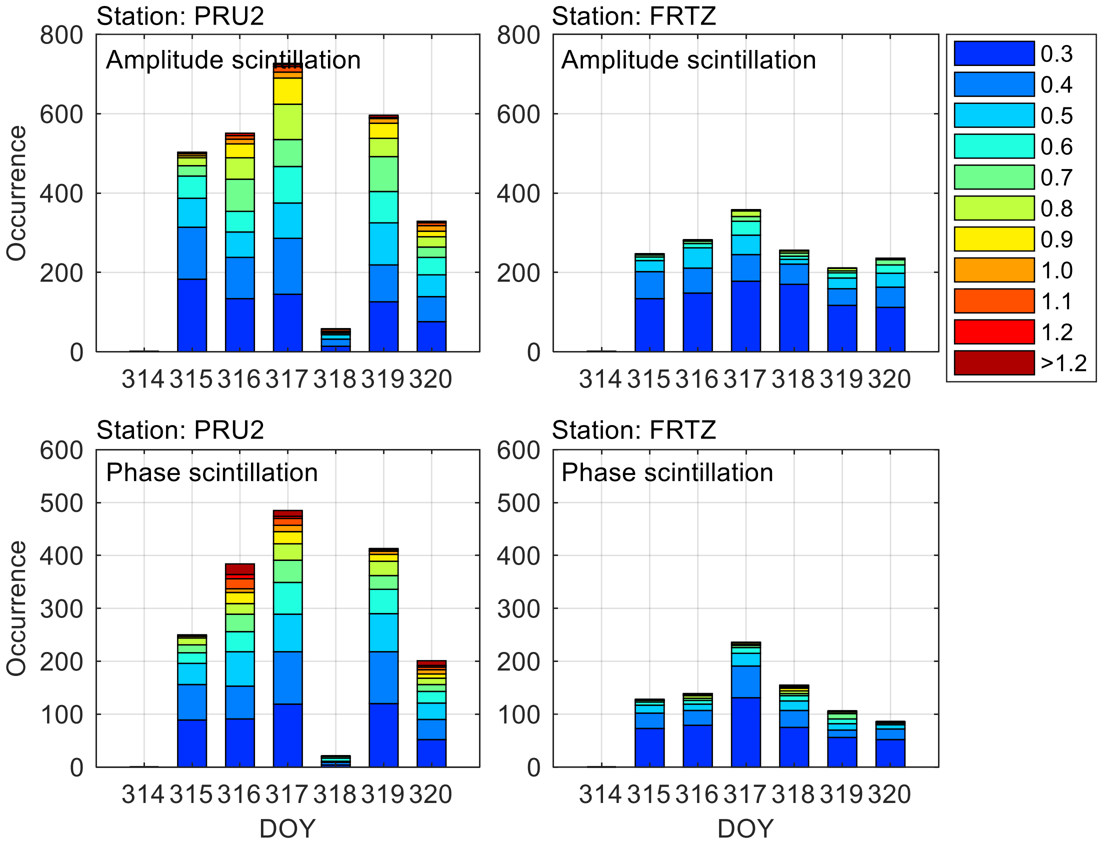

Figure 5.3 Occurrence of different levels of amplitude and phase scintillation captured on GPS L1 C/A signal at PRU2 (left) and FRTZ (right) stations from DOY 314 to 320 in 2014

Figure 5.4 shows the overall occurrence of amplitude and phase scintillation in relation to $S4$ and $Phi60$ at PRU2 and FRTZ stations. It can be seen that the scintillation occurrence decreases gradually with the increase in the scintillation levels at both stations. Compared with the scintillation observed at PRU2 station in the left panel, it is much less and weaker at FRTZ station in the right panel. This is due to the fact that the PRU2 station is located in the crest of the EIA region, while the FRTZ station is in the edge of this region.

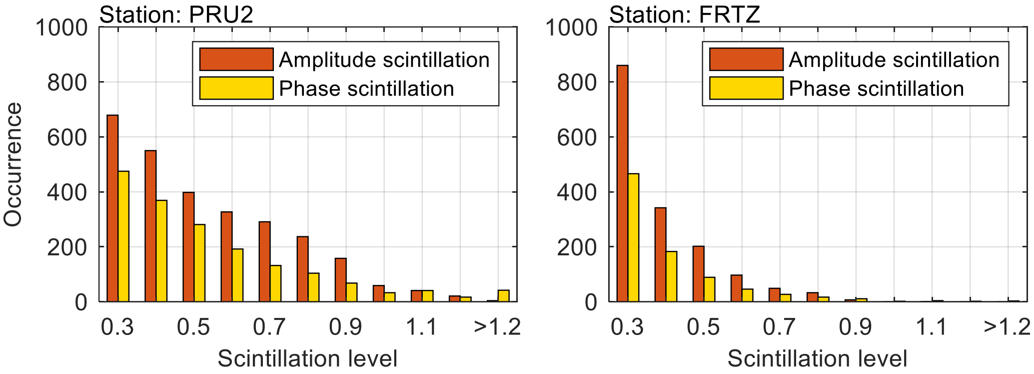

Figure 5.4 Overall occurrence of the amplitude and phase scintillation in relation to $S4$ and $Phi60$ captured on GPS L1 C/A signal at PRU2 (left) and FRTZ (right) stations observed from DOY 314 to 320 in 2014

The scintillation observed on GPS L1 C/A signal at the high latitude stations from DOY 241 to 246 in 2019 is also counted. Due to the fact that the number of amplitude scintillation occurrences captured at LYB0 and SACC station only reaches 59 and 14, respectively, and the $S4$ levels are all less than 0.4, only the phase scintillation occurrence is presented, as shown in Figure 5.5. It can be seen in the top panels that on DOY 241 when the geomagnetic activity is quiet, there is almost no scintillation observed at either stations, while on DOY 243 when Kp index reaches the maximum during this storm, the total occurrence of phase scintillation reaches the peak simultaneously at these two stations. The bottom panels show the overall occurrence of the phase scintillation as a function of $Phi60$. With the increase in $Phi60$, the occurrence decreases dramatically at both stations, while apparent increases are observed when $Phi60$ overtakes 1.2 rad.

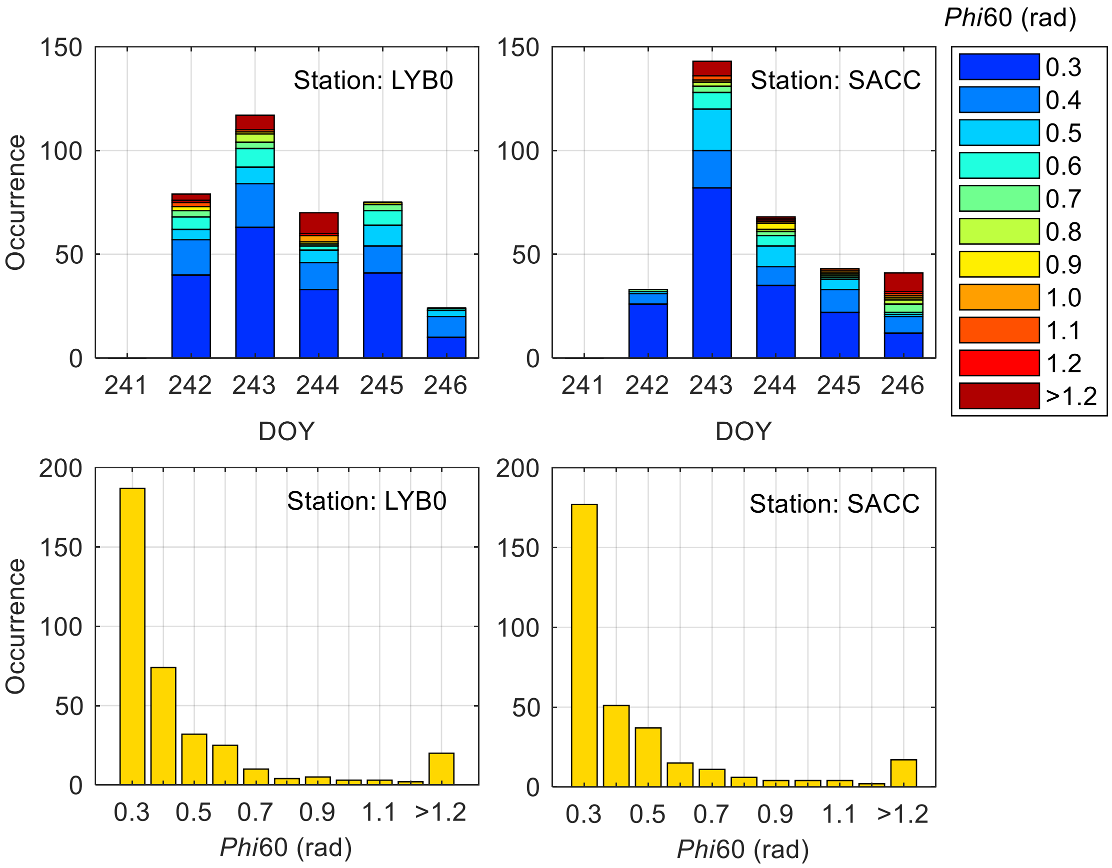

Figure 5.5 Occurrence of different levels of phase scintillation (top) and overall phase scintillation occurrence in relation to $Phi60$ (bottom) observed on GPS L1 C/A signal from DOY 241 to 246 in 2019 at LYB0 and SACC stations

It should be noted that although the scintillation captured at LYB0 and SACC stations is much less than that observed at PRU2 and FRTZ stations, extremely strong phase scintillation with $Phi60 > 1.2$ rad is frequently seen on DOY 242, 243 and 244 at LYB0 station and on DOY 243 and 246 at SACC station. Based on these scintillation data, the 1-second scintillation index is estimated using the approach described in the next section.

5.2.2 Estimation of 1-second scintillation index

The proposed approach to estimate 1-second amplitude and phase scintillation indices using the 50 Hz signal amplitude and phase measurements is introduced in this section. The 1-second amplitude scintillation index, denoted as $S4^{-}$, is calculated following a similar procedure as for the 1-minute $S4$ calculation described in Section 3.1.1. However, the standard deviation and normalization in Eq. (3.3) are performed within an interval of 1 second instead of 1 minute, and given by

$$S4_{total}^{-} = \sqrt{\frac{\langle P_{det}^{2}\rangle_{1s} - \langle P_{det}\rangle_{1s}^{2}}{\langle P_{det}\rangle_{1s}^{2}}} \tag{5.1}$$

where P_{det} is the detrended signal intensity obtained following the processing described in Section 3.1.1. Figure 5.6 shows an example of the variation in the detrended signal intensity P_{det}, $C/N0$ and the estimated 1-second $S4^{-}$ index under strong scintillation ($S4 = 0.84$) captured at PRU2 station. It can be seen in the top panel that P_{det} varies significantly within this minute. Large second-to-second variabilities are observed. The fadings are generally with a depth higher than -5 dB, while the deepest fading reaches -14 dB in the 21st second. A similar variation is seen in the 1-second $C/N0$ value, which fluctuates obviously following the detrended signal intensity. In the bottom panel, the estimated 1-second $S4^{-}$ also presents large differences between individual seconds. Obvious increases in $S4^{-}$ are seen when there are rapid fluctuations in P_{det} shown in the top panel. Additionally, it is seen that the 1-second $S4^{-}$ values in this minute are all lower than the 1-minute $S4$ value. This is reasonable as while calculating the 1-minute $S4$ index, the variation of the 1-second $C/N0$ values is also considered.

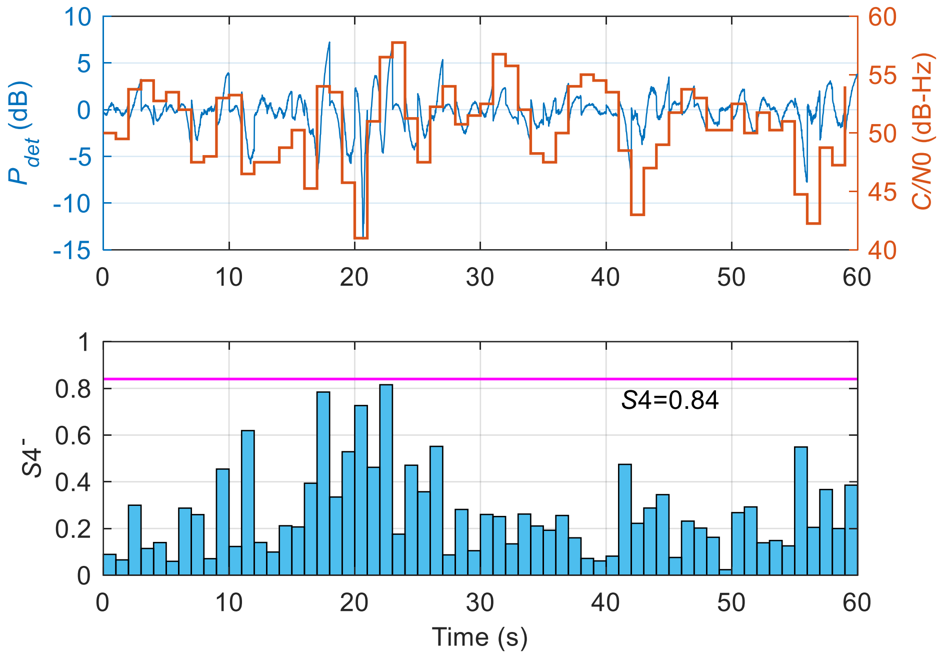

Figure 5.6 Variation of the detrended signal intensity P_{det} and $C/N0$ (top) and the estimated 1-second amplitude scintillation index $S4^{-}$ (bottom) on GPS L1 C/A signal of PRN25 at UTC 23:48 on DOY 316 in 2014 at PRU2 station

The 1-second phase scintillation spectral parameters p and T cannot be computed directly using the 50 Hz phase measurements following the procedures introduced in Section 3.1.2, as there are not enough samples to estimate the PSD curves within an interval of 1 second. To address this issue, an alternative approach is proposed which exploits the relationship between the $Phi60$ and p indices. Based on the scintillation data introduced in the previous section, the p index in relation to the $Phi60$ captured on GPS L1 C/A signal at each station is shown in Figure 5.7. It can be seen in all the panels that with the increase in $Phi60$, the p value first roughly increases and then maintains within a range of around 2 to 3.5.

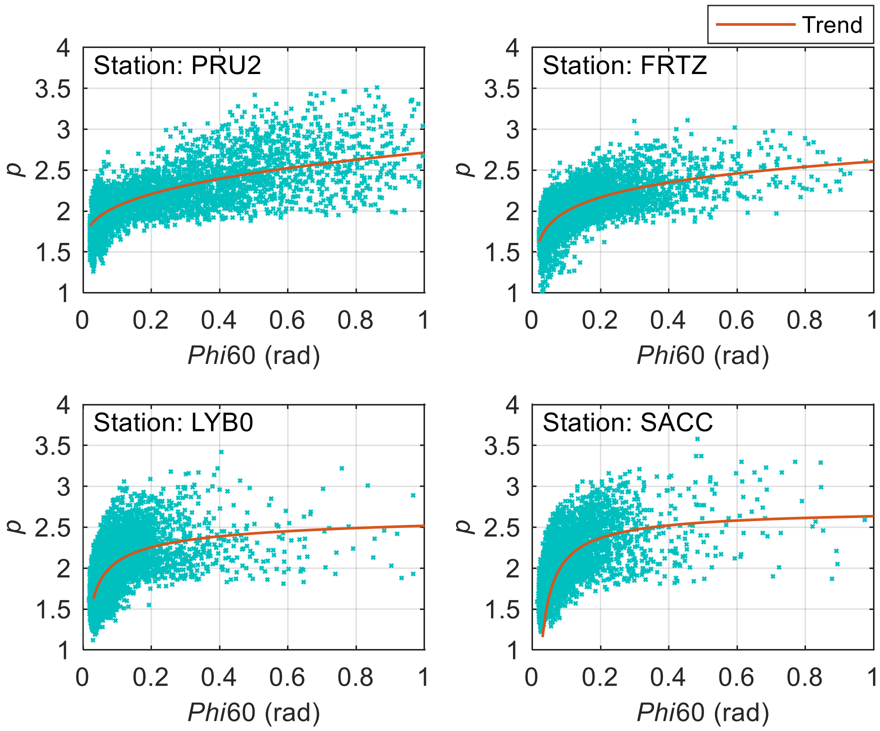

Figure 5.7 Variation of the p index in relation to $Phi60$ captured on GPS L1 C/A signal observed at PRU2, FRTZ, LYB0 and SACC stations during the data collection periods listed in Table 5.1

A power function given by

$$p_{(1\text{min})} = a * Phi60^{b} + c \tag{5.2}$$

is then used to fit the trend between the p and $Phi60$ indices, which is shown by the red lines in Figure 5.7. With a MATLAB curve fitting tool, which uses a nonlinear least-squares formulation and an iterative approach to fit power function models, the coefficients a, b and c at each station are then calculated, as listed in Table 5.2. In this study, it is assumed that the trend represented by Eq. (5.2) is still true between the corresponding 1-second scintillation indices. Thus, Eq. (5.2) is modified as

$$p_{(1\text{s})} = a * \left(\sigma_{\varphi}\right)^{b} + c \tag{5.3}$$

In Eq. (5.3), the 1-second σ_φ index can be measured using the 50 Hz phase measurements, given by

$$\sigma_\varphi = \sqrt{\langle\varphi_{det}^2\rangle_{1s} - \langle\varphi_{det}\rangle_{1s}^2} \tag{5.4}$$

where φ_{det} is the detrended phase measurements. With Eq. (5.3), (5.4) and the relationship between σ_φ, p and T expressed by Eq. (3.9), the 1-second p and T index can be finally estimated.

Table 5.2 Coefficients of the power function given by Eq. (5.2) calculated at PRU2, FRTZ, LYB0 and SACC station

Coefficient	a	b	c
PRU2	1.244	0.3251	1.47
FRTZ	3.81	0.07564	-1.206
LYB0	-0.2886	-0.4014	2.806
SACC	-1.099	-0.1378	3.703

It is worth mentioning that although the 1-second p index is only roughly estimated using Eq. (5.3), it is sufficiently accurate to be used in the calculation of the 1-second T index and the PLL phase jitter hereafter, because (1) the phase scintillation induced phase jitter estimated using Eq. (4.3) remains at a relatively stable value when the p index varies from 2 to 3, as shown in Figure 4.2; (2) according to the discussion of Figure 3.4, T index is not sensitive to the variation of the p value. As a result, a rough estimation of p is sufficient for the analysis in this study. Furthermore, it should be noted that the coefficients given in Table 5.2 are only applicable to the scintillation data sets analysed in this study. However, Eq. (5.3) can still be generally applied to other scintillation data sets at other stations, but the corresponding coefficients need to be re-estimated based on their observed scintillation indices.

Figure 5.8 shows an example of the 1-second phase scintillation indices estimated using the proposed approach, along with the variation of the detrended phase measurement φ_{det}

recorded at LYB0 station. In this minute, the 1-minute $Phi60$ reaches a very high value of 1.49 rad, however, the φ_{det} in the top panel remains relatively steady in the first 20 seconds, after which strong fluctuations are observed, leading to the increases in the estimated 1-second σ_{φ} and T values shown in the bottom panel.

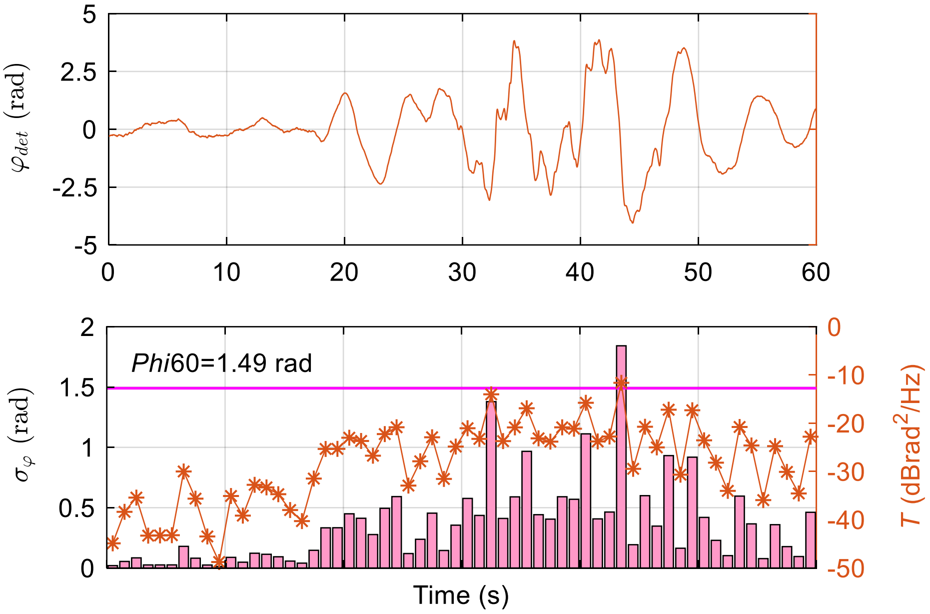

Figure 5.8 Variation of the detrended phase measurements φ_{det} (top) and the newly proposed 1-second scintillation indices (bottom) measured on GPS L1 C/A signal of PRN 16 at UTC 18:45 on DOY 243 at LYB0 station

Based on the analysis of Figure 5.6 and Figure 5.8, it is seen that the detrended signal intensity and the carrier phase measurements present large second-to-second variabilities. Increases in the estimated 1-second amplitude and phase scintillation index are observed following the signal intensity and phase fluctuations in each second. Thus, compared with 1-minute scintillation indices, the 1-second indices can better describe the signal fluctuations under scintillation in this analysis.

5.3 Relationship and comparison of 1-second and 1-minute scintillation indices

In this section, the relationship between the newly proposed 1-second index and the ISMR output 1-minute scintillation index is shown. The difference of using the 1-second and the 1-minute scintillation indices to describe the signal fluctuations under scintillation is also presented.

5.3.1 Relationship between 1-second and 1-minute scintillation indices

Following the approach described in Section 5.2.2, the 1-second amplitude and phase scintillation indices are estimated for all visible satellites observed at the four stations listed in Table 5.1. The percentage of the proposed 1-second scintillation indices of different levels as a function of the 1-minute $S4$ and $Phi60$ values at PRU2 and FRTZ stations is calculated, as shown in Figure 5.9. It is seen from the figure that the percentages of the 1-second indices with $S4^{-} < 0.3$ and $\sigma_{\varphi} < 0.3$ rad decrease gradually with the increase in the 1-minute index $S4$ and $Phi60$ at both stations, however, they still account for a significant percentage even when $S4$ or $Phi60$ is higher than 1.0. Compared with the 1-second scintillation index estimated at FRTZ station, there are more large values observed at PRU2 station, especially the 1-second phase scintillation index σ_{φ}. This agrees with the result shown in Figure 5.3 that the scintillation observed at PRU2 station is more severe and more frequent.

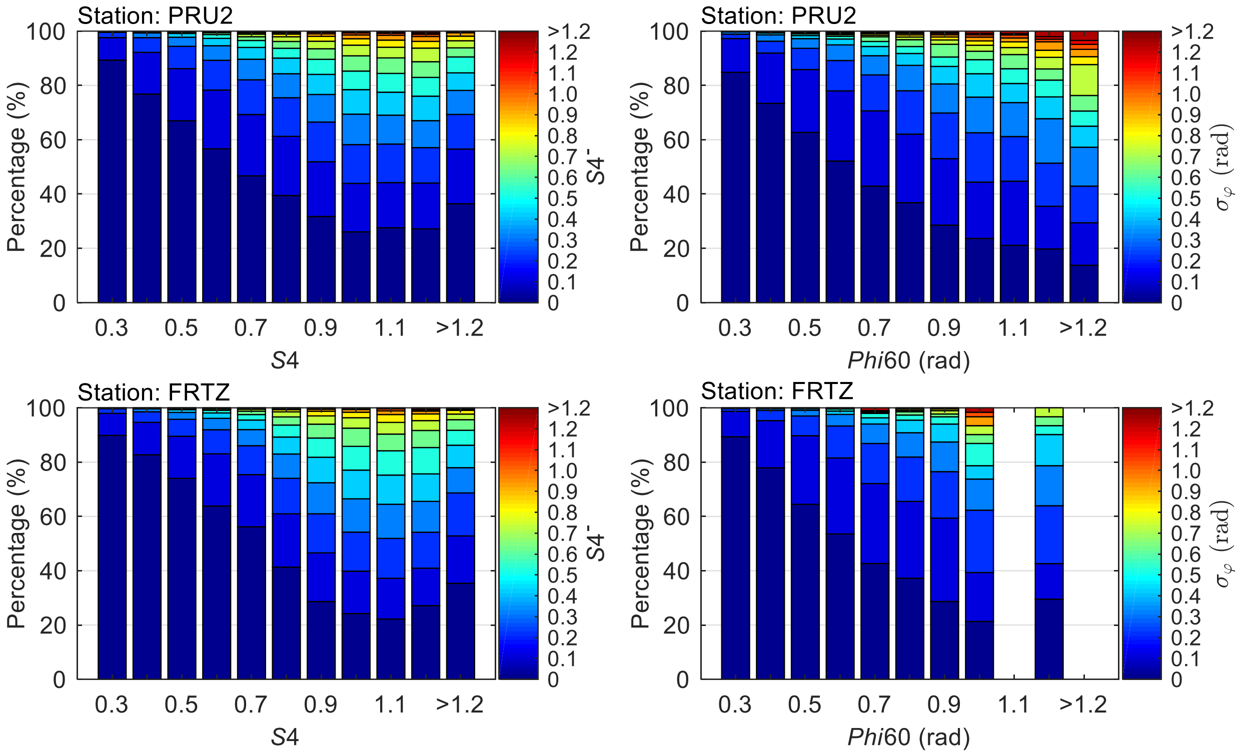

Figure 5.9 Percentages of the estimated 1-second amplitude and phase scintillation index of different levels as a function of 1-minute index $S4$ and $Phi60$ values measured on GPS L1 C/A signal observed at PRU2 (top) and FRTZ (bottom) stations from DOY 314 to 320 in 2014

Figure 5.10 similarly presents the percentage of the 1-second scintillation index in relation to the 1-minute one measured at LYB0 and SACC stations. As the amplitude scintillation occurrence observed at these two stations are very few, only the phase scintillation index is shown. It can be seen from the figure that the 1-second σ_φ lower than 0.3 rad accounts for large percentages in all $Phi60$ levels at both stations. Even when $Phi60$ is higher than 1.2 rad, around 60% of the 1-second σ_φ is still less than 0.4 rad. This indicates that most of the phase fluctuations are not severe within an interval of 1 second in the presence of the high latitude scintillation analysed in this work.

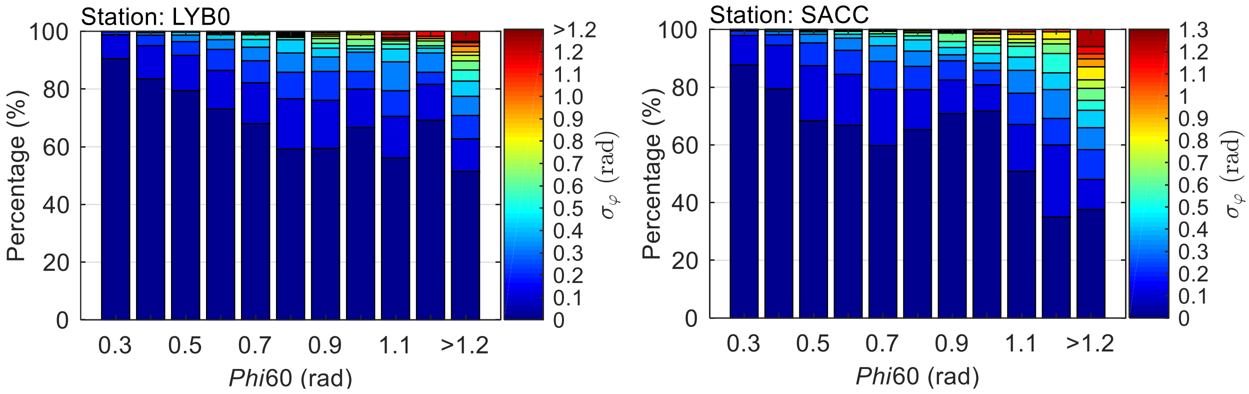

Figure 5.10 Percentages of the proposed 1-second phase scintillation index σ_φ of different levels as a function of the 1-minute index $Phi60$ measured on GPS L1 C/A signal observed at LYB0 (left) and SACC (right) stations from DOY 241 to 246 in 2019

5.3.2 Comparison of 1-second and 1-minute scintillation indices

In order to demonstrate the difference between the proposed 1-second scintillation indices and the 1-minute ones in describing the signal fluctuations caused by scintillation, the 1-second amplitude and phase scintillation indices are decimated to a sampling rate of 60 second and aligned with the time stamp of the 1-minute indices. The differences between the decimated 1-second $S4^-$, σ_φ, p and T and the 1-minute $S4$, $Phi60$, p and T, denoted as $\Delta S4^-$, $\Delta\sigma_\varphi$, Δp and ΔT, are calculated. The mean and the standard deviation of these differences on each day at each station are then estimated.

Figure 5.11 shows the mean and the standard deviation of the scintillation index differences calculated at PRU2 and FRTZ stations. As the left panels show, the standard deviations of $\Delta S4^-$, $\Delta\sigma_\varphi$ and ΔT are obviously larger on DOY 315, 316, 317, 319 and 320 at PRU2 station, when strong amplitude and phase scintillation is frequently observed. This indicates larger differences between the newly proposed 1-second indices and the 1-minute scintillation indices. On the other hand, obvious increases in the standard deviations of $\Delta S4^-$, $\Delta\sigma_\varphi$ and ΔT

at FRTZ station in the right panels are also observed on those days when scintillation occurs, however, they remain relatively stable compared with those calculated at PRU2 station. This is reasonable as the scintillation observed at FRTZ station is mostly at weak and moderate levels, the signal amplitude and phase fluctuations are relatively stable. Thus the 1-minute scintillation indices are closer to the 1-second ones. Furthermore, it is seen that the standard deviations of Δp at both stations are in the range of 0.15 to 0.22 over all the days. This is due to the rough estimation of the 1-second p using Eq. (5.3). Nevertheless, it has a very limited effect on the estimation of phase scintillation induced phase jitter, as explained in Section 5.2.2.

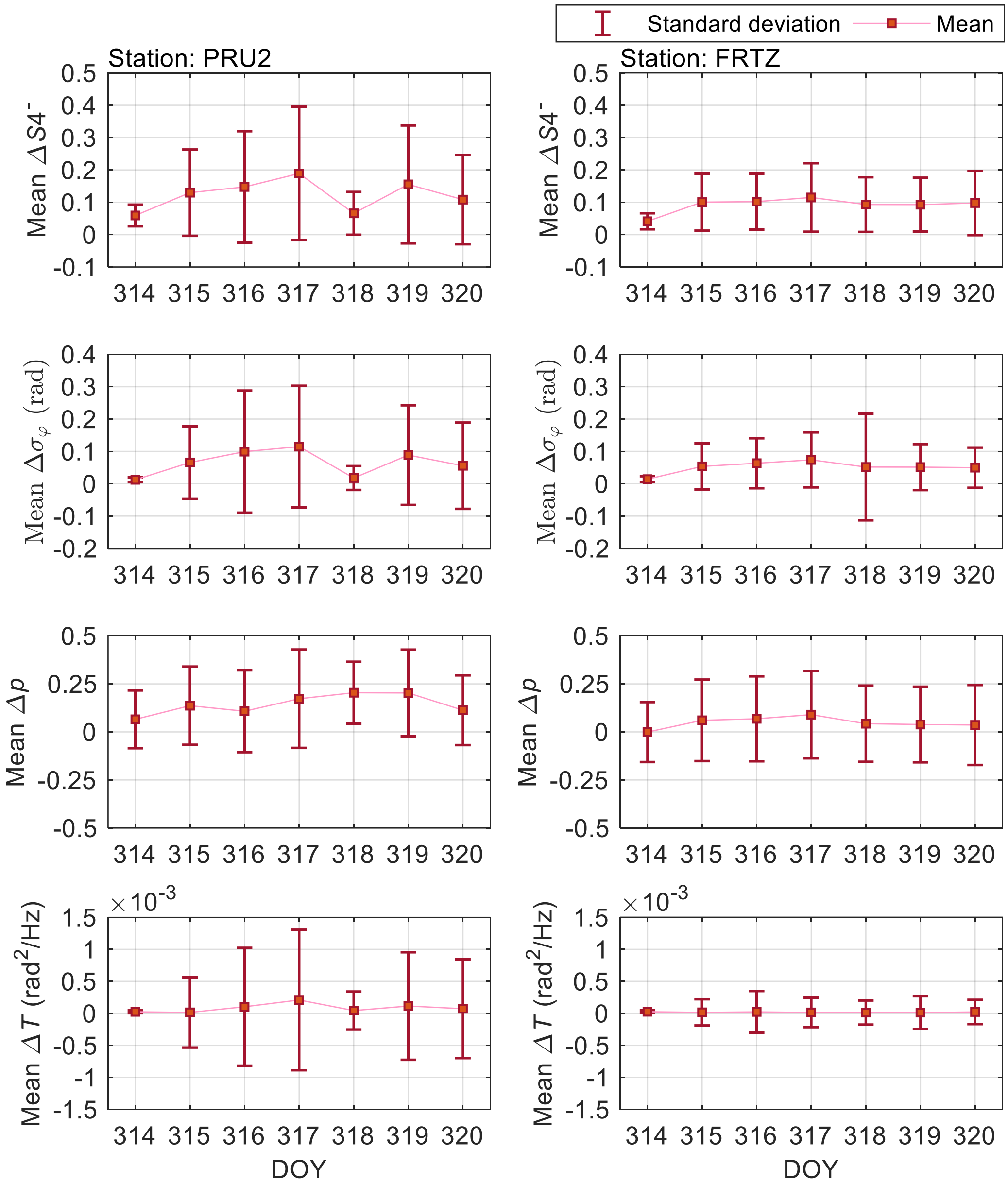

Figure 5.11 Mean and standard deviation of the differences between the proposed 1-second amplitude and phase scintillation indices and the ISMR output 1-minute ones from DOY 314 to 320 at PRU2 (left) and FRTZ (right) stations

Figure 5.12 shows the 1-second and 1-minute scintillation index differences measured at LYB0 and SACC stations. The amplitude scintillation index is again not shown. It can be seen that the standard deviations of $\Delta\sigma_{\varphi}$ and ΔT increase obviously on DOY 242, 243 and 244 at LYB0 station and on DOY 243, 244 and 246 at SACC station, while they tend to be smaller on DOY 241 and 246 at LYB0 station and DOY 241, 242 and 245 at SACC station when weak or no scintillation occurs. This is also due to the fact that when there is only weak or no phase scintillation, the phase fluctuations are generally stable, thus the 1-minute scintillation indices are comparable to the 1-second ones. However, under strong phase scintillation, large second-to-second variabilities in phase may appear, which results in the obvious differences between the 1-minute and 1-second indices. This also highlights the effectiveness of the proposed 1-second scintillation index in describing the signal fluctuations under scintillation. Moreover, it is seen that the standard deviations of Δp are more comparable over all the days at both stations. This is similar to the result shown in Figure 5.11 and is also due to the rough estimation of the 1-second p index.

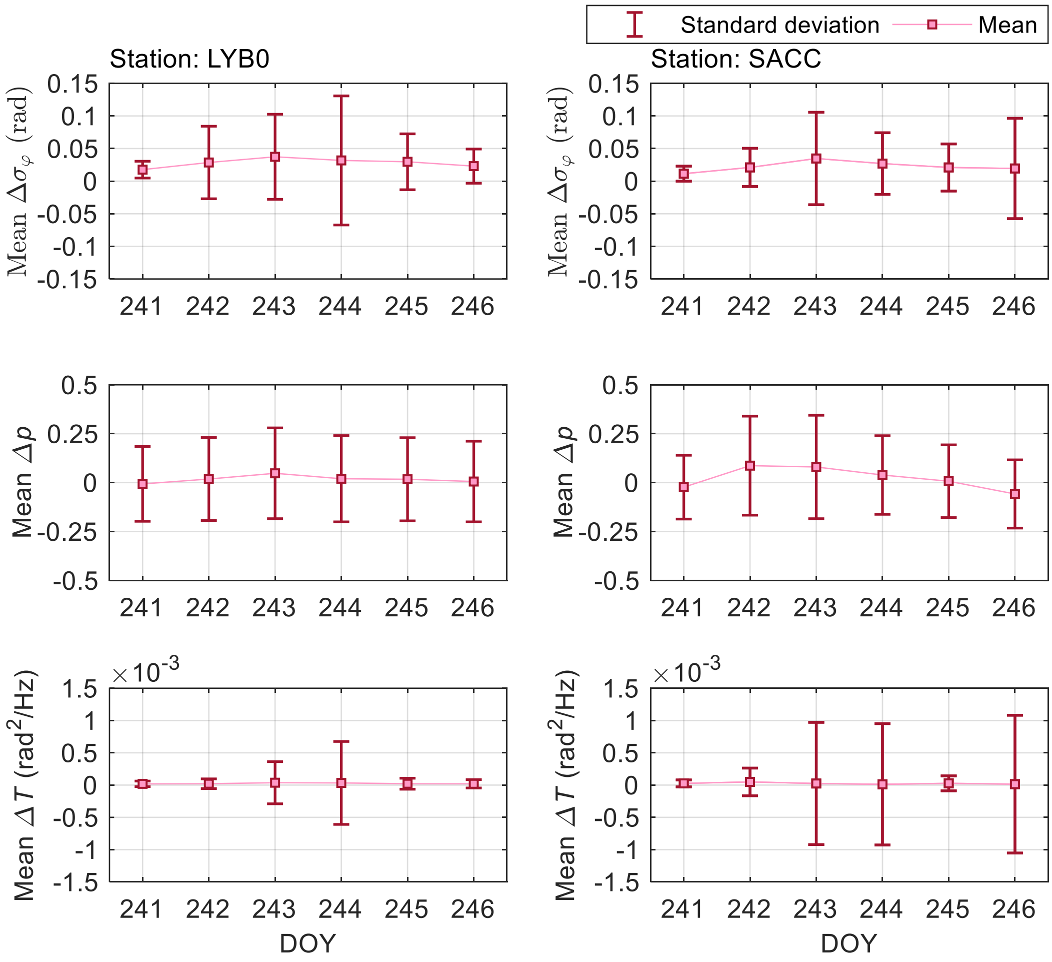

Figure 5.12 Means and standard deviation of the differences between the proposed 1-second phase scintillation indices σ_φ, p and T and the ISMR output 1-minute ones on DOY 241 to 246 at LYB0 (left) and SACC (right) stations

5.4 Scintillation effects on GNSS positioning

The effects of scintillation observed at low and high latitudes on the GNSS positioning accuracy are presented in this section. As the PPP processing can minimize the non-scintillation effects in the position estimation, it is applied in this analysis aiming to demonstrate the positioning errors caused by scintillation. The strategies of the PPP calculation are introduced next. Following the strategies, the positioning errors under the scintillation described in Section 5.2.1 are calculated and presented.

5.4.1 PPP models

The PPP in this study is performed using the University of Nottingham in-house POINT software as described in Section 2.3.3. In the PPP calculation, the code and carrier phase measurements on GPS L1 C/A and L2 P signals are used to form the ionosphere-free linear combinations. The IGS precise orbits and clock products estimated by the Centre for Orbit Determination in Europe (CODE) are used to constrain the PPP model. CODE Differential Code Biases (DCB) and satellite and receiver antenna corrections from IGS are implemented. The MWWL combinations, formed based on the code and carrier phase measurements on L1 C/A and L2 P signals, and the ionospheric TECRs are respectively calculated to detect cycle slips. The strategies of the PPP calculation are summarized in Table 5.3.

Table 5.3 Strategies for the PPP calculation

Items	Strategies
Observations	Ionosphere-free linear combination of the code and carrier phase measurements on GPS L1 C/A and L2 P signals
Default measurement noise	0.3 m for the code measurement and 0.01 cycle for the carrier phase measurement
Weighting strategies	(1) Satellite elevation weighting (Mohammed 2017): $\sigma_{obs} * \frac{1.001}{\sqrt{0.002001+\sin^2(E)}}$, where σ_{obs} is the default measurement noise, E is the satellite elevation; (2) Receiver phase and code jitter weighting
Observation sampling interval	60 second
Elevation mask angle	7°
Ionospheric delay	Ionosphere-free linear combinations
Satellite orbit and clock	IGS CODE products
Tropospheric delay	Troposphere estimated as a random walk process (0.05 m/$\sqrt{hour}$)
Receiver coordinate	Static and kinematic models
Model errors	DIA algorithm using Kalman filter post-fit residuals (Teunissen 1998)
Others	Absolute phase centre variation (PCV) correction, ocean tide loading (OTL) correction, DCB correction

It is worth mentioning that in this analysis, the precise coordinates of the receivers are estimated using the static PPP model based on the code and carrier phase measurements collected on the first day at each station, when no obvious scintillation is observed. These coordinates are set as the precise reference coordinates. The positioning errors in the north, east and up directions are then obtained by comparing the coordinates estimated through the kinematic PPP process using a satellite elevation weighting strategy against those precise coordinates. To analyse the positioning accuracy improvements with scintillation mitigation approaches, the root mean squares (RMSs) of the positioning errors are calculated in this thesis. This method is widely used in scintillation mitigation studies. On the other hand, the positioning precisions are estimated by calculating the standard deviations of the positioning results. The improvements in positioning precisions are also presented when the scintillation mitigation approaches are applied.

5.4.2 Positioning errors under scintillation

Following the strategies summarised in Table 5.3, PPP is performed at the four stations listed in Table 5.1. Figure 5.13 shows an example of the positioning errors under the scintillation effects observed at PRU2 station on DOY 316 in 2014. It can be seen from the figure that when there is no obvious scintillation, the positioning errors in the east (ΔE), north (ΔN) and up (ΔU) directions are generally less than 0.2 m after the convergence process. By contrast, when strong scintillation occurs from around UTC 23:40 to 02:00, the positioning errors increase significantly and can be greater than 1.0 m. It can be seen that the positioning errors in the up direction show more prominent fluctuations, indicating that the positioning accuracy in this direction is more susceptible to the effects of scintillation.

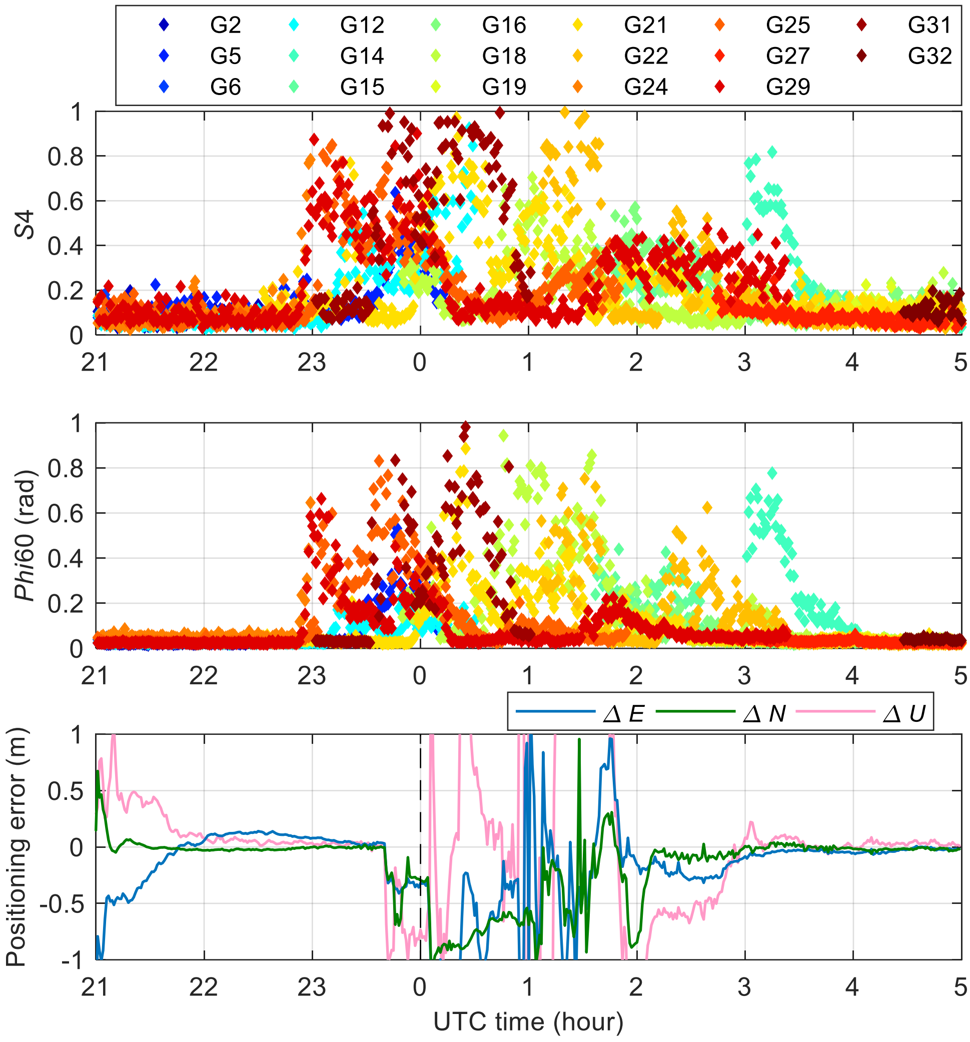

Figure 5.13 Example of the low latitude scintillation effects on the GNSS positioning errors observed at PRU2 station from UTC 21:00 12 November to 05:00 13 November in 2014. The panels are: the amplitude and phase scintillation captured on GPS L1 C/A signal on all the visible satellites (top and middle); positioning errors in the east, north and up directions obtained by comparing the kinematic PPP results against the reference coordinates (bottom)

Figure 5.14 presents the positioning errors as well as the scintillation occurrence observed on DOY 243 in 2019 at SACC station. From UTC 06:00 to 09:00 and 12:00 to 13:00, when strong scintillation occurs, the positioning errors in the east, north and up directions each increase to different extents, with the error in the up direction relatively larger, in agreement with the result shown in Figure 5.13.

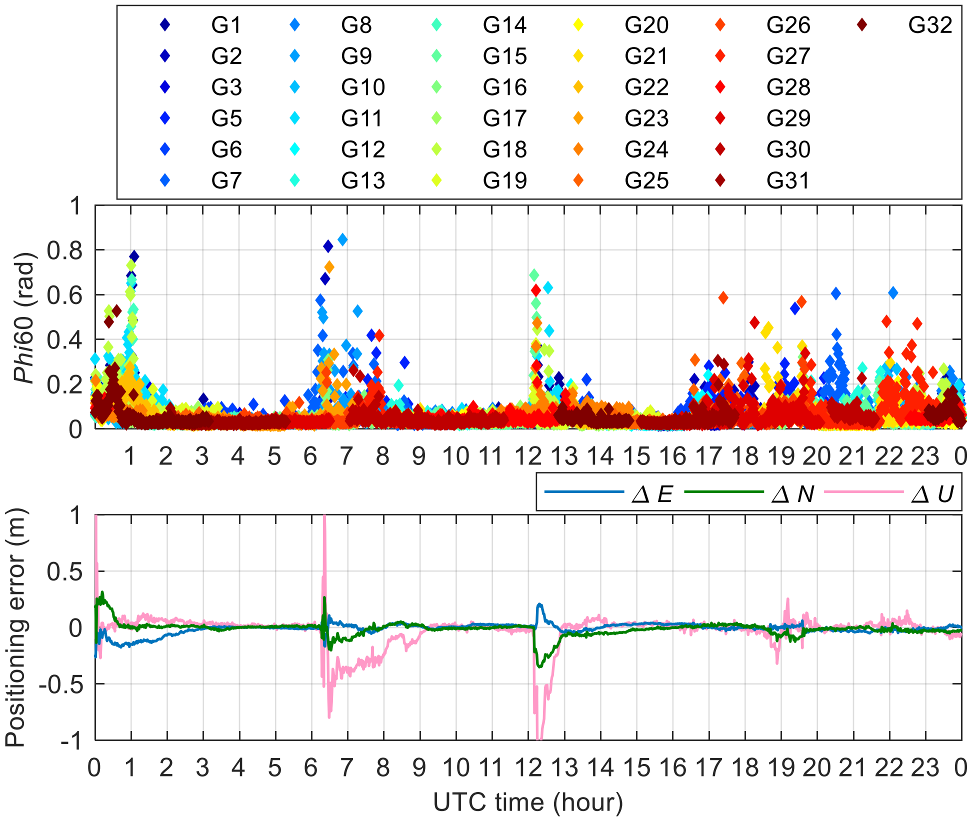

Figure 5.14 Example of the high latitude scintillation effects on the GNSS positioning errors observed at SACC station from UTC 00:00 to 23:59 on 31 August 2019. The panels are: the phase scintillation captured on GPS L1 C/A signals on all the visible satellites (top); positioning errors in the east, north and up directions obtained by comparing the kinematic PPP results against the reference coordinates (bottom)

To further demonstrate the scintillation effects on the positioning accuracy at each station, the RMS of the 3D positioning errors obtained by the kinematic PPP on each day is computed. Due to the PPP convergence process, the first 1 hour of the positioning error time series is not considered. Figure 5.15 shows the daily 3D positioning errors at PRU2 and FRTZ stations. As the left panel shows, large positioning errors are observed on DOY 315 to 317, 319 and 320 at PRU2 station, when strong amplitude and phase scintillation are frequently observed as shown in the left panels of Figure 5.3. The positioning error at this station peaks on DOY316, reaching 1.31 m. By contrast, it is relatively smaller at FRTZ station in the right panel (note that the y axis has a different scale). When there is no scintillation on DOY 314, the positioning achieves an accuracy of 0.07 m, worsening to 0.21 m on DOY 317 and 0.24 m on DOY 320, respectively. The difference in the positioning accuracy between PRU2 and FRTZ stations is mainly due to the scintillation occurrence and its different levels. The scintillation observed at PRU2 station is much stronger and more frequent, as shown in Figure 5.3.

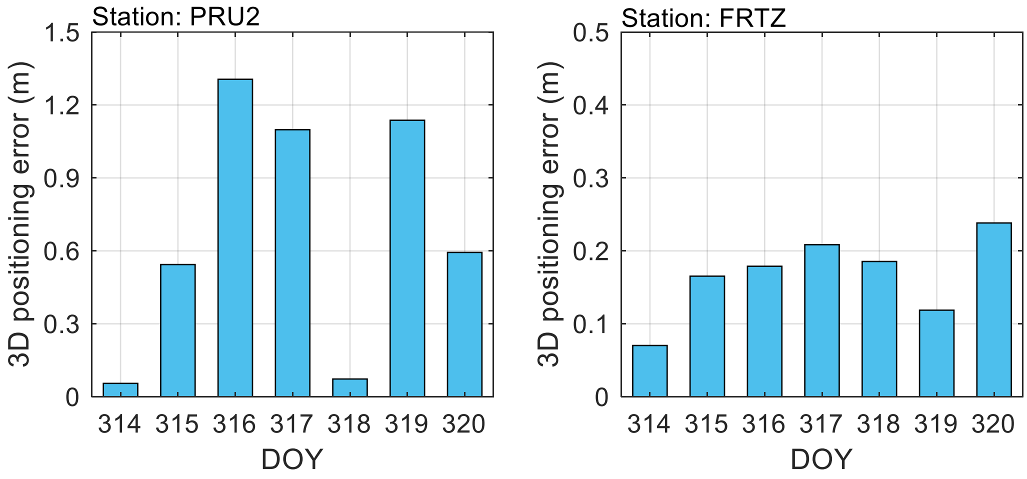

Figure 5.15 RMS of the 3D positioning errors from DOY 314 to 320 in 2014 at PRU2 and FRTZ stations. The positioning errors are obtained by performing kinematic PPP with an elevation weighting strategy

Figure 5.16 shows the positioning errors from DOY 241 to 246 in 2019 at LYB0 and SACC stations. It can be seen that the daily RMSs of 3D PPP errors are less than 0.05 m when there is only weak or no scintillation on DOY 241 and 246 at LYB0 station and on DOY 241 and 245 at SACC station. However, when strong phase scintillation occurs on DOY 244 at LYB0 station and on DOY 246 at SACC station, the positioning errors increase to 0.21 m and to 0.87 m, respectively, which are more than 5 times higher than those on the weak or no scintillation days. It is interesting to note that the PPP errors peak on different days between these two stations. The maximum positioning error occurs on DOY 244 at LYB0 station, while on DOY 246 at SACC station, although the geomagnetic activity is quiet on this day according to the Kp index shown in Figure 5.2. This may be due to the varying responses of the ionosphere at different high latitude regions to the geomagnetic storm, which is worth analysing further in future studies.

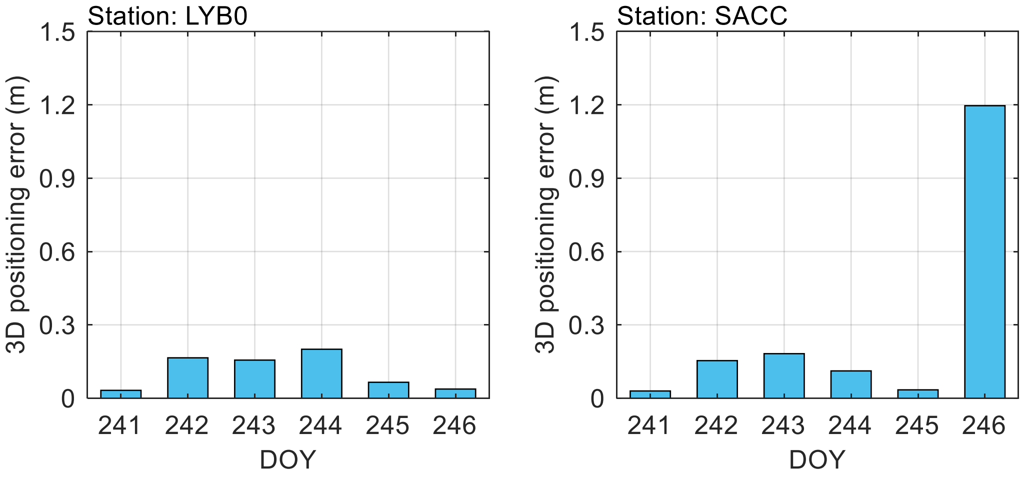

Figure 5.16 RMS of the 3D positioning errors from DOY 241 to 246 in 2019 at LYB0 and SACC stations. The positioning errors are obtained by performing kinematic PPP with an elevation weighting strategy

5.5 Scintillation mitigation on positioning errors using 1-second scintillation indices

The mitigation of scintillation effects on GNSS positioning errors is presented in this section. By introducing the newly proposed 1-second scintillation indices into the receiver phase and code jitter estimation models described in Section 4.1.1, the 1-second jitter is estimated and subsequently used to modify the least square stochastic models in positioning following the approach introduced in Section 5.1.1. The improvements in the positioning accuracy achieved at the low and high latitude stations are presented next.

5.5.1 Scintillation mitigation at PRU2 and FRTZ stations

The kinematic PPP is recalculated at PRU2 and FRTZ stations using the configurations summarized in Table 5.3, however, with a phase and code jitter weighting strategy instead of the elevation based weighting. In order to compare the performance of the 1-minute scintillation index and the newly proposed 1-second ones in scintillation mitigation, the phase and code jitter are estimated using both of these two types of indices, respectively. Firstly, the 1-minute phase and code jitter is calculated directly using the 1-minute scintillation indices and the 1-minute averaged $C/N0$ values output by the ISMRs. Secondly, the 1-second jitter is estimated using the proposed 1-second scintillation indices but down-sampled to a rate of 60 second to align with the time stamp of code and carrier phase measurements. Those two types of jitter values are then used respectively to modify the stochastic models in the kinematic PPP calculation at each station.

Figure 5.17 shows the positioning errors in the up direction when performing kinematic PPP using elevation, 1-minute and 1-second jitter weighting strategies, respectively, from DOY 314 to 320 in 2014 at PRU2 and FRTZ stations. As the figure shows, the 1-minute and 1-second jitter weighting can generally achieve better positioning accuracies in the up direction compared with those when an elevation weighting strategy is used. The spikes in the positioning errors are reduced to different extents with the jitter weighting strategy, especially on DOY 315 and 316 at PRU2 station and on DOY 315 to 317 at FRTZ station, when more amplitude scintillation is observed. However, large positioning errors still remain on DOY 316 and 317 at PRU2 station in the top panels even when the jitter weighting strategy is used. This may be due to the fact that the scintillation occurrence on this day is too strong, thus the GNSS observations used for positioning are seriously disrupted, making it more difficult to achieve a good positioning accuracy.

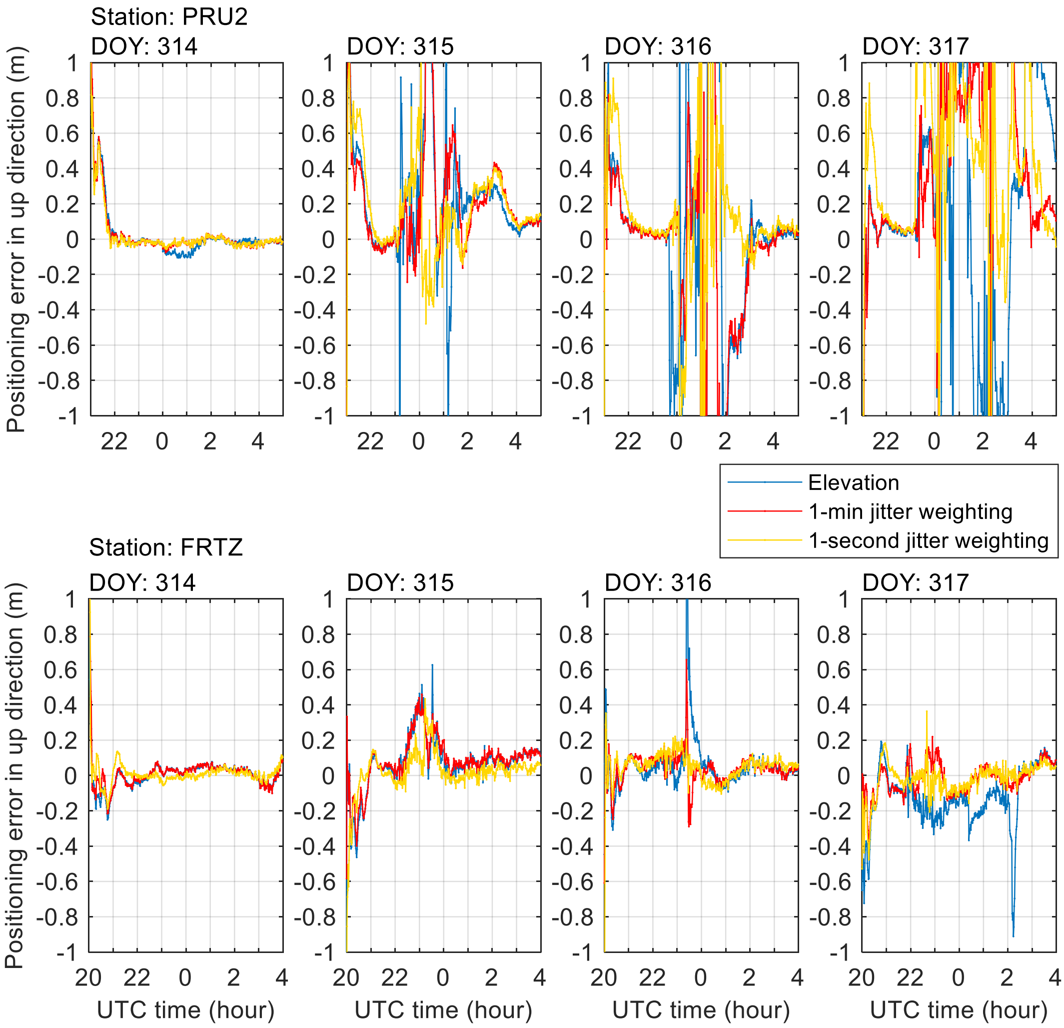

Figure 5.17 Variation of the positioning errors in the up direction from DOY 314 to 317 in 2014 at PRU2 (top) and FRTZ (bottom) stations. The positioning errors are obtained by performing the kinematic PPP respectively using elevation, 1-minute and 1-second phase and code jitter weighting strategies

Figure 5.18 presents the horizontal positioning error ΔH obtained at PRU2 and FRTZ stations, which is calculated by

$$\Delta H = \sqrt{(\Delta E)^2 + (\Delta U)^2} \tag{5.5}$$

As the figure shows, when the jitter weighting strategy is used, the horizontal positioning errors are mostly mitigated with respect to using an elevation weighting, while the 1-second jitter weighting generally entails greater improvement in the positioning accuracy, e.g., on DOY 315 and 316 at both stations. Moreover, it is also seen that the positioning errors on DOY 316 and 317 at PRU2 station are still large even when the 1-second jitter weighing strategy is applied, which is similar to the result shown in Figure 5.17.

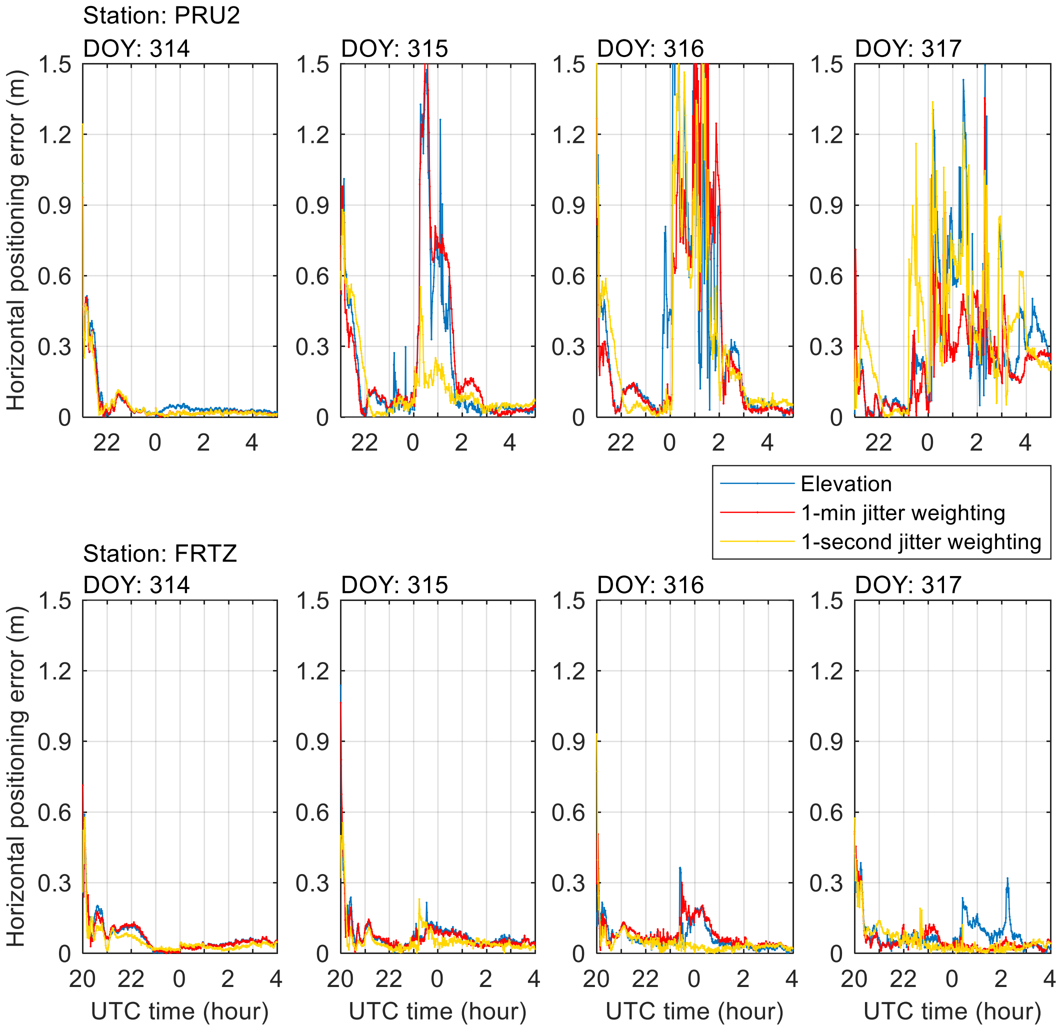

Figure 5.18 Variation of the positioning errors in the horizontal direction from DOY 314 to 317 in 2014 at PRU2 (top) and FRTZ (bottom) stations. The positioning errors are obtained by performing kinematic PPP respectively using elevation, 1-minute and 1-second phase and code jitter weighting strategies

The RMSs of the 3D positioning errors obtained with the three different weighting strategies at PRU2 and FRTZ stations are calculated, as shown in Figure 5.19. It can be seen that when the 1-minute jitter weighting strategy is used, the positioning errors are reduced by different extents at both stations. Relatively larger decreases are seen on DOY 319 at PRU2 station and on DOY 317 and 320 at FRTZ stations, while on DOY 315 and 320 at PRU2 station and on

DOY 315 and 318 at FRTZ station, only slight improvements are achieved in the positioning accuracy. However, when the 1-second jitter weighting strategy is used, a better positioning accuracy is generally achieved. On those days when the 1-minute jitter weighting achieves a lower improvement, the 1-second one can reduce the positioning errors even further. This indicates a better performance when exploiting the 1-second phase and code jitter in the scintillation mitigation.

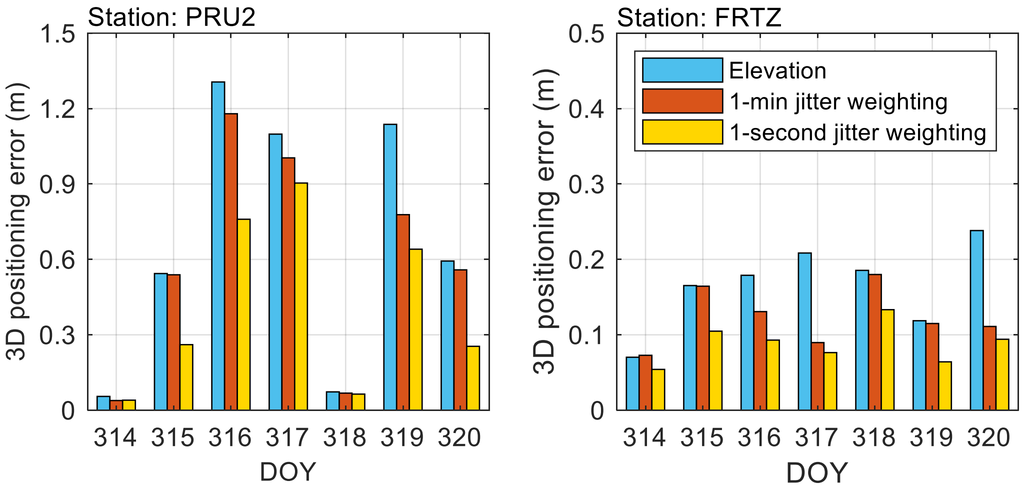

Figure 5.19 RMSs of the 3D positioning errors obtained by performing kinematic PPP respectively using elevation, 1-minute and 1-second phase and code jitter weighting strategies from DOY 314 to 320 in 2014 at PRU2 (left) and FRTZ (right) stations

Table 5.4 summarizes the percentage improvements in the 3D positioning errors when using phase and code jitter weighting strategies compared with using an elevation weighting corresponding to the results shown in Figure 5.19. As it can be seen from the table, the 1-minute and 1-second jitter weighting strategies both help to mitigate the positioning errors generally, however, the greatest improvements are mostly observed when the latter is used. An improvement of 57% and 63% are respectively achieved with the 1-second jitter weighting on DOY 320 at PRU2 station and on DOY 317 at FRTZ station.

Table 5.4 Percentage improvements in the 3D positioning errors when using receiver phase and code jitter weighting strategies in positioning with respect to using an elevation weighting strategy from DOY 314 to 320 in 2014 at PRU2 and FRTZ stations

Station	Weighting strategy	RMS of 3D positioning error improvement						
		314	315	316	317	318	319	320
PRU2	1-minute jitter	30%	1%	10%	9%	7%	32%	6%
	1-second jitter	27%	52%	42%	18%	12%	44%	57%
FRTZ	1-minute jitter	-4%	1%	27%	57%	3%	3%	53%
	1-second jitter	23%	37%	48%	63%	28%	46%	61%

It should be noted that on DOY 317 at PRU2 station, the positioning errors are not greatly reduced by using either the 1-minute or the 1-second weighting strategy. This may be caused by the extremely strong scintillation observed on this day, which may contribute to frequent losses of GNSS measurements, thus the degraded positioning accuracy even when the mitigation approach is applied. Therefore, it is necessary to develop an alternative tool for scintillation mitigation, which could be the focus of the follow-on work.

5.5.2 Scintillation mitigation at LYB0 and SACC stations

The scintillation mitigation by exploiting the proposed 1-second scintillation indices at LYB0 and SACC stations is presented in this section. Figure 5.20 shows the positioning errors in the up direction obtained when performing kinematic PPP using elevation, 1-minute and 1-second phase and code jitter weighting strategies from DOY 243 to 246. It is clear that compared with the elevation weighting strategy, the 1-minute and 1-second jitter weighting can generally achieve better positioning accuracies in the up direction, especially on DOY 243 and 244 at LYB0 station and on DOY 243, 244 and 246 at SACC station when phase scintillation is frequently observed, as shown in Figure 5.5.

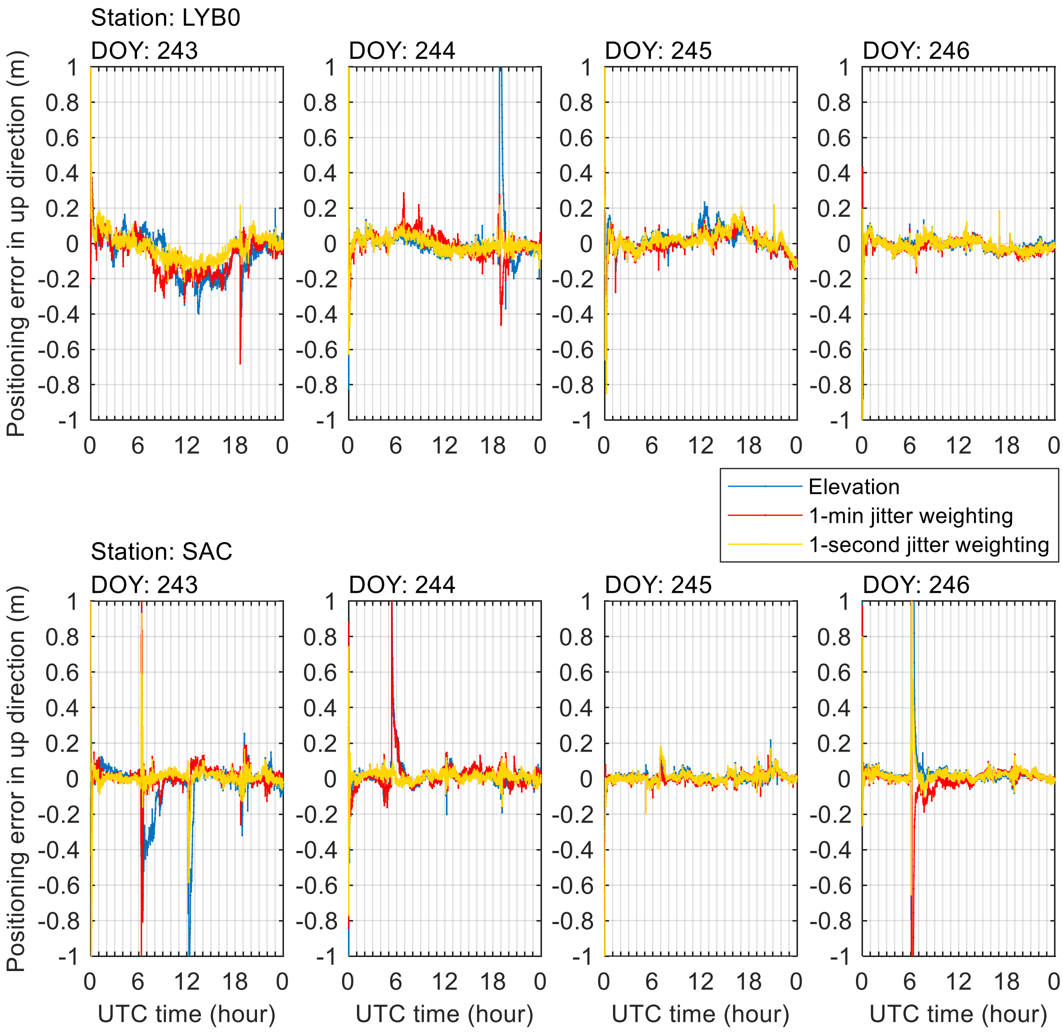

Figure 5.20 Variation of the positioning errors in the up direction from DOY 243 to 246 in 2019 at LYB0 (top) and SACC (bottom) stations. The positioning errors are obtained by performing kinematic PPP respectively using elevation, 1-minute and 1-second phase and code jitter weighting strategies

The horizontal positioning errors obtained through kinematic PPP with elevation, 1-minute and 1-second jitter weighting are shown in Figure 5.21. When an elevation weighting is used, large increases and spikes are observed in the horizontal positioning errors on DOY 243 and 244 at LYB0 station and on DOY 243, 244 and 246 at SACC station, while these spikes are mostly reduced by applying the jitter weighting strategy.

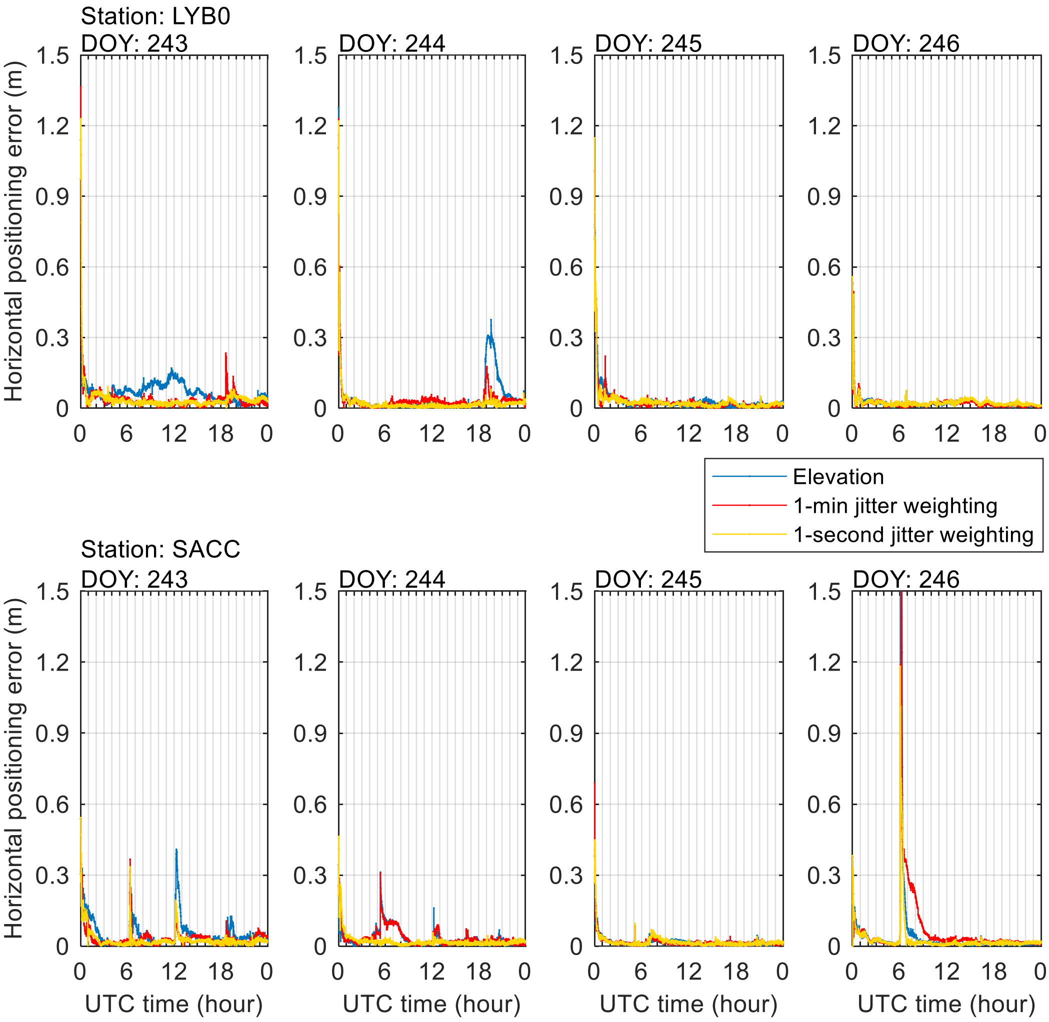

Figure 5.21 Variation of the positioning errors in the horizontal direction from DOY 243 to 246 in 2019 at LYB0 (top) and SACC (bottom) stations. The positioning errors are obtained by performing kinematic PPP respectively using elevation, 1-minute and 1-second phase and code jitter weighting strategies

The RMSs of the 3D positioning errors with the three different weighting strategies at LYB0 and SACC stations are presented in Figure 5.22. As the figure shows, the PPP errors are greatly reduced when the jitter weighting strategies are applied. On DOY 244 at LYB0 station, the positioning error is reduced respectively to 0.08 m and 0.04 m by the 1-minute and the 1-second jitter weighting strategy, manifesting great improvements with respect to the elevation weighting strategy. Additionally, although the 3D positioning error on DOY 246 at SACC station is only reduced to 0.40 m by the 1-minute jitter weighting, the 1-second one reduces the error to 0.21 m with an improvement of 83% in the positioning accuracy.

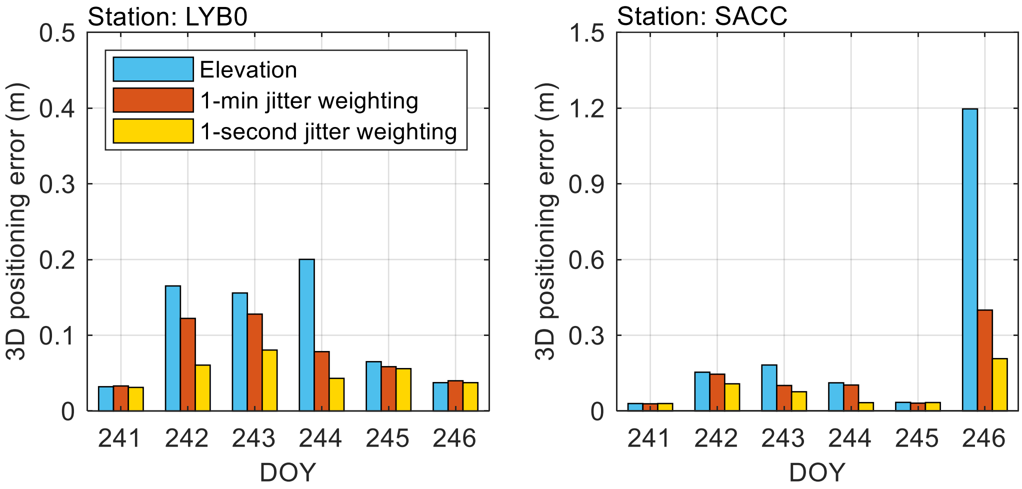

Figure 5.22 RMSs of the 3D positioning errors obtained by performing kinematic PPP respectively using elevation, 1-minute and 1-second phase and code jitter weighting strategies from DOY 241 to 246 in 2019 at LYB0 (left) and SACC (right) stations.

Table 5.5 summarizes the percentage improvements in the 3D positioning errors using the phase and code jitter weighting compared with the elevation weighting corresponding to the results shown in Figure 5.22. As it can be seen, both the 1-minute and 1-second jitter weighting strategies can improve the positioning accuracy under scintillation, while the 1-second jitter weighting can achieve a better improvement, which is similar to the results shown in Table 5.4. Consequently, it can be concluded that the 1-second jitter weighting strategy performs better in the positioning error mitigation compared with the 1-minute one under the scintillation analysed in this study.

Table 5.5 Improvements in the 3D positioning errors when using receiver phase and code jitter weighting strategies in positioning with respect to using an elevation weighting strategy from DOY 241 to 246 in 2019 at LYB0 and SACC stations

Station	Weighting strategy	RMS of 3D positioning error improvement					
		241	242	243	244	245	246
LYB0	1-minute jitter	-3%	26%	18%	61%	10%	-7%
	1-second jitter	3%	63%	48%	78%	14%	0%
SACC	1-minute jitter	3%	5%	45%	8%	9%	67%
	1-second jitter	0%	30%	58%	70%	2%	83%

It is noticed that on DOY 241 and 246 at LYB0 station, as well as on DOY 314 at FRTZ station, the positioning errors when using the 1-minute jitter weighting are slightly higher than using an elevation weighting, however the difference is less than 0.005 m and is ignorable. Additionally, when only weak to moderate or no scintillation is present, e.g., on DOY 241, 245 and 246 at LYB0 station and DOY 241 and 245 at SACC station, comparable performance is observed when the 1-second and the 1-minute jitter weighting strategies are used. This may be due to the fact that under weak or moderate scintillation, the signal fluctuations are relatively stable, thus the 1-minute scintillation indices are comparable to the 1-second ones as shown in Figure 5.12. Therefore, the 1-minute jitter may equally represent the measurement noise level, which results in the comparable positioning accuracy. Furthermore, it is seen that although the 1-second jitter weighting strategy significantly mitigates the strong scintillation effects on positioning, it can barely achieve a positioning accuracy comparable to the non-scintillation days. As a result, scintillation mitigation approaches must be further improved. This should be the focus of follow-on work.

5.6 Positioning precision improvements using 1-second scintillation indices

This section presents the improvements in positioning precisions with the implementation of 1-second scintillation indices in phase and code jitter weighting strategies. The precisions of positioning are obtained by calculating the standard deviation of the estimated positions, which are different from the positioning accuracy that is obtained by measuring the discrepancy of the estimated coordinates with respect to the precise reference coordinates.

Figure 5.23 shows the precisions of the positioning results in horizontal directions at PRU2 station on DOY 315 in 2014 and at LYB0 station on DOY 244 in 2019. The positions are estimated by performing kinematic PPP following the configurations summarized in Table 5.3, with elevation based, 1-minute and 1-second phase and code jitter weighting strategies, respectively. It can be seen from the figure that when the 1-minute jitter weighting strategy is implemented at PRU2 station in the left of the middle panels, the horizontal precision remains similar to the precision when an elevation based weighting is applied, as shown in the top left panel. However, with the 1-second jitter weighting, which exploits the newly proposed 1-second scintillation indices, the positioning result reaches the best precision, as the bottom left panel shows. On the other hand, the positioning precision at LYB0 station in the right panels increases apparently when the 1-minute and 1-second jitter weighting strategies are respectively used (note that the y axes have a different scale), while it reaches the highest when the latter is applied. The positioning accuracies, denoted by the green lines, are also shown in the figure, aiming to demonstrate the differences in relation to the positioning precision.

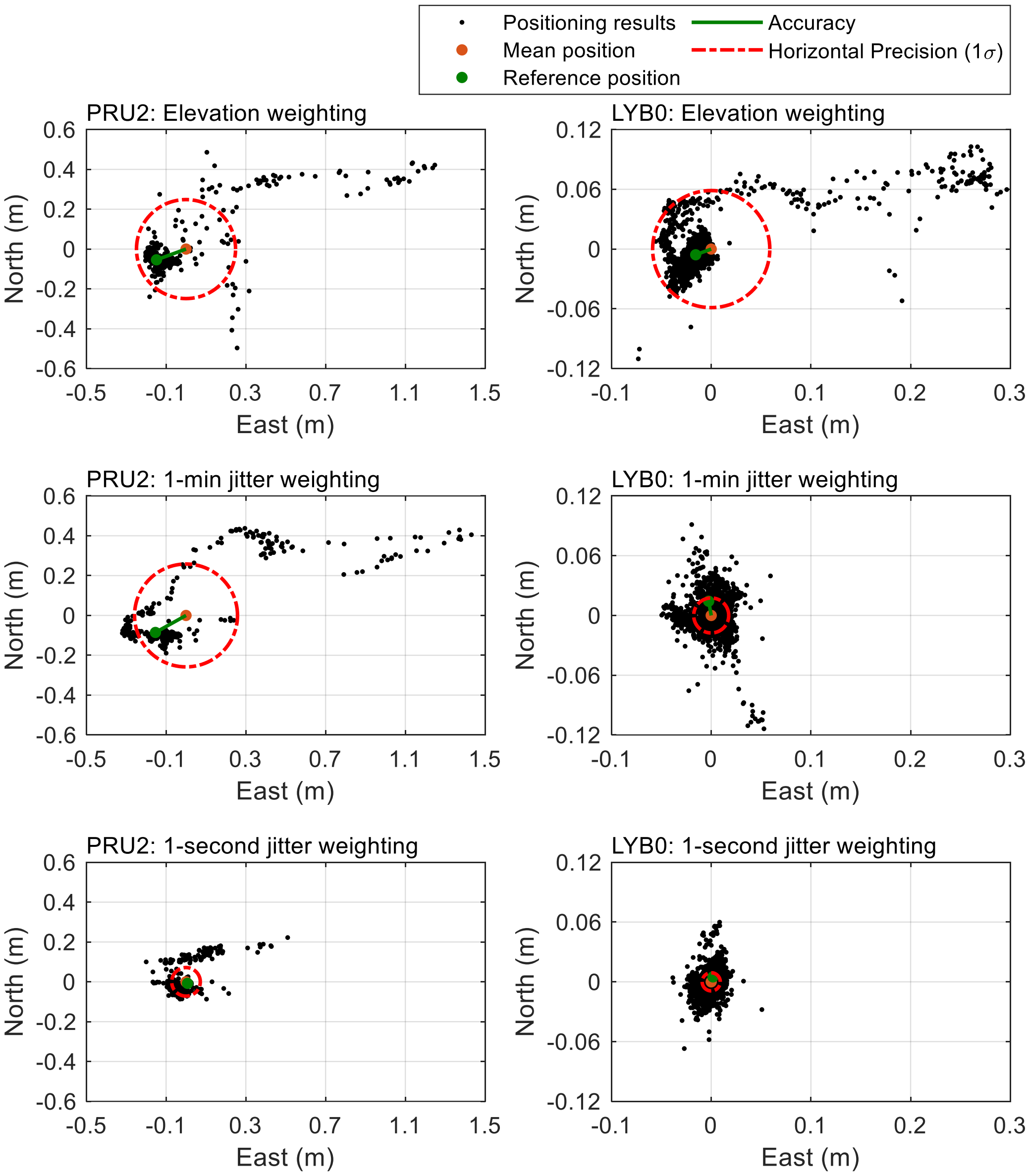

Figure 5.23 Positioning results and precisions in the horizontal directions at PRU2 stations on DOY 315 in 2014 (left) and at LYB0 stations on DOY 244 in 2019 (right). The positioning results are calculated by performing kinematic PPP respectively using elevation, 1-minute and 1-second phase and code jitter weighting strategies

The daily 3D positioning precisions at PRU2 and FRTZ stations from DOY 314 to 320 in 2014 and at LYB0 and SACC stations from DOY 241 to 246 in 2019 are shown in Figure 5.24. It should be noted that the y axes in the top left and bottom right panels are different from the rest. As the figure shows the positioning precision obtained with 1-minute and 1-second jitter weighting strategies is generally improved compared with that when an elevation weighting strategy is applied, particularly on these days when strong and frequent scintillation events are observed, for example, on DOY 315, 316, 317 and 319 at PRU2 station and on DOY 242, 243 and 244 at LYB0 station. Furthermore, the 1-second jitter weighting can mostly achieve the best improvement, which is similar to the results shown in Sections 5.5.1 and 5.5.2. However, compared with the positioning precision when there is only less or no scintillation, it is still markedly worse on these days when strong scintillation events are frequently observed even using the 1-second jitter weighting strategy. Thus, scintillation mitigation approaches should be improved to further increase the positioning precision under scintillation, which agrees with the conclusion in Section 5.5.2.

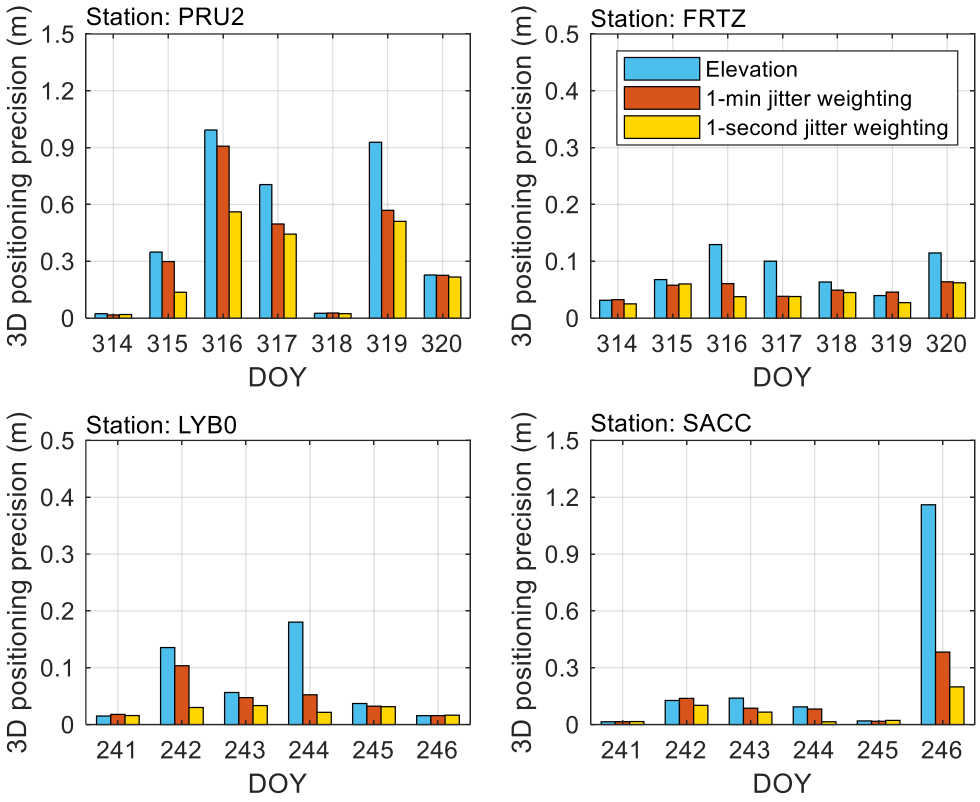

Figure 5.24 Comparison of 3D positioning precisions at PRU2, FRTZ, LYB0 and SACC stations by performing kinematic PPP respectively using elevation, 1-minute and 1-second phase and code jitter weighting strategies

5.7 Summary

This chapter introduced the approach to mitigate the scintillation effects on GNSS positioning exploited in this research work, as well as proposals to circumvent its limitations. To address one of its limitations, a new approach to calculate the 1-second amplitude and phase scintillation index is proposed which uses the 50 Hz signal intensity and carrier phase measurements logged by ISMRs. Based on the raw scintillation data collected at low and high latitude ISMR stations, the newly proposed 1-second scintillation index is calculated. Its relationship with the widely used 1-minute scintillation index measured by the ISMRs is provided. The adverse effects of scintillation on GNSS positioning are then presented by calculating the positioning errors using the kinematic PPP at the ISMR stations. With the proposed 1-second scintillation indices, the 1-second PLL phase jitter and DLL code jitter were calculated and further used to improve the stochastic models in positioning. The positioning accuracies and precisions calculated by performing the kinematic PPP respectively using the elevation, 1-minute and 1-second jitter weighting strategies are compared. Results show that both the 1-minute and 1-second jitter weighting help to improve the positioning accuracy and precision under scintillation. However, the latter performs even better than the former under strong scintillation. In the next chapter, the concept of receiver jitter maps and their potential use are provided. In particular, their application on scintillation mitigation for generic navigation receivers is explored, which will address the second limitation of the mitigation approach studied in this work.

6 Exploiting phase and code jitter maps to mitigate scintillation effects on GNSS positioning

As mentioned in Section 5.1.2, the approach to mitigate scintillation effects on GNSS positioning discussed in Aquino et al. (2009) has so far been used only in connection with ISMRs. To implement this approach to generic receivers, i.e., the receivers that are not able to measure and record scintillation data, this study exploits the phase and code jitter maps, which can be used to retrieve the jitter values of the corresponding signals used in the positioning solution. The procedure for the generation of receiver phase and code jitter maps are introduced first, followed by the jitter maps generated based on the dense ISMR network deployed as part of the CHAIN in the northern Canadian region. The potential uses of the jitter maps are described thereafter. The cycle slips experienced by the ISMRs and their relationship with the phase jitter extracted from the jitter maps are given subsequently, followed by the calculated positioning errors under scintillation, respectively, at stations equipped with ISMRs and stations equipped with generic receivers. The mitigation of scintillation on positioning by exploiting the phase and code jitter maps is shown. Errors induced by the mapping function used for the generation of phase jitter maps are studied finally.

6.1 Introduction to phase and code jitter maps

Receiver phase and code jitter maps are 2D contour plots of the interpolated vertical phase or code jitter in the ionospheric layer (Sreeja et al. 2011). It should be noted that in Sreeja et al. (2011), these maps are termed as “tracking jitter variance maps”. Due to the fact that “phase jitter” and “code jitter”, respectively, are used in this study to represent the noise levels at the

PLL and DLL outputs, as described in Section 2.2, the terminology of "phase jitter maps" and "code jitter maps" is used instead throughout this thesis. In this section, the procedure for the generation of the phase and code jitter maps and their potential applications are provided.

6.1.1 Generation of phase and code jitter maps

In the generation of the maps, the PLL phase jitter and DLL code jitter for each GNSS signal are measured and verticalized to an ionospheric layer by exploiting a suitable mapping function and interpolation technique. In this study, the phase and code jitters are calculated using the jitter estimation models developed in Conker et al. (2003), which are described in detail in Section 4.1.1. To ensure the accuracy of the interpolated jitter values, a large number of ionosphere pierce points (IPPs) is required, which depends on a dense network of ISMRs that is able to record raw scintillation data. The procedure for the generation of phase and code jitter maps, as shown in Figure 6.1, is summarized as follows:

(1) Measure the amplitude and phase scintillation indices at the current epoch T for all signals received by all the ISMRs that are used in the map generation

(2) Calculate the PLL phase jitter and the DLL code jitter for each signal using the jitter estimation models given by Eq. (4.1) to (4.6)

(3) Calculate the IPP latitude and longitude of all the satellite-to-receiver links according to the satellite and receiver locations as (Shone 2000)

$$\psi = \frac{\pi}{2} - E - \sin^{-1}\left[\frac{R_e}{R_e + h_{iono}}\cos(E)\right] \tag{6.1}$$

$$\phi_{IPP} = \sin^{-1}[\sin(\phi_r)\cos(\psi) + \cos(\phi_r)\sin(\psi)\cos(Az)] \tag{6.2}$$

$$\lambda_{IPP} = \lambda_r + \sin^{-1}\left[\frac{\sin[\psi]\sin(Az)}{\cos(\phi_{IPP})}\right] \tag{6.3}$$

where E and Az are the satellite elevation and azimuth, respectively. R_e is the radius of the Earth. h_{iono} is the chosen ionospheric height. ϕ_{IPP} and λ_{IPP} are respectively the geographic latitude and longitude of the IPP. ϕ_r and λ_r are respectively the latitude and longitude of the receiver

(4) Convert the slant phase and code jitters to the vertical equivalents at each IPP with an ionospheric mapping function, i.e.,

$$\sigma_V = \frac{\sigma_S}{M(E)} \tag{6.4}$$

where σ_V and σ_S are the verticalized and slant jitters, respectively. $M(E)$ is the mapping function, which is related to satellite elevation E

(5) By representing the vertical jitter at the IPPs and applying interpolation algorithms, generate the contour maps, namely, jitter maps

(6) Follow the same steps to generate the jitter maps at the next epoch $T + t_{update}$, where t_{update} is the updating interval of the jitter maps

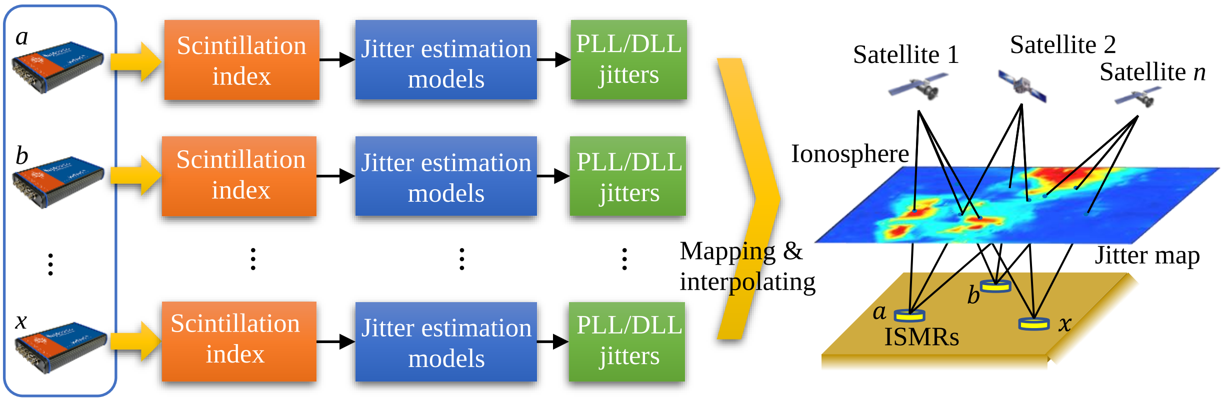

Figure 6.1 Procedure for the generation of the phase and code jitter maps by exploiting a network of ISMRs

The shortest updating time of the phase and code jitter maps is determined by the rate at which the scintillation data is available. In this study, the newly proposed 1-second scintillation indices described in Section 5.2.2 is exploited to generate the jitter maps, thus the jitter maps can be updated every second at the fastest. It should be noted that scintillation measurements recorded on satellites with elevations lower than 30° are also considered in the generation of these maps, which is different from the analysis in Section 3.3 where an elevation mask of 30°

is used to remove the non-scintillation effects, like multipath. This difference is due to the fact that the phase and code jitter maps constructed in this thesis actually contains all the interferences/effects that contribute to the phase and code jitter. Thus scintillation, as well as other effects, like multipath, are all integrated in the generation of these maps.

6.1.2 Potential uses of phase and code jitter maps

The potential uses of the phase and code jitter maps can be summarized as follows (Sreeja et al. 2011):

(1) These maps provide the overall receiver tracking conditions for users in the area under the current ionospheric environment, as the levels of phase and code jitters indicate the tracking performance of the PLL and DLL, respectively. Thus, the users can assess how the prevailing scintillation conditions could affect the receiver tracking performance

(2) These maps can play a role as a scintillation threat alert tool, as they can warn users of the potential issues to GNSS receivers caused by scintillation. For instance, if a signal passing through the jitter maps experiences a very large jitter value, the user receiver may be more likely to undergo loss of lock or cycle slip issues when tracking the signal, which may ultimately lead to a degradation of the positioning accuracy

(3) These maps can be exploited to mitigate GNSS positioning errors caused by scintillation. As mentioned in Section 5.1.2, the scintillation mitigation approach described in Aquino et al. (2009) is currently not used for generic receivers which are not able to measure the scintillation data that allows the estimation of the phase and code jitter. With the help of the jitter maps, a generic receiver can retrieve the jitter values for each signal passing through the maps, as shown in Figure 6.2.

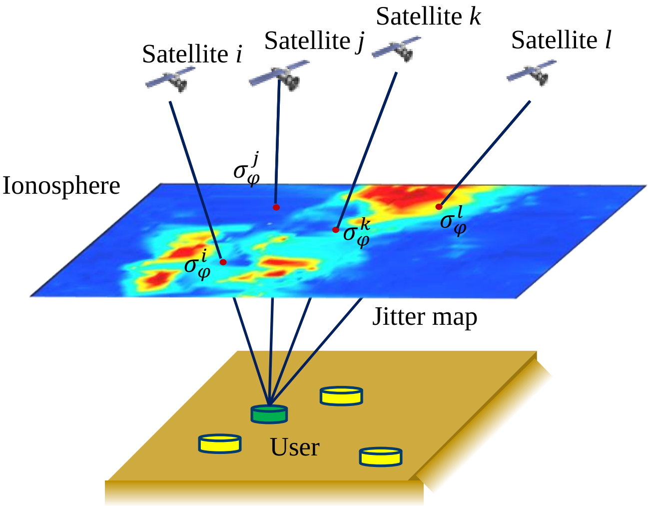

Figure 6.2 Illustration of retrieving jitter values from the phase and code jitter maps for GNSS signals received by the user receiver

It is worth mentioning that when applying the retrieved phase and code jitter values on generic receivers, these values can only be used as an approximation of the actual values for the generic receiver tracking loops, as the jitter maps are generated based on the ISMRs, which may have different loop configurations compared with the generic receivers. This approximation is reasonable, because: (1) according to the analyses in Section 4.2.2, the total phase jitter estimated for the PLL with different bandwidths and integration times shares a similar trend, indicating that different PLL configurations are similarly affected by scintillation, regardless of the fact that the jitter values may not be exactly the same under scintillation; (2) these jitter values mainly define the relative relationship between the precision of the measurements in the positioning stochastic model. Measurements more affected by scintillation will always result in a lower weight in the stochastic model and vice versa, in spite of the tracking loop configurations. Therefore, it is reasonable to apply these jitter values retrieved from the jitter maps on generic receivers. The approach to mitigate scintillation effects on GNSS positioning by exploiting the phase and code jitter maps is given in detail in Section 6.4.1.

6.2 Regional jitter maps generated in northern Canada

In this section, regional phase and code jitter maps are generated by exploiting the ISMRs deployed as part of the CHAIN network in the northern Canadian region. The scintillation data logged by the ISMRs and the scintillation occurrence are presented first. The jitter maps generated following the procedure introduced in Section 6.1.1 are shown thereafter.

6.2.1 Scintillation dataset

As mentioned in Section 6.1.1, the generation of the phase and code jitter maps requires a dense network of ISMRs, such as the CHAIN deployed in the northern Canadian region, as described in Section 2.4.3. Due to the fact that the two types of ISMRs, i.e., GSV4004B and PolaRxS Pro, equipped in the CHAIN network have different receiver tracking loop configurations, the phase and code jitter calculated based on the jitter estimation models given by Eq. (4.1) to (4.6) for the two types of receivers may differ even under the same levels of scintillation. Additionally, according to the analysis in Section 3.2.2, there are also obvious differences in the phase scintillation spectral indices measured by the two types of ISMRs. Therefore, it is not appropriate to mix the phase and code jitter values measured by the two types of ISMRs in the generation of the jitter maps. In this study, the scintillation data recorded by the twelve ISMR stations equipped with PolaRxS Pro receivers, as shown by the blue triangles in Figure 2.11, are used to conduct the analysis. The locations of these stations are listed in Table 2.2. The scintillation data was collected from 6 to 9 September 2017, during which a geomagnetic storm occurred. Figure 6.3 shows the variation of the geomagnetic activity levels over these four days. It can be seen that the geomagnetic activity, indicated by the yellow region between the AU, AL, AE and AO curves, increases gradually from 6 to 7 September and peaks on 8 September, when the strongest geomagnetic disturbance is observed from around UTC 12:00.

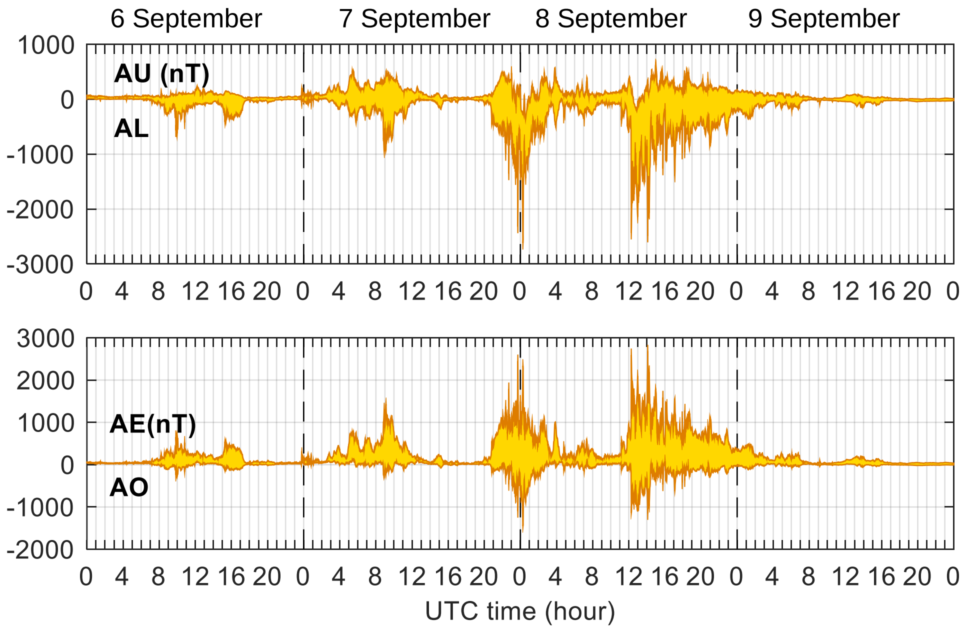

Figure 6.3 Variations of the geomagnetic activity indices AU, AL (top) and AE, AO (bottom) from 6 to 9 September 2017

Based on the raw scintillation data logged by the ISMRs, the 1-second amplitude and phase scintillation indices are calculated using the approach proposed in Section 5.2.2. Due to the fact that the phase scintillation at high latitudes is more severe and the amplitude scintillation is generally very weak, this section focuses only on phase scintillation occurrence. Figure 6.4 shows the occurrence of the phase scintillation with the 1-second index $\sigma_\varphi > 0.3$ rad, measured on the GPS L1 C/A signal from 6 to 9 September at the twelve ISMR stations. It can be seen that the total occurrence of scintillation over the four days varies significantly among each individual station. More scintillation is observed on 7 and 8 September when the geomagnetic activity levels are obviously increased, while the largest phase scintillation occurrence is observed on 8 September, when the geomagnetic activity reaches the peak. It is worth mentioning that only satellites with the elevation higher than 30° are considered in this analysis aiming to remove possible multipath effects.

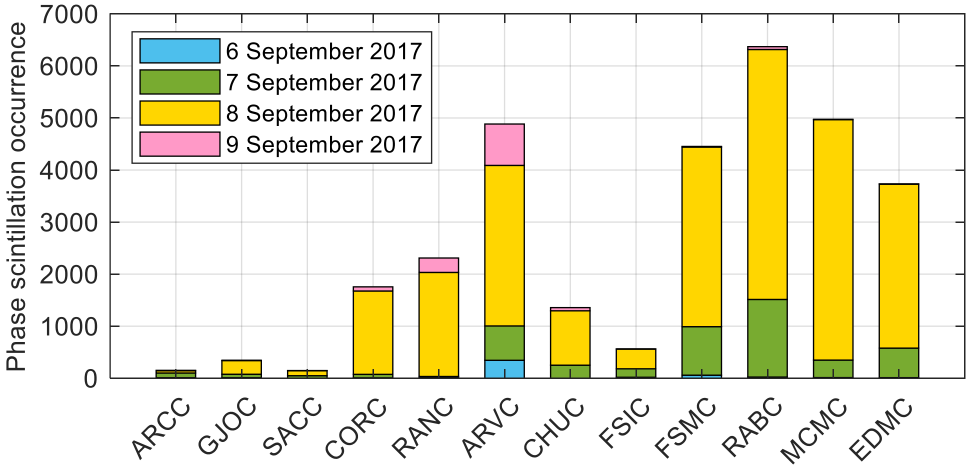

Figure 6.4 Occurrence of phase scintillation with the 1-second index $\sigma_\varphi > 0.3$ rad measured on the GPS L1 C/A signal at the twelve ISMR stations equipped with PolaRxS Pro receivers deployed as part of the CHAIN from 6 to 8 September 2017

The occurrence of the phase scintillation with the 1-second index $\sigma_\varphi > 0.3$ rad observed by all the twelve ISMRs as a function of the IPP latitude and UTC time from 6 to 9 September 2017 is shown in Figure 6.5. The IPP location is calculated using Eq. (6.1) to (6.3) at an ionospheric height of 350 km. The resolution of the grid in the time axis of the figure is 5 minutes, while it is 2° in the latitude axis. It can be seen that compared with the scintillation captured on 6 and 9 September, there is more phase scintillation occurring on 7 and 8 September. Additionally, the phase scintillation occurrence is not evenly distributed. It is more likely to occur at the latitudes from around 50 to 60°N. Moreover, more scintillation is observed from around UTC 22:00 on 7 September to 04:00 and from 12:00 to 19:00 on 8 September, when the level of geomagnetic activity increases obviously.

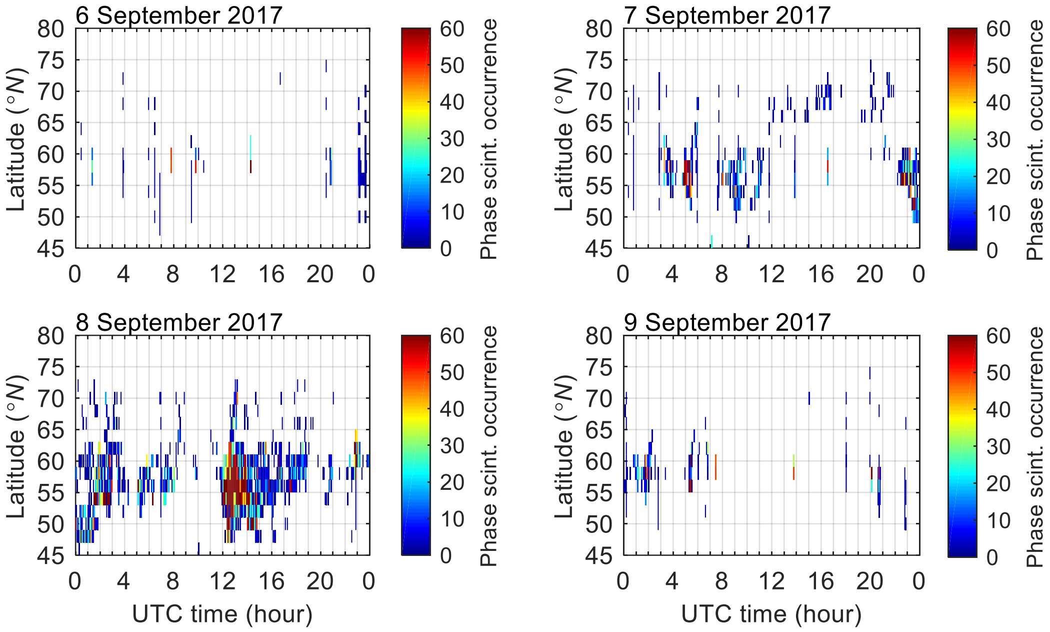

Figure 6.5 Occurrence of the phase scintillation with the 1-second index $\sigma_{\varphi} > 0.3$ rad in relation to the IPP latitude and UTC time from 6 to 9 September 2017. The scintillation index was measured on the GPS L1 C/A signal observed by the twelve ISMR stations equipped with PolaRxS Pro receivers deployed as part of the CHAIN

6.2.2 Phase and code jitter maps

With the 1-second scintillation index, the PLL phase jitter and DLL code jitter are calculated according to Eq. (4.1) to (4.6). Following the procedure described in Section 6.1.1, regional phase and code jitter maps are generated with the configurations summarised in Table 6.1. The jitter maps are generated at an ionospheric height of 350 km with the resolution set as 1° in both the latitude and longitude directions. To convert the estimated slant jitter value to the vertical equivalent, a single layer cosine mapping function is applied in this study, given by (Hobiger and Jakowski 2017)

$$M(E) = \sqrt{1 - \left(\frac{R_e \cos(E)}{R_e + h_{iono}}\right)^2} \tag{6.5}$$

where R_e, E and h_{iono} have the same meanings as in Eq. (6.1) to (6.3). A 2D linear interpolation algorithm is then implemented to estimate the verticalized jitter values. As the 1-second scintillation indices are used in the phase and code jitter calculation, the phase and code jitter maps can be updated at every 1 second.

Table 6.1 Configurations in the generation of the jitter maps

Items	Settings	Items	Settings
Ionosphere height	350 km	Interpolation	2D linear
Grid resolution	1° Lat. x 1° Lon.	Mapping function	Cosine function
Update rate	1 second		

Figure 6.6 shows an example of the PLL phase jitter map for the GPS L1 C/A and L2 P signals generated at UTC 12:49:00 and 12:50:00 on 8 September 2017, along with the phase scintillation occurrence captured at the same epoch. As the top panels show, moderate and strong phase scintillation is captured in different regions of the ionosphere. Meanwhile, relatively larger PLL phase jitter is observed in the middle and bottom panels in the same region where scintillation occurs, for example, in the region between around 95 to 115 $°W$ and 55 to 60 $°N$. This means that the signals crossing these ionospheric regions would experience larger jitter values and may present a lower PLL tracking performance. It is also seen that the PLL phase jitter on the L2 P signal in the bottom panels is generally larger than that on the L1 C/A signal in the middle panels. This is reasonable as the L2 P signal is more susceptible to scintillation effects, as explained in Section 3.1.3. Moreover, the $C/N0$ levels for the L2 P signal are generally lower than for the L1 C/A, which is mentioned in Section 4.1.1.

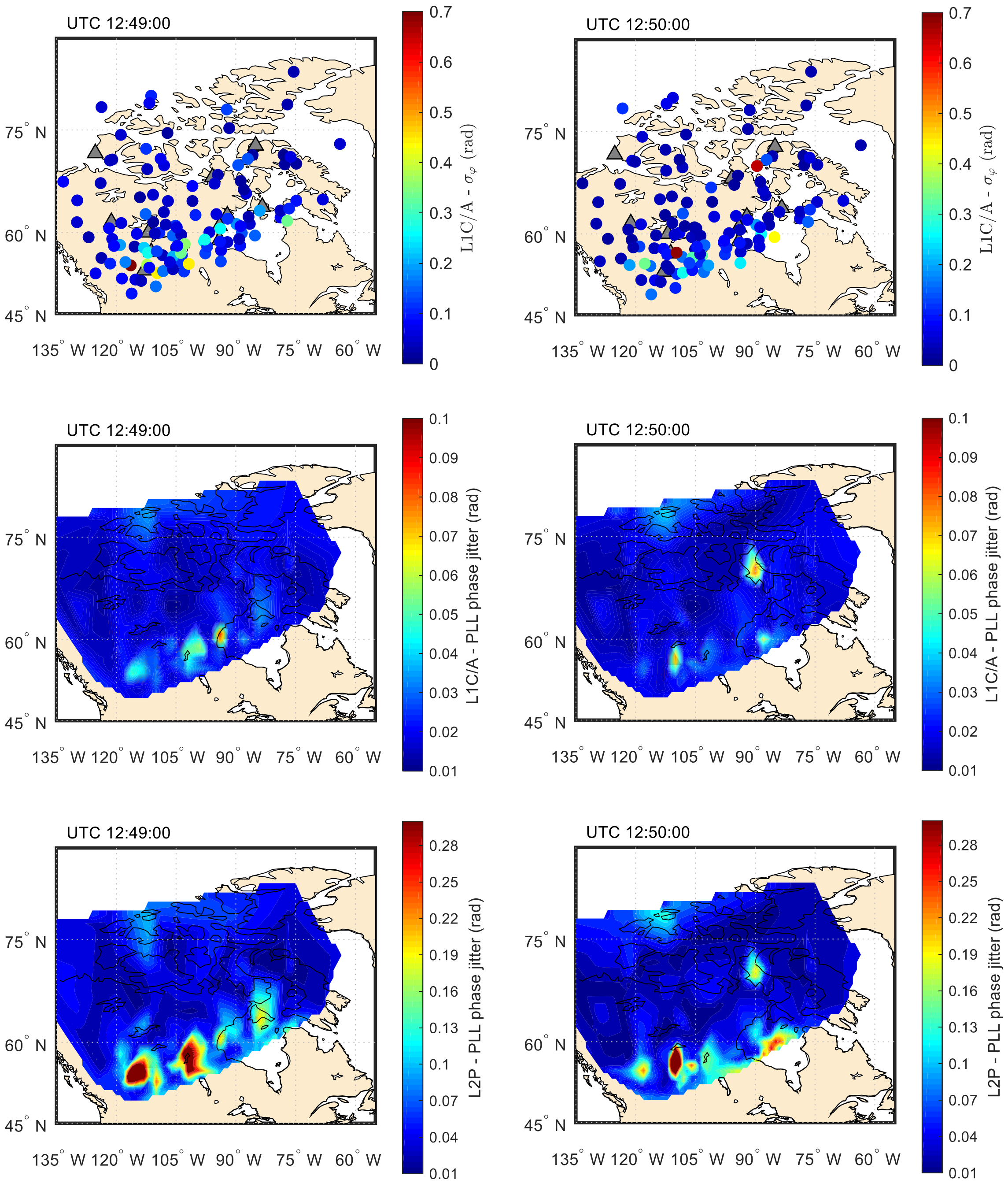

Figure 6.6 Phase scintillation occurrence captured on the GPS L1 C/A signal observed by the twelve ISMR stations equipped with PolaRxS Pro receivers deployed as part of the CHAIN (top) and the regional PLL phase jitter maps for the GPS L1 C/A signal (middle) and the L2 P signal (bottom) generated at UTC 12:49:00 and 12:50:00 on 8 September 2017

As described in Section 6.1.2, these phase and code jitter maps can be used to warn users of potential issues faced by GNSS receivers when tracking the signals crossing the map regions. In the next section, an example is given on how the phase jitter maps can be helpful in identifying the cycle slips.

6.3 Cycle slip and positioning error under scintillation

In this section, the cycle slips detected at the ISMR and the generic GNSS receiver stations under the high latitude scintillation shown in Figure 6.4 are analysed. The relationship between the cycle slips and the corresponding phase jitter levels are investigated. The positioning errors caused by scintillation are calculated and presented.

6.3.1 Cycle slip occurrence and phase jitter

Cycle slip occurrence and its relationship with the phase jitter is studied in this section. The cycle slip is detected based on the code and carrier phase measurements following the approach introduced in Section 2.3.3. It should be noted that only the cycle slips detected on the signals with the satellite elevation higher than 30° are considered, as on the signals with a lower elevation the cycle slip may be caused by strong multipath effects rather than scintillation. Figure 6.7 shows the occurrence of cycle slips in relation to the signal IPP latitude and the UTC time during 6 to 9 September 2017. The cycle slips are detected at the twelve ISMR stations used in the generation of the jitter maps. The size of the grid in this figure is the same as that in Figure 6.5, i.e., 2° in the latitude direction and 5 minutes in the time axis. As the figure shows, cycle slips are frequently detected on each day, even on 6 and 9 September when not much phase scintillation is captured, as shown in Figure 6.5. However, from around UTC 22:00 on 7 September to 04:00 and from 12:00 to 16:00 on 8 September, more cycle slips are observed at the latitudes ranging from 50 to $60°N$, when the phase scintillation occurrence increases markedly. This indicates that the phase scintillation can enhance the probability of cycle slip occurrence.

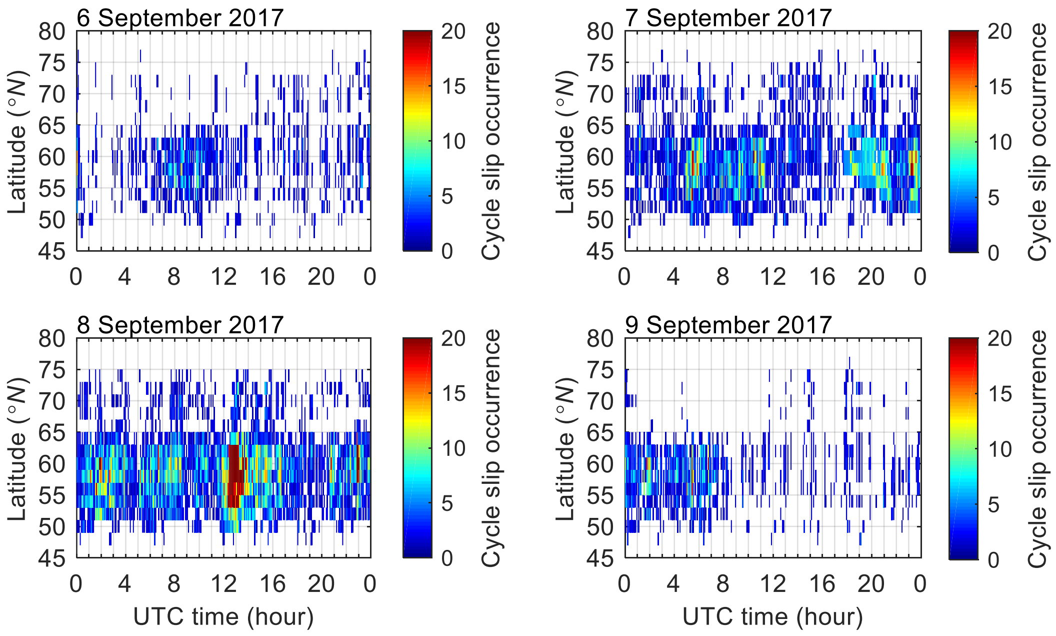

Figure 6.7 Occurrence of the cycle slips in relation to the IPP latitude and UTC time from 6 to 9 September 2017. The cycle slips are detected at the twelve ISMR stations equipped with PolaRxS Pro receivers deployed as part of the CHAIN

Figure 6.8 presents the maximum of the verticalized PLL phase jitter as a function of the IPP latitude and UTC time. The maximum jitter value is calculated on the GPS L1 C/A signal in a similar grid size as that in Figure 6.5 and Figure 6.7. It is seen that the max values of the phase jitter on 6 and 9 September are generally lower than around 0.03 rad, while on 7 and 8 September, obviously larger jitter values are frequently observed, particularly in the latitude region of around 50 to 60°N from around UTC 12:00 to 16:00 on 8 September. This is in agreement with the region where more cycle slips are detected, as shown in Figure 6.7. Thus, the occurrence of cycle slips is also related to the levels of the phase jitter in the jitter maps, indicating that the phase jitter maps produced in this study are helpful for users to identify potential receiver issues caused by scintillation, such as cycle slips.

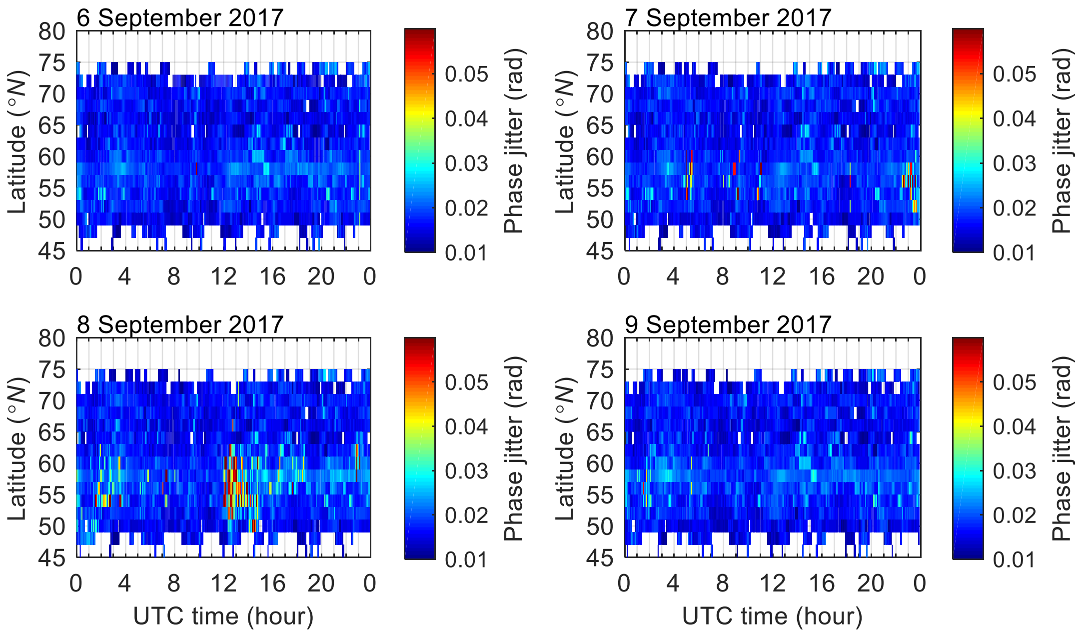

Figure 6.8 The max value of the verticalized phase jitter measured for the GPS L1 C/A signal as a function of the IPP latitude and the UTC time. The maximum jitter value is calculated in the same size of the grid as that in Figure 6.5 and Figure 6.7

To further demonstrate the effectiveness of the phase jitter maps in warning the potential cycle slip related issues for user receivers, the cycle slip occurrence and its percentage of occurrence in relation to the phase jitter are studied. It should be noted that the phase jitter here is the slant value retrieved from the phase jitter maps following the procedure that is to be introduced in Section 6.4.1. Figure 6.9 shows the cycle slip occurrence in relation to the phase jitter calculated on the GPS L1 C/A signal. Cycle slips are detected on 8 September 2017 at FSMC station, equipped with a PolaRxS Pro ISMR as part of the CHAIN network, and RNKN station, equipped with a generic GNSS receiver operational as part of the Canadian Active Control System (CACS). The location of RNKN station and the type of receiver deployed at this station are given in Table 6.2 in the next section. It can be seen that with the increase in the PLL phase jitter, the cycle slip percentage in the bottom panels increases markedly at both stations, indicating that the signal experiencing a larger phase jitter would more probably be impacted by cycle slips. For example, if a signal observed at FSMC station experiences a phase jitter that is more than 0.05 rad, it may encounter cycle slips at a probability of more than 60%. This further shows that the PLL phase jitter maps are helpful to identify potential tracking issues for the signals passing through the maps. It is worth mentioning that there are also many cycle slip occurrences in the top panels when the phase jitter values are less than 0.04 rad at both stations. This is due to the fact that the cycle slip can also be related to factors other than the increased PLL phase jitter. This would be worth analysing in future studies.

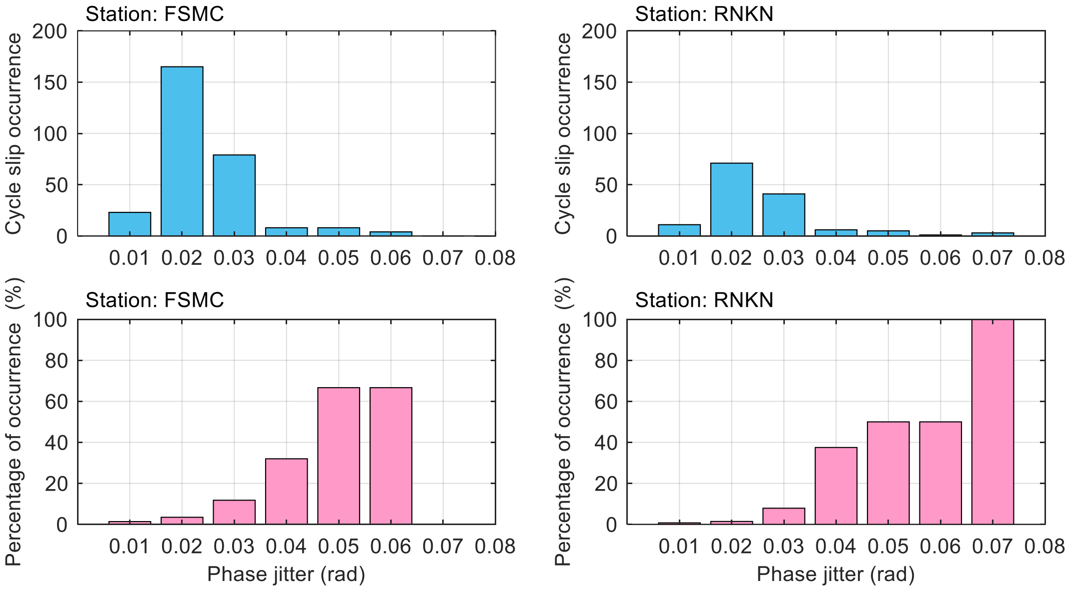

Figure 6.9 Cycle slip occurrence and its percentage of occurrence in relation to the PLL phase jitter at FSMC and RNKN stations. The phase jitter is the slant value retrieved from the phase jitter maps generated on 8 September 2017

6.3.2 Positioning errors under scintillation

To demonstrate the effects of the high latitude scintillation observed during the September 2017 geomagnetic storm on GNSS positioning, the positioning errors are calculated in this section at four ISMR stations equipped with PolaRxS Pro receivers, namely FSMC, RANC, MCMC and RABC, all part of the CHAIN network. Details of the locations of these four stations can be found in Table 2.2. Apart from the ISMR stations, another six stations operational as part of the CACS are chosen, which are equipped with different types of high precision dual-frequency receivers, as listed in Table 6.2. The distribution of the stations used for the analysis in this section is shown in Figure 6.10.

Table 6.2 Locations and receiver types of the stations operational as part of the CACS

Station abbreviation	Lat. (°N)	Long. (°E)	Receiver
DRNG	64.86	248.42	TRIMBLE NETR9
REPL	66.52	273.77	TRIMBLE NETR9
YELL	62.48	245.52	JAVAD TRE_3N DELTA
TKTO	62.49	256.72	TRIMBLE NETR9
CHUR	58.76	265.91	TPS NET-G3A
RNKN	62.81	267.91	TRIMBLE NETR8

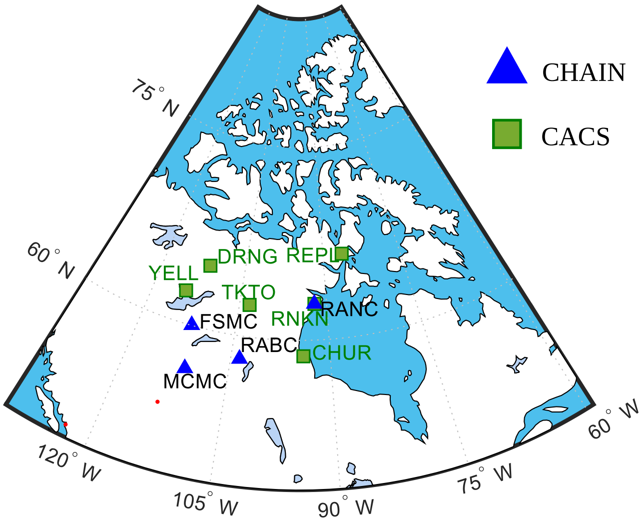

Figure 6.10 Distribution of the four ISMR stations deployed as part of the CHAIN and the six stations operational as part of the CACS equipped with generic receivers

Following the positioning strategies summarised in Table 5.3, the precise reference coordinates of each station shown in Figure 6.10 are calculated by performing static PPP processing using the POINT software based on the GPS L1 C/A and L2 P measurements recorded on 6 September 2017, when less or no scintillation is observed. The positioning errors are calculated subsequently by comparing the reference coordinates with the coordinates estimated by performing kinematic PPP with a satellite elevation weighting strategy.

Figure 6.11 shows the positioning errors in the east, north and up directions along with the 1-second phase scintillation index measured on the GPS L1 C/A signal at the four ISMR stations from 6 to 9 September 2017. It can be seen that the occurrence of strong phase scintillation increases markedly from 6 to 8 September at all the stations. On 8 September, most of the phase scintillation occurs from around UTC 00:00 to 07:00 and 12:00 to 18:00, despite the fact that its intensity varies at different stations. When there is less scintillation captured on 6 September at RANC, MCMC and RABC stations, the positioning errors in all the directions are less than 0.20 m, while they increase obviously by different extents on 7 and 8 September during the scintillation occurrence. The largest positioning errors are seen on 8 September at all these four ISMR stations, when the geomagnetic disturbance reaches the highest level, which is shown in Figure 6.3.

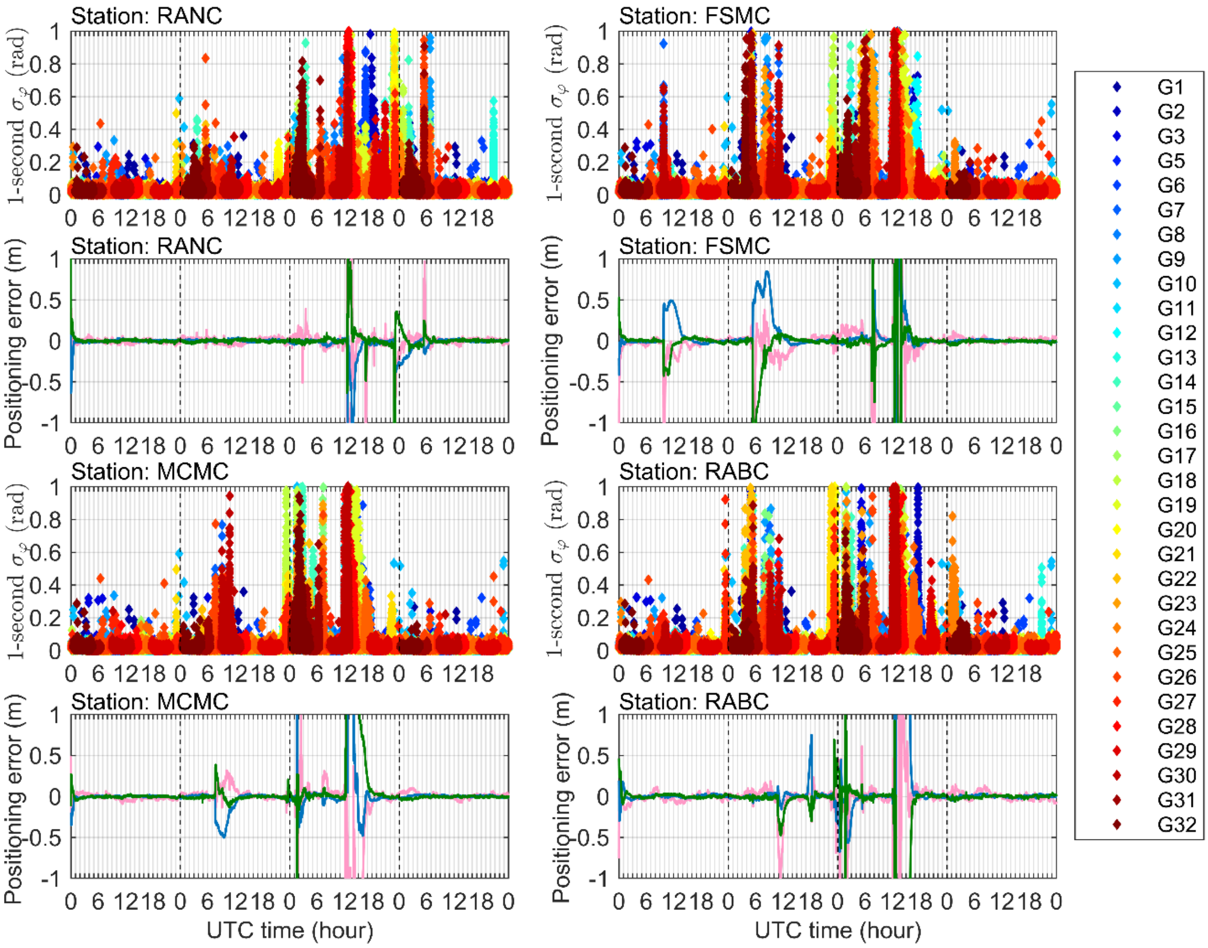

Figure 6.11 1-second phase scintillation index measured on GPS L1 C/A signal and the positioning errors in the east, north and up directions calculated at FSMC, RANC, MCMC and RABC stations from 6 to 9 September 2017

Figure 6.12 presents the positioning errors calculated at the six stations equipped with different types of generic receivers deployed as part of the CACS from 6 to 9 September 2017. Increases in the positioning errors are frequently seen at each station during these four days, while relatively larger errors are mostly observed from around UTC 12:00 to 16:00 on 8 September, exactly when strong scintillation is frequently observed. Additionally, it is seen that the stations deployed at lower latitudes, e.g., TKTO, RNKN and CHUR stations, tend to experience larger positioning errors, which agrees with the spatial distribution of the phase scintillation, as shown in Figure 6.5. Thus, the degradation in positioning accuracy at these stations is very likely caused by scintillation.

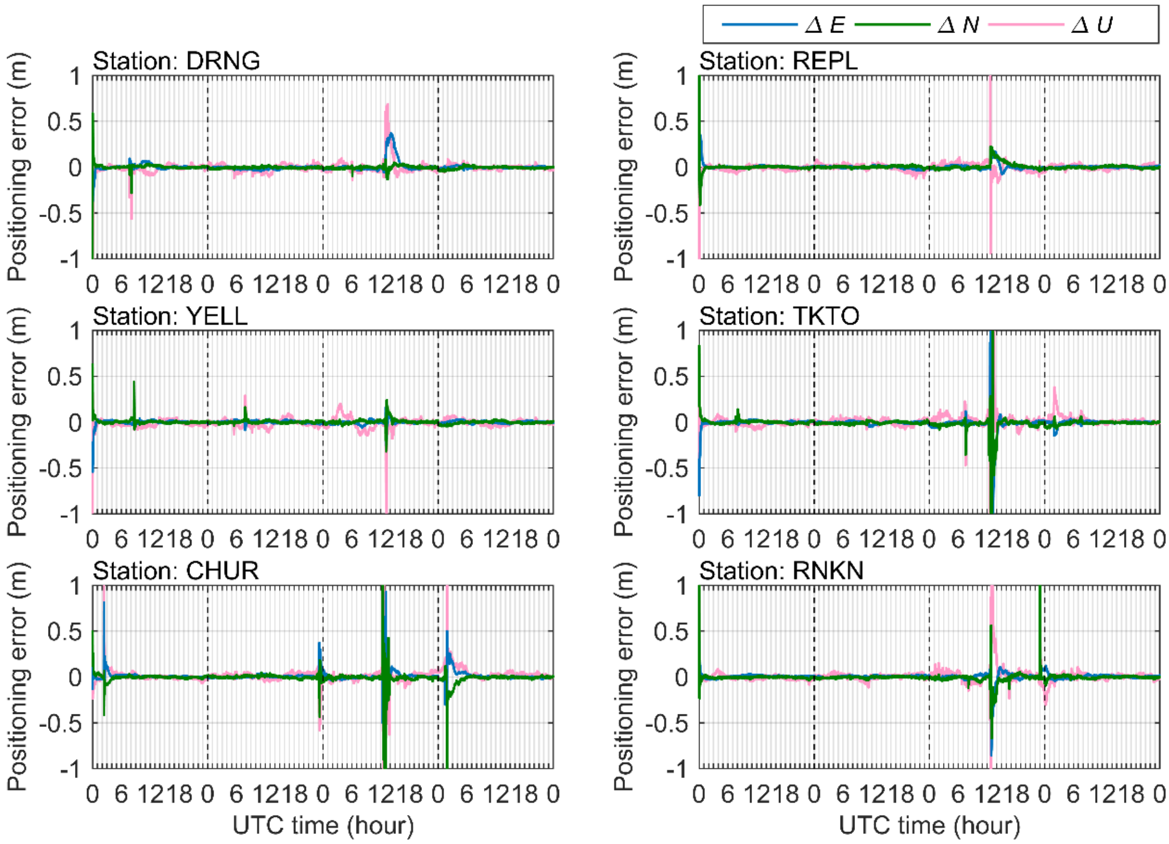

Figure 6.12 Positioning errors in the east, north and up directions calculated at the six GNSS stations equipped with different types of generic receivers operational as part of the CACS from 6 to 9 September 2017

In order to reduce the positioning errors under scintillation, the mitigation approach described in Section 5.1.1 can be implemented on the ISMR stations, as the phase and code jitter can be directly calculated based on the measured scintillation indices. However, the stations equipped with a generic receiver cannot measure the scintillation indices, therefore offering a suitable opportunity to exploit the phase and code jitter maps produced in Section 6.2.2. Details of the approach to mitigate the scintillation effects on positioning by exploiting the jitter maps and the achieved improvements in the positioning accuracy are given in the next section.

6.4 Scintillation mitigation on GNSS positioning using jitter maps

In this section, the approach to mitigate the scintillation effects on positioning accuracy by using the phase and code jitter maps generated in this study is provided. The improvements in the positioning accuracy achieved at the ISMR stations and the stations equipped with generic receivers are presented.

6.4.1 Approach to mitigate positioning error with jitter maps

Due to the fact that generic receivers are not able to estimate the scintillation indices and thus the phase and code jitter, the scintillation mitigation approach described in Section 5.1.1 cannot be directly implemented. With the help of the phase and code jitter maps generated in this study, the values of the phase and code jitter corresponding to the signals can be retrieved from these maps, making the mitigation approach applicable to the generic receivers. Figure 6.13 presents the concept to mitigate the scintillation effects on GNSS positioning errors by exploiting the phase and code jitter maps. As the figure shows, the jitter maps are generated based on the scintillation indices measured by the ISMRs deployed in a dense network, e.g., the CHAIN. On the other hand, the IPP locations for each signal passing through the maps are calculated at the user station according to Eq. (6.1) to (6.3). By searching the PLL or DLL jitter maps according to the IPP latitude and longitude, the grid in the maps that the signal crosses can be located. Through a linear interpolation of the verticalized jitter values at the four corners of the grid, e.g., a, b, c and d in the figure, the corresponding verticalized jitter $\sigma_{vertical}$ at the IPP can be interpolated. Through an inverse mapping process, the slant jitter value can be finally obtained, which is further used to modify the stochastic models in positioning following the mitigation approach described in Section 5.1.1.

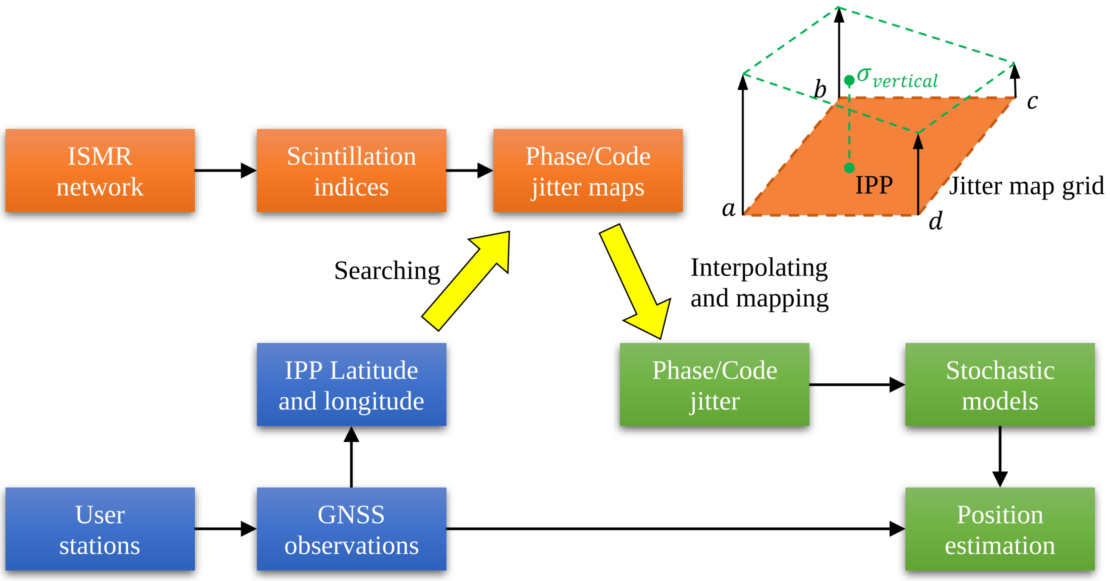

Figure 6.13 Concept of mitigating GNSS positioning errors under scintillation by exploiting the phase and code jitter maps

It is worth mentioning that when interpolating the vertical jitter value and converting to the slant equivalent in the process shown in Figure 6.13, the same interpolation technique and mapping function are respectively used as in the jitter map generation process, which is summarised in Table 6.1. Additionally, if the signal received by the user receiver passes outside of the maps, which may frequently happen when the user receiver is located in the edge region covered by the maps, the corresponding phase and code jitter are deemed not valid. In this case, the measurement precision calculated based on an elevation weighting strategy is used to replace the invalid phase or code jitters in the construction of the stochastic models.

The mitigation approach by exploiting the jitter maps presented in Figure 6.13 is suitable to both ISMRs and generic receivers. With this approach, the positioning errors are recalculated at the four ISMR and the six generic stations by performing kinematic PPP with a phase and code jitter weighting strategy. The improvements in the positioning accuracy with respect to that obtained with an elevation weighting are calculated and shown in the next section. It should be noted that when the user station is equipped with an ISMR, the corresponding scintillation data is sacrificed in the generation of the jitter maps used in the next section in order to ensure independence in the tests.

6.4.2 Scintillation mitigation for ISMRs using jitter maps

By modifying the position estimation stochastic models using the phase and code jitter retrieved from the jitter maps, the positioning errors at RANC, FSMC, MCMC and RABC stations are calculated by performing kinematic PPP using a jitter weighting strategy. As a PolaRxS Pro ISMR is deployed at these stations, the 1-second scintillation indices and the 1-second phase and code jitter are also calculated, using the approach introduced in Section 5.2.2 and the jitter estimation models given in Section 4.1.1, respectively. This directly calculated jitter is also implemented in the jitter weighting strategy in positioning, aiming to compare the performance of the retrieved and directly calculated jitter in scintillation mitigation. Additionally, due to the fact that the positioning errors caused by scintillation are more severe and concentrated on 8 September 2017 at all the stations, as shown in Figure 6.11 and Figure 6.12, the scintillation mitigation is only performed on this day in this analysis.

Figure 6.14 shows the positioning errors in the up and horizontal directions at the four ISMR stations on 8 September 2017, calculated by the kinematic PPP solution with elevation and the 1-second jitter weighting, with the jitter extracted from the jitter maps and calculated by the jitter estimation models, respectively. It can be seen that when using an elevation weighting strategy, significant positioning errors are seen in both the up and the horizontal directions. Large spikes in the positioning errors are frequently observed from UTC 12:00 to 14:00 at each station. These spikes are generally reduced when the 1-second jitter weighting is implemented, indicating that the 1-second phase and code jitter weighting generally achieves a better positioning accuracy under scintillation. On the other hand, the positioning errors obtained by the 1-second jitter weighting strategy with the jitter directly calculated by the jitter estimation models are, as expected, smaller than when the jitter is retrieved from the jitter maps.

Additionally, it is worth mentioning that even with the 1-second jitter weighting, the positioning errors caused by the scintillation cannot be totally removed. Obvious errors still remain in both the up and the horizontal directions. This means that there is scope for further improvement in the proposed scintillation mitigation approach, which may be the subject of future research.

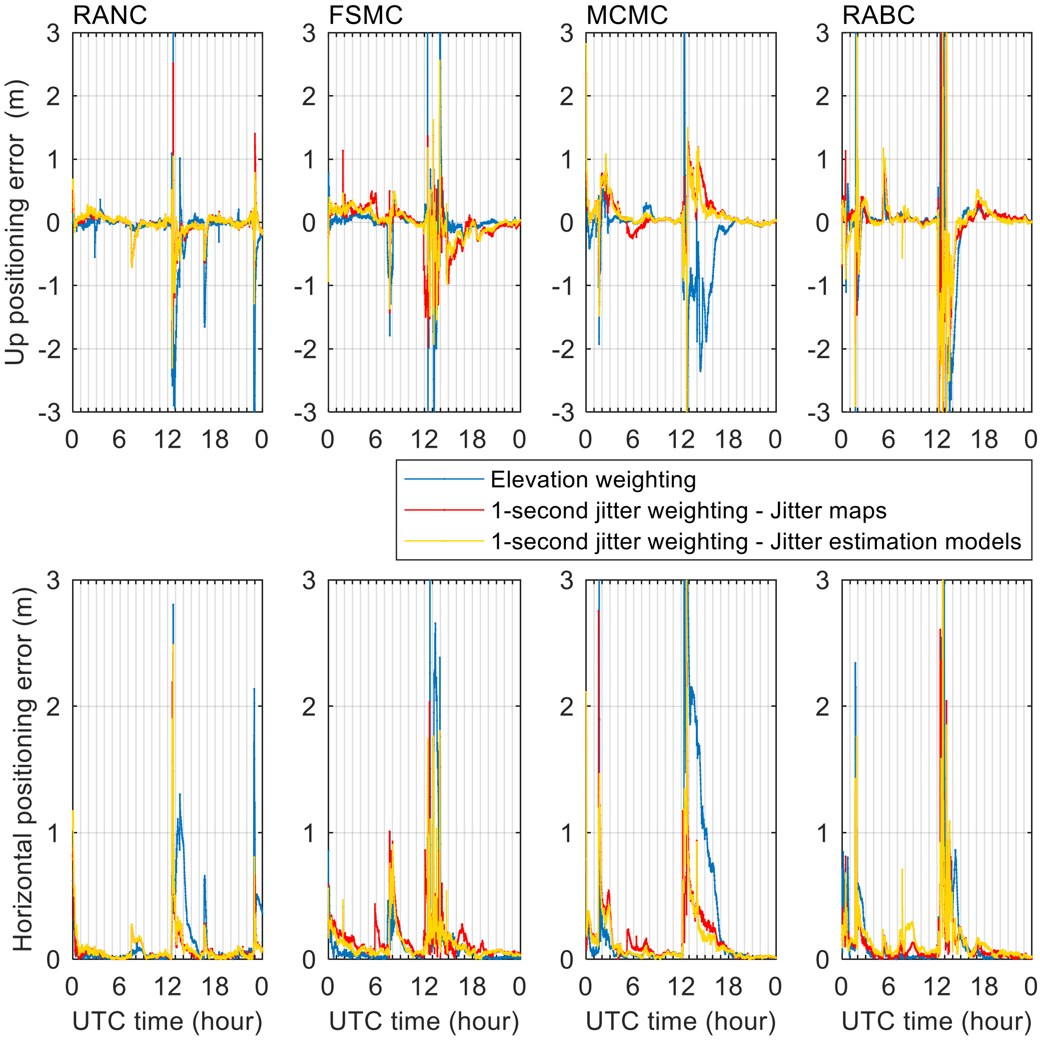

Figure 6.14 Variation of the positioning errors in the up (top) and horizontal (bottom) directions calculated on 8 September 2017 at RANC, FSMC, MCMC and RABC stations. The positioning errors are estimated by performing the kinematic PPP respectively using elevation and 1-second phase and code jitter weighting strategies

Figure 6.15 presents the 3D positioning errors calculated at RANC, FSMC, MCMC and RABC stations on 8 September 2017. The positioning errors are estimated by performing kinematic PPP with the three different weighting strategies. Due to the PPP convergence process, the first hour of the positioning error time series calculated at each station is not considered. As the figure shows, the elevation based weighting strategy presents the largest 3D positioning errors at all the stations. At MCMC station, the daily RMS of the 3D positioning error reaches 1.11 m, while it is reduced to 0.50 and 0.48 m when the two other approaches, based on the 1-second jitter weighting, are used, respectively. By comparing the results of the two jitter weighting strategies it becomes clear that the use of the maps entails a performance nearly as good as the use of the actual jitter values estimated directly by the models. The differences are most probably due to possible imprecisions/inadequacies in the mapping function and the interpolation process, leaving scope for future research on potential improvement in these two areas. Nevertheless, the results of the comparison are encouraging and can be regarded as a validation of the maps, confirming the potential of their use in mitigating the positioning errors under scintillation conditions when it is not possible to estimate directly the jitter errors.

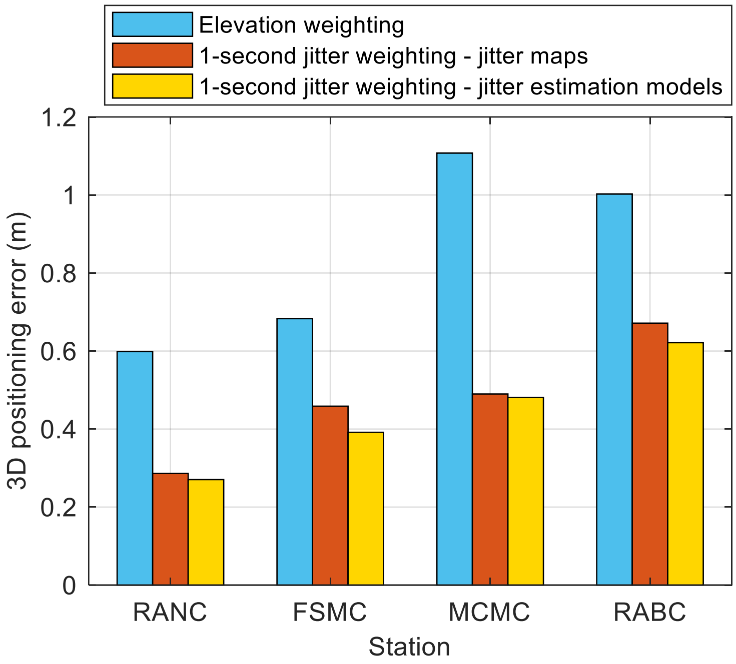

Figure 6.15 RMSs of the 3D positioning errors calculated by performing the kinematic PPP respectively using elevation and 1-second phase and code jitter weighting strategies on 8 September 2017 at RANC, FSMC, MCMC and RABC stations

The percentage improvements in the 3D positioning errors when using the 1-second jitter weighting strategies in positioning, corresponding to the results shown in Figure 6.14 and Figure 6.15, are summarised in Table 6.3. It can be seen that with the assistance of the phase and code jitter maps, the positioning accuracies at all the stations are generally improved. Improvement of, respectively, 55% at MCMC station and 52% at RANC station, is achieved. Therefore, it can be concluded that the jitter maps generated in this study can be used to mitigate the scintillation effects on GNSS positioning at the ISMR stations in this analysis.

Table 6.3 Percentage improvements in the 3D positioning errors when using phase and code jitter weighting strategies in positioning with respect to using an elevation weighting strategy calculated on 8 September 2017 at RANC, FSMC, MCMC and RABC stations

1-second jitter weighting strategy	Station			
	RANC	FSMC	MCMC	RABC
Jitter maps[1]	52%	33%	56%	33%
Jitter estimation models[2]	55%	43%	57%	38%

[1] 1-second jitter retrieved from jitter maps

[2] 1-second jitter calculated by the jitter estimation models using the measured 1-second scintillation indices

6.4.3 Scintillation mitigation for generic receivers using jitter maps

The positioning errors in the up and horizontal directions on 8 September 2017 at the six stations operational as part of the CACS are calculated by performing kinematic PPP respectively using the elevation and the jitter map based 1-second jitter weighting strategies, as shown in Figure 6.16. The jitter value used in the jitter weighting strategy is retrieved from the phase and code jitter maps, following the approach described in Section 6.4.1. As the figure shows, the positioning errors in the up and horizontal directions are generally reduced when the 1-second jitter weighting strategy is applied in comparison to the elevation weighting strategy. The positioning error calculated using the elevation weighting at YELL station reaches more than -3 m in the up direction and 3 m in the horizontal direction at around UTC 12:10, while are reduced to -2.4 m and 0.65 m respectively when using the 1-second jitter weighting strategy. However, it is also seen that although the 1-second jitter weighting strategy can help to mitigate the positioning errors under scintillation, it can barely reach an accuracy comparable to non-scintillation conditions.

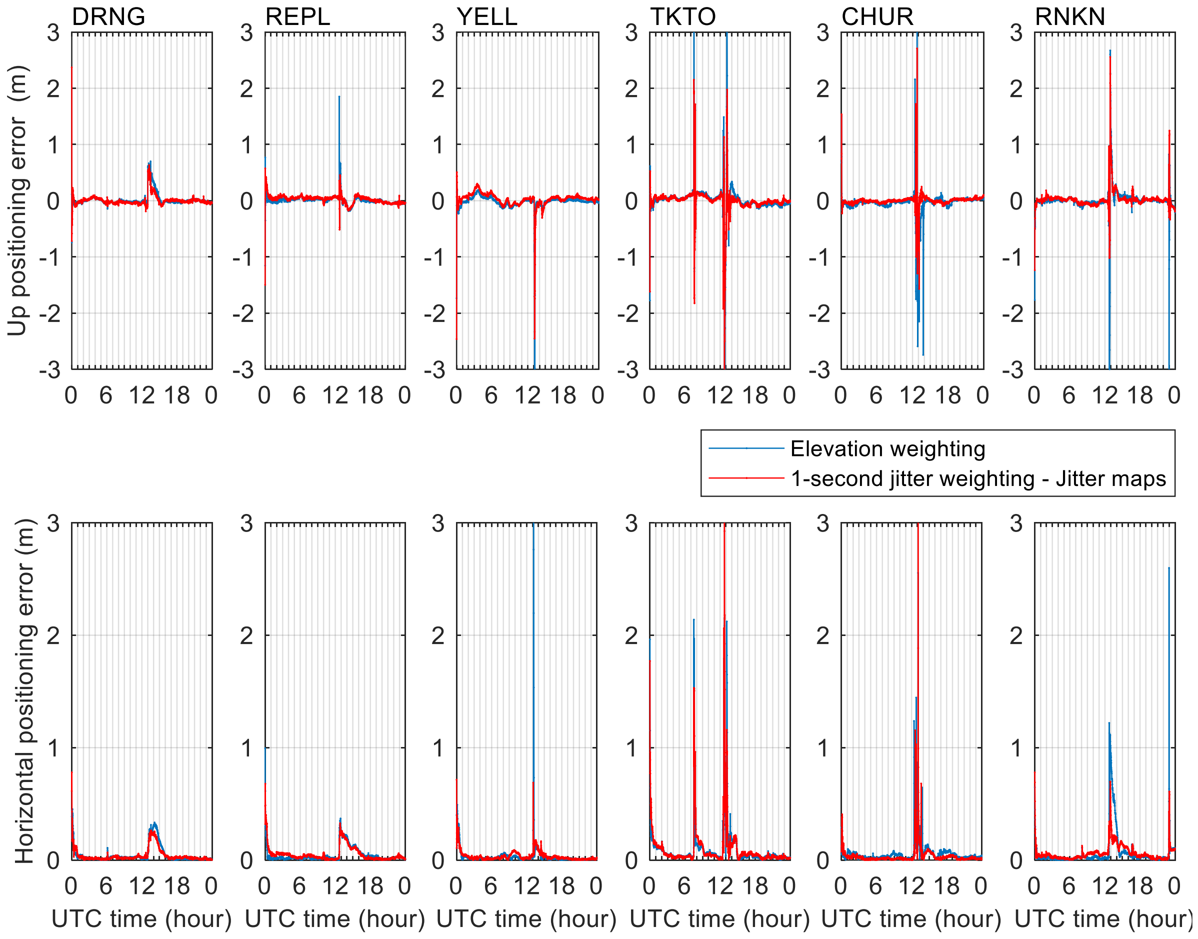

Figure 6.16 Variation of the positioning errors in the up (top) and horizontal (bottom) directions calculated on 8 September 2017 at DRNG, REPL, YELL, TKTO, CHUR and RNKN stations. The positioning errors are estimated by performing the kinematic PPP respectively using elevation and 1-second phase and code jitter weighting strategies

Figure 6.17 shows the RMSs of the 3D positioning errors calculated with the two different weighting strategies on 8 September 2017 at the six stations. It can be seen that the 3D positioning errors estimated using the elevation weighting strategy are generally reduced by using the 1-second jitter weighting strategy. At the stations where the positioning errors are more affected by scintillation, e.g., at YELL, TKTO and RNKN station, the 3D positioning errors are reduced by 0.17, 0.15 and 0.18 m, respectively, indicating the effectiveness of exploiting jitter maps in the positioning error mitigation under scintillation. However, it is noticed that the positioning errors at DRNG and REPL station are only reduced by 0.03 and 0.02 m, respectively. Thus, a future study can be carried out to further improve the performance of the jitter maps in scintillation mitigation.

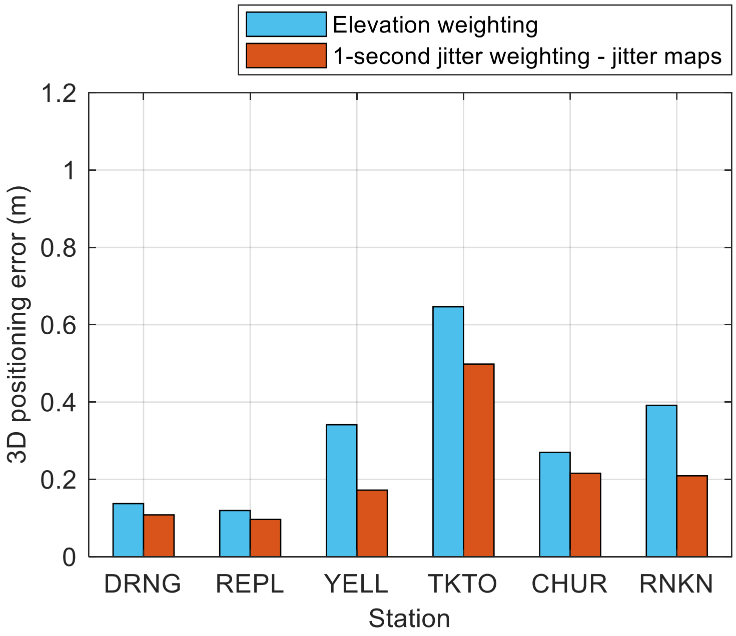

Figure 6.17 RMSs of the 3D positioning errors calculated by performing the kinematic PPP respectively using elevation and 1-second phase and code jitter weighting strategies on 8 September 2017 at DRNG, REPL, YELL, TKTO, CHUR and RNKN stations

Table 6.4 summarizes the percentage improvements in the 3D positioning errors when using a 1-second jitter weighting strategy in the kinematic PPP calculation, compared to when an elevation weighting is used. It can be seen that the positioning accuracy is generally improved at all the stations. Improvements, respectively, of 50% at YELL station and 47% at RNKN station are achieved, indicating that exploiting the 1-second jitter extracted from the jitter maps generated in this study can help to improve the positioning accuracy under scintillation. However, it is also seen that the 1-second jitter weighting approach only achieves an improvement of around 20% at DRNG, REPL, TKTO and CHUR stations. This may be due to the following reasons: (1) as mentioned in Section 6.4.2, extra errors may be added to the phase and code jitter extracted from the jitter maps through the mapping and interpolation techniques in the generation of the maps, which decrease the effectiveness of using the phase and code jitter to respectively represent the precision of carrier phase and pseudorange measurements; (2) the CHUR station is located at the southeast edge of the jitter maps, as shown in Figure 6.10, which results in invalid jitter values used in the stochastic models in position estimation using a jitter weighting strategy; (3) as mentioned in Section 6.1.2, the phase and code jitter values retrieved from the maps, constructed based on ISMRs, are used to approximate those in generic receiver tracking loops. The difference in the tracking loop configurations between generic receivers and ISMRs may also result in the decreased effectiveness of the retrieved jitter in representing the precision of measurements of generic receivers. Due to the time limitation of this study, these possible reasons affecting the performance of the jitter maps in scintillation mitigation have not been fully investigated. In the next section, the jitter errors induced by the mapping function are investigated.

Table 6.4 Percentage improvements in the 3D positioning errors when using receiver phase and code jitter weighting strategies in positioning with respect to using an elevation weighting strategy on 8 September 2017 at DRNG, REPL, YELL, TKTO, CHUR and RNKN stations

1-second jitter weighting strategy	Station					
	DRNG	REPL	YELL	TKTO	CHUR	RNKN
Jitter maps	21%	19%	50%	23%	20%	47%

Based on the analysis in this section, it is seen that the phase and code jitter maps generated in this work can help both ISMRs and generic receivers to improve the positioning accuracy under scintillation. Due to the fact that the generation of these maps requires a dense network of ISMRs, which is only currently available in the CHAIN deployed in northern Canada, the scintillation mitigation exploiting the jitter maps in other regions, such as in equatorial regions, is not carried out in this thesis.

6.5 Phase jitter errors induced by the mapping function

As mentioned in the previous sections, the mapping function used in the construction of the phase and code jitter maps can potentially induce errors in the phase and code jitter values retrieved from the maps, which in turn affects their performance when used in the mitigation of scintillation effects on GNSS positioning. Due to the fact that phase scintillation is the dominant effect observed over the data collection period, this section focuses on the mapping function induced phase jitter errors in the generation of the phase jitter maps. The relationship between these errors and various factors, including satellite elevation, scintillation indices and $C/N0$ levels, are presented.

6.5.1 Coinciding points and phase jitter errors

The mapping function induced phase jitter errors in the generation of the phase jitter maps are studied by analysing the deviations between the verticalized phase jitter values that are converted on signals passing through the coinciding point, as Figure 6.18 shows. In the figure, the signals propagated from satellite A to ISMR a through IPP_A, denoted as link A, and from satellite B to ISMR b through IPP_B, denoted as link B, cross the same ionospheric pierce point, referred to as coinciding point (Nava et al. 2007), by satisfying the following conditions

$$\left|IPP_{A\_Lat} - IPP_{B\_Lat}\right| < 1° \tag{6.6}$$

$$\left|IPP_{A\_Lon} - IPP_{B\_Lon}\right| < 1° \tag{6.7}$$

where IPP_{A_Lat} and IPP_{A_Lon} are the latitude and longitude of IPP_A, respectively. IPP_{B_Lat} and IPP_{B_Lon} are the latitude and longitude of IPP_B, respectively. With the mapping function, the phase jitter values calculated on link A, denoted as σ_{S_A}, and link B, denoted as σ_{S_B}, are verticalized to their equivalents σ_{V_A} and σ_{V_B}, respectively, as shown in the figure. If the mapping function perfectly represents the jitter conversion from slant to vertical direction, σ_{V_A} should be equal to σ_{V_B}. In practice, σ_{V_A} is not always equal to σ_{V_B}. The difference between them is defined as the mapping function induced phase jitter error MF_{error}, given by

$$MF_{error} = \sigma_{V\_B} - \sigma_{V\_A} \tag{6.8}$$

It should be noted that Eq. (6.8) can also be used to estimate the code jitter error induced by the mapping function, provided that σ_{V_A} and σ_{V_B} are the verticalized code jitter values.

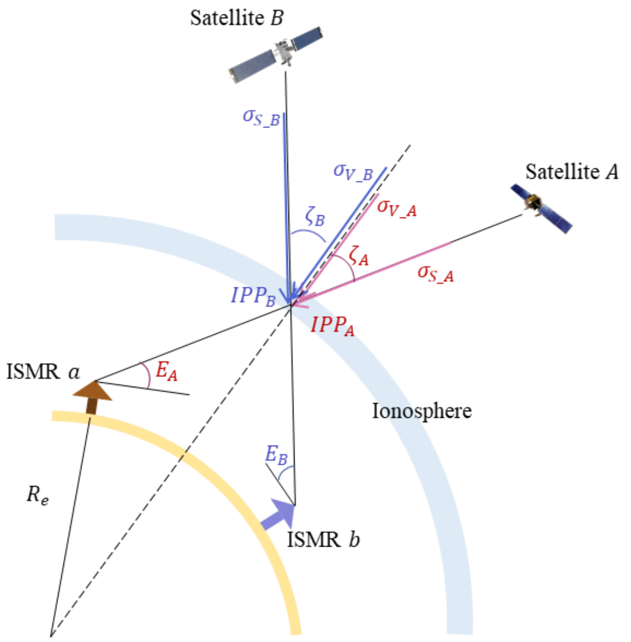

Figure 6.18 Example of signals cross the coinciding point in the ionosphere

The coinciding points are detected in the generation of the phase jitter maps on 8 September 2017, based on the scintillation data sets recorded by the twelve ISMRs described in Section

6.2.1. On this day, a total number of 4800 coinciding points are detected with the conditions given by Eq. (6.6) and (6.7) satisfied. Figure 6.19 presents the spatial distribution of the coinciding points coloured according to the levels of mapping function induced phase jitter error MF_{error}. It can be seen that the values of MF_{error} are generally low. They tend to randomly distribute in the ionospheric region. Some relatively larger values are observed in the edge of the region, such as in the regions of around 60 to 70°N, 120 to 135°W and 70 to 75°N, 70 to 100°W.

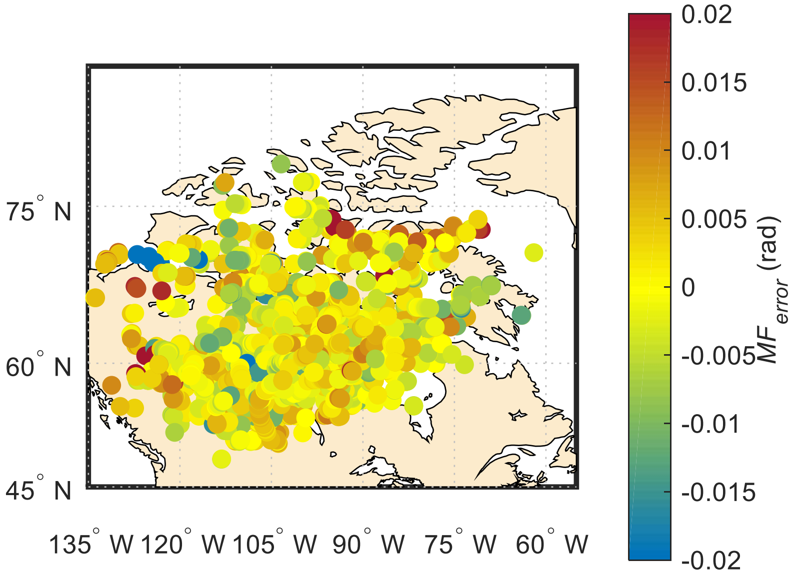

Figure 6.19 Spatial distribution of the coinciding points coloured according to the levels of mapping function induced phase jitter error MF_{error}. The coinciding points are detected during the generation of phase jitter maps for the GPS L1 C/A signal on 8 September 2017.

Figure 6.20 shows the histogram of the phase jitter error MF_{error} corresponding to the coinciding points presented in Figure 6.19. As the figure shows, most MF_{error} fall into the range between -0.01 to 0.01 rad. The standard deviation and mean of MF_{error} are 0.0057 and 0.00039 rad, respectively, indicating that the mapping function induced phase jitter errors are generally small. In the next section, the factors that affect the levels of phase jitter errors induced by mapping function are investigated.

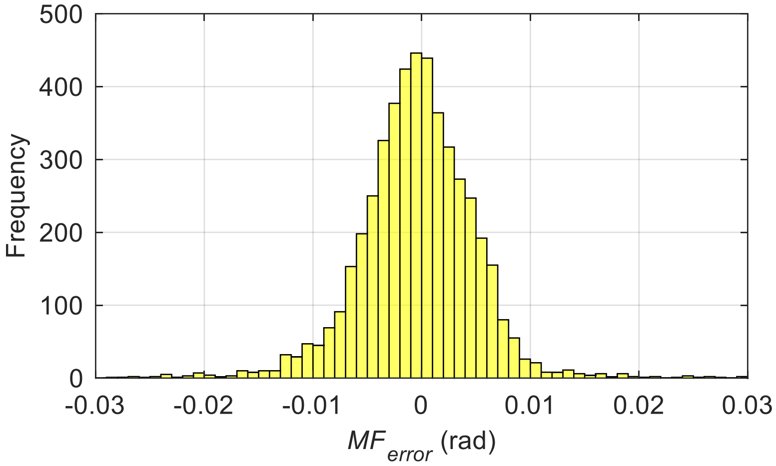

Figure 6.20 Histogram of the mapping function induced phase jitter error MF_{error} calculated at the coinciding points, which are detected during the generation of the phase jitter maps for the GPS L1 C/A signal on 8 September 2017

6.5.2 Factors affecting mapping function induced phase jitter errors

The relationships between the mapping function induced phase jitter error MF_{error} and satellite elevation, the 1-second phase scintillation index, as well as $C/N0$ levels are analysed, as shown in Figure 6.21. It can be seen in the top panel that MF_{error} is more likely to be larger when the difference between the elevations of satellites A and B is high. For instance, when the elevation is around 15° for satellite A and around 45 to 90° for satellite B, more MF_{error} is observed in the range between -0.02 to -0.01 rad. This means that the mapping function induced phase jitter errors are related to the satellite elevation. The middle panel of the figure presents the variation of MF_{error} in relation to the 1-second phase scintillation index σ_{φ} measured on the GPS L1 C/A signals of satellites A and B. As it shows, when σ_{φ} measured on both signals is at a lower level,

MF_{error} tends to be smaller. However, when σ_φ measured on the signal of satellite B is obviously larger than that on satellite A and vice versa, MF_{error} increases markedly, indicating that the large difference in the scintillation levels also contributes to a larger MF_{error}. Nevertheless, there are only a few cases when the scintillation levels measured on the signals crossing the coinciding points are significantly different.

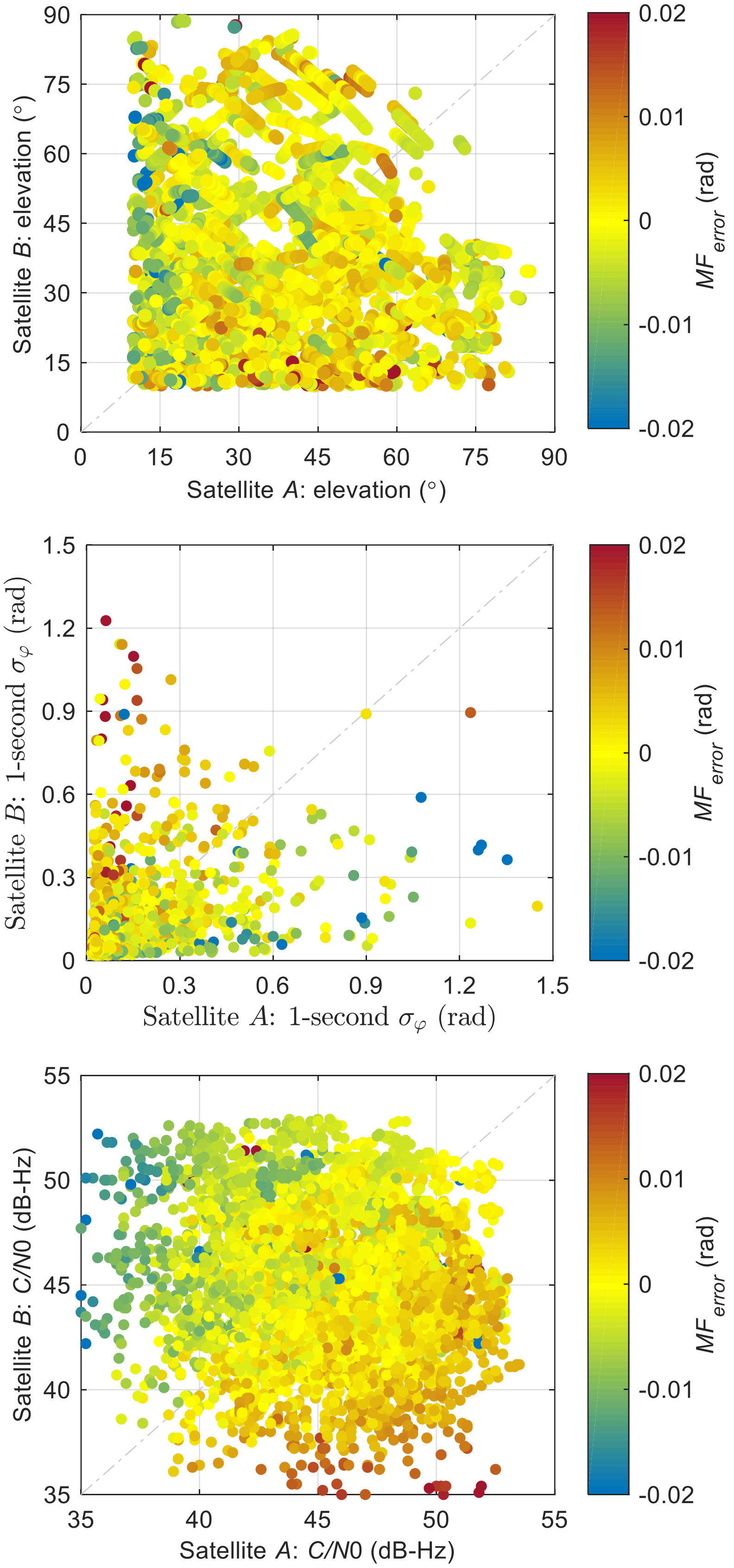

Figure 6.21 Relationships between the mapping function induced phase jitter error MF_{error} and satellite elevation (top), 1-second phase

scintillation index σ_φ (middle), as well as $C/N0$ levels (bottom). MF_{error} is calculated for the GPS L1 C/A signals that cross the coinciding points detected during the generation of the phase jitter maps on 8 September 2017

The bottom panel shows the variation of MF_{error} as a function of the $C/N0$ level. It is obviously seen that when $C/N0$ measured on the signals crossing the coinciding points is comparable, the values of MF_{error} are generally smaller, falling into the range between -0.01 to 0.01 rad. By contrast, when there are apparent differences between $C/N0$ levels of the signals crossing the coinciding points, MF_{error} increases obviously. The largest MF_{error} tends to occur when the $C/N0$ levels have the largest difference, e.g., when $C/N0$ is around 50 dB-Hz measured on the signal of satellite A and lower than 40 dB-Hz on satellite B and vice versa.

Based on the analysis in this section, it is found that the phase jitter errors induced by the mapping function are related to the satellite elevation, the phase scintillation intensities and $C/N0$ levels. The errors tend to increase when large differences of these factors are observed on the signals crossing the coinciding points. Therefore, it is necessary to consider these factors in the development of novel mapping functions, which is suggested as the focus of future work.

6.6 Summary

This chapter introduced the application of the phase and code jitter maps in the scintillation mitigation on GNSS positioning. The procedure for the generation of the jitter maps and their potential use were given, followed by the jitter maps generated based on the scintillation data recorded at the ISMRs deployed as part of the CHAIN during the geomagnetic storm that took place in September 2017. The relationship between cycle slips and the corresponding phase jitter values retrieved from the jitter maps was investigated. It is found that the jitter maps are beneficial in warning the occurrence of and identifying potential cycle slips for users.

Subsequently, the positioning errors due to scintillation were calculated at the four ISMR stations of the CHAIN and the six stations operational as part of the CACS, the latter equipped with different types of generic receivers. Results show that the positioning errors at different stations increased significantly under scintillation. To mitigate the scintillation effects on GNSS positioning, the 1-second jitter weighting strategy is implemented, where the jitter values were extracted from the generated jitter maps. Results show that the positioning errors for both ISMRs and the generic receivers were reduced when using the jitter weighting strategy, indicating that the jitter maps generated in this work can help to improve the positioning accuracy under scintillation. The phase jitter errors induced by the mapping function in the generation of the phase jitter maps are studied. The factors that affect the levels of these errors are investigated. It is found that the mapping function induced phase jitter errors are generally small. They are related to the satellite elevation, phase scintillation levels as well as the signal $C/N0$ levels. In order to maximize the performance of the jitter maps, novel mapping function and interpolation techniques may be developed, which is proposed as the focus of future study.

7 Summary, conclusions and future work

In the presence of scintillation, the GNSS signal quality and receiver performance can be significantly degraded, thus increasing the errors in positioning and navigation. Under strong scintillation, the GNSS receiver can even lose the lock on the signals, which poses serious threats to safety-critical GNSS applications and precise positioning. In summary, the aims of research reported in this thesis are (1) characterizing the GNSS signal intensity fadings under scintillation, (2) modelling scintillation effects on receiver tracking loops and (3) developing scintillation mitigation approaches, aiming to support high accuracy GNSS positioning under scintillation.

For a deeper understanding of scintillation effects on GNSS signals, signal intensity fadings due to amplitude scintillation were characterized using 3 months of real scintillation data during the solar maximum year of 2014 recorded at PRU2 station in Brazil, where a PolaRxS Pro receiver was deployed. The variation of the fading depth, duration and occurrence in relation to amplitude scintillation index $S4$ was mathematically modelled. Additionally, the relationship between signal intensity fadings and GNSS receiver tracking errors was analysed. To better describe how the signal intensity fadings affect PLL tracking errors, for the first time the fading speed defined as the ratio of fading depth to duration, was proposed in this thesis. This analysis is helpful to acquire better knowledge of scintillation effects on receiver tracking loops.

ISMRs of different types are deployed globally to monitor scintillation and study the ionospheric morphology. An interesting question which arises is whether the scintillation indices measured by the different types of ISMRs can be mixed up together in scintillation studies. To address this question, a common dataset of simulated scintillation data, generated by a GNSS hardware signal simulator - GSS8000-series Radio Frequency Constellation Simulator, was processed by the two types of widely used ISMRs, i.e., PolaRxS Pro and GSV4004B. The amplitude and phase scintillation indices calculated, respectively, based on the raw 50 Hz data logged by these two receivers were compared. Additionally, by processing the simulated scintillation data using a PolaRxS Pro receiver with its PLL configured to different bandwidths and integration times, the effects of PLL tuning on scintillation indices calculation were studied, which contributes to a deeper understanding of the effects of ISMR PLL tracking loop configurations on scintillation monitoring.

In order to quantitatively evaluate scintillation effects on receiver tracking loops, the phase and code jitter estimation models developed in Conker et al. (2003) were studied in this thesis, which estimated the phase and code jitter at the PLL and DLL outputs, respectively. There are still concerns with regards to these models, such as: (1) these models are only valid when amplitude scintillation index $S4$ is lower than $\frac{\sqrt{2}}{2}$; (2) these models have a strong dependence on the PLL and DLL configurations, as described in Section 4.1.3. To address these concerns, the effects of PLL bandwidth and integration time tuning on the phase jitter estimation were studied by processing scintillation data using the PLL with different bandwidths and integration times. Furthermore, an alternative approach was developed in this study which estimates the phase and code jitter under scintillation by exploiting the raw discriminator output. On the other hand, in order to measure the scintillation effects on the PLL tracking errors, the distribution of tracking errors under scintillation was studied. A custom-defined PDF was proposed in this study to fit the measured distribution curves of the tracking errors under scintillation, which provides an alternative way to model the scintillation effects on receiver tracking errors.

The approach to mitigate scintillation effects on GNSS positioning was studied. In this thesis, the scintillation mitigation approach, referred to as the phase and code jitter weighting approach developed in Aquino et al. (2009) was applied, which improves the stochastic models in positioning by exploiting the PLL phase jitter and DLL code jitter estimated using the models developed in Conker et al. (2003). However, there are still two limitations of this approach, namely: (1) when using the 1-minute phase and code jitter, calculated based on the 1-minute scintillation indices, to represent the noise levels of GNSS instantaneous measurements, the 1-minute jitter values may not be the best solution, as it was shown in this thesis that signal fluctuations caused by scintillation vary significantly within 1 minute and present large second-to-second variabilities; (2) this mitigation approach has so far been only used in connection with ISMRs, which are capable of measuring scintillation indices. For generic GNSS receivers which are not able to estimate scintillation indices and consequently the phase and code jitter, this mitigation approach cannot be implemented directly. A detailed description of the limitations is given in Section 5.1.2. To address the first limitation, an approach to calculate the 1-second scintillation indices was proposed in this thesis. These indices were further used to estimate the phase and code jitter and mitigate the scintillation effects on GNSS positioning. To address the second limitation, the concept of phase and code jitter maps introduced in Sreeja et al. (2011) was exploited. In this way, the generic receivers can extract and calculate the jitter values directly from these maps for each measurement, which can subsequently be used to mitigate the positioning errors under scintillation based on the phase and code jitter weighting strategy. In this thesis, regional phase and code jitter maps were constructed using the scintillation data recorded during the geomagnetic storm in September 2017 by PolaRxS Pro receivers deployed as part of the CHAIN. With the help of the phase and code jitter maps, scintillation mitigation on GNSS positioning for ISMRs and generic receivers was studied.

In the following subsection, the conclusions drawn from the studies of this thesis are summarized. The recommendations for future work are given next.

7.1 Conclusions and remarks

Based on the research in this thesis, the following conclusions can be drawn:

(1) In characterising signal intensity fadings under low latitude scintillation, it was found that most of the fading depths are between -5 dB to -15 dB and durations are within 1 second for all levels of scintillation. An inverse relationship was observed between the fading depth and duration (Guo et al. 2019a). Additionally, it was concluded that the fadings with depth around -20 dB are more damaging and more likely to degrade the PLL performance, and fadings with shorter durations tend to greatly increase the PLL tracking errors. It was also observed that with the increase in fading speed, the tracking error variance increases gradually (Guo et al. 2019a).

(2) In investigating the difference between the PolaRxS Pro and GSV4004B receivers in scintillation monitoring, it was found that the scintillation indices $S4$ and $Phi60$ calculated based on the scintillation data logged by the two types of ISMRs are similar, while the calculated phase scintillation spectral indices p and T present more deviations, which is due to the differences in the background noise of the carrier phase measurements output by these two types of receivers. This suggests that the phase scintillation spectral indices measured by these two types of ISMRs cannot be mixed directly in scintillation study. Additionally, results showed that the calculation of $S4$ and $Phi60$ indices is less affected by the PLL loop bandwidth and the integration time, however, increasing the PLL bandwidth and the integration time can respectively increase the T and p levels (Guo et al. 2020a).

(3) Based on the phase and code jitter estimation models developed in Conker et al. (2003), the effects of the PLL bandwidth and integration time tuning on the phase jitter calculation were studied. Results showed that an increase in the PLL bandwidth can decrease the levels of phase scintillation induced phase jitter, indicating that the PLL

with a lower bandwidth is more susceptible to phase scintillation. By contrast, the thermal noise component in the phase jitter increases gradually with the increase in the loop bandwidth. In conclusion, increasing the PLL bandwidth has an opposite effect on the phase jitter components induced by thermal noise and phase scintillation. There is a trade-off when selecting the PLL bandwidth for receiver manufacturers (Guo et al. 2020a).

(4) An alternative approach was proposed in this study to estimate the phase and code jitter by exploiting the raw PLL and DLL discriminator outputs. By processing the real scintillation data collected at low and high latitude stations using an SDR receiver, the phase and code jitter were estimated, respectively, using the jitter estimation models described in Conker et al. (2003) and the approach proposed in this study. Results showed that using the model and the proposed approach achieve a good match in the phase and code jitter estimation under scintillation, while the proposed approach has its advantage, i.e., the jitter estimated by the proposed approach better reflects the actual tracking performance under scintillation (Guo et al. 2020b).

(5) The probability density distribution of the phase tracking errors in the PLL was analysed by exploiting the scintillation data collected and processed by the SDR receiver. It was concluded that moderate and strong scintillation can cause the distribution of the phase tracking errors to deviate from the standard Gaussian distribution (Guo et al. 2020b). Additionally, using the proposed PDF, the distribution of the tracking errors under different levels of scintillation was successfully described (Guo et al. 2020b).

(6) The 1-second amplitude and phase scintillation indices proposed in this study showed more effectiveness in describing the signal fluctuations under scintillation, compared with the widely used 1-minute scintillation indices. To compare the performance of the

phase and code jitter weighting approaches in mitigating scintillation effects on positioning errors by respectively exploiting the 1-minute scintillation indices output by ISMRs and the newly proposed 1-second scintillation indices, the positioning accuracy and precision were calculated by performing kinematic PPP with three different weighting strategies, i.e., elevation based, 1-minute and 1-second phase and code jitter weighting strategies. Results showed that both the 1-minute and 1-second jitter weighting strategies help to improve the positioning accuracy and precision under scintillation. However, the latter performed even better under strong scintillation (Guo et al. 2021).

(7) The concept of the phase and code jitter maps (Sreeja et al. 2011) was exploited, which enables the estimation of the line of sight jitter values to the corresponding signals passing through the maps arriving at generic receivers. The positioning errors at four stations equipped with ISMRs and six stations equipped with generic receivers were calculated under scintillation during the September 2017 geomagnetic storm. To mitigate the positioning errors, the 1-second phase and code jitter weighting strategy was implemented, where the jitter values were retrieved from the generated jitter maps. Results showed that the positioning errors for ISMRs and the generic receivers can be reduced, respectively, by up to 56% and 50% when using the 1-second jitter weighting strategy, compared with using an elevation based weighting strategy, thus suggesting that the jitter maps generated in this thesis can help to improve the positioning accuracy under scintillation.

7.2 Future work

The relevant recommendations suggested for future work are given as follows:

(1) In the analysis of the PLL bandwidth tuning effects on the phase jitter under scintillation, it was found that increasing the PLL bandwidth has opposite effects on the

thermal noise component and the phase scintillation induced phase jitter. As a result, an optimal or adaptive bandwidth can be investigated in future work aiming to decrease the total phase jitter and maximize the receiver performance in the presence of scintillation.

(2) A custom-defined PDF was proposed which successfully described the distribution of the PLL tracking errors under scintillation. In this thesis, the parameters of the PDF were solved through a nonlinear least-square formulation and an iterative approach integrated in a MATLAB curve fitting tool. A further study can be conducted to model the relationship between the scintillation indices and the parameters in the proposed PDF, which will make it possible to directly determine the PDF of the PLL tracking errors under scintillation using the measured scintillation indices.

(3) With the help of the newly proposed 1-second scintillation indices and the phase and code jitter maps generated in this study, the GNSS positioning errors caused by scintillation can be greatly mitigated by using the phase and code jitter weighting strategy. However, it was found that under extreme levels of scintillation, the positioning accuracy achieved with the mitigation approach still falls short of what can be achieved in a non-scintillation environment, indicating that there is still room to further improve the positioning accuracy under scintillation by exploring alternative scintillation mitigation approaches.

(4) The phase and code jitter maps generated in this study were successfully used for the mitigation of the positioning errors under scintillation. It was also found that the achieved improvements in the positioning accuracy was only around 20% at some stations equipped with generic geodetic receivers. This may be caused by the extra errors in the phase and code jitter induced by the mapping function and the interpolation technique used in the construction of the phase and code jitter maps, or the difference

in the tracking loop configurations between the generic receivers and ISMRs, as described in Section 6.4.3. Therefore, future work can be carried out to investigate the reasons and the potential methods to improve the performance of the phase and code jitter maps in scintillation mitigation.

Reference

Aarons J (1982) Global morphology of ionospheric scintillations. Proceedings of the IEEE 70(4):360-378. https://doi.org/10.1109/PROC.1982.12314

Aarons J, Mullen JP, Koster JP et al (1980) Seasonal and geomagnetic control of equatorial scintillations in two longitudinal sectors. Journal of Atmospheric and Terrestrial Physics 42(9-10):861-866. https://doi.org/10.1016/0021-9169(80)90090-2

Akala AO, Doherty PH, Carrano CS, Valladares CE, Groves KM (2012) Impacts of ionospheric scintillations on GPS receivers intended for equatorial aviation applications. Radio Science 47:RS4007. http://doi.org/10.1029/2012RS004995

Alfonsi L, Cilliers PJ, Romano V, Hunstad I, Correia E, Linty N, Dovis F, Terzo O, Ruiu P, Ward J, Riley P (2016) First observations of GNSS ionospheric scintillations from DemoGRAPE project. Space Weather 14(10):704-709. https://doi.org/10.1002/2016SW001488

Aquino M, Moore T, Dodson A, Waugh S, Souter J, Rodrigues FS (2005) Implications of ionospheric scintillation for GNSS users in Northern Europe. Journal of Navigation 58(2):241-256. https://doi.org/10.1017/S0373463305003218

Aquino M, Andreotti M, Dodson A, Strangeways H (2007) On the use of ionospheric scintillation indices as input to receiver tracking models. Advances in Space Research 40(3):426-435. https://doi.org/10.1016/j.asr.2007.05.035

Aquino M, Monico JFG, Dodson AH et al (2009) Improving the GNSS positioning stochastic model in the presence of ionospheric scintillation. Journal of Geodesy 83(10):953–966. https://doi.org/10.1007/s00190-009-0313-6

Aquino M, Sreeja V (2013) Correlation of scintillation occurrence with interplanetary magnetic field reversals and impact on Global Navigation Satellite System receiver tracking performance. Space Weather 11(5):219-224. https://doi.org/10.1002/swe.20047

Basu S, MacKenzie E, Basu S (1988) Ionospheric constraints on VHF/UHF communications links during solar maximum and minimum periods. Radio Science 23(3):363-378. https://doi.org/10.1029/RS023i003p00363

Basu S, Groves KM, Basu S, Sultan PJ (2002) Specification and forecasting of scintillations in communication/navigation links: current status and future plans. Journal of

Atmospheric and Solar-terrestrial Physics 64(16):1745-1754. https://doi.org/10.1016/S1364-6826(02)00124-4

Borre K, Akos DM, Bertelsen N, Rinder P, Jensen SH (2007) A software-defined GPS and Galileo receiver: a single-frequency approach. Springer Science & Business Media.

Bougard B, Simsky A, Sleewaegen JM, Park J, Aquino M, Spogli L, Romano V, Mendonça M, Galera Monico JF (2013) CALIBRA: mitigating the impact of ionospheric scintillation on precise point positioning in Brazil. In 7th GNSS vulnerabilities and solutions conference.

Breitsch B, Morton YT, Rino C, Xu D (2020) GNSS Carrier phase cycle slips due to diffractive ionosphere scintillation: simulation and characterization. IEEE Transactions on Aerospace and Electronic Systems. https://doi.org/10.1109/TAES.2020.2979025

Briggs B, Parkin IA (1963) On the variation of radio star and satellite scintillations with zenith angle. Journal of Atmospheric and Terrestrial Physics 25(6):339-366. https://doi.org/10.1016/0021-9169(63)90150-8

Chen W, Gao S, Hu C, Chen Y, Ding X (2008) Effects of ionospheric disturbances on GPS observation in low latitude area. GPS Solutions 12:33-41. https://doi.org/10.1007/s10291-007-0062-z

Conker RS, El-Arini MB, Hegarty CJ, Hsiao T (2003) Modelling the effects of ionospheric scintillation on GPS/satellite-based augmentation system availability. Radio Science 38(1):1-1-1-23. https://doi.org/10.1029/2000RS002604

Cristodaro C, Dovis F, Linty N, Romero R (2018) Design of a configurable monitoring station for scintillations by means of a GNSS software radio receiver. IEEE Geoscience and Remote Sensing Letters 15(3):325-329. https://doi.org/10.1109/LGRS.2017.2778938

Curran JT, Bavaro M, Fortuny J, Morrison A (2014) Developing an ionospheric scintillation monitoring receiver. Inside GNSS 9(5):60-72.

da Silva HA, de Oliveira Camargo P, Monico JFG, Aquino M, Marques HA, De Franceschi G, Dodson A (2010) Stochastic modelling considering ionospheric scintillation effects on GNSS relative and point positioning. Advances in Space Research 45(9):1113-1121. https://doi.org/10.1016/j.asr.2009.10.009

Dabove P, Linty N, Dovis F (2019) Analysis of multi-constellation GNSS PPP solutions under phase scintillations at high latitudes. Applied Geomatics. https://doi.org/10.1007/s12518-019-00269-4

Datta-Barua S, Doherty PH, Delay SH, Dehel T, Klobuchar JA (2003) Ionospheric scintillation effects on single and dual frequency GPS positioning. In: Proceedings of ION

GPS/GNSS 2003. Institute of Navigation, Portland, OR, 9-12 September 2003, pp 336 - 346

Davies K (1990) Ionospheric radio. Peter Perrgrinus Ltd., London

Demyanov VV, Sergeeva MA, Yasyukevich AS (2019a) GNSS high-rate data and the efficiency of ionospheric scintillation indices. In: Demyanov VV, Becedas J (ed) Satellites Missions and Technologies for Geosciences 1st edn. Intech Open Limited, London, pp 3

Demyanov VV, Yasyukevich YV, Jin S, Sergeeva MA (2019b) The second-order derivative of GPS carrier phase as a promising means for ionospheric scintillation research. Pure and Applied Geophysics 176(10):4555-4573. https://doi.org/10.1007/s00024-019-02281-6

Forte B, Radicella SM (2002) Problems in data treatment for ionospheric scintillation measurements. Radio Science 37(6):1-5. https://doi.org/10.1029/2001RS002508

Fortes LPS, Lin T, Lachapelle G (2015) Effects of the 2012–2013 solar maximum on GNSS signals in Brazil. GPS Solutions 19(2):309-319. https://doi.org/10.1007/s10291-014-0389-1

Fremouw EJ, Leadabrand RL, Livingston RC, Cousins MD, Rino CL, Fair BC, Long RA (1978) Early results from the DNA Wideband satellite experiment-Complex-signal scintillation. Radio Science 13(1):167-187. https://doi.org/10.1029/RS013i001p00167

Fremouw EJ, Livingston RC, Miller DA (1980) On the statistics of scintillating signals. Journal of Atmospheric and Terrestrial Physics 42(8):717-731. https://doi.org/10.1016/0021-9169(80)90055-0

Ganguly S, Jovancevic A, Brown A, Kirchner M, Zigic S, Beach T, Groves KM (2004) Ionospheric scintillation monitoring and mitigation using a software GPS receiver. Radio Science 39(1):1-9. https://doi.org/10.1029/2002RS002812

Gardner FM (2005) Phaselock techniques. Hoboken, New Jersey: John Wiley & Sons.

Guo K, Aquino M, Veettil SV (2019a) Ionospheric scintillation intensity fading characteristics and GPS receiver tracking performance at low latitudes. GPS Solutions 23(2):1-12. https://doi.org/10.1007/s10291-019-0835-1

Guo K, Aquino M, Veettil Vadakke S, Liu Z, Chen W, Marques HA (2019b) Analysis of ionospheric scintillation and its impact on PPP at low latitudes, In: Proceedings of the ION 2019 Pacific PNT Meeting. Institute of Navigation, Honolulu, Hawaii, 8-11 April 2019, pp 835-845. https://doi.org/10.33012/2019.16842

Guo K, Aquino M, Vadakke Veettil S (2020a) Effects of GNSS receiver tuning on the PLL tracking jitter estimation in the presence of ionospheric scintillation. Space Weather 18(7):p.e2019SW002362. https://doi.org/10.1029/2019SW002362

Guo K, Savas C, Vadakke Veettil S, Aquino M, Dovis F (2020b) Measuring ionospheric scintillation effects on carrier tracking loops using a software defined radio GNSS receiver, Manuscript ready for submission

Guo K, Veettil SV, Weaver BJ, Aquino M (2021) Mitigating high latitude ionospheric scintillation effects on GNSS Precise Point Positioning exploiting 1-s scintillation indices. Journal of Geodesy 95(3):1-15. https://doi.org/10.1007/s00190-021-01475-y

Grewal MS, Andrews AP, Bartone CG (2020) Global navigation satellite systems, inertial navigation, and integration. John Wiley & Sons.

Groves PD (2013) Principles of GNSS, inertial, and multisensor integrated navigation systems. Artech House, Boston & London

Hauschild A (2017a) Basic observation equations. In: Teunissen P, Montenbruck O (eds) Springer handbook of global navigation satellite systems, 1st edn. Springer, New York, pp 561-582

Hauschild A (2017b) Combinations of observations. In: Teunissen P, Montenbruck O (eds) Springer handbook of global navigation satellite systems, 1st edn. Springer, New York, pp 583-604

Hegarty C, El-Arini MB, Kim T, Ericson S (2001) Scintillation modelling for GPS-wide area augmentation system receivers. Radio Science 36(5):1221–1231. https://doi.org/10.1029/1999RS002425

Hobiger T, Jakowski N (2017) Atmospheric signal propagation. In: Teunissen P, Montenbruck O (eds) Springer handbook of global navigation satellite systems, 1st edn. Springer, New York, pp 165-193

Humphreys TE, Psiaki ML, Kintner PMJ, Ledvina BM (2005) GPS carrier tracking loop performance in the presence of ionospheric scintillations. In: Proceedings of ION GNSS 2005, Institute of Navigation, Long Beach, CA, USA, September 13-16, pp 156-167

Humphreys TE, Psiaki ML, Kintner PM (2010) Modeling the effects of ionospheric scintillation on GPS carrier phase tracking. IEEE Transactions on Aerospace and Electronic Systems 46(4):1624-1637. https://doi.org/10.1109/TAES.2010.5595583

Hysell DL, Kudeki E (2004) Collisional shear instability in the equatorial F region ionosphere. Journal of Geophysical Research: Space Physics 109:A11301. https://doi.org/10.1029/2004JA010636

Irsigler M, Eissfeller B (2002) PLL tracking performance in the presence of oscillator phase noise. GPS Solutions 5(4):45-57. https://doi.org/10.1007/PL00012911#

Jacobsen KS, Andalsvik YL (2016) Overview of the 2015 St. Patrick's day storm and its consequences for RTK and PPP positioning in Norway. Journal of Space Weather and Space Climate 6:A9. https://doi.org/10.1051/swsc/2016004

Jayachandran PT, Langley RB, MacDougall JW et al (2009) Canadian high arctic ionospheric network (CHAIN). Radio Science 44(01):1-10. https://doi.org/10.1029/2008RS004046

Jiao Y, Morton YT (2015) Comparison of the effect of high-latitude and equatorial ionospheric scintillation on GPS signals during the maximum of solar cycle 24. Radio Science 50(9):886-903. https://doi.org/10.1002/2015RS005719

Jiao Y, Dongyang X, Morton Y, Rino C (2016) Equatorial scintillation amplitude fading characteristics across the GPS frequency bands. Navigation: Journal of The Institute of Navigation 63(3):267–281. https://doi.org/10.1002/navi.146

Juan JM, Aragon-Angel A, Sanz J, González-Casado G, Rovira-Garcia A (2017) A method for scintillation characterization using geodetic receivers operating at 1 Hz. Journal of Geodesy 91(11):1383-1397. https://doi.org/10.1007/s00190-017-1031-0

Juan JM, Sanz J, González-Casado G, Rovira-Garcia A, Camps A, Riba J, Barbosa J, Blanch E, Altadill D, Orus R (2018) Feasibility of precise navigation in high and low latitude regions under scintillation conditions. Journal of Space Weather and Space Climate 8:A05. https://doi.org/10.1051/swsc/2017047

Kaplan E, Hegarty C (2017) Understanding GPS: principles and applications. Artech House, Boston & London

Kaplan ED, Bets JW, Hegarty CJ, Parisi SJ, Milbert D et al. (2017) Fundamentals of satellite navigation. In: Kaplan E, Hegarty C (eds) Understanding GPS: principles and applications, 3rd edn. Artech House, Boston & London, pp 19-88

Knight M, Finn A (1998) The effects of ionospheric scintillations on GPS. In: Proceedings of ION 1998, Institute of Navigation, Nashville, TN, USA, September 15-18, pp 673-685.

Linty N, Dovis F, Alfonsi L (2018) Software-defined radio technology for GNSS scintillation analysis: bring Antarctica to the lab. GPS Solutions 22(4):96. https://doi.org/10.1007/s10291-018-0761-7Liu Z (2011) A new automated cycle slip detection and repair method for a single dual-frequency GPS receiver. Journal of Geodesy 85(3):171-183. https://doi.org/10.1007/s00190-010-0426-y

Luo X, Lou Y, Xiao Q, Gu S, Chen B, Liu Z (2018) Investigation of ionospheric scintillation effects on BDS precise point positioning at low-latitude regions. GPS Solutions 22(3):63. https://doi.org/10.1007/s10291-018-0728-8

Luo X, Lou Y, Gu S, Song W (2019) A strategy to mitigate the ionospheric scintillation effects on BDS Precise Point Positioning: cycle-slip threshold model. Remote Sensing 11(21):2551. https://doi.org/10.3390/rs11212551

Luo X, Gu S, Lou Y, Chen B, Song W (2020) Better thresholds and weights to improve GNSS PPP under ionospheric scintillation activity at low latitudes. GPS Solutions 24(1):17. https://doi.org/10.1007/s10291-019-0924-1

Marques HAS, Monico JFG, Marques HA (2016) Performance of the L2C civil GPS signal under various ionospheric scintillation effects. GPS Solutions 20(2):139-149. https://doi.org/10.1007/s10291-015-0472-2

Marques HA, Marques HAS, Aquino M, Veettil SV, Monico JFG (2018) Accuracy assessment of Precise Point Positioning with multi-constellation GNSS data under ionospheric scintillation effects. Journal of Space Weather and Space Climate 8:A15. https://doi.org/10.1051/swsc/2017043

Mathworks (2021) Curve Fitting Toolbox: User's Guide (R2021a). Retrieved 11 June 2021 from https://uk.mathworks.com/help/pdf_doc/curvefit/curvefit.pdf

McCaffrey AM, Jayachandran PT (2017) Spectral characteristics of auroral region scintillation using 100 Hz sampling. GPS Solutions 21(4):1883-1894. https://doi.org/10.1007/s10291-017-0664-z

Meggs RW, Mitchell CN, Honary F (2008) GPS scintillation over the European Arctic during the November 2004 storms. GPS Solutions 12:281-287. https://doi.org/10.1007/s10291-008-0090-3

Meurer M, Antreich F (2017) Signal and modulation. In: Teunissen P, Montenbruck O (eds) Springer handbook of global navigation satellite systems, 1st edn. Springer, New York, pp 91-120

Mohammed JJ (2017) Precise Point Positioning (PPP): GPS vs. GLONASS and GPS+ GLONASS with an alternative strategy for tropospheric Zenith Total Delay (ZTD) estimation. Dissertation, University of Nottingham

Moraes A, Costa E, de Paula ER, Perrella WJ, Monico JFG (2014) Extended ionospheric amplitude scintillation model for GPS receivers. Radio Science 49(5):315-329. https://doi.org/10.1002/2013RS005307

Moraes ADO, Rodrigues FDS, Perrella WJ, Paula ERD (2012) Analysis of the characteristics of low-latitude GPS amplitude scintillation measured during solar maximum conditions and implications for receiver performance. Surveys in Geophysics 33(5):1107-1131. https://doi.org/10.1007/s10712-011-9161-z

Mushini SC, Jayachandran PT, Langley RB, MacDougall JW, Pokhotelov D (2012) Improved amplitude- and phase-scintillation indices derived from wavelet detrended high-latitude GPS data. GPS Solutions 16(3):363-373. https://doi.org/10.1007/s10291-011-0238-4

Nava B, Radicella SM, Leitinger R, Coïsson P (2007) Use of total electron content data to analyze ionosphere electron density gradients. Advances in Space Research 39(8):1292-1297. https://doi.org/10.1016/j.asr.2007.01.041

Park J, Veettil SV, Aquino M, Yang L, Cesaroni C (2017) Mitigation of ionospheric effects on GNSS positioning at low latitudes. Navigation: Journal of The Institute of Navigation 64(1):67-74. https://doi.org/10.1002/navi.177

Parkinson B, Spilker J, Axelrad P, Enge P (1996) Global positioning system: theory and applications, vol II. American Institute of Aeronautics and Astronautics Inc, Washington

Pi X, Iijima BA, Lu W (2017) Effects of ionospheric scintillation on GNSS-based positioning. Navigation 64:3-22. https://doi.org/10.1002/navi.182

Prikryl P, Sreeja V, Aquino M, Jayachandran PT (2013) Probabilistic forecasting of ionospheric scintillation and GNSS receiver signal tracking performance at high latitudes. Annals of Geophysics 56(2):0222. https://doi.org/10.4401/ag-6219

Razavi A, Gebre-Egziabher D, Akos DM (2008) Carrier loop architectures for tracking weak GPS signals. IEEE Transactions on Aerospace and Electronic Systems 44(2):697-710. https://doi.org/10.1109/TAES.2008.4560215

Rino CL (1979) A power law phase screen model for ionospheric scintillation: 1. Weak scatter. Radio Science 14(6):1135-1145. https://doi.org/10.1029/RS014i006p01135

Rougerie S, Ait-Ighil M, Fabbro V (2016) Impact of GNSS receiver tuning on the estimation of scintillation index. In: Proceedings of ION GNSS+ 2016, Institute of Navigation, Portland, Oregon, USA, pp 1664-1671. https://doi.org/10.33012/2016.14769

RTCA (1996) Minimum operational performance standards for Global Positioning System/Wide Area Augmentation System airborne equipment: Hauptbd, RTCA

Saastamoinen J (1972) Contributions to the theory of atmospheric refraction. Bulletin Géodésique (1946-1975) 105(1):279-298. https://doi.org/10.1007/BF02521844

Savas C, Falco G, Dovis F (2019) A comparative analysis of polar and equatorial scintillation effects on GPS L1 and L5 tracking loops. In: Proceedings of ION ITM 2019, Institute of Navigation, Reston, VA, USA, pp 28-31. https://doi.org/10.33012/2019.16677

Seo J, Walter T, Chiou TY, Enge P (2009) Characteristics of deep GPS signal fading due to ionospheric scintillation for aviation receiver design. Radio Science 44(1):1–10. https://doi.org/10.1029/2008RS004077

Skone S (2000) TECANALYSTM operating manual version 1.0. University of Calgary, Alberta

Skone S, Kundsen K, de Jong M (2001) Limitation in GPS receiver tracking performance under ionospheric scintillation conditions. Physics and Chemistry of the Earth (A) 26:613–621. https://doi.org/10.1016/S1464-1895(01)00110-7

Sleewaegen JM, De Wilde W, Hollreiser M (2004) Galileo AltBOC receiver. Triangle 2:3.

Spirent Communication plc (2016) SimGEN Software User Manual.

Spogli L, Alfonsi L, Romano V, De Franceschi G, Monico JFG, Shimabukuro MH, Bougard B, Aquino M (2013) Assessing the GNSS scintillation climate over Brazil under increasing solar activity. Journal of Atmospheric and Solar-Terrestrial Physics 105-106:199-206. https://doi.org/10.1016/j.jastp.2013.10.003

Sreeja V, Aquino M, Elmas ZG (2011) Impact of ionospheric scintillation on GNSS receiver tracking performance over Latin America: Introducing the concept of tracking jitter variance maps. Space Weather 9(10):1-6. https://doi.org/10.1029/2011SW000707

Sreeja V, Aquino M, Elmas ZG, Forte B (2012) Correlation analysis between ionospheric scintillation levels and receiver tracking performance. Space Weather 10:S06005. https://doi.org/10.1029/2012SW000769

Steenburgh RA, Smithtro CG, Groves KM (2008) Ionospheric scintillation effects on single frequency GPS. Space Weather 6(4):S04D02. https://doi.org/10.1029/2007SW000340

Stevanovic S, Pervan B (2018) A GPS phase-locked loop performance metric based on the phase discriminator output. Sensors 18(1):296. https://doi.org/10.3390/s18010296

Strangeways HJ, Ho YH, Aquino MH, Elmas ZG, Marques HA, Monico JFG, Silva HA (2011) On determining spectral parameters, tracking jitter, and GPS positioning improvement by scintillation mitigation. Radio Science 46(06):1-14. https://doi.org/10.1029/2010RS004575

Tawk Y, Botteron C, Jovanovic A, Farine P (2012) Analysis of Galileo E5 and E5ab code tracking. GPS Solutions 16:243–258. https://doi.org/10.1007/s10291-011-0226-8

Teunissen PJ (1998) Quality control and GPS. In: Kleusberg A, Teunissen PJ (eds) GPS for Geodesy, 2nd edn. Springer, Berlin, Heidelberg, pp 271-318

Teunissen P, Montenbruck O (eds) (2017) Springer handbook of global navigation satellite systems. Springer.

Ward PW (2017) GNSS receivers. In: Kaplan E, Hegarty C (eds) Understanding GPS: principles and applications, 3rd edn. Artech House, Boston & London, pp 339-548

Won JH, Pany T (2017) Signal processing. In: Teunissen P, Montenbruck O (eds) Springer handbook of global navigation satellite systems, 1st edn. Springer, New York, pp 401-442

Vadakke Veettil S, Aquino M, Spogli L, Cesaroni C (2018) A statistical approach to estimate Global Navigation Satellite Systems (GNSS) receiver signal tracking performance in the presence of ionospheric scintillation. Journal of Space Weather and Space Climate 8:A51. https://doi.org/10.1051/swsc/2018037

Vadakke Veettil S, Aquino M, Marques HA, Moraes A (2020) Mitigation of ionospheric scintillation effects on GNSS precise point positioning (PPP) at low latitudes. Journal of Geodesy 94(2). https://doi.org/10.1007/s00190-020-01345-z

Van Dierendonck AJ (1999) Eye on the ionosphere: measuring ionospheric scintillation effects from GPS signals. GPS Solutions 2(4):60-63. https://doi.org/10.1007/PL00012769

Van Dierendonck AJ, Arbesser-Rastburg B (2004) Measuring ionospheric scintillation in the equatorial region over Africa, including measurements from SBAS geostationary satellite signals. In: Proceedings of ION GNSS 2004. Institute of Navigation, Long Beach, CA, September 21-24, pp 316-324

Van Dierendonck AJ, Fenton P, Ford T (1992) Theory and performance of narrow correlator spacing in a GPS receiver. Navigation 39(3):265-283. https://doi.org/10.1002/j.2161-4296.1992.tb02276.x

Van Dierendonck AJ, Klobuchar J, Hua Q (1993) Ionospheric scintillation monitoring using commercial single frequency C/A code receivers. In: Proceedings of ION GPS 1993. Institute of Navigation, Salt Lake City, UT, September 22-24, pp 1333-1342

Vani BC, Shimabukuro MH, Monico JFG (2017) Visual exploration and analysis of ionospheric scintillation monitoring data: The ISMR Query Tool. Computers & Geosciences 104:125-134. https://doi.org/10.1016/j.cageo.2016.08.022

Vani BC, Forte B. Monico JFG, Skone S, Shimabukuro MH, de Oliveira Moraes AO, Portella IP, Marques HA (2019) A novel approach to improve GNSS Precise Point Positioning during strong ionospheric scintillation: theory and demonstration. IEEE Transactions on Vehicular Technology 68(5):4391-4403. https://doi.org/10.1109/TVT.2019.2903988

Verhagen S, Teunissen P (2017) Least-squares estimation and Kalman filtering. In: Teunissen P, Montenbruck O (eds) Springer handbook of global navigation satellite systems, 1st edn. Springer, New York, pp 639-660

Xu D, Morton Y (2017) A semi-open loop GNSS carrier tracking algorithm for monitoring strong equatorial scintillation. IEEE Transactions on Aerospace and Electronic Systems 54(2):722-738. https://doi.org/10.1109/TAES.2017.2764778

Xu R, Liu Z, Li M, Yu M, Chen W (2012) An analysis of low-latitude ionospheric scintillation and its effects on precise point positioning. Journal of Global Positioning Systems 11(1):22-32. http://dx.doi.org/10.5081%2Fjgps.11.1.22

Yeh KC, Liu CH (1982) Radio wave scintillations in the ionosphere. Proceedings of the IEEE 70(4):324–360. https://doi.org/10.1109/PROC.1982.12313

Zhang X, Guo F, Zhou P (2014) Improved precise point positioning in the presence of ionospheric scintillation. GPS Solutions 18(1):51-60. https://doi.org/10.1007/s10291-012-0309-1